

Isogeometric topology optimization for auxetic metamaterials and structures

by JIE GAO

Thesis submitted in fulfilment of the requirements for
the degree of

Doctor of Philosophy

under the supervision of Zhen Luo, Liya Zhao, Liang Gao

University of Technology Sydney
Faculty of Engineering and Information Technology

09/2019

Title of the thesis:

Isogeometric topology optimization for auxetic metamaterials and structures

Ph.D. student:

Jie Gao

E-mail: jie.gao-7@student.uts.edu.au

Supervisor:

A/Prof. Zhen Luo

E-mail: zhen.luo@uts.edu.au

Co-Supervisor and joint-supervisor:

Dr. Liya Zhao

E-mail: Liya.Zhao@uts.edu.au

Prof. Liang Gao

E-mail: gaoliang@mail.hust.edu.cn

Address:

School of Mechanical and Mechatronic Engineering

The University of Technology Sydney, Sydney, NSW 2007, Australia

Certificate of Original Authorship

I certify that the work in this thesis has not previously been submitted for a degree nor has it been submitted as part of requirements for a degree except as fully acknowledged within the text.

I also certify that the thesis has been written by me. Any help that I have received in my research work and the preparation of the thesis itself has been acknowledged. In addition, I certify that all information sources and literature used are indicated in the thesis.

This thesis is the result of a research candidature conducted jointly with Huazhong University of Science and Technology as part of a collaborative degree.

Signature of Student:

Production Note:
Signature removed prior to publication.

JIE GAO

Date: 12/12/2019

Acknowledgments

I would like to take this opportunity to express my deep gratitude to all those who helped me throughout my candidature.

First and foremost, I would like to extend my sincere gratitude to my principal supervisor, A/Prof. Z Luo. During the studying of the course and the writing of the thesis, he had contributed greatly by giving useful suggestions and constructive criticism. He devoted a considerable portion of his time to reading my manuscripts and making suggestions for further revisions. Moreover, he gave me many encouragements and other help in my study and life. Also, I would like to express my heartfelt gratitude to my joint supervisor Prof. L Gao and co-supervisor Liya Zhao for their support and guidance. Their outstanding knowledge, intelligence and wisdom have a profound influence on me.

I also wish to express my gratitude to Dr. Hao Li and Dr Yiqiang Wang. They offered me great help and gave me many valuable suggestions. My sincere thanks should also go to my colleagues Huipeng Xue, Jing Zheng, Shuhao Wu and Xianfeng Man for their support.

My last and special thanks would go to my beloved family for their loving considerations and great confidence in me all through these years.

Jie Gao

Sydney, 2019

Publications and Conference Contributions

International scientific journal publications

- [1] **J Gao**, HP Xue, L Gao & Z Luo. Topology optimization for auxetic metamaterials based on isogeometric analysis. *Computer Methods in Applied Mechanics and Engineering*. 2019, 352: 211-236.
- [2] **J Gao**, Z Luo, H Li & L Gao. Topology optimization for multiscale design of porous composites with multi-domain microstructures. *Computer Methods in Applied Mechanics and Engineering*. 2019, 334: 451-476.
- [3] **J Gao**, L Gao, Z Luo & PG Li. Isogeometric topology optimization for continuum structures using density distribution function. *International Journal for Numerical Methods in Engineering*. 2019, 119: 991-1017
- [4] **J Gao**, Z Luo, H Li, PG Li & L Gao. Dynamic multiscale topology optimization for multi-regional micro-structured cellular composites. *Composite structures*. 2019, 211: 401-417.
- [5] **J Gao**, Z Luo, L Xia & Gao L. Concurrent topology optimization of multiscale composite structures in Matlab. *Structural and Multidisciplinary Optimization*. 2019, Doi:10.1007/s00158-019-02323-6.
- [6] **J Gao**, H Li, Z Luo, L Gao & PG Li. Topology optimization of micro-structured materials featured with the specific mechanical properties. *International Journal of*

Computational Methods. 2019, 15 (8): 1850144.

- [7] **J Gao**, H Li, L Gao & M Xiao. Topological shape optimization of 3D micro-structured materials using energy-based homogenization method. Advances in Engineering Software. 2018, 116: 89-102.
- [8] J Zheng, Z Luo, C Jiang & **J Gao**. Robust topology optimization for concurrent design of dynamic structures under hybrid uncertainties. Mechanical Systems and Signal Processing. 2019, 120: 540-559.
- [9] H Li, Z Luo, M Xiao, L Gao & **J Gao**. A new multiscale topology optimization method for multiphase composite structures of frequency response with level sets. Computer Methods in Applied Mechanics and Engineering. 2019, 356: 116-144

International conference publications

- [10] **J Gao**, Z Luo & L Gao. An Isogeometric Topology Optimization Method for Materials and Structures. In: The World Congress of Structural and Multidisciplinary Optimization, (WCSMO2019) Beijing, China
- [11] **J Gao**, Z Luo, H Li & Gao L. Multiscale Topology Optimization for Integrated Design of the Structure and Materials. In: 13th World Congress on Computational Mechanics (WCCM 2018), New York.

List of Figures

Figure 2-1 Three subfields of structural optimization [1]	7
Figure 2-2 An engineering case using structural optimization [6]	8
Figure 2-3 the basic principle of the homogenization method [2]	11
Figure 2-4 The flowchart of the SIMP method [11]	13
Figure 2-5 The level set function to represent the structural topology [83]	19
Figure 2-6 Estimation of time costs of each component for engineering structure [89]	21
Figure 2-7 Comparisons between FEA and IGA [89]	22
Figure 2- 8 Some results of the IGA-based material description models	26
Figure 2-9 Some results of the IGA-based boundary description models	27
Figure 2-10 Applications of ITO methods	30
Figure 2-11 The NPR behavior of auxetic metamaterials [127]	31
Figure 2-12 Several 2D and 3D auxetic metamaterials	32
Figure 2-13 The framework of the current work with the logical relationship	36
Figure 3-1 NURBS-based IGA for 3D Bridge-type structure	40
Figure 3-2 Cross-sectional view of the IGA mesh for the 3D Bridge-type structure	47
Figure 3-3 The flowchart of the ITO method	53
Figure 3-4 The details of the Cantilever beam	54
Figure 3-5 The initial design of cantilever beam	55
Figure 3-6 The optimized results of cantilever beam	55
Figure 3-7 The intermediate DDFs	55
Figure 3-8 Convergent histories	58
Figure 3-9 The optimized results in three cases	59
Figure 3-10 Intermediate topologies	61
Figure 3-11 Nodal densities at control points in three cases	62
Figure 3-12 The optimized designs in three cases	63
Figure 3-13 Quarter annulus	63
Figure 3-14 The initial design of quarter annulus	64
Figure 3-15 The optimized results of quarter annulus	64
Figure 3-16 The intermediate DDFs	65
Figure 3-17 Convergent histories	65
Figure 3-18 The optimized designs in three cases	67
Figure 3-19 The details of the complex structure	67
Figure 3-20 The optimized designs	68

Figure 3-21 Convergent histories.....	68
Figure 3-22 The details of 3D Michell structure.....	69
Figure 3-23 Convergent histories.....	70
Figure 3-24 The intermediate topologies	71
Figure 3-25 3D printing prototype of the 3D Michell structure	71
Figure 4-1 The construction of the DVF	76
Figure 4-2 Multi-material topology description in the N-MMI model	79
Figure 4-3 The expression and evolving mechanisms of design variables and topology variables	79
Figure 4-4 The details of MBB beam	87
Figure 4-5 Initial design of the MBB beam	88
Figure 4-6 The optimized design of the MBB beam.....	88
Figure 4-7 Convergent histories.....	91
Figure 4-8 Initial design of the MBB beam	92
Figure 4-9 The optimized design of the MBB beam.....	94
Figure 4-10 Convergent histories.....	95
Figure 4-11 The details of Cantilever beam.....	95
Figure 4-12 Convergent histories.....	96
Figure 4-13 Convergent histories.....	100
Figure 4-14 Convergent histories.....	101
Figure 4-15 The details of quarter annulus	105
Figure 4-16 The details of 3D Michell structure.....	107
Figure 5-1 The bulk material composed of a kind of material microstructure	112
Figure 5-2 Nodal densities assigned to control points	116
Figure 5-3 The flowchart of the ITO formulation for auxetic metamaterials	122
Figure 5-4 The initial design of material microstructure	124
Figure 5-5 The optimized designs of material microstructure	125
Figure 5-6 Intermediate density response surfaces of the DDF	125
Figure 5-7 Rotating mechanisms in the optimized 2D auxetic metamaterial	127
Figure 5-8 Iterative curves of 2D auxetic metamaterial.....	127
Figure 5-9 Numerical results of the former twelve cases	128
Figure 5-10 Auxetic microstructures in twelve cases	130
Figure 5-11 3D material microstructure.....	131
Figure 5-12 Four initial designs for 3D material microstructure	131
Figure 5-13 3D auxetic microstructure No. 1	132
Figure 5-14 3D auxetic microstructure No. 2	133
Figure 5-15 3D auxetic microstructure No. 3	133

Figure 5-16 3D auxetic microstructure No. 4	134
Figure 5-17 The 2D-views for four auxetic microstructures	134
Figure 5-18 Convergent histories of Cases 1 and 2	136
Figure 5-19 Intermediate results of Case 1	136
Figure 5-20 Intermediate results of Case 2	137
Figure 5-21 3D auxetic microstructures No. 5 and No.6	137
Figure 5-22 3D auxetic microstructure No. 1	138
Figure 5-23 Auxetic metamaterial and its finite element mesh.....	139
Figure 5-24 Boundary conditions imposed on the auxetic metamaterial.....	139
Figure 5-25 Displacement responses of auxetic metamaterial.....	139
Figure 5-26 Mechanical responses of auxetic metamaterial	140
Figure 5-27 3D printing samples for six auxetic microstructures.....	141
Figure 6-1 The bulk material composed of a kind of material microstructure	144
Figure 6-2 IGA mesh with Gauss quadrature points	147
Figure 6-3 The flowchart of the ITO formulation for auxetic composites.....	152
Figure 6-4 Initial design of the two-material microstructure	155
Figure 6-5 The optimized designs	156
Figure 6-6 The optimized auxetic composite with two materials	158
Figure 6-7 Intermediate results of the combined distributions	159
Figure 6-8 Convergent histories of the objective function and volume fractions.....	160
Figure 6-9 The optimized designs	161
Figure 6-10 The optimized auxetic composite with three materials	163
Figure 6-11 Iterative curves of objective function and volume fractions	163
Figure 6-12 Intermediate results of the combined distributions	164
Figure 6-13 The 3D material microstructure	165
Figure 6-14 The optimized topology of 3D auxetic composite 1 with two materials.....	166
Figure 6-15 The details of the 3D auxetic composite No.1 with $3 \times 3 \times 3$ microstructures...	167
Figure 6-16 Iterative curves of the objective function and volume fractions of two materials	167
Figure 6-17 The optimized topology of 3D auxetic composite 2 with two materials.....	169
Figure 6-18 The details of the 3D auxetic composite No.2 with $3 \times 3 \times 3$ microstructures...	170
Figure 6-19 The optimized topology of 3D auxetic composite No.3 with two materials...	170
Figure 6-20 The details of the 3D auxetic composite No.3 with $3 \times 3 \times 3$ microstructures...	171
Figure 6-21 The optimized topology of 3D auxetic composite No.4 with two materials...	171
Figure 6-22 The details of the 3D auxetic composite No.4 with $3 \times 3 \times 3$ microstructures...	172
Figure 6-23 The deformation mechanisms of four auxetic composites	173
Figure 6-24 The details of the 2D auxetic composite	175
Figure 6-25 Boundary conditions imposed on the 2D auxetic composite	176

Figure 6-26 Displacement responses of the 2D auxetic composite	176
Figure 6-27 3D auxetic composite microstructure No.1	177
Figure 6-28 Auxetic composite No.1 and its finite element mesh with an enlarged view..	178
Figure 6-29 Boundary conditions imposed on the 3D auxetic composite No.1	178
Figure 6-30 Displacement responses of the 3D auxetic composite No.1	179

List of Tables

Table 3-1 The optimized results of the cantilever beam	57
Table 3-2 Knot vectors in three cases	58
Table 3-3 The numerical results in three cases	59
Table 3-4 The optimized results in two cases	60
Table 3-5 The numerical results in three cases	63
Table 3-6 Knot vectors in three cases	66
Table 3-7 The numerical results in three cases	67
Table 3-8 The optimized results of 3D Michell structure	70
Table 4-1 Four “virtual” isotropic solid materials.....	86
Table 4-2 The optimized results of the MBB beam with two materials	90
Table 4-3 The optimized results of the MBB beam with three materials	93
Table 4-4 The optimized results of cantilever beam with two materials	98
Table 4-5 The optimized results of cantilever beam with two materials	99
Table 4-6 The optimized results of cantilever beam with three materials	103
Table 4-7 The optimized results of quarter annulus with M2 and M3 materials	105
Table 4-8 The optimized results of quarter annulus with M2, M3 and M4 materials.....	106
Table 4-9 The optimized results of 3D Michell structure with M2 and M3 materials.....	108
Table 4-10 The optimized results of 3D Michell structure with M2, M3 and M4 materials	109
Table 5-1 The optimized 2D auxetic metamaterial	126
Table 5-2 Numerical results of three cases	130
Table 5-3 The homogenized elastic tensors of four 3D auxetic microstructures	134
Table 5-4 Homogenized elastic tensors of 3D auxetic microstructures No. 5 and 6	137
Table 6-1 Three “virtual” isotropic solid materials	153
Table 6-2 The optimized 2D auxetic composite microstructure	158
Table 6-3 The optimized 2D auxetic composite with three materials	163
Table 6-4 Homogenized elastic tensors of four auxetic composites	172

Abbreviations

SIMP	Solid Isotropic Material with Penalization
ESO	Evolutionary Structural Optimization
BESO	Bi-directional Evolutionary Structural Optimization
LSM	Level Set Method
PLSM	Parameterized Level Set Method
CSRBF	Compactly Supported Radial Basis Function
HJ-PDE	Hamilton-Jacobian Partial Derivative Equation
OC	Optimality Criteria
MMA	Method of Moving Asymptotes
IGA	Isogeometric Analysis
ITO	Isogeometric Topology Optimization
M-ITO	Multi-material Isogeometric Topology Optimization
DDF	Density Distribution Function
TVF	Field of Topology Variable
DVF	Field of Design Variable
NPR	Negative Poisson's Ratio
NURBS	Non-Uniform Rational B-splines

Abstract

It is known that topology optimization is located at the conceptual design phase, which can effectively determine the numbers, connectivity and existence of holes in the structural design domain and evolve design elements to improve the concerned performance. General speaking, topology optimization works as an important tool to seek for the optimal material distribution, which has been identified as one of the most promising sub-field of structural optimization due to its superior features occurring in the conceptual design stage without prior knowledge of the design domain. In the current work, the main intention is to propose a novel numerical method for the topology optimization with more effectiveness and efficiency for the single-material structures and structures with multiple materials. Meanwhile, the proposed topology optimization method is also applied to implement the rational design of auxetic metamaterials and auxetic composites. In Chapter 1, we provide a brief description for the main intention of the current work. In Chapter 2, the comprehensive review about the developments of topology optimization, isogeometric topology optimization and the rational design of auxetic materials is provided.

In Chapter 3, a more effective and efficient topology optimization method using isogeometric analysis is proposed for continuum structures using an enhanced density distribution function (DDF). The construction of the DDF mainly involves two steps: (1) the smoothness of nodal densities is improved by the Shepard function; (2) the higher-order NURBS basis functions are combined with the smoothed nodal densities to construct the DDF with the continuity. A topology optimization formulation to minimize the structural mean compliance is developed

using the DDF and isogeometric analysis (IGA) is applied to solve structural responses. An integration of the geometry parametrization and numerical analysis offer several benefits for the optimization.

The Chapter 4 intends to develop a Multi-material Isogeometric Topology Optimization (M-ITO) method. Firstly, a new Multi-material Interpolation model is established with the use of NURBS (Non-uniform Rational B-splines), termed by the “N-MMI” model, which mainly involves three components: (1) Multiple Fields of Design Variables (DVF); (2) Multiple Fields of Topology Variables (TVF); (3) Multi-material interpolation. Two different M-ITO formulations are developed using the N-MMI model to address the problems with multiple volume constraints and the total mass constraint, respectively. The decoupled expression and serial evolving of the DVFs and TVFs can effectively eliminate numerical difficulties in the multi-material problems.

In Chapter 5, the proposed ITO method is applied for the systematic design of both 2D and 3D auxetic metamaterials. An energy-based homogenization method (EBHM) to evaluate the macroscopic effective properties is numerically implemented by IGA, with the imposing of periodic boundary formulation on material microstructure. An ITO formulation for 2D and 3D auxetic metamaterials is developed using the DDF, where the objective function is defined as a combination of the homogenized elastic tensor. A relaxed optimality criteria (OC) method is used to update the design variables, due to the non-monotonic property of the problem.

In Chapter 6, the proposed M-ITO method is applied for the systematic design of both 2D and 3D auxetic composites. The homogenization, that evaluates macroscopic effective properties

of auxetic composites, is numerically implemented by IGA, with the imposing of the periodic boundary formulation on composite microstructures. The developed N-MMI model is applied to describe the multi-material topology and evaluate the multi-material properties. A topology optimization formulation for the design of both two-dimensional (2D) and three-dimensional (3D) auxetic composites is developed. Finite element simulations of auxetic composites are discussed using the ANSYS to show different deformation mechanisms.

Finally, conclusions and prospects are given in Chapter 7.

Key words: Topology optimization; Isogeometric analysis, Auxetic metamaterials; Auxetic composites; Homogenization.

Contents

Certificate of Original Authorship	I
Acknowledgments	II
Publications and Conference Contributions.....	III
List of Figures	V
List of Tables.....	IX
Abbreviations.....	X
Abstract.....	XI
Contents	i
Chapter 1 Introduction.....	1
1.1 Overview of the project.....	1
1.2 Research contribution	3
1.3 Outline of the thesis	4
Chapter 2 Background and literature review.....	6
2.1 Literature review of topology optimization	6
2.1.1 Homogenization method	10
2.1.2 Solid Isotropic Material with Penalization (SIMP) method.....	11
2.1.3 Evolutionary Structural Optimization (ESO) method.....	13
2.1.4 Level Set Method (LSM)	15
2.2 Literature review of isogeometric topology optimization.....	20
2.2.1 Isogeometric analysis (IGA)	20
2.2.2 Methods of isogeometric topology optimization (ITO)	23
2.2.3 Applications of isogeometric topology optimization (ITO)	28
2.3 Literature review of auxetic metamaterials.....	30
2.4 The framework of the thesis.....	35
Chapter 3 An ITO method using density distribution function (DDF).....	37
3.1 NURBS-based IGA.....	37
3.1.1 NURBS basis functions	38

3.1.2 Geometrical model and spatial discretization	39
3.1.3 Galerkin's Formulation for elastostatics	41
3.2 Density distribution function (DDF).....	43
3.2.1 Smooth nodal densities using the Shepard function	43
3.2.2 NURBS for the construction of the DDF	45
3.3 Isogeometric topology optimization (ITO).....	48
3.3.1 ITO formulation to minimize static compliance	48
3.3.2 Design sensitivity analysis	49
3.4 Numerical implementations	52
3.5 Numerical examples.....	53
3.5.1 Cantilever beam	54
3.5.2 Quarter annulus.....	63
3.5.3 Complex structure.....	67
3.5.4 3D Michell structure	69
3.6 Conclusions.....	72
Chapter 4 A multi-material ITO (M-ITO) method using a NURBS-based Multi- material Interpolation (N-MMI).....	73
4.1 NURBS-based Multi-Material Interpolation (N-MMI)	75
4.1.1 The Field of Design Variables (DVF)	75
4.1.2 The Field of Topology Variables (TVF).....	78
4.1.3 Multi-material interpolation	80
4.2 Multi-material Isogeometric topology optimization (M-ITO)	81
4.2.1 M-ITO formulation to minimize the structural mean compliance	81
4.2.2 Sensitivity analysis of the objective function.....	82
4.2.3 Sensitivity analysis of constraint functions.....	85
4.3 Numerical Examples	86
4.3.1 Messerschmitt-Bolkow-Blohm (MBB) beam	87
4.3.2 Cantilever beam	95
4.3.3 Quarter annulus.....	104
4.3.4 3D Michell structure	107
4.4 Conclusions.....	110

Chapter 5 Rational design of auxetic metamaterials using ITO method	111
5.1 IGA-based EBHM	111
5.2 Isogeometric topology optimization (ITO)	114
5.2.1 Density distribution function (DDF)	114
5.2.2 ITO formulation for auxetic metamaterials	116
5.2.3 Design Sensitivity analysis	118
5.3 A relaxed OC method	120
5.4 Numerical Examples	122
5.4.1 2D auxetic metamaterials	123
5.4.2 Discussions of the weight parameter	128
5.4.3 3D auxetic metamaterials	130
5.4.4 Simulating validation based on ANSYS	138
5.5 Conclusions	142
Chapter 6 Rational design of auxetic composites using M-ITO method	143
6.1 IGA-based Homogenization	144
6.2 Isogeometric topology optimization (ITO) for auxetic composites	147
6.2.1 ITO formulation	147
6.2.2 Design Sensitivity analysis	149
6.3 Numerical implementations	152
6.4 Numerical Examples	153
6.4.1 2D auxetic composites	154
6.4.2 3D auxetic composite	164
6.4.3 Simulating validation based on ANSYS	174
6.5 Conclusions	180
Chapter 7 Summary and prospects	181
7.1 Summary	181
7.2 Prospects in future works	183
References	185

Chapter 1 Introduction

1.1 Overview of the project

In the last three decades, topology optimization has been accepted extensive discussions about not only the research to promote the developments of the theory, but also applications in many engineering fields to save the cost of materials, time, money and etc. As we know, topology optimization mainly lies in the initial conceptual and preliminary design stage, which aims to offer a basic material distribution with the improved structural performance in the prescribed design space. Compared to size optimization and shape optimization, topology optimization is featured with more challenges in the field of structural optimization, owing to the unknown prior knowledge before the optimization. However, the final solutions obtained from topology optimization can provide more beneficial information for the latter processing of structures, like the detailed design to modify sizes and shapes or the manufacturing. Hence, the extremely high requirements of topology optimization facilitate its developments in many engineering fields. It is of great importance to develop an efficient and effective numerical framework for the implementation of topology optimization.

Meanwhile, metamaterials, which can be regarded as a kind of artificial materials, has been gradually obtained interests among many researchers and engineers. In the viewpoint of the engineering, metamaterials consist of a large number of material microstructures, which are periodically distributed in metamaterials. In the last three decades, the homogenization theory has been proposed to evaluate macroscopic effective properties of porous materials using the information from material microstructures, like the constituent material property, the micro-

architecture and etc. In the recent research works for metamaterials, a critical standpoint that macroscopic effective properties of metamaterials mostly depend on the micro-configuration. Hence, topology optimization work as an efficient numerical tool to seek for the reasonable topology with the expected performance, which has extended to the research area of material science for the design of the micro-architecture with the desired properties. Up to now, several novel metamaterials with the novel micro-architectures are successfully achieved, for instance the electromagnetic metamaterials, acoustic metamaterials, auxetic metamaterials and so on. One of which, auxetic metamaterials, was a kind of metamaterials with the Negative Poisson's Ratios (NPRs), which has several positive mechanic behaviors and many superior engineering applications, like the enhanced shear resistance, indentation resistance, fracture toughness.

Hence, the main intention of the current thesis is to propose a novel numerical method for the topology optimization with more effectiveness and efficiency not only for the single-material structures, but also the structures with multiple materials. Additionally, the currently proposed topology optimization method has been employed to implement the rational design of auxetic metamaterials and also auxetic composites. In Chapter 2, we firstly offer the literature review of several topology optimization methods and discuss the corresponding features of methods, also of isogeometric topology optimization and address the existed research works for it, also of rational design of auxetic metamaterials and composites with the brief descriptions about the multi-material topology optimization. In Chapter 3, the development of a new ITO method for the optimization of the classic static compliance problems has been addressed, and several positive features are presented. In Chapter 4, an efficient N-MMI model is developed for the representation of multiple materials and the computation of the multi-material properties, and

then incorporated into the ITO to develop the M-ITO method for the structures with multiple materials. In Chapter 5, the ITO method combined with the homogenization implemented in the framework of IGA is applied to optimize auxetic metamaterials in both 2D and 3D, and several novel and interesting auxetic microstructures can be found. In Chapter 6, the M-ITO method is employed to discuss the topology optimization of auxetic composites and the IGA-based EBHM is applied to evaluate macroscopic effective properties of auxetic composites.

Finally, it is imperative to notice that the current work is a preliminary research for the ITO method with the simple applications on auxetic materials. In the further, the distinct features of the ITO method need to be sufficiently discussed, including the positive features of IGA, the merits of the DDF to represent the structural topology. Moreover, the further applications of the ITO method also should be performed, such as the macro-scale topology optimization problems in different physical fields, the micro optimization problems of materials design and etc. The utmost important is located at how to implement the ITO method on the engineering applications, like the development of the engineering software.

1.2 Research contribution

The specific objectives and main contributions are provided as follows:

- (1) A novel Isogeometric Topology Optimization (ITO) method with more effectiveness and efficiency is developed. Firstly, a sufficiently smooth and continuity Density Distribution Function (DDF) is developed for the representation of the structural topology, which has the capability to effectively remove several numerical artifacts in previous works. Secondly, the NURBS is innovatively applied to construct the DDF, the structural geometry and numerical

solution space in the analysis to calculate the structural responses, and integrated them into a same mathematical formula. Finally, IGA is an effective and efficient method to guarantee the numerical precision and save the computational cost, which is considered to develop the ITO method.

(2) A novel NURBS-based Multi-Material Interpolation (N-MMI) model is developed and then combined with the ITO method to develop an effective and efficient M-ITO method for the structures with multiple materials. In the construction of the N-MMI model, two kinds of variables are introduced, respectively, namely the Fields of Design Variables (DVs) and the Fields of Topology Variables (TVFs), which are formulated in a manner of the decoupled expression and serial evolving, rather than the coupled and parallel manner. The decoupled expression and serial evolving of the DVs and TVFs can make sure all constraint functions are separate and linear with respect to TVFs, which can provide more benefits for solving the multi-material problems, particularly for the problem with the total mass constraint.

(3) With the use of ITO method, a myriad of novel and interesting auxetic metamaterials with the periodical microstructures are found, particularly in 3D auxetic microstructures.

(4) With the use of M-ITO method, a series of novel and interesting auxetic composites are found and the deformation mechanisms in auxetic composites are presented, including the re-entrant and the chiral types, particularly for 3D auxetic composite microstructures.

1.3 Outline of the thesis

The thesis consists of 7 chapters, shown as follows:

Chapter 1: The background and the overview of this thesis are introduced.

Chapter 2: A literature review of topology optimization, isogeometric topology optimization and auxetic metamaterials is presented in this chapter.

Chapter 3: The descriptions for the development of ITO method, which aims to optimize the DDF with the desired smoothness and continuity, rather than the spatial arrangements of the discrete elements, are provided.

Chapter 4: The N-MMI model for the representation of multiple materials and the calculation of multi-material properties is developed and then combined with the ITO method to construct the M-ITO method for the structures with multiple materials.

Chapter 5: The ITO method is combined with the IGA-based EBHM to study the optimization of auxetic metamaterials and find a series of novel and interesting auxetic microstructures.

Chapter 6: The M-ITO method is combined with the IGA-based EBHM to realize the rational design of auxetic composites and also address different deformation mechanisms of auxetic composite microstructures.

Chapter 7: Conclusions of this work are given and further recommendations are summarized.

Chapter 2 Background and literature review

2.1 Literature review of topology optimization

Structural optimization is a discipline that aims to deal with the optimal design of the load-carrying mechanical structures, which have been considered as a powerful tool to determine structural features, such as the connectivity of holes, the shapes of boundaries and the sizes, in the past decades. As far as the design stage, three subfields are mainly involved in the field of structural optimization, including the topology optimization, shape optimization and size optimization, shown in Figure 2-1. Firstly, size optimization intends to optimize the structural performance by changing the sizes of structural features, like the width, height and the cross-sectional scales, under the pre-defined structural topology and shapes. Secondly, the intention of shape optimization is to evolve the shapes of structural boundaries, like changing from the straight line to a curve of geometry, and then improve the structural performance, where the structural topology should be kept unchanged. Finally, topology optimization lies in the stage of the conceptual design, which determines the numbers, connectivity and existence of holes in the structural domain and advances design elements to improve the concerned performance. Overall speaking, topology optimization working as an important tool to seek for the optimal material distribution in a prescribed design domain, which has been identified as one of the most promising subfield of structural optimization due to its superior features occurring the conceptual design stage without prior knowledge of the design domain. Hence, the extreme requirements of topology optimization pose more challenges during the solving of several different research problems compared to size optimization and shape optimization.

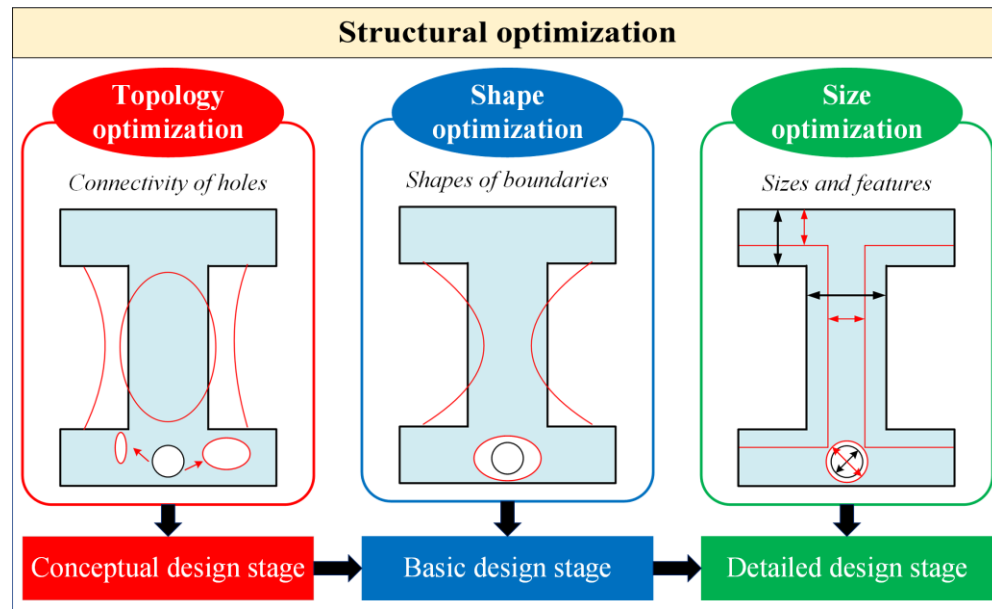


Figure 2-1 Three subfields of structural optimization [1]

Since the seminar work of topology optimization was performed by Bendsøe MP and Kikuchi N [2] where a classic homogenization approach is proposed, topology optimization have been accepted a myriad of applications ranging from the classic mechanical field to other physical disciplines, including the fluids, acoustics, optics and electromagnetics [1,3–5]. As shown in Figure 2-2, an engineering case, namely the structural optimization for the chassis of ford car, is provided. Before the optimization, a suitable design domain needs to be pre-defined, which determines the distribution space of materials. Then, topology optimization, size optimization and shape optimization are applied to evolve the corresponding design elements in the design space, respectively. We can easily find, topology optimization provides a basic distribution of materials including the numbers, connectivity and locations of many holes for the latter size and shape optimization. In the stage of topology optimization, the consumptions of materials have been reduced extensively, in which the structural performance is still improved and can arrive at the basic requirements of the engineering application.

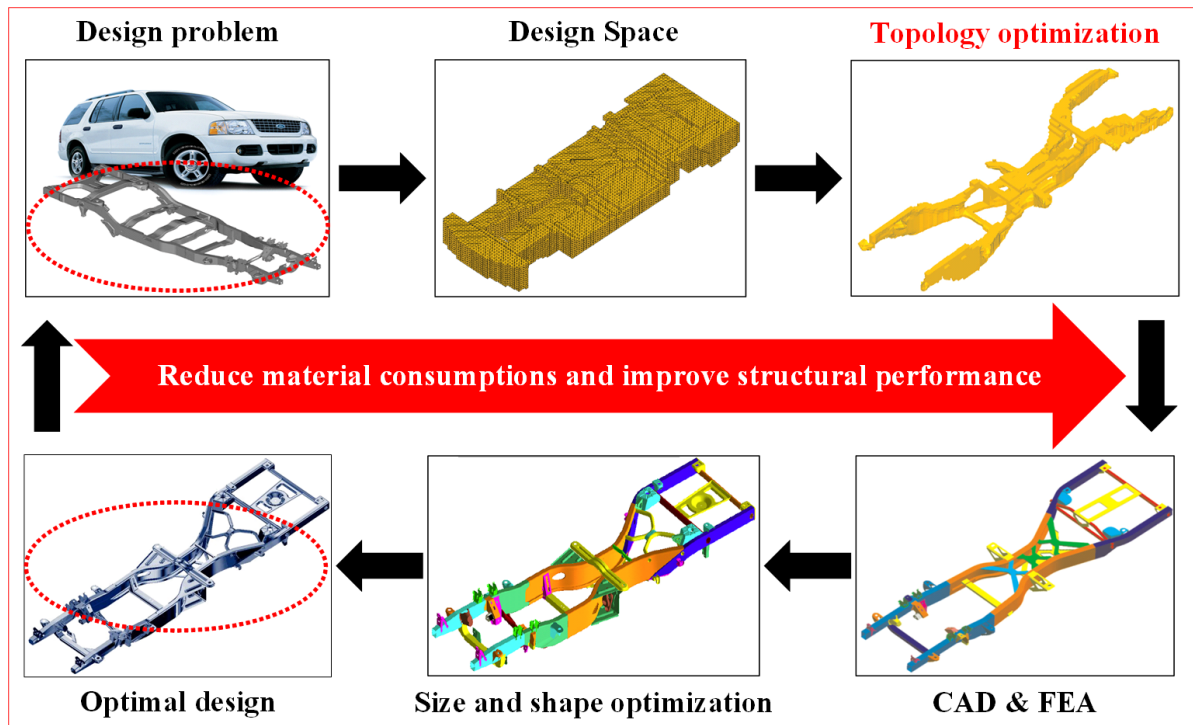


Figure 2-2 An engineering case using structural optimization [6]

As we know, topology optimization is originated from the work in 1904 by Michell [7], where the problem of the limits of economy of material in a frame-structures was studied. However, as far as structural optimization for continuum structures, the research on seeking for the best design of solid elastic plates was addressed by Cheng and Olhoff [8,9], which can be viewed as the seminar works in the field of continuum structural optimization and attracts a wide of discussions in the later three decades. Until 1988, Bendsøe MP and Kikuchi N [2] proposed the homogenization approach based on the theory of porous continuum media distribution, where the structural topology was evolved by changing the sizes and orientations of holes in the domain. So far, several different topology optimization methods with the unique positive features have been developed. In the viewpoint of the topology representation model, several topology optimization methods can be mainly divided into two branches. The first branch of methods mainly consist of the classic homogenization approach [2], Solid Isotropic Material

with Penalization (SIMP) method [10,11] and Evolutionary Structural Optimization (ESO) [12] method, where material description models (MDMs) are used to represent the structural topology in these methods. In the second branch, boundary description models are applied to display the structural topology, and the related methods include the classic Level Set Method (LSM) [13–15], the phase field method [16,17] and the recently proposed Moving Morphable Components (MMC) method [18,19]. A similar feature of these methods in the second branch is that the contour of a high-dimension function is applied to represent structural boundaries. In terms of the first branch, these methods are featured with the conceptual clarity and easily numerical implementations. The methods of the second branch have the rigorous theoretical derivations and smooth structural boundaries of the optimized solutions. Currently, a simple formulation of topology optimization for continuum structures can be read as:

$$\begin{cases} \underset{x}{\text{Minimize}} & J(\chi) \\ \text{S.t.} & \begin{cases} \alpha(\chi) = 0 \\ \beta(\chi) \leq 0 \end{cases} \end{cases} \quad (2-1)$$

where χ denotes topology variables, equal to 0 or 1. 0 indicates voids in design domain and 1 represents solids in space. J is the objective function which is depended on the problem. $\alpha(\chi)$ is the equilibrium equation where structures should be maintained, and $\beta(\chi)$ denotes the constraint equations that should be considered in the optimization, for example material volume constraint. Later, we will provide the details of several different methods, including the homogenization method SIMP, ESO, LSM and MMC for a brief and clear descriptions about the developments of different topology optimization methods in recent years. Moreover, the corresponding basic principle of them is also presented.

2.1.1 Homogenization method

In 1970s, the homogenization method originates from the research field of cellular composites. In cellular composites, a large number of microstructures are periodically distributed leading to a result that cellular composites are highly heterogeneous. The homogenization theory is proposed to evaluate the effective macroscopic properties of cellular composites based on the information from material microstructures [20,21]. Hence, in the area of cellular composites, the homogenization method has been regarded as an efficient way to predict the macroscopic effective properties of porous composites using the micro information. In the light of the area of cellular composites, the macroscopic structure can be viewed as a combination of a series of material microstructures with the corresponding periodicity. In 1988, Bendsøe and Kikuchi employed the specific optimization algorithm to change the spatial directions and geometrical sizes of material microstructures and then evolve the material distribution in microstructures, so that the macro topology has been evolved with the advancement of the features of material microstructures [2]. As shown in Figure 2-3, the key principle of the homogenization method for the topology optimization is given, where the macrostructure with the boundary conditions and material microstructure with the features including the shape, sizes and spatial angles are contained. The topology optimization of structures to improve the static performance has been studied in the first work of the homogenization method by Bendsøe and Kikuchi [2]. Then, Suzuki and Kikuchi [22] used the homogenization method to realize the shape and topology optimization of structures. In [23], the solutions to shape and topology optimization for the eigenvalue problems are studied by the homogenization method, and then Díaz and Kikuchi also employed the homogenization method to address the problem of structures with multiple

loading conditions [24]. After that, Hassani and Hinton [25–27] provided a systematic review about the homogenization theory, the numerical solutions and how to combine the optimality criterion algorithm for address the topology optimization.

As we know, the homogenization method has the rigorous mathematical derivations to ensure the existence and uniqueness of the topology optimization, which has been accepted a wide of attention and applications. Meanwhile, it is noticed that the core of the homogenization method is to transform the discrete problem of the topology optimization for structures into a continuous problem. However, there are also some drawbacks of the homogenization method, such as a large number of design variables, the complex theoretical derivations, the optimal design with the porous form introducing several difficulties for the latter manufacturing.

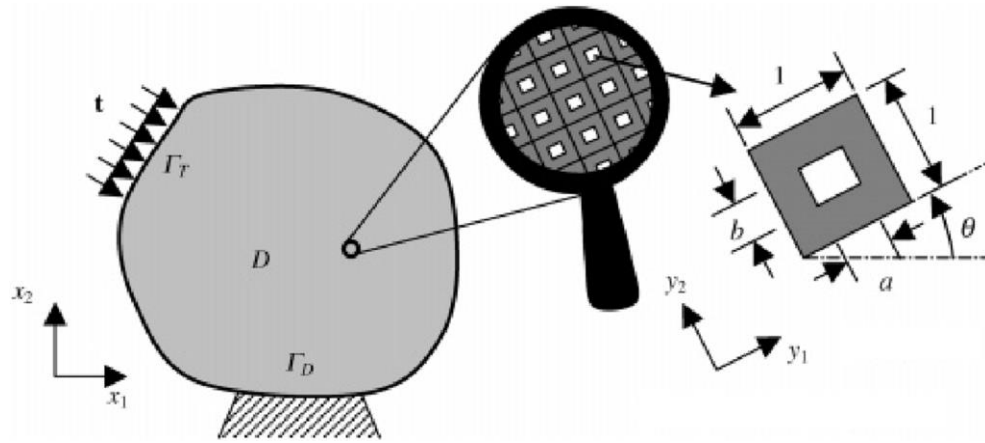


Figure 2-3 the basic principle of the homogenization method [2]

2.1.2 Solid Isotropic Material with Penalization (SIMP) method

After the development of the homogenization method for the topology optimization, a large number of research workers have devoted to solving the numerical difficulties of this method and proposing several improvements. Later, the density method with an effective and efficient manner has gradually developed by Bendsøe, Rozvany and Sigmund [10,11], for example the

well-known Solid Isotropic Material with Penalization (SIMP) method. In the SIMP method, a family of artificial continuous element densities within the range $[0, 1]$ are introduced and then an isotropic material interpolation model is developed with the use of the element density to predict material elastic property, which realizes an explicit description between the material elastic property and the artificial element densities. Meanwhile, a penalization mechanism is developed to enforce element densities to be equal 0 or 1, which aims to reduce the existence of intermediate densities in the final design. As we can see, the SIMP method uses the values of densities to determine the existence of materials in the design domain, such as 0 (voids) and 1 (solids), rather than the features of material microstructures in homogenization method. However, it is important to note that several numerical difficulties are existed in the optimized designs due to the introducing of the artificial densities, such as the mesh dependency, local designs and the checkerboards, which have a significant influence on the effectiveness of the SIMP method. Certainly, several numerical techniques have been proposed to address these problems, like the filtering mechanism and perimeter control constraint [28–30].

As shown in Figure 2-4, the flowchart of the SIMP method for the topology optimization of structures is provided, which mainly contains the finite element analysis to solve the unknown structural responses, the calculation of sensitivity analysis, the filtering mechanism to element densities, the computation of the objective and constraint functions and the evolving of design variables using OC algorithm. We can easily see that the zig-zag features are always existed in the final topologically optimized designs using the SIMP method. Hence, it is imperative to introduce several post-processing mechanisms to smooth the structural boundaries for the latter manufacturing. It is known that the clarity concept and easy numerical implementations

of the SIMP method have attracted a large number of researchers to perform the research or the applications. The SIMP method have been also successfully applied to solve a myriad of problems, such as the dynamic [31–33], compliant mechanisms [34,35], the electromagnetic [36,37], the acoustic [38,39], the geometrical nonlinearities [40,41], the robust optimization [42,43], the piezoelectric systems [44,45] and etc.

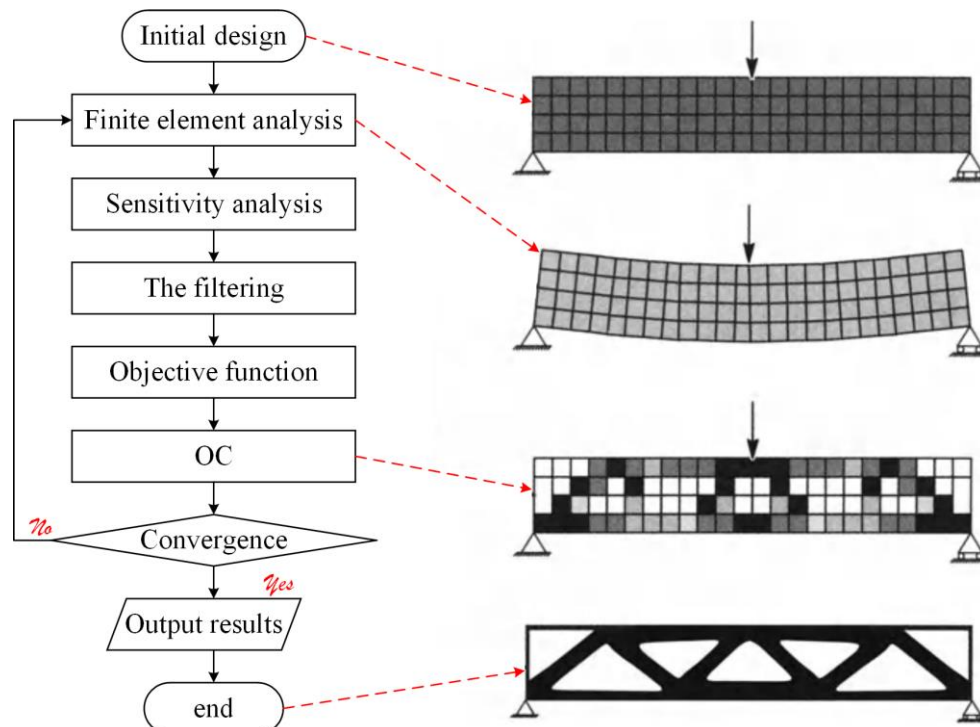


Figure 2-4 The flowchart of the SIMP method [11]

2.1.3 Evolutionary Structural Optimization (ESO) method

In 1993, Xie and Steven [12] have developed an Evolutionary Structural Optimization (ESO) method based on the natural evolution. Compared to the SIMP method, the ESO method also introduce the artificial element densities to represent the structural topology. However, there are no intermediate element densities, and the densities in the optimization by ESO method are equal to 0 (voids) or 1 (Solids). In comparison with the SIMP method, the ESO method

has several similar features in the optimization, such as the finite element analysis to discretize the design domain into a series of elements, the introducing of densities in any elements acting as design variables, the imposing of boundary and load conditions and the computation of the objective and constraint functions. However, the utmost important characteristic of the ESO method is to develop an appropriate criterion to evaluate the contribution of each element on the structural performance, and the contribution of each element will determine its existence in the next optimization stage. In the early stage, the ESO method can only remove elements with the lowest contribution, namely the hard-killing manner. Later, Huang and Xie [46,47] proposed a soft-killing mechanism which cannot only eliminate the elements with the lowest contribution, but also adding the elements with the increasing contribution in the optimization, namely Bi-directional evolutionary structural optimization (BESO) method.

Overall speaking, ESO/BESO method is more intuitive to realize the topology optimization compared to other methods. Meanwhile, the easy numerical implementations of ESO/BESO method also attract several researchers, which also have been gained a myriad of applications on several problems with its effectiveness. In 1996, Xie and Steven has successfully addressed the effectiveness of the ESO method on the dynamic problems [48]. Liu et al also employed the BESO method to realize the sound insulation of the pyramidal lattice sandwich structure [49], which can be effectively utilized for designing light-weight load bearing structures for ranging from ground to aerospace vehicles. Zhao et al [50] addressed the internal architecture of emergent plants using the BESO method, who provided a comprehensive discussion about the main reason of the organs in plants living in the same natural environment and evolving into a wide variety of geometric architecture. Huang, Radman and etc [51–53] also used the

ESO/BESO method to discuss the topology optimization of material microstructures with the extreme material properties, like the maximal bulk modulus and maximal shear modulus. Xia et al [54–56] realized the multiscale topology optimization for the nonlinear design of material microstructures and the macrostructure using the BESO method. Recently, Xia et al also [57] provided a systematic and comprehensive review about the BESO method on the topology optimization of structures and materials. However, a critical problem that interpret the final optimal solution to the manufacturable structure also exists in the ESO/BESO method, mainly due to the zigzag structural boundaries.

2.1.4 Level Set Method (LSM)

Level set method is known as a numerical technique to track the interface and shape, which has been extensively used in the computation of the evolving curve in the Cartesian grid. The basic principle of the LSM is to introduce a higher-dimension level set function to represent the structure, namely the implicit boundary representation model, where the zero-level set of the function is applied to represent the structural boundaries, the negative and positive values of the level set function are applied to represent the voids and solids in design domain. Hence, the evolving of the zero-level set of the function can describe the advancing of the structural boundaries with respect to the time, and the LSM is suitably applied to the problems with the considerations of the structural interface, like the descriptions of the image, the modelling of the fire in spatial and etc [58,59]. A critical feature that the structural boundaries is gradually changed with respect to the time in spatial occurs in the level set method, which provides the possibility to advance the structural topology and improve the structural performance during the optimization.

The first work of the LSM to the topology optimization can be go back to [13], where Sethian and Wiegmann employed the level set function to describe the structural topology and used the structural stress to construct the evolving mechanism for the changing of the structural boundaries. The evolving of the zero-level set of the function realize the representation of the advancing of the structural topology with respect to the time and the space. Later, Sethian and Wiegmann [60] also employed the LSM to discuss the frequency problem of a two-density inhomogeneous drum, where the objective function is defined by the difference between the 2-order eigenfrequency and the 1-order eigenfrequency. After that, Michael Wang et al [14] developed the level-set topology optimization method based on the combination of the shape derivatives and the level set method, in which the normal velocities of the structural boundary evolving bridge the Hamilton-Jacobi Partial Differential Equations (H-J PDEs) and the shape derivatives. In the level-set topology optimization method, the upwind scheme and the finite difference method are employed to solve the H-J PDEs to advance the structural boundaries. Later, Michael Wang et al [61] also applied the level-set topology optimization method to the multi-material problems in structures using a “color” level set mechanism. Allaire et al [15] developed a level-set topology optimization method based on a combination of the classical shape derivatives and of the level-set method for front propagation, where the velocities are obtained by the rigorous derivations of the shape derivatives, and then the proposed level-set topology optimization method has been successfully applied to address the problems of the structural eigenfrequency [62]. Based on the previously-mentioned works of [14,15], a novel framework of the level-set topology optimization method with the solutions of the H-J PDEs to advance the structural topology is gradually developed, which attracts many researchers to study different topology optimization problems.

Based on the proposed level-set topology optimization method using a combination of shape derivatives and the LSM for front propagation, several classic problems have been addressed successfully, like the static compliance [14,15], the dynamic optimization [62,63], the stress minimization [64,65], the compliant mechanisms [66,67] and etc. until now, this method has experienced the considerable developments with a wide range of applications including fluid mechanics, combustion, computer vision, image processing, material science, and so on. As we know, the success of the level-set topology optimization method can be attributed to the role of curvature in numerical regulation, which can assure a meaningful vanishing viscosity solution. Compared to material distribution models, such as the SIMP method and ESO/BESO, the level-set topology optimization is actually a shape optimization method but with a superior capability to implement the shape and topology optimization. Hence, the optimized topologies will be featured with the smooth boundaries which can provide several benefits for the latter manufacturing. In the other viewpoint, the level-set topology optimization method can be also viewed as a numerical process of the dynamic implicit interfaces that possesses the positive features of both the explicitly boundary-based method and also the material distribution-based methods. Hence, several inherent physical merits will be presented by the level-set topology optimization method: (1) a smooth and distinct boundary description for the optimized design, (2) the shape fidelity and higher topological flexibility during the optimization, (3) the shape and topology optimization are performed simultaneously and (4) a physical meaning solution of the H-J PDEs.

However, the level-set topology optimization method also has several numerical difficulties during the optimization due to the rigorous mathematical solutions, where the upwind scheme

and finite difference method are applied to solve the H-J PDEs to derive the evolving of the structural topology during the optimization. In the direct solving the H-J PDEs using the upwind scheme, the strict Courant-Friedrichs-Lewy (CFL) condition should be satisfied, where the step of the finite difference should be smaller than the time step to ensure the stability of the optimization. However, this feature will lead to a large number of iterations occurred in the optimization, which causes the computational cost to be increased. On the other side, the velocities at the structural boundaries should be extended to a narrow area or the whole design domain, which can ensure the reasonably evolving of the structural boundaries. However, the extension scheme of the velocities will have a significant effect on the optimization. Finally, the most important aspect of the level-set topology optimization is a numerical technique of shape optimization, which in actual cannot nucleate the new holes in the optimization due to the non-existence of the generation mechanism for holes. So that, the initial design needs to be homogeneously filled with several holes which can make sure the advancing of the holes to trigger the topologically changes in the optimization. Hence, the effectiveness of the level set topology optimization method will be comprised to some extent. In response to numerical difficulties in the level-set topology optimization method, several variants have been proposed. In [68], a combination of both the level-set topology optimization method and the topological derivation is considered to ensure the generation of new holes. Later, Xia et al [69] developed a semi-lagrange method for level-set-based structural topology and shape optimization, which can effectively eliminate the CFL condition to improve the computational efficiency. One of variants termed by the parametric level set method (PLSM) [70,71] has been considered as a powerful alternative level set method for the topology optimization, which not only inherits the positive merits, but also eliminates the unfavorable features of the standard LSM. In the

PLSM, the time-space coupled level set function is interpolated by the Compactly Supported Radial Basis Functions (CSRBFs), so that the advancing of structural boundaries is equivalent to the evolution of the sizes of expansion coefficients of the CSRBFs. Hence, the complicated structural optimization has been transformed into a much easier “size” optimization problem. Moreover, many well-established efficient optimization algorithms can be directly cooperated into the PLSM to improve the optimization efficiency, like the optimality criteria (OC) [10] and method of moving asymptotes (MMA) [72]. After that, many advanced problems have been discussed by the PLSM to show its effectiveness, like the manufacturing constraint [73], functional graded materials [74,75], multi-materials [76], robust optimization [77], the micro optimization to obtain the novel metamaterials [78–80], the multiscale topology optimization for porous composites [81–84]. Later, in order to improve the computational efficiency in the construction of CSRBFs, a more efficient PLSM was proposed by combining with the discrete wavelet transform scheme for the global and local frequency response optimization problems [85]. Additionally, the distance regularized scheme is also considered in the PLSM to improve the numerical stability in the optimization [86–88].

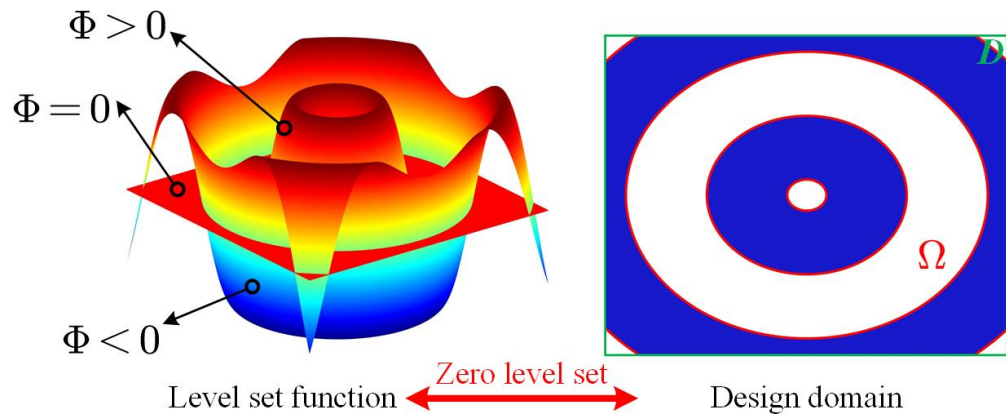


Figure 2-5 The level set function to represent the structural topology [83]

In a word, compared to material distribution models, like the SIMP method and ESO/BESO, an important characteristic of the level set method is that the topological changes are triggered by the advancing of the structural boundaries during the optimization. The topologies during the optimization have the smooth boundaries and clear interfaces all the time.

2.2 Literature review of isogeometric topology optimization

2.2.1 Isogeometric analysis (IGA)

As we know, the period of an engineering structure should experience from the initial design using the engineering Software to the last manufacturing. In the period, the initial Computer Aided Design (CAD) files should be translated into the analysis-suitable geometries, and then meshed, input the engineering analysis software to achieve the Computer Aided Engineering (CAE) files. This period is trivial with a prohibitive computational cost, particularly for the complex engineering structures. As displayed in Figure 2-6, the estimation of the time costs of each component for the engineering structure is provided [89,90]. We can see that the task for the CAD takes over 80% of the overall analysis time. Engineering designs are becoming increasingly more complex. However, the analysis-suitable models cannot be automatically obtained from the meshes of the CAD geometry. The time is consumed to a great extent for the preparatory steps involved, and no finite element mesh is no longer enough. Hence, the today's bottleneck in CAD-CAE integration is not only automated mesh generation, it lies with efficient creation of appropriate "simulation-specific geometry". As shown in Figure 2-6, mesh generation costs 20% of overall analysis time, and the creation of the "simulation-specific" geometry accounts for about 60% and only 20% of overall time is actually devoted

to the analysis. The 80/20 modelling/analysis ratio is a very common industrial experience and it is desirable to reverse it. Hence, it is imperative to perform the integration of CAD and CAE to save the time cost for engineering structures from the CAD to CAE. Meanwhile, it also seems that fundamental changes should take place to fully integrate the engineering design and analysis processes, namely the way to construct CAD and CAE.

On the other side, the conventional finite element method (FEM) is employed to perform the numerical analysis to predict the unknown structural responses. The inherent deficiencies of the FEM would introduce several numerical difficulties in the latter analysis. The first is that the finite element mesh cannot capture the exact structural geometry, which will considerably lower the numerical precision [89,90]. The second is the lower-order (C0) continuity between the neighboring finite elements, also existed in the higher-order elements. The final drawback is the low efficiency of the FEA in achieving a high quality of the finite element mesh. It can be easily observed that the above shortcomings significantly affect the numerical precision.

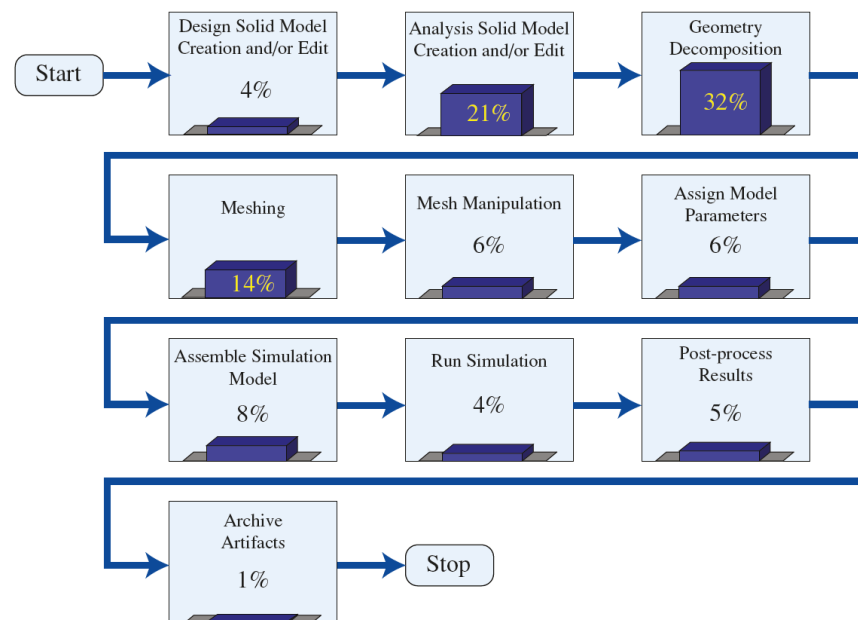


Figure 2-6 Estimation of time costs of each component for engineering structure [89]

The isogeometric analysis (IGA) proposed by Hughes and his co-workers [89,90] might be viewed as a logical extension and generalization method to perform the numerical analysis. The central idea is that the basis functions employed to construct the structural geometry are simultaneously applied to develop the finite dimensional solution space in numerical analysis, so that the geometrical model and the numerical analysis model can be consistent. In the IGA, several different B-splines techniques can be employed, for example the initial B-splines basis functions [89,90]. Although the B-splines are flexible for modeling many geometries, some important shapes can not be exactly presented, like the circles and ellipsoids. Hence, non-uniform Rational B-splines (NURBS) working as a generalization of B-splines is introduced, where the NURBS basis functions are formed by assigning a positive weight to each B-spline basis functions [91,92]. Recently, other candidate computational geometry technologies have been applied into IGA, like the T-splines [93]. In terms of the B-splines, they possess several useful mathematical properties, such as the ability to be refined by knot insertion, the higher-order continuity for the geometry and analysis, the variation diminishing to remove the local oscillatory and the convex hull properties.

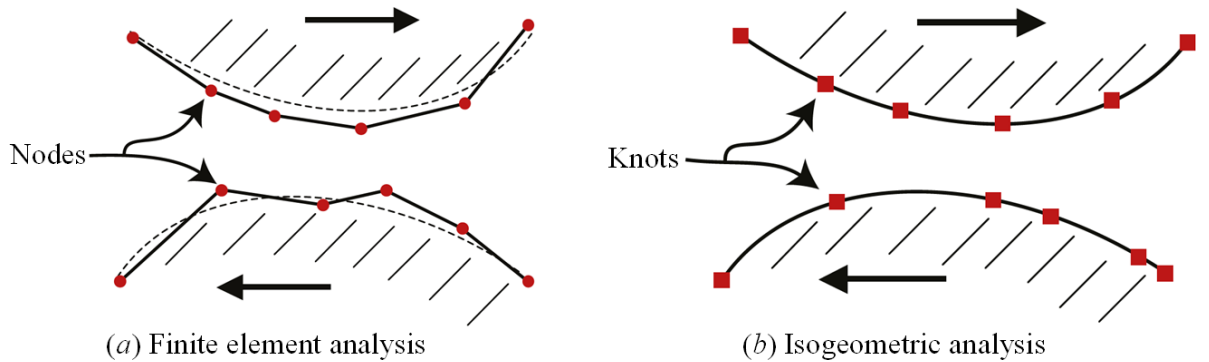


Figure 2-7 Comparisons between FEA and IGA [89]

As shown in Figure 2-7, an example for the sliding contact using the finite element analysis and isogeometric analysis is presented. It can be easily seen that the nodes in the finite element

analysis are not located at the structural boundaries, which cannot exactly represent structural geometry. However, in the isogeometric analysis, the constructed geometry can have a perfect coincidence compared with the initial structural geometry.

2.2.2 Methods of isogeometric topology optimization (ITO)

Since IGA was proposed by Hughes and his co-workers [89,90] to integrate CAD and CAE in a mathematical model and remove several numerical difficulties in the conventional finite element analysis, several researchers have devoted to developing new topology optimization methods using IGA, rather than the finite element methods. As previously pointed out in the above paragraphs, three drawbacks of the finite element methods will significantly affect the effectiveness of the topology optimization for structures. The first work introducing IGA into topology optimization might go back to [94], where the trimmed spline surfaces were applied to present the boundaries in an isogeometric topology optimization framework. Later, we aim to provide an extensive discussion about the application of IGA into topology optimization, which will be mainly divided into two branches, including material description models and boundary description models.

In terms of material description models, the SIMP method is a known numerical technique to search for the optimal material distribution in the prescribed structural design domain, subject to the pre-defined boundary and load conditions. The earlier work to introduce IGA into the SIMP method can be track to [95], where the control point-based SIMP method is developed and material density is considered as a continuous function approximated by the NURBS in the design domain. Later, Qian [96] also developed a B-spline space for topology optimization on the basis of the SIMP method and simultaneously provided a detailed discussion for the

B-spline filter to remove the numerical difficulties. Yin et al [97] developed an isogeometric bi-directional evolutionary structural optimization method for the topology optimization of structures using ESO/BESO method. It should be noticed that the intrinsic feature of material description models is inherited in previously mentioned works, where densities works as the design variables to represent the structural topology.

As we know, the SIMP method and its most variants assign the densities to all finite elements to discretize the domain, where element densities are gradually evolved, and the densities will be piecewise constant in each element. Hence, the key purpose to search for the continuous material distribution in the space is fully converted into the spatial arrangement of the element densities. An alternative variant that the nodal design variables have been introduced in the optimization formulations, is developed to eliminate the numerical difficulties and generate the distinct material interfaces. Matsui and Terada [98] proposed a CAMD (the continuous approximation of material distribution) method to emphasis the material density field in the structural design domain. A Q4/Q4 numerical implementation to maintain the C0 continuity of the design variables in the SIMP-based model is presented to suppress the checkerboard pattern [99]. However, an important numerical issue, the ‘islanding’ or ‘layering’ structures, is occurred in the optimized solutions. After that, Paulino et al [100] rearranged the design variables points in Q4 elements to avoid the ‘islanding’ phenomenon by the internal averaging technique. Guest et al [101] introduced the nodal design variables and a projection scheme to control the minimum length. Kang and Wang [102,103] developed the interpolation scheme by the Shepard function to avoid the ‘islanding’ or ‘layering’ structures and addressed the physical meanings of the nodal design variables. Later, Luo et al [104] developed a dual-level

density interpolation by the Shepard function within the framework of the meshless Galerkin method. As we can conclude, the density distribution function in previous works is developed by the interpolation schemes using the Lagrange polynomials. However, the oscillatory of the Lagrange polynomials might lower the smoothness and continuity of the DDF. In the IGA-based SIMP methods, the similar feature is that densities are both defined at all control points, and then the density of each IGA element is approximately defined by the central point. Later, Gao et al [105] also developed an isogeometric topology optimization for structures using a Density Distribution Function (DDF) with the desired smoothness and continuity to represent the structural topology, where densities at Gauss quadrature points are evaluated to compute the IGA stiffness matrix.

As shown in Figure 2-8, some numerical results of the IGA-based material description models are provided, where the results of Figure 2-8 (A) are from [95], the results of Figure 2-8 (B) are from [96] and the results of Figure 2-8 (C) are from [105]. As we can easily see, the results in Figure 2-8 (C) are featured with the smooth structural boundaries and the distinct interfaces between solids and voids, due to the sufficiently smooth and continuous DDF to represent the structural topology. However, the structural boundaries of two previous results displayed in Figure 2-8 (A and B) are still zig-zag and also wavy.

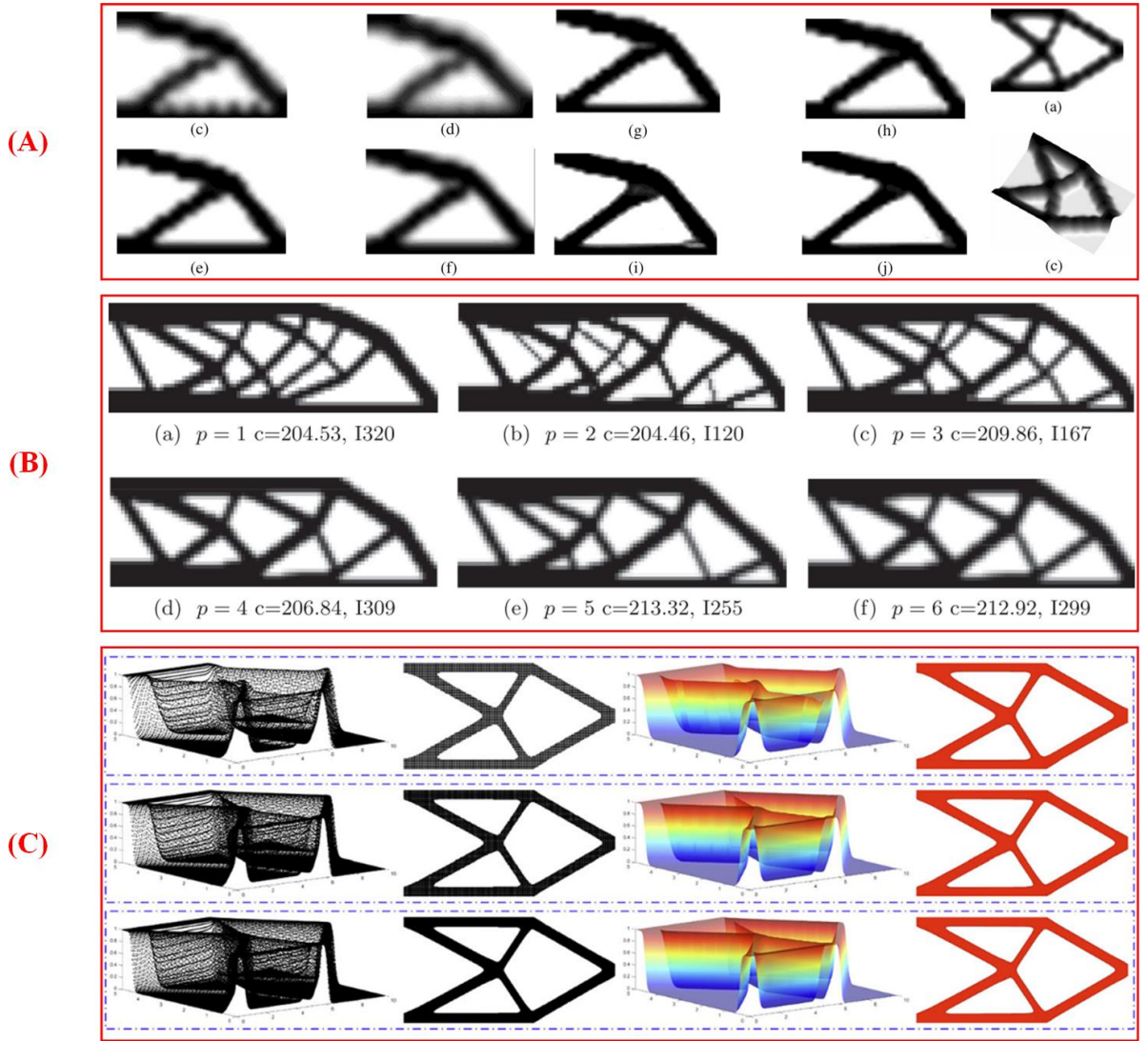


Figure 2- 8 Some results of the IGA-based material description models

In IGA, it is known that NURBS are applied to construct the structural geometry, which have some similar features compared to the level set function. Hence, the IGA has been extensively discussed in boundary description models. The earlier work uses the trimmed spline surface to present the structural boundaries [94]. Later, Dedè et al. also [106] developed a phase field model with the IGA to solve the mean compliance problem. After that, the level-set topology optimization combined with the IGA has been extensively studied, where a higher-dimension level set function was constructed by the NURBS basis functions with the values of the level

set function defined at the control points. In [107,108], a parametrized LSM-based structural topology using the IGA is studied, where the NURBS-based level set function is interpolated by the NURBS basis functions. Later, Kang et al. [109] also performed the IGA-based level-set topology optimization but for shell structures with the use of the trimmed NURBS surfaces. In [110], the IGA-based level-set topology optimization for flexoelectric materials was also addressed. Later, Jahangiry et al [43] discussed the IGA-based LSM topology optimization framework for stress optimization problems. After that, a new IGA-based moving morphable component (MMC) topology optimization method was developed based on R-functions and collocation schemes [111], and the IGA-based MMC topology optimization method was also studied by Hou et al [112].

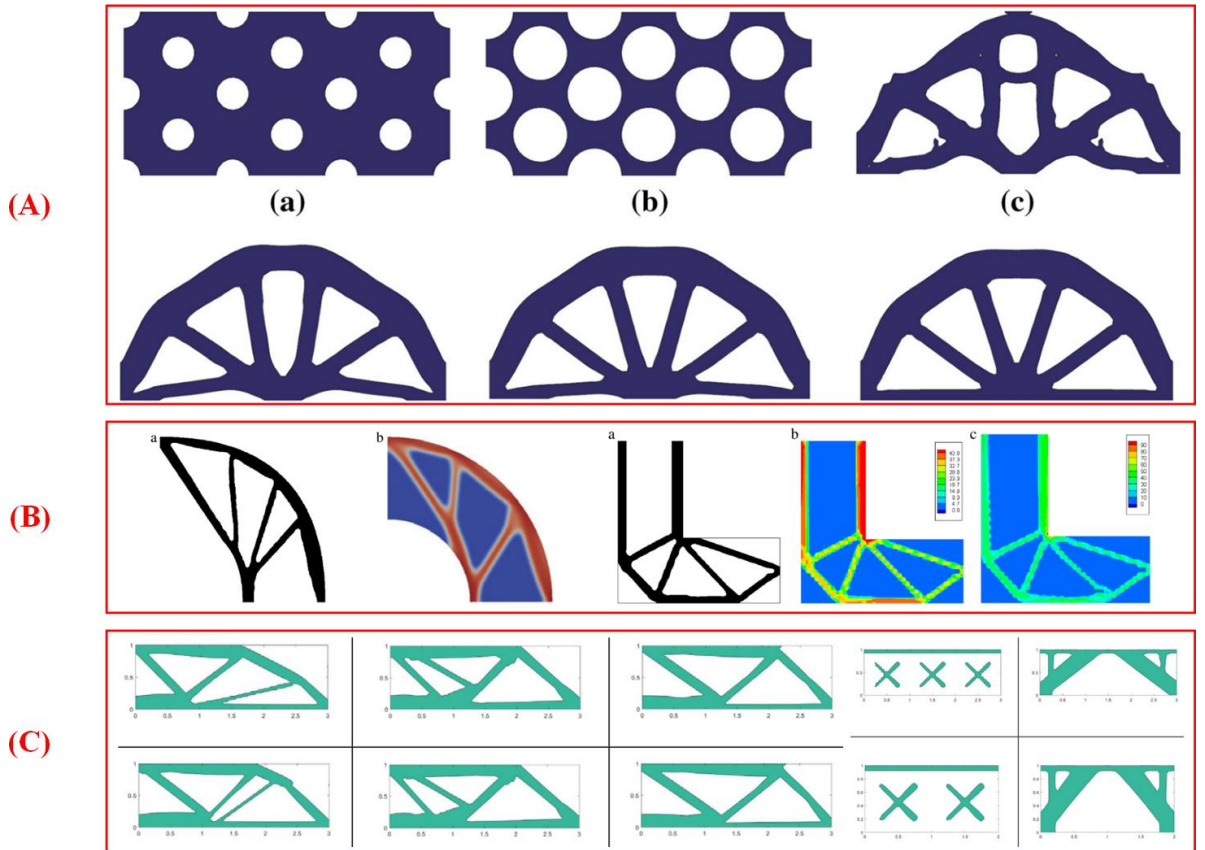


Figure 2-9 Some results of the IGA-based boundary description models

As displayed in Figure 2-9, we provide some results of the IGA-based boundary description models, mainly including the level-set topology optimization method and the MMC method. The results of Figure 2-9 (A) from [107,108] and of Figure 2-9 (B) from [43] are presented, where the level-set topology optimization method is considered. The results of Figure 2-9 (C) from [112] are performed on the basis of the MMC method. As we can see, a similar feature of the results is that the optimized designs are featured with the smooth structural boundaries and distinct interfaces between solids and voids, which shows a perfect connection between the boundary description models and IGA.

2.2.3 Applications of isogeometric topology optimization (ITO)

In the above discussions about the methods of ITO, we can find that the combination of the conventional topology optimization methods and IGA have been discussed sufficiently, from the material description models to boundary description models. Here, we will provide a brief description about the applications of ITO methods.

Firstly, with the discussions of the combination of several topology optimization methods and IGA, the static problems with the maximization of the stiffness performance are considered in the IGA-based topology optimization, such as the IGA-based material description models [95,96,105] and the IGA-based boundary description models [106–108,110–114]. After that, the dynamic problems considering the optimal eigenfrequencies or free vibration have been studied by Taheri et al [115,116]. The IGA-based level-set topology optimization have been applied to different objects, such as the optimization of shell structures [109] and flexoelectric materials [110]. The multiresolution topology optimization and then application to the design of multiple materials in the design domain have been addressed by the IGA-based material

description models, respectively in [117] and [118]. [119] have performed the size and shape optimization of multidirectional functionally graded plates using an isogeometric multi-mesh design approach. Later, the isogeometric approach to topology optimization of the multi-material distribution and functional graded materials is studied by Taheri and Suresh [120]. The geometrical constraints was also discussed in the topology optimization of structures on the basis of the IGA-based material description models [121]. Additionally, the stress-related topology optimization problems were also discussed by the IGA-based material description models [122] and the IGA-based boundary description models [114]. The IGA-based level-set topology optimization method was also applied to the realization of shape optimization using the dual evolution [123]. As we can see, most of the existed works using IGA are only performed for the macro-scale topology optimization problems. Although the IGA-based shape optimization has already been studied in the applications of the smoothed petal auxetic structures [124], only a limited number of works are devoted to the optimization of 2D and 3D auxetic metamaterials using the IGA-based material description models [125]. Wang et al [126] addressed the multiscale topology optimization for lattice materials using an IGA-based SIMP method, where lattice materials with uniform and graded relative density are considered and mechanical properties are expressed by a function of the relative density of the unit cell. Hence, we can find that the discussions of the IGA-based topology optimization on different applications are also performed in a great number, not only in the conventional macro-scale topology optimization problems, but also considering the micro optimization in the design of auxetic metamaterials and lattice materials, shown in Figure 2-10.

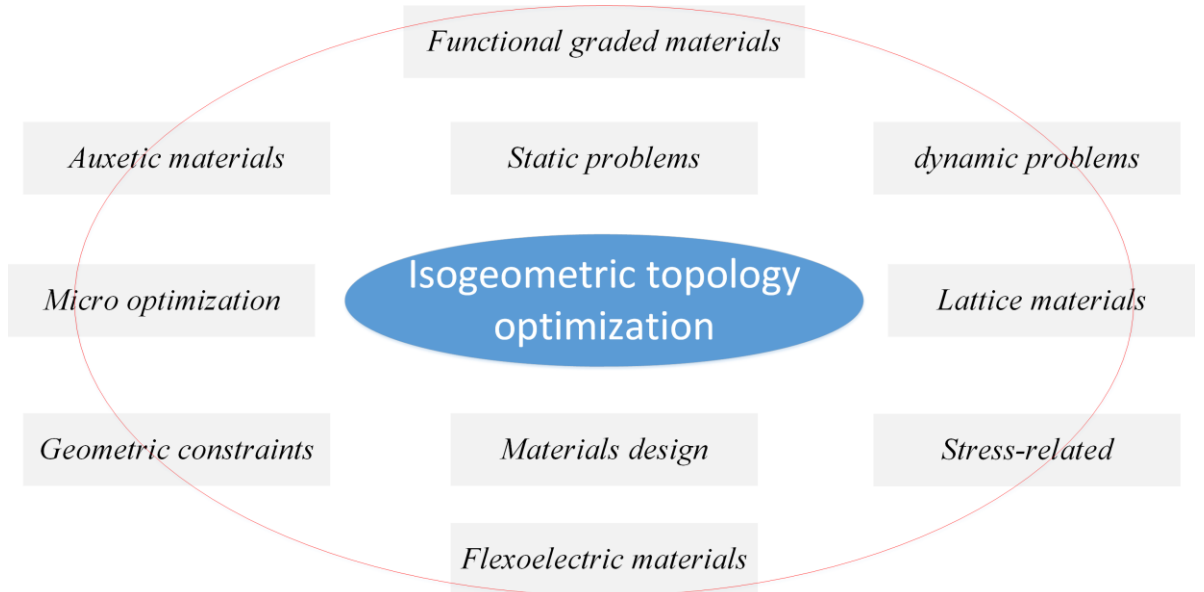


Figure 2-10 Applications of ITO methods

2.3 Literature review of auxetic metamaterials

Auxetic metamaterials are a kind of rationally artificial materials with the Negative Poisson's Ratio (NPR), which exhibit the counterintuitive dilatational behavior. As shown in Figure 2-11, the NPR behavior of auxetic metamaterials is presented. In terms of the nature materials, if we expand materials along one normal direction, and materials will be contracted in other normal directions. As far as auxetic metamaterials, the structural deformation is completely different compared to nature materials, that is expanding laterally if stretched and contracting laterally when compressed. The first of auxetic behavior was firstly found in foam structures by Lake [127]. After that, auxetic metamaterials have gained a wide range of applications in engineering, due to their enhanced shear resistance, indentation resistance, fracture toughness and etc [128].

As already noted in the definition of the rationally designed artificial materials [127,129], it is well-known that the effective macroscopic properties of auxetic metamaterials are mainly

dependent on the architecture of the microstructure that are periodically distributed in the bulk material, rather than the constituent properties of the base material. Hence, many works have devoted to adjusting the geometrical configuration of material microstructures to achieve the artificial materials with the NPRs behavior, including the sizes and shapes of microstructures [130–133]. Up to now, many auxetic metamaterials with different deformation mechanisms are provided, such as the re-entrant structures [130,134], the chiral mechanism [131,135,136], the rotating-type structure [137]. A comprehensive review for the state-of-the-art of auxetic metamaterials with different deformation mechanisms can refer to [128,138,139]. As we can see, the earlier analytical, numerical or experimental methods are developed on the basis of the human intuition and insight to derive the evolution of the structural sizes or shapes in the design of auxetic materials, which might be a limitation to constrain the further findings of auxetic materials. Topology optimization [1], which is a mathematical programming method, has great promise to enable the finding of the optimal material distribution with the expected concerned performance in the domain. Meanwhile, Since the homogenization method [20] is developed to evaluate macroscopic effective properties of porous composites, an inverse homogenization procedure is proposed to realize the optimization of a base material cell with the prescribed negative Poisson ratio -1 [140] using topology optimization.

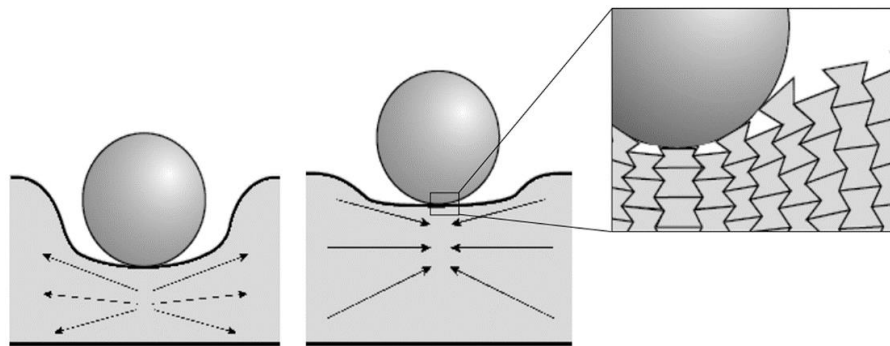


Figure 2-11 The NPR behavior of auxetic metamaterials [127]

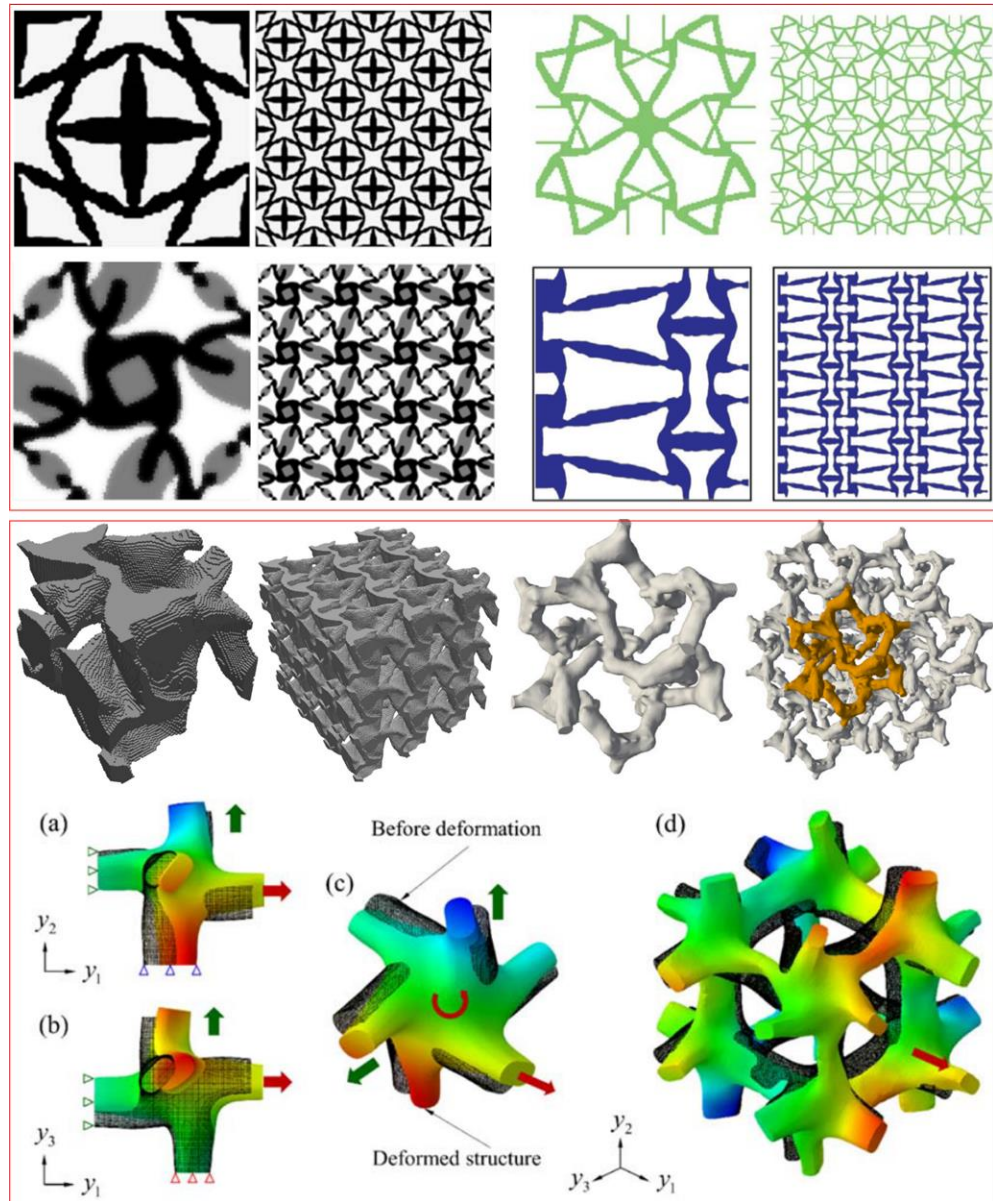


Figure 2-12 Several 2D and 3D auxetic metamaterials

Later, this work is inspired and extended to the topology optimization of rationally artificial materials with the extreme or novel properties [141], particularly for auxetic metamaterials with the NPRs behavior. By now, there are a great number of research works for the topology optimization of material microstructures with the auxetic behavior, e.g. [142–149]. The earlier work to find auxetic materials using topology optimization might go back to [150], where an

3D optimized auxetic microstructure was achieved. After that, several works were performed to optimize 2D auxetic materials with auxetic behavior [146,151,152] using many methods. In [144,148,153], the nonlinear properties were also considered in the optimization of material microstructures with the programmable Poisson's ratios, and a subsequent shape optimization was applied to achieve any given Poisson's ratio in 3D auxetic microstructures [148]. Zong et al [149] developed a two-step design process for microstructures with the desired Poisson's ratios, where material optimization method was firstly used to generate a preliminary solution and then boundary evolution optimization was applied to refine the quality of the structural surfaces for the manufacturing. The PLSM was also used to optimize auxetic microstructures [143]. The polygonal finite elements were employed to realize the topology optimization of auxetic structures with the use of compliant mechanisms [152]. Topology optimization has been applied to implement 3D auxetic microstructures, but it still keeps challenging when the iterative efficiency comes into the picture. For instance, in [142], a highly dense finite element mesh (100^3) to ensure the numerical precision was used in the optimization of 3D material microstructures with the auxetic behavior, but with a large number of iterations (overall 3000), which might limit the further applications of most topology optimization methods in finding the novel auxetic microstructures. An alternative strategy, that the geometric symmetries are pre-imposed on material microstructures, is discussed to reduce the design freedoms to a great extent [148,149]. However, the reduced design space might lower the possibility to search for the novel auxetic microstructures. Hence, a more effective and efficient topology optimization method for designing 3D auxetic metamaterials is still in demand. As shown in Figure 2-11, several auxetic metamaterials with the NPR microstructures in both 2D and 3D are provided. In the first red box of Figure 2-11, a series of 2D auxetic metamaterials are presented, where

the corresponding auxetic microstructures are optimized by topology optimization methods on the basis of material description models and boundary description models. In the second red box of Figure 2-11, 3D auxetic metamaterials with the re-entrant deformation mechanism and the chiral deformation mechanism are also provided, where material description models and boundary description models are both employed.

Additionally, a composite material, which is made from two or more constituent materials, has significantly or preferably physical, chemical or mechanical properties [154] if compared to traditional materials, like stronger, lighter or less expensive. Recently, the applications of the composites have made great progress in some engineering fields. It is known that one of the main limitations of auxetic materials is too porous to afford structural loads in the designs (not stiff enough) [127–129,135]. Hence, the auxetic composites with the multiple functionals has become more and more important in the engineering. [155] proposed a concept to develop composite structures with isotropic NPR behavior, and the fabrication of a 3D double-arrow-head auxetic structures was also discussed in [156]. Hybrid materials with spherical and cubic inclusions were addressed in [157]. As far as topology optimization for auxetic composites, a reconciled level set method was employed to optimize the bi-material microstructures with the NPRs [158], where a series of 2D re-entrant auxetic composite microstructures and only a 3D case were found. Topology optimization for the chiral auxetic composites with the bi-material microstructures in 2D were also studied [151], where the specific initial designs with the chiral features were defined to ensure the generation of the chiral deformation mechanism in final designs. As we can conclude, only a few numbers of works have been performed for auxetic composites, particularly in 3D, which constrains their further engineering applications.

Moreover, a unified topology optimization formulation for the re-entrant and chiral auxetic composites is still in demand. Hence, we can easily see that a rational design and realization for 2D and 3D auxetic composites is still in demand. It is an important and meaningful attempt to develop the IGA-based topology optimization methods for the rational design of material microstructures with the auxetic behavior.

2.4 The framework of the thesis

Firstly, as far as topology optimization methods, the material description models with several positive features have been widely employed to solve many engineering problems, as already discussed in the previous sections. However, the previous works that topology optimization methods are developed using the IGA-based material description models, still have several challenges, like the unfavorable designs, numerical issues to affect the optimization stability, and so on. The advantages of IGA cannot be sufficiently considered in the developments of topology optimization methods using material description models. Hence, in the current work, the main intention is to develop a new isogeometric topology optimization method based on material description models, which can naturally inherit the positive features of IGA and also material description models. The developed ITO method can offer more benefits for the latter researches to solve many optimization problems.

Secondly, as far as the topology optimization for auxetic materials, including metamaterials and composites, the previous works still encounter several numerical difficulties, such as the high computational cost of 3D problems to find the novel topologies of auxetic metamaterials, the rational discussions about how to obtain auxetic metamaterials with different deformation mechanisms, including the chiral-type and re-entrant features. Hence, in the current work, the

key intention is to find a series of novel and interesting auxetic metamaterials and composites using the proposed ITO method, which can be also applied to demonstrate its superior abilities on the problem of metamaterials design.

As shown in Figure 2-13, a basic framework of the current work with the logical relationship is provided. In Chapter 3, the ITO method with the superior features is firstly proposed, and its efficiency and efficacy are validated. Chapter 4 presents a new multi-material interpolation model and then which is considered in the ITO method to develop the M-ITO method for the optimization of multiple materials. In Chapter 5, the ITO is combined with an energy-based homogenization method to develop materials design formulation for auxetic metamaterials with a series of novel and interesting topologies in both 2D and 3D. In Chapter 6, the designs of auxetic composites are also studied using M-ITO method combined with the energy-based homogenization method, where a family of novel and interesting auxetic composites can be also found in not only 2D, but also 3D. Finally, Chapter 7 shows the summary and prospects.

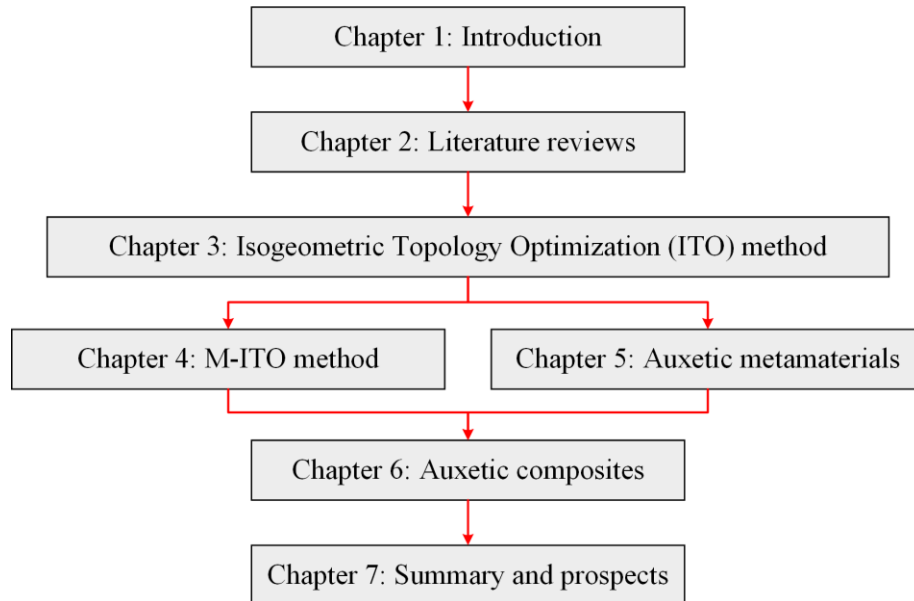


Figure 2-13 The framework of the current work with the logical relationship

Chapter 3 An ITO method using density distribution function (DDF)

In this chapter, we aim to develop a new Isogeometric Topology Optimization (ITO) method using an enhanced Density Distribution Function (DDF) with the sufficient smoothness and continuity, that will be more effective and efficient. It should be noted that the work in this chapter comes from the published paper [105]. In the DDF, the Shepard function is firstly applied to improve the overall smoothness of nodal densities at control points, and the DDF is constructed by NURBS basis functions linearly with the smoothed nodal densities. The IGA and DDF are further employed to develop the ITO formulation for minimizing the structural mean compliance. The ITO method will be applied to optimize not only 2D structures with the rectangle, curved and complex design domains, but also the 3D scenario. Meanwhile, the SLS technique is used to fabricate the optimized 3D designs, which demonstrates the benefits of the additive manufacture for the realization of topologically optimized results.

3.1 NURBS-based IGA

It is known that the key intention of IGA is to keep the geometry exact using the same NURBS basis functions for CAD and CAE models, and the basis functions used to exactly model the geometry serve as the basis for the solution space in numerical methods, like the Galerkin's method [159]. Currently, a large number of candidate computational geometry technologies can be applied into IGA, where NURBS work as the industry standard because of the major strengths to exactly model a wide array of objects [92].

3.1.1 NURBS basis functions

A knot vector with an ordered set of increasing parameters is introduced for the definition of the B-spline curve, written $\Xi = \{\xi_1, \xi_2, \dots, \xi_{n+p+1}\}$, where $\xi_i \in \mathbb{R}$ ($\xi_i \leq \xi_{i+1}$) is the i^{th} knot, n is the number of basis functions to build the B-spline curve and p is the polynomial order. The knot vector partitions the parametric space into a series of sub intervals, generally referred to knot spans. The interval $[\xi_1, \xi_{n+p+1}]$ is called a patch in the parametric space. The B-spline basis functions are defined recursively by the Cox-de-Boor formula, starting with piecewise constants ($p = 0$):

$$N_{i,0}(\xi) = \begin{cases} 1 & \text{if } \xi_i \leq \xi_{i+1} \\ 0 & \text{otherwise.} \end{cases} \quad (3-1)$$

For $p \geq 1$, the basis functions are defined by

$$N_{i,p}(\xi) = \frac{\xi - \xi_i}{\xi_{i+p} - \xi_i} N_{i,p-1}(\xi) + \frac{\xi_{i+p+1} - \xi}{\xi_{i+p+1} - \xi_{i+1}} N_{i+1,p-1}(\xi) \quad (3-2)$$

In the above equation, the fractions with the form 0/0 are defined as zero. It can be observed that the basis functions with $p = 0, 1$ defined in Eqs. (3-1) and (3-2) are same as the standard piecewise constant and the linear finite element functions. The B-spline basis functions with the high order are completely different. Some important properties are listed as follows:

- (1) **Nonnegativity:** $N_{i,p}(\xi) \geq 0$.
- 2) **Local support:** the support of each basis function $N_{i,p}$ is contained in the interval $[\xi_i, \xi_{i+p+1}]$. Also, at most $p + 1$ number of B-spline basis functions are nonzero in the given knot span $[\xi_i, \xi_{i+1}]$, namely the $N_{i-p,p}, \dots, N_{i,p}$.

(3) **Partition of unity:** For an arbitrary knot span, $\forall \xi \in [\xi_i, \xi_{i+1}]$, $\sum_{j=i-p}^i N_{j,p}(\xi) = 1$.

(4) **Continuity:** C^{p-k} where k is the multiplicity of the knots.

Although B-splines are flexible for modeling many geometries, some important shapes are not be exactly described, like circles and ellipsoids. Hence, NURBS acting as a generalization form of B-splines is introduced, and the NURBS basis functions are expressed by the B-spline basis functions with a positive weight ω_i , expressed as:

$$R_{i,p}(\xi) = \frac{N_{i,p}(\xi)\omega_i}{\sum_{j=1}^n N_{j,p}(\xi)\omega_j} \quad (3-3)$$

In two and three dimensions, NURBS basis functions can be constructed as:

$$\begin{cases} R_{i,j}^{p,q}(\xi, \eta) = \frac{N_{i,p}(\xi)M_{j,q}(\eta)\omega_{ij}}{\sum_{i=1}^n \sum_{j=1}^m N_{i,p}(\xi)M_{j,q}(\eta)\omega_{ij}} \\ R_{i,j,k}^{p,q,r}(\xi, \eta, \zeta) = \frac{N_{i,p}(\xi)M_{j,q}(\eta)L_{k,r}(\zeta)\omega_{ijk}}{\sum_{i=1}^n \sum_{j=1}^m \sum_{k=1}^l N_{i,p}(\xi)M_{j,q}(\eta)L_{k,r}(\zeta)\omega_{ijk}} \end{cases} \quad (3-4)$$

where $M_{j,q}$ and $L_{k,r}$ are the B-spline basis functions in other two parametric directions, using knot vectors $\mathcal{H} = \{\eta_1, \eta_2, \dots, \eta_{m+q+1}\}$ and $\mathcal{Z} = \{\zeta_1, \zeta_2, \dots, \zeta_{l+r+1}\}$. q, r are the polynomial orders in two parametric directions, respectively.

3.1.2 Geometrical model and spatial discretization

As shown in Figure 3-1 for the representation of a 3D Bridge-type structure, the 3D NURBS basis functions with a set of control points are employed. The structural design domain, the NURBS solid and the discretized IGA mesh are displayed in Figure 3-1 (a), Figure 3-1 (b),

and Figure 3-1 (c), respectively. The NURBS basis functions in three parametric directions are respectively listed in Figure 3-1 (d), (e) and (f). Given a control lattice $\mathbf{P}_{i,j,k} \in \mathbb{R}^3$, a tensor product NURBS solid $\mathbf{S}(\xi, \eta, \zeta)$ is defined in mathematical form, as:

$$\mathbf{S}(\xi, \eta, \zeta) = \sum_{i=1}^n \sum_{j=1}^m \sum_{k=1}^l R_{i,j,k}^{p,q,r}(\xi, \eta, \zeta) \mathbf{P}_{i,j,k} \quad (3-5)$$

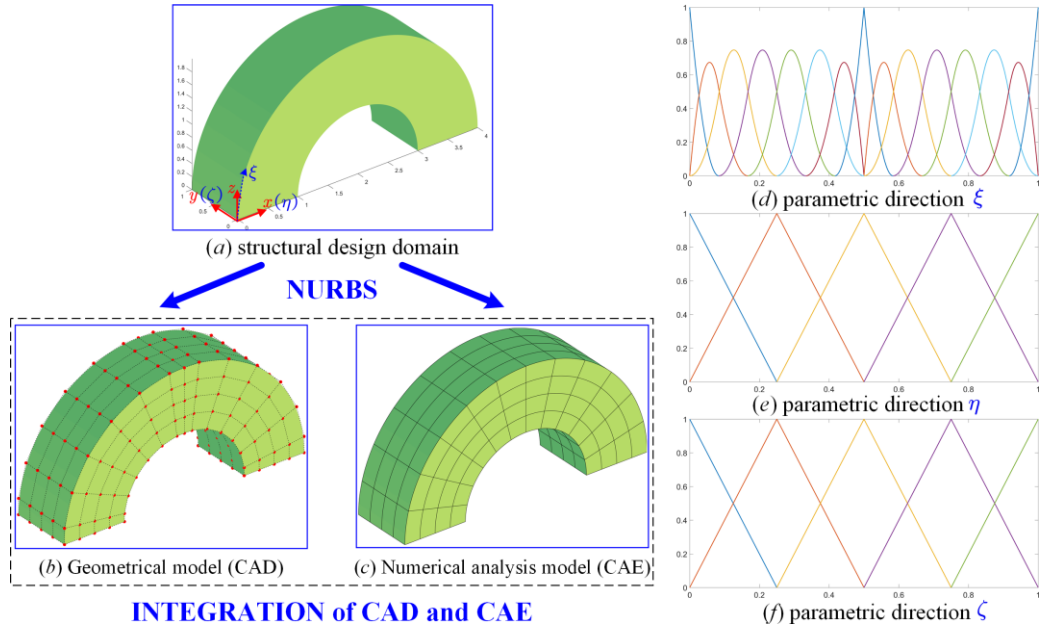


Figure 3-1 NURBS-based IGA for 3D Bridge-type structure

$$\Xi = \{0, 0, 0, 0.0833, \dots, 0.9167, 1, 1, 1\}, \mathcal{H} = \{0, 0, 0.25, 0.5, 0.75, 1, 1, 1\}, \\ \mathcal{Z} = \{0, 0, 0.25, 0.5, 0.75, 1, 1, 1\}; n = 15, m = 5, l = 5; p = 2, q = 1, r = 1.$$

As already pointed out in [89,90], NURBS has some important properties, namely 1) Strong convex hull property; 2) Differentiability; 3) Local modification; 4) Variation diminishing property. The properties are important for the later construction of the DDF. In Figure 3-1 (a), it can be seen that the structure can be exactly represented by the NURBS basis functions with control points. The knot vectors partition the whole patch in the parametric space into an array of knot spans, called elements. In order to distinguish the elements in FEM, the knot spans are named by “IGA elements”. The IGA mesh is also presented Figure 3-1 (c). As displayed

in Figure 3-1 (b) and (c), the control points do not coincide with the nodes in IGA elements. The IGA mesh model is consistent with the geometrical model of the 3D Bridge-type structure.

3.1.3 Galerkin's Formulation for elastostatics

As an example of application of the NURBS-based IGA, the linear elasticity is considered only for the sake of numerical simplicity but without losing any generality. A strong form of the boundary value problem for a design domain Ω bounded by the boundary Γ is formally stated. Given $f_i: \Omega \rightarrow \mathbb{R}$, $g_i: \Gamma_{D_i} \rightarrow \mathbb{R}$, and $h_i: \Gamma_{N_i} \rightarrow \mathbb{R}$, find $u_i: \bar{\Omega} \rightarrow \mathbb{R}$ such that

$$\begin{cases} \sigma_{ij,j} + f_i = 0 & \text{in } \Omega \\ u_i = g_i & \text{on } \Gamma_{D_i} \\ \sigma_{ij} n_j = h_i & \text{on } \Gamma_{N_i} \end{cases} \quad (3-6)$$

where σ is stress tensor, f_i is the body force, and g_i is the prescribed boundary displacement on the Dirichlet boundary Γ_D . h_i is the boundary traction on the Neumann boundary Γ_N . n_j is the unit normal vector to Ω . Defining a trial solution space $\mathcal{S} = \{\mathbf{u} | u_i \in \mathcal{S}_i\}$ and a weight space by $\mathcal{V} = \{\mathbf{w} | w_i \in \mathcal{V}_i\}$, where each trial solution u_i satisfies the Dirichlet condition $u_i = g_i$ on Γ_{D_i} and each weight function w_i is equal to 0 on the Dirichlet boundary Γ_{D_i} . Given $\mathbf{f} = \{f_i\}$, $\mathbf{g} = \{g_i\}$ and $\mathbf{h} = \{h_i\}$, find $\mathbf{u} \in \mathcal{S}$ such that for all $\mathbf{w} \in \mathcal{V}$,

$$\int_{\Omega} \boldsymbol{\varepsilon}(\mathbf{w})^T \mathbf{D} \boldsymbol{\varepsilon}(\mathbf{u}) d\Omega = \int_{\Omega} \mathbf{f} \mathbf{w} d\Omega + \int_{\Gamma_N} \mathbf{h} \mathbf{w} d\Gamma_N \quad (3-7)$$

where $\boldsymbol{\varepsilon}$ corresponds to the strain matrix, \mathbf{D} is the elastic tensor matrix. In the Galerkin's method, the finite-dimensional approximants of the spaces \mathcal{S} and \mathcal{V} are constructed by the NURBS basis functions, denoted by \mathcal{S}^h and \mathcal{V}^h , which includes all linear combinations of the NURBS basis functions. The finite-dimensional nature of the function converts the weak form of the problem into a system of linear algebraic equations, and stated as a form:

$$\int_{\Omega} \boldsymbol{\varepsilon}(\mathbf{w}^h)^T \mathbf{D} \boldsymbol{\varepsilon}(\mathbf{v}^h) d\Omega = \int_{\Omega} \mathbf{w}^h \mathbf{f} d\Omega + \int_{\Gamma_N} \mathbf{w}^h \mathbf{h} d\Gamma_N - \int_{\Omega} \boldsymbol{\varepsilon}(\mathbf{w}^h)^T \mathbf{D} \boldsymbol{\varepsilon}(\mathbf{g}^h) d\Omega \quad (3-8)$$

Introducing a set containing all NURBS basis functions, denoted by \mathcal{A} , and a sub set containing the basis functions that are equal to 0 on the Dirichlet boundary Γ_D , symbolled by \mathcal{B} ($\mathcal{B} \subset \mathcal{A}$). The trial solution $\mathbf{u}^h \in \mathcal{S}^h$ and weight $\mathbf{w}^h \in \mathcal{V}^h$ can be stated as a function of the basis functions with control variables:

$$\begin{cases} \mathbf{u}^h = \sum_{j \in \mathcal{A} \setminus \mathcal{B}} R_j g_j + \sum_{i \in \mathcal{B}} R_i d_i \\ \mathbf{w}^h = \sum_{j \in \mathcal{A} \setminus \mathcal{B}} R_j c_j \end{cases} \quad (3-9)$$

where c is the arbitrary to hold for all $\mathbf{w}^h \in \mathcal{V}^h$. Substituting Eq. (3-9) into Eq. (3-8), the Galerkin form is transformed into the next equation, given as:

$$\left(\int_{\Omega} \boldsymbol{\varepsilon}(R_i)^T \mathbf{D} \boldsymbol{\varepsilon}(R_j) d\Omega \right) d_i = \int_{\Omega} R_j \mathbf{f} d\Omega + \int_{\Gamma_N} R_j \mathbf{h} d\Gamma_N - \int_{\Omega} \boldsymbol{\varepsilon}(R_j)^T \mathbf{D} \boldsymbol{\varepsilon}(g^h) d\Omega \quad (3-10)$$

Proceeding to define

$$\begin{cases} K_{ij} = \int_{\Omega} \boldsymbol{\varepsilon}(R_i)^T \mathbf{D} \boldsymbol{\varepsilon}(R_j) d\Omega \\ F_j = \int_{\Omega} R_j \mathbf{f} d\Omega + \int_{\Gamma_N} R_j \mathbf{h} d\Gamma_N - \int_{\Omega} \boldsymbol{\varepsilon}(R_j)^T \mathbf{D} \boldsymbol{\varepsilon}(g^h) d\Omega \end{cases} \quad (3-11)$$

Hence, Eq. (3-10) can be expanded a more compact matrix form, as:

$$\mathbf{K} \mathbf{d} = \mathbf{F} \quad (3-12)$$

where,

$$\mathbf{K} = [K_{ij}]; \quad \mathbf{d} = \{d_i\}; \quad \mathbf{F} = \{F_j\} \quad (3-13)$$

In IGA, the NURBS basis functions is firstly applied to model the exact geometry, and then discretize the structural geometry into a series of IGA elements, as well as serving as the basis

functions to construct the solution space and weight space. Hence, the NURBS basis functions can integrate the geometry construction, spatial discretization and numerical analysis into a framework.

3.2 Density distribution function (DDF)

It is known that the problem of the material distribution has been transformed to the spatial arrangement of finite elements in several previous works. The structural topology is expressed by the spatial arrangement of finite elements. Two basic requirements must be satisfied to ensure a justified density distribution [102–104]: 1) The nonnegativity of element densities; 2) The strict bounds of element densities, namely $[0, 1]$. In this subsection, the main focus is the construction of the enhanced DDF with the sufficient smoothness and continuity. Firstly, the Shepard function is applied to enhance the smoothness of nodal densities at control points. Secondly, the NURBS basis functions are combined with the preciously smoothed nodal densities to construct the DDF. In this way, The DDF can be regarded as a response surface with a higher dimension with respect to the nodal densities, which is used to represent the density distribution for the design domain.

3.2.1 Smooth nodal densities using the Shepard function

As shown in Figure 3-2, the cross-sectional view of the IGA mesh for the 3D Bridge-type structure is given, including the Gauss quadrature points plotted with the black, the control points shown by the red and green dots and the IGA elements bounded by black lines. In the NURBS solid, each control point is assigned by a nodal density, and a lattice of nodal densities at control points is defined. In the DDF, the overall smoothness of nodal densities should be improved to make sure the sufficient smoothness of the DDF. The basic principle is that each

nodal density is equal to the mean value of all nodal densities located at the local support area of the current nodal density, as shown by the purple circular area in Figure 3-2 (a), as:

$$\mathcal{G}(\rho_{i,j,k}) = \sum_{i=1}^{\mathcal{N}} \sum_{j=1}^{\mathcal{M}} \sum_{k=1}^{\mathcal{L}} \psi(\rho_{i,j,k}) \rho_{i,j,k} \quad (3-14)$$

where $\mathcal{G}(\rho_{i,j,k})$ is the smoothed nodal density assigned to the $(i,j,k)_{th}$ control point, and $\rho_{i,j,k}$ is the initial defined nodal density which should maintain the nonnegative and the range-bounded by 0 and 1. \mathcal{N} , \mathcal{M} and \mathcal{L} are the numbers of the nodal densities located at the local support area of the current nodal density in three parametric directions respectively. $\psi(\rho_{i,j,k})$ is the value of Shepard function [160] at the $(i,j,k)_{th}$ nodal density, and expressed as:

$$\psi(\rho_{i,j,k}) = \frac{w(\rho_{i,j,k})}{\sum_{\hat{i}=1}^{\mathcal{N}} \sum_{\hat{j}=1}^{\mathcal{M}} \sum_{\hat{k}=1}^{\mathcal{L}} w(\rho_{\hat{i},\hat{j},\hat{k}})} \quad (3-15)$$

where $w(\rho_{i,j,k})$ is the weight function of the $(i,j,k)_{th}$ nodal density, and the function can be constructed by many functions, such as the widely used inverse distance weighting function, the exponential cubic spline, quartic spline functions and radial basis functions (RBFs) [161]. The compactly supported RBFs (CSRBFs) with C^4 continuity are used due to the compactly supported, the high-order continuity and the nonnegativity, by:

$$w(r) = (1-r)_+^6 (35r^2 + 18r + 3) \quad (3-16)$$

where $r = d/d_m$, and d is the Euclidean distance between the current nodal density and the other nodal density located at the local support domain. d_m is the radius of the local support domain which reflects the scale of the local support domain, as shown in Figure 3-2 (a). The symbol $+$ denotes the choice of the values larger than 0. It can be seen that the smoothed

nodal densities assigned to the control lattice by the Shepard function can meet the necessary conditions for a physically meaningful material density.

3.2.2 NURBS for the construction of the DDF

In this section, the NURBS basis functions are linearly combined with the nodal densities of control points with the enhanced smoothness to construct a function for the material density.

Assuming that the DDF in the structural design domain is denoted by $\mathcal{X}(\xi, \eta, \zeta)$, given as:

$$\mathcal{X}(\xi, \eta, \zeta) = \sum_{i=1}^n \sum_{j=1}^m \sum_{k=1}^l R_{i,j,k}^{p,q,r}(\xi, \eta, \zeta) \mathcal{G}(\rho_{i,j,k}) \quad (3-17)$$

It can be easily seen that Eq. (3-17) for the DDF has the same mathematical formulation for NURBS solid in Eq. (3-5). The main difference lies in the physical meanings of the control coefficients. Here, the initial NURBS-based geometrical model for 3D structure has been converted into a representation of the 3D DDF. As already pointed out in Section 3.1.1, the NURBS basis functions have the local support property. The global form of the DDF can be expanded as a local form depended on the local support domain of the current knot $(\xi, \eta, \zeta) \in [\xi_i, \xi_{i+1}] \times [\eta_j, \eta_{j+1}] \times [\zeta_k, \zeta_{k+1}]$ ($0 \leq \xi, \eta, \zeta \leq 1$), that

$$\mathcal{X}(\xi, \eta, \zeta) = \sum_{e=i-p}^i \sum_{f=j-q}^j \sum_{g=k-r}^k R_{e,f,g}^{p,q,r}(\xi, \eta, \zeta) \mathcal{G}(\rho_{e,f,g}) \quad (3-18)$$

It can be seen that the properties 1 to 3 of the NURBS basis functions can ensure the DDF with two properties: 1) the Nonnegativity; 2) Strict bounds. Hence, the DDF in Eq. (3-18) can be featured with the strict physical meanings in the optimization formulation. It is important to note that the NURBS basis functions do not satisfy the interpolation property, which has no effect on the DDF. The main reason is that control points are not necessary on the design

domain. The nodal densities only work as control coefficients in the combination with the NURBS basis functions to construct the DDF. This is the key difference compared to the previous works where material density functions are developed by Lagrange polynomials [98–104]. Moreover, the variation diminishing property of NURBS removes the oscillatory of Lagrange polynomials [89,90], which ensure the sufficient smoothness and continuity of the DDF. In the Galerkin IGA formulation, the system stiffness matrix and load vector are achieved by assembling the local stiffness matrix and load vector, respectively. The design domain is discretized by a series of IGA elements. The evaluation of the IGA element stiffness matrix is performed by the Gauss quadrature. In the physical space, the IGA element stiffness matrix and force vector are calculated by:

$$\begin{cases} \mathbf{K}_e = \int_{\Omega_e} \mathbf{B}^T \mathbf{D} \mathbf{B} d\Omega_e \\ \mathbf{F}_e = \int_{\Omega_e} R \mathbf{f} d\Omega_e + \int_{\Gamma_N^e} R \mathbf{h} d\Gamma_N^e - \mathbf{K}_e \mathbf{g}_e \end{cases} \quad (3-19)$$

where Ω_e is the physical domain of the IGA element, as displayed in Figure 3-2, Γ_N^e is the Neumann boundary condition of the IGA element and \mathbf{g}_e is the Dirichlet boundary condition of the IGA element. \mathbf{B} is the strain-displacement matrix calculated by the partial derivatives of the NURBS basis functions with respect to the parametric coordinates, as defined by Eq. (3-11). The isoparametric formulation has been employed in evaluating the element stiffness matrix. As shown in Figure 3-2, a mapping $\mathbf{X}: \hat{\Omega}_e \rightarrow \Omega_e$ from the parametric space to the physical space and an affine mapping $\mathbf{Y}: \tilde{\Omega}_e \rightarrow \hat{\Omega}_e$ from the bi-unit parent element to the element in the parametric space are introduced. The integral for the IGA element stiffness matrix is pulled back first onto the parametric element and then onto the bi-unit parent element, which involves the inverses of the two mappings. The detailed form is given by:

$$\mathbf{K}_e = \int_{\tilde{\Omega}_e} \mathbf{B}^T \mathbf{D} \mathbf{B} |\mathbf{J}_1| |\mathbf{J}_2| d\tilde{\Omega}_e \quad (3-20)$$

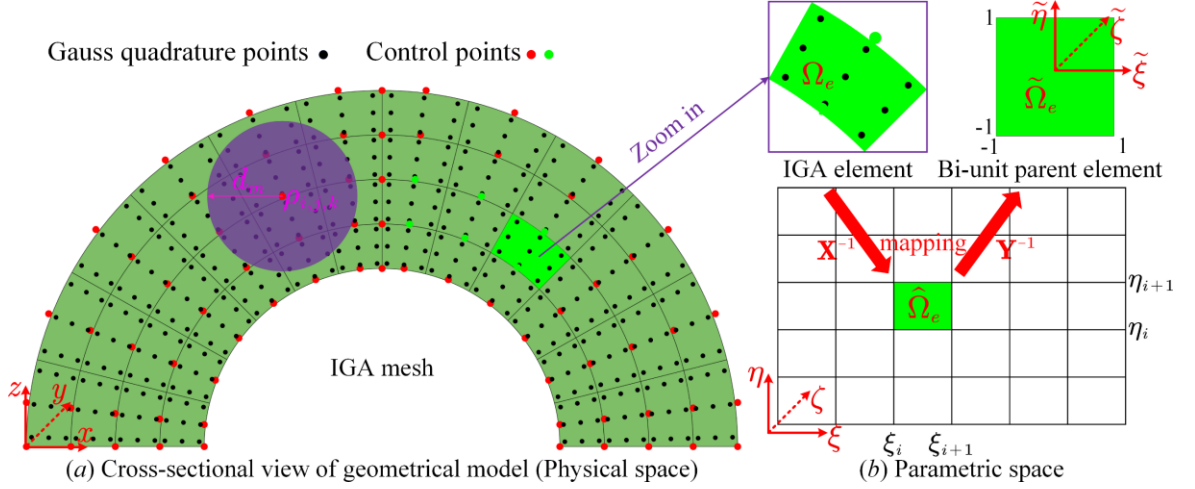


Figure 3-2 Cross-sectional view of the IGA mesh for the 3D Bridge-type structure

where \mathbf{J}_1 and \mathbf{J}_2 are the Jacobi matrices of the two mappings, respectively. All the Gauss quadrature points in the IGA mesh and a 3×3 of the Gauss quadrature points in each IGA element are shown in Figure 3-2. The detailed numerical computation is given by:

$$\mathbf{K}_e = \sum_{i=1}^3 \sum_{j=1}^3 \sum_{k=1}^3 \{ \mathbf{B}^T(\xi_i, \eta_j, \zeta_k) \mathbf{D} \mathbf{B}(\xi_i, \eta_j, \zeta_k) |\mathbf{J}_1(\xi_i, \eta_j, \zeta_k)| |\mathbf{J}_2| w_i w_j w_k \} \quad (3-21)$$

where w_i, w_j and w_k are the corresponding quadrature weights. In the material description model, the elasticity property of the isotropic material is assumed to be a power function of the density with a penalty parameter. Hence, IGA element stiffness matrix can be expressed as a function of the material densities of the Gauss points, rather than the constant element density [98–103], as follows:

$$\mathbf{K}_e = \sum_{i=1}^3 \sum_{j=1}^3 \sum_{k=1}^3 \{ \mathbf{B}^T(\xi_i, \eta_j, \zeta_k) (\mathcal{X}(\xi_i, \eta_j, \zeta_k))^\gamma \mathbf{D}_0 \mathbf{B} |\mathbf{J}_1| |\mathbf{J}_2| w_i w_j w_k \} \quad (3-22)$$

where $\mathcal{X}(\xi_i, \eta_j, \zeta_k)$ is the density of the (ξ_i, η_j, ζ_k) Gauss quadrature point, and γ denotes the penalization parameter. \mathbf{D}_0 is the elastic tensor matrix for the solid density.

3.3 Isogeometric topology optimization (ITO)

3.3.1 ITO formulation to minimize static compliance

In this Section, the DDF is adopted to develop the ITO formulation, with the IGA applied to calculate the related structural responses. Hence, the ITO formulation will iteratively optimize the density distribution represented by the DDF in the design domain, until the topology has the optimal stiffness performance. Here, nodal densities work as design variables at here to evolve the DDF during the optimization, given as:

$$\left\{ \begin{array}{l} \text{Find: } \rho_{i,j,k} \quad (i = 1, 2, \dots, n; j = 1, 2, \dots, m; k = 1, 2, \dots, l) \\ \text{Min: } J(\mathbf{u}, \mathcal{X}) = \frac{1}{2} \int_{\Omega} \boldsymbol{\varepsilon}(\mathbf{u})^T \mathbf{D}(\mathcal{X}(\xi, \eta, \zeta)) \boldsymbol{\varepsilon}(\mathbf{u}) d\Omega \\ \text{S.t: } \left\{ \begin{array}{l} G(\mathcal{X}) = \frac{1}{|\Omega|} \int_{\Omega} \mathcal{X}(\xi, \eta, \zeta) v_0 d\Omega - V_0 \leq 0 \\ a(\mathbf{u}, \delta \mathbf{u}) = l(\delta \mathbf{u}), \quad \mathbf{u}|_{\Gamma_D} = \mathbf{g}, \quad \forall \delta \mathbf{u} \in H^1(\Omega) \\ 0 \leq \rho_{i,j,k} \leq 1 \end{array} \right. \end{array} \right. \quad (3-23)$$

where $\rho_{i,j,k}$ is the initial defined nodal densities to the control points. J is the objective. G is the volume constraint, in which V_0 is the maximum material consumption and v_0 is the volume fraction of the solid material. \mathcal{X} is the DDF. \mathbf{u} is the displacement field within the structural design domain Ω , and \mathbf{g} is the prescribed displacement vector on the Dirichlet boundary Γ_D . $\delta \mathbf{u}$ is the virtual displacement field defined in the Sobolev space $H^1(\Omega)$. a and l are the bilinear energy and the linear load functions, defined as:

$$\left\{ \begin{array}{l} a(\mathbf{u}, \delta \mathbf{u}) = \int_{\Omega} \boldsymbol{\varepsilon}(\mathbf{u})^T \mathbf{D}(\mathcal{X}(\xi, \eta, \zeta)) \boldsymbol{\varepsilon}(\delta \mathbf{u}) d\Omega \\ l(\delta \mathbf{u}) = \int_{\Omega} \mathbf{f} \delta \mathbf{u} d\Omega + \int_{\Gamma_N} \mathbf{h} \delta \mathbf{u} d\Gamma_N \end{array} \right. \quad (3-24)$$

where \mathbf{f} is the body force and \mathbf{h} is the boundary traction on the Neumann boundary Γ_N .

3.3.2 Design sensitivity analysis

The sensitivities of the objective and constraint functions with respect to the design variables are required to evolve the structural topology. In Eq. (3-23), the design variables are the nodal densities, and the derivative of the objective with respect to the DDF can be derived as:

$$\frac{\partial J}{\partial \mathcal{X}} = \int_{\Omega} \boldsymbol{\varepsilon}(\dot{\mathbf{u}})^T \mathbf{D}(\mathcal{X}) \boldsymbol{\varepsilon}(\mathbf{u}) d\Omega + \frac{1}{2} \int_{\Omega} \boldsymbol{\varepsilon}(\mathbf{u})^T \frac{\partial \mathbf{D}(\mathcal{X})}{\partial \mathcal{X}} \boldsymbol{\varepsilon}(\mathbf{u}) d\Omega \quad (3-25)$$

where $\dot{\mathbf{u}}$ is the first-order of the displacement field with respect to the DDF. Performing the derivative on both sides of the equilibrium state equation given in Eq. (3-24), given by:

$$\begin{cases} \frac{\partial a}{\partial \mathcal{X}} = \left\{ \int_{\Omega} \boldsymbol{\varepsilon}(\dot{\mathbf{u}})^T \mathbf{D}(\mathcal{X}) \boldsymbol{\varepsilon}(\delta \mathbf{u}) d\Omega + \int_{\Omega} \boldsymbol{\varepsilon}(\mathbf{u})^T \mathbf{D}(\mathcal{X}) \boldsymbol{\varepsilon}(\delta \dot{\mathbf{u}}) d\Omega \dots \right. \\ \left. + \int_{\Omega} \boldsymbol{\varepsilon}(\mathbf{u})^T \frac{\partial \mathbf{D}(\mathcal{X})}{\partial \mathcal{X}} \boldsymbol{\varepsilon}(\delta \mathbf{u}) d\Omega \right. \\ \frac{\partial l}{\partial \mathcal{X}} = \int_{\Omega} \mathbf{f} \delta \dot{\mathbf{u}} d\Omega + \int_{\Gamma_N} \mathbf{h} \delta \dot{\mathbf{u}} d\Gamma_N \end{cases} \quad (3-26)$$

where $\delta \dot{\mathbf{u}}$ is the first-order derivative of the virtual displacement field with respect to the DDF. Considering that $\delta \dot{\mathbf{u}} \in H^1(\Omega)$, the equilibrium state equation is given as:

$$\int_{\Omega} \boldsymbol{\varepsilon}(\mathbf{u})^T \mathbf{D}(\mathcal{X}) \boldsymbol{\varepsilon}(\delta \dot{\mathbf{u}}) d\Omega = \int_{\Omega} \mathbf{f} \delta \dot{\mathbf{u}} d\Omega + \int_{\Gamma_N} \mathbf{h} \delta \dot{\mathbf{u}} d\Gamma_N \quad (3-27)$$

Substituting Eq. (3-27) into Eq. (3-26) and removing all the terms containing $\delta \dot{\mathbf{u}}$, and a much more compact form of Eq. (3-26) can be obtained, as:

$$\int_{\Omega} \boldsymbol{\varepsilon}(\dot{\mathbf{u}})^T \mathbf{D}(\mathcal{X}) \boldsymbol{\varepsilon}(\delta \mathbf{u}) d\Omega = - \int_{\Omega} \boldsymbol{\varepsilon}(\mathbf{u})^T \frac{\partial \mathbf{D}(\mathcal{X})}{\partial \mathcal{X}} \boldsymbol{\varepsilon}(\delta \mathbf{u}) d\Omega \quad (3-28)$$

As we know, the static compliance problems are self-adjoint [1]. Eq. (3-28) can be expanded as a form:

$$\int_{\Omega} \boldsymbol{\varepsilon}(\dot{\mathbf{u}})^T \mathbf{D}(\mathcal{X}) \boldsymbol{\varepsilon}(\mathbf{u}) d\Omega = - \int_{\Omega} \boldsymbol{\varepsilon}(\mathbf{u})^T \frac{\partial \mathbf{D}(\mathcal{X})}{\partial \mathcal{X}} \boldsymbol{\varepsilon}(\mathbf{u}) d\Omega \quad (3-29)$$

Substituting Eq. (3-29) into Eq. (3-25). The first-order sensitivity of the structural compliance with respect to the DDF is gained, explicitly as:

$$\frac{\partial J}{\partial \mathcal{X}} = - \frac{1}{2} \int_{\Omega} \boldsymbol{\varepsilon}(\mathbf{u})^T \frac{\partial \mathbf{D}(\mathcal{X})}{\partial \mathcal{X}} \boldsymbol{\varepsilon}(\mathbf{u}) d\Omega \quad (3-30)$$

It can be easily seen that the final form of the sensitivity of the optimized objective can be directly gained by calculating the first-order derivative of the elastic tensor with respect to the DDF. As given in Eq. (3-22), the elastic tensor of the isotropic material is assumed to be an exponential function of the DDF. Eq. (3-30) can be expanded as a new form, by:

$$\frac{\partial J}{\partial \mathcal{X}} = - \frac{1}{2} \int_{\Omega} \boldsymbol{\varepsilon}(\mathbf{u})^T (\gamma \mathcal{X}^{\gamma-1} \mathbf{D}_0) \boldsymbol{\varepsilon}(\mathbf{u}) d\Omega \quad (3-31)$$

where γ is the penalty parameter, equal to 3, and \mathbf{D}_0 is the material constitutive elastic tensor.

The first-order derivative of the volume constraint is given as:

$$\frac{\partial G}{\partial \mathcal{X}} = \frac{1}{|\Omega|} \int_{\Omega} v_0 d\Omega \quad (3-32)$$

As described in Section 3.2, the DDF is developed by the NURBS basis functions with the smoothed nodal densities of the control points. The smoothed nodal densities of the control points are developed by the Shepard function. Firstly, the sensitivity analysis of the DDF with respect to the smoothed nodal densities of the control points are derived by:

$$\frac{\partial \mathcal{X}(\xi, \eta, \zeta)}{\partial \mathcal{G}(\rho_{i,j,k})} = R_{i,j,k}^{p,q,r}(\xi, \eta, \zeta) \quad (3-33)$$

where $R_{i,j,k}^{p,q,r}(\xi, \eta, \zeta)$ denotes the NURBS basis function at the computational point (ξ, η, ζ) .

The derivatives of the smoothed nodal densities with respect to nodal densities are given as:

$$\frac{\partial \mathcal{G}(\rho_{i,j,k})}{\partial \rho_{i,j,k}} = \psi(\rho_{i,j,k}) \quad (3-34)$$

where $\psi(\rho_{i,j,k})$ is the value of the Shepard function at the current control point (i, j, k) . It is important to note that the above computational point (ξ, η, ζ) is different from the control point (i, j, k) . The control points are not on the structural design domain and only work as the control coefficients to construct the DDF. However, the computational points are located at the design domain. In the current formulation, the computational points correspond to the Gauss quadrature points. The first-order derivatives of the objective and constraint functions with respect to the nodal densities are derived based on the chain rule, and the final detailed form of the first-order derivatives is explicitly described by:

$$\begin{cases} \frac{\partial J}{\partial \rho_{i,j,k}} = -\frac{1}{2} \int_{\Omega} \boldsymbol{\varepsilon}(\mathbf{u})^T \gamma(\mathcal{X}(\xi, \eta, \zeta))^{\gamma-1} R_{i,j,k}^{p,q,r}(\xi, \eta, \zeta) \psi(\rho_{i,j,k}) \mathbf{D}_0 \boldsymbol{\varepsilon}(\mathbf{u}) d\Omega \\ \frac{\partial G}{\partial \rho_{i,j,k}} = \frac{1}{|\Omega|} \int_{\Omega} R_{i,j,k}^{p,q,r}(\xi, \eta, \zeta) \psi(\rho_{i,j,k}) v_0 d\Omega \end{cases} \quad (3-35)$$

It can be easily seen that the first-order derivatives of the objective are negative due to the nonnegativity of the NURBS basis functions and the Shepard function.

3.4 Numerical implementations

The OC method [162] is applied to solve the formulation due to its superior characteristic for the optimization problems with a large number of design variables and only a few constraints. An efficient heuristic updating scheme is given and the detailed formulation can refer to [79,83,163], as:

$$\rho_{i,j,k}^{(\kappa+1)} = \left\{ \begin{array}{ll} \max\{(\rho_{i,j,k}^{(\kappa)} - m), \rho_{min}\} & \text{if } \left\{ \begin{array}{l} (\Pi_{i,j,k}^{(\kappa)})^\zeta \rho_{i,j,k}^{(\kappa)} \leq \\ \max\{(\rho_{i,j,k}^{(\kappa)} - m), \rho_{min}\} \end{array} \right\} \\ (\Pi_{i,j,k}^{(\kappa)})^\zeta \rho_{i,j,k}^{(\kappa)} & \text{if } \left\{ \begin{array}{l} \max\{(\rho_{i,j,k}^{(\kappa)} - m), \rho_{min}\} \\ < (\Pi_{i,j,k}^{(\kappa)})^\zeta \rho_{i,j,k}^{(\kappa)} \\ < \min\{(\rho_{i,j,k}^{(\kappa)} + m), \rho_{max}\} \end{array} \right\} \\ \min\{(\rho_{i,j,k}^{(\kappa)} + m), \rho_{max}\} & \text{if } \left\{ \begin{array}{l} \min\{(\rho_{i,j,k}^{(\kappa)} + m), \rho_{max}\} \\ \leq (\Pi_{i,j,k}^{(\kappa)})^\zeta \rho_{i,j,k}^{(\kappa)} \end{array} \right\} \end{array} \right\} \quad (3-36)$$

where m , ζ are the move limit and the damping factor, respectively. $\Pi_{i,j,k}^{(\kappa)}$ is the updating factor for the $(i,j,k)_{th}$ design variable at the κ^{th} iteration step.

$$\Pi_{i,j,k}^{(\kappa)} = -\frac{\partial J}{\partial \rho_{i,j,k}} / \max\left(\mu, \Lambda^{(\kappa)} \frac{\partial G}{\partial \rho_{i,j,k}}\right) \quad (3-37)$$

μ is a very small positive constant to avoid the zero term in the denominator. $\Lambda^{(\kappa)}$ is the Lagrange multiplier at the κ^{th} iteration step, which is updated by a bi-sectioning algorithm [1]. The flowchart of the current developed ITO framework is shown in Figure 3-3. The main parts are given within red boxes, namely: (1) The geometrical model constructed by NURBS; (2) The development of the numerical analysis model (the IGA mesh); (3) The improvement of the smoothness of the nodal densities by the Shepard function; (4) The construction of the DDF using NURBS for 2D and 3D; (5) The evaluation of the unknown structural responses by the NURBS-based IGA; (6) The evolving of the DDF.

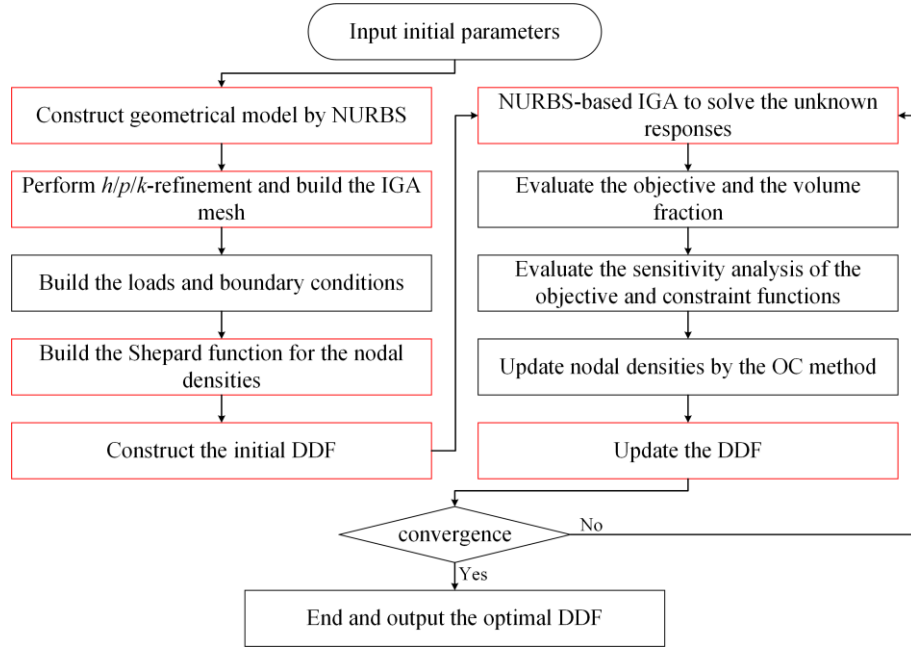


Figure 3-3 The flowchart of the ITO method

According to the flowchart of the ITO method, the NURBS basis functions bridge the density distribution function and IGA to solve the unknown structural responses. In the DDF, NURBS basis functions are applied to construct the NURBS to represent material density, and which are then employed to construct the solution space. Hence, the geometrical model and analysis model can be integrated into a same mathematical formula, namely the IGA. Additionally, the current isogeometric topology optimization formulation intends to optimize the DDF with the improvement of structural performance, rather than seeking for an appropriate distribution of an array of discrete element densities.

3.5 Numerical examples

In this section, several numerical examples in 2D and 3D are provided to demonstrate the effectiveness and efficiency of the ITO method. In all examples, the Young's moduli for solid materials are set as 1. The Poisson's ratio is set to be 0.3. The imposed point load magnitude is defined as 1. The Gauss quadrature points with 3×3 (2D) or $3 \times 3 \times 3$ (3D) are chosen in each

IGA element. Meanwhile, it is noted that no filtering schemes are contained in the current work. The initial nodal densities assigned to the control points are all defined to be 1, and the penalty factor γ for all examples is defined to be 3. The terminal criterion is that the L_∞ norm of the difference of the nodal densities between two consecutive iterations is less than 1% or the maximum 150 iteration steps are reached.

3.5.1 Cantilever beam

The structural design domain of the cantilever beam with the loads and boundary conditions is defined in Figure 3-4 (a), and two indices L and H are defined as 10 and 5, respectively. The NURBS surface to model the cantilever beam with the control net of points is displayed in Figure 3-4 (b) and the IGA mesh to discrete the design domain with Gauss quadrature points is shown in Figure 3-4 (c). The related modeling details are attached below Figure 3-4. The allowable material volume fraction V_0 is set as 30%. As shown in Figure 3-5 (a), an initial set of the nodal densities is provided, and all values are equal to 1. The corresponding densities at Gauss quadrature Points are given in Figure 3-5 (b), and the DDF of the cantilever beam is displayed in Figure 3-5 (c).

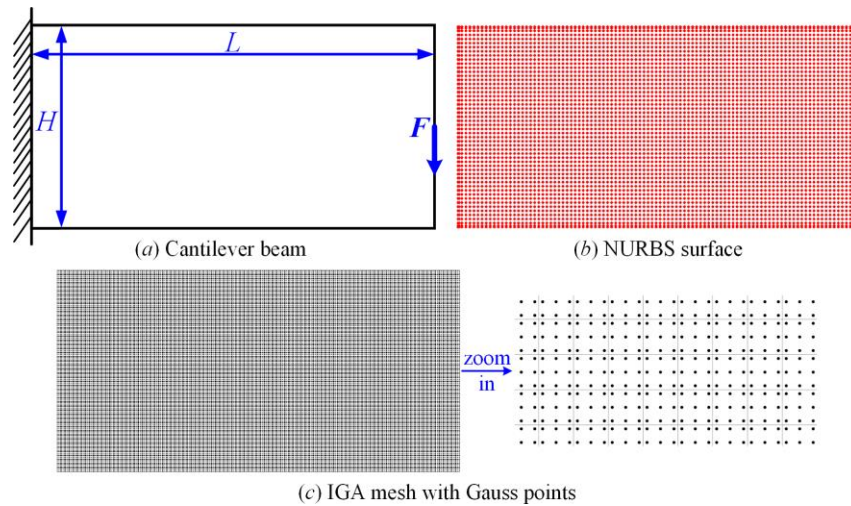


Figure 3-4 The details of the Cantilever beam

IGA elements 100×50 ; $\Xi = \{0, 0, 0, 0, 0.01, \dots, 0.99, 1, 1, 1, 1\}$,
 $\mathcal{H} = \{0, 0, 0, 0, 0.02, \dots, 0.98, 1, 1, 1, 1\}$; $n = 103$, $m = 53$; $p = 3$, $q = 3$;

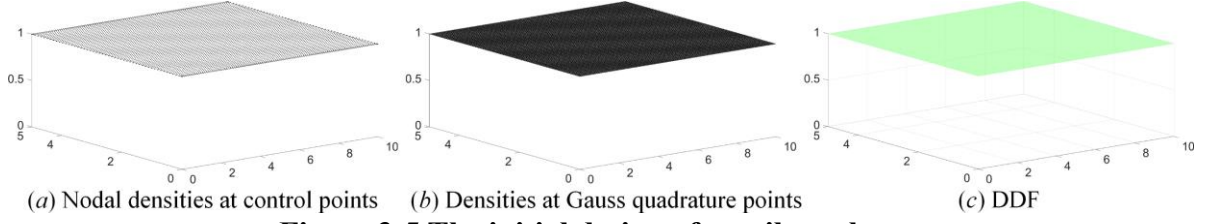


Figure 3-5 The initial design of cantilever beam

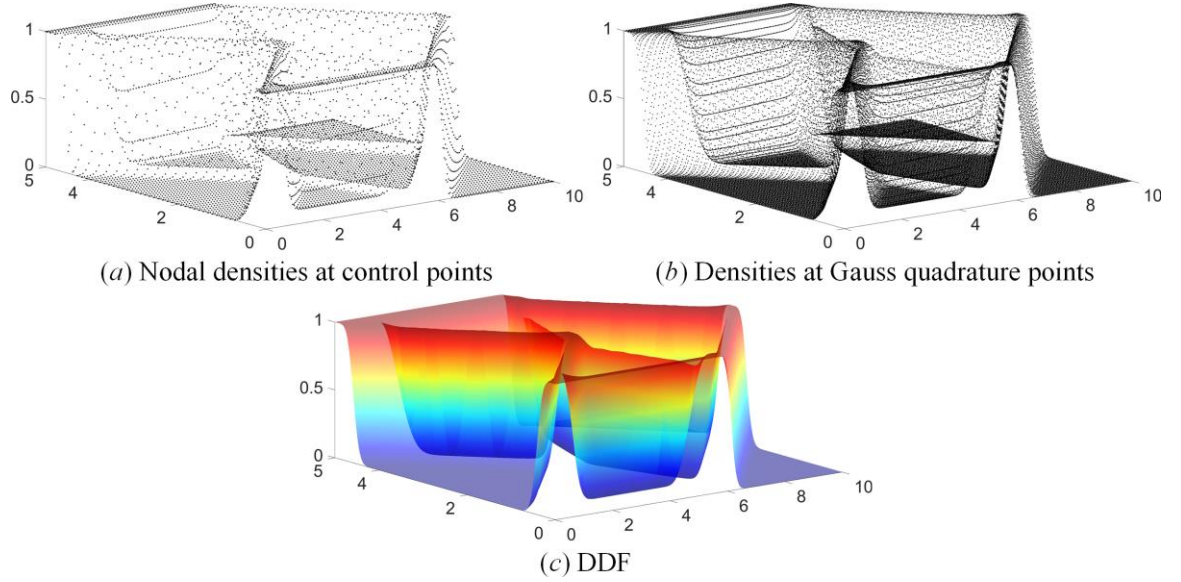


Figure 3-6 The optimized results of cantilever beam

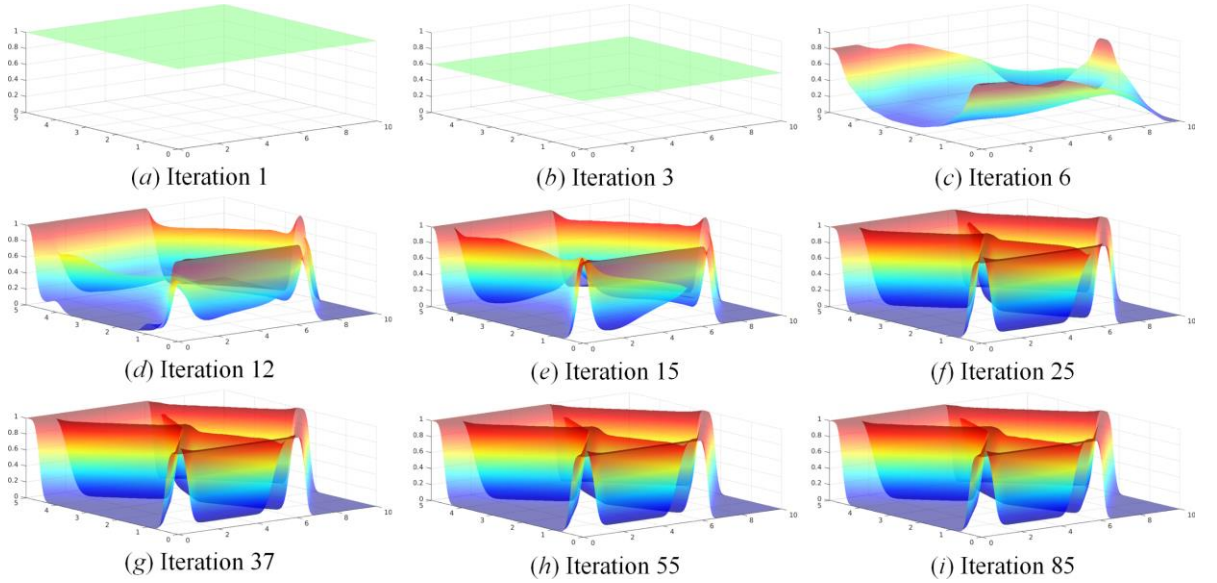


Figure 3-7 The intermediate DDFs

As shown in Figure 3-6, the optimized results are given, including the optimized distribution of nodal densities at the control points in Figure 3-6 (a), densities at Gauss quadrature points in Figure 3-6 (b) and the DDF in Figure 3-6 (c). As we can see, the optimized response surface of the DDF is featured with the sufficient smoothness and continuity, which will be beneficial to represent the structural topology. As already pointed out in Section 3.2, it mainly originates from the Shepard function and NURBS basis functions. The former can guarantee the overall smoothness of nodal densities at control points. The latter assure the high-order continuity of the DDF, considerably depended on the orders of NURBS basis functions. Meanwhile, the intermediate results of the DDF during the optimization from iterations 1 to 85 are also shown in Figure 3-7. As we can see, the updating of the DDF in the optimization is very stable.

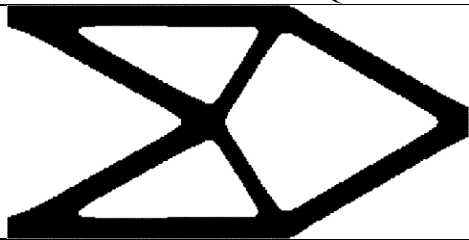
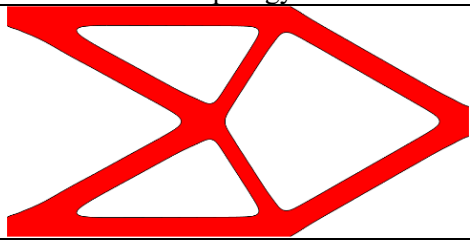
As displayed in Figure 3-6, the optimized densities in the DDF mostly approach the lower or upper bounds, namely 0 or 1. In order to achieve an appropriate architecture of the cantilever beam, a heuristic criterion is introduced to define the structural topology using the optimized DDF. The corresponding mathematical model is expressed in Eq. (3-38), as:

$$\begin{cases} 0 \leq \mathcal{X}(\xi, \eta) < \mathcal{X}_c & \text{void} \\ \mathcal{X}(\xi, \eta) = \mathcal{X}_c & \text{boundary} \\ \mathcal{X}_c < \mathcal{X}(\xi, \eta) \leq 1 & \text{solid} \end{cases} \quad (3-38)$$

where \mathcal{X}_c is a constant. Hence, structural boundaries of the optimized topology are expressed by the iso-contour of the response surface expressed by the DDF. The densities smaller than \mathcal{X}_c of the DDF denote voids in the optimized topology and the DDF with the densities larger than \mathcal{X}_c describe the solids. It can be seen that the heuristic scheme to define the structural topology using the DDF is similar to the LSM [13–15]. However, the proposed ITO method

for the optimization of continuum structures is not developed in a framework of the Hamilton-Jacobi partial differential equation. The mechanism in Eq. (3-38) can be just viewed as a post-processing scheme to define the topology. The core of the ITO method is the optimization of the sufficiently smooth and continuous DDF. In this work, $\mathcal{X}_c = 0.5$ is a suitable value to define the topology using the DDF, owing to the optimized densities of the DDF are mostly distributed nearly 0 or 1. The final topology of the cantilever beam is provided in the second column of Table 3-1, and densities at Gauss quadrature points with the values larger than 0.5 in a 2D view are given in Table 3-1. As we can see, the 2D view with $\mathcal{X}_c \geq 0.5$ is similar to the topology. A minor difference is that the topology is featured with the sufficiently smooth boundaries and clear interfaces between the solids and voids. The optimized objective value and the total iterative step are also given. A limited number of the iterations to arrive at the convergent condition shows the efficiency of the ITO method.

Table 3-1 The optimized results of the cantilever beam

The 2D-view DGQP	Topology	Obj	Num
		129.88	85

Finally, the iterative curves for the objective function and volume fraction are displayed in Figure 3-8, with the red curve to represent the evolving of the objective function and the blue curve to show the variation of the volume fraction. It can be easily seen that the convergent curves are featured with a clear, smooth and fast convergence, which shows the effectiveness and efficiency of the ITO method. The intermediate results of the topology are also provided in Figure 3-8.

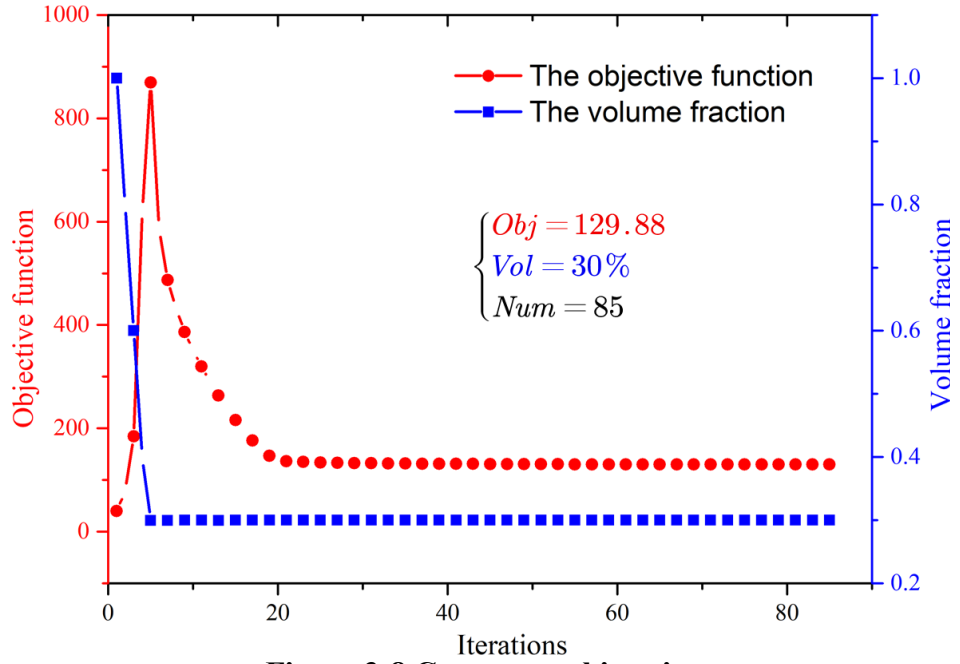


Figure 3-8 Convergent histories

3.5.1.1 Discussions of mesh dependency

In this subsection, we discuss the influence of the IGA mesh on the optimization. The knot vectors in three cases are listed in Table 3-2, and the corresponding IGA meshes have 80×40 , 120×60 and 140×70 elements in cases 1, 2 and 3, respectively. The numbers of control points are 83×43 , 123×63 and 143×73 , respectively. The maximum volume fraction is set as 30%.

Table 3-2 Knot vectors in three cases

Case	Knot vectors
1	$\Xi = \{0, 0, 0, 0, 0.0125, \dots, 0.9875, 1, 1, 1, 1\},$ $\mathcal{H} = \{0, 0, 0, 0, 0.0250, \dots, 0.9750, 1, 1, 1, 1\}.$
2	$\Xi = \{0, 0, 0, 0, 0.0083, \dots, 0.9917, 1, 1, 1, 1\},$ $\mathcal{H} = \{0, 0, 0, 0, 0.0167, \dots, 0.9833, 1, 1, 1, 1\}.$
3	$\Xi = \{0, 0, 0, 0, 0.0071, \dots, 0.9929, 1, 1, 1, 1\},$ $\mathcal{H} = \{0, 0, 0, 0, 0.0143, \dots, 0.9857, 1, 1, 1, 1\}.$

The initial values of nodal densities at control points are still defined to be 1. The optimized results of three cases are shown in Figure 3-9, including densities at Gauss quadrature points,

the 2D view of the densities with the values larger than 0.5, the DDF and the topology. The corresponding numerical results in three cases, consisting of the optimized objective function, the total iterations, the volume fraction of the topology are listed in Table 3-3, respectively. As we can see, the optimized DDFs and topologies in three cases are mostly identical, which demonstrates the ability of the ITO method to eliminate the mesh dependency. The main cause is that the NURBS for the representation of the DDF has the intrinsic filter [96]. As discussed in [96], the filter scale is dependent on the orders of NURBS basis functions and knot spans in all parametric directions. Moreover, the topology in Case 3 with the finest IGA mesh has the best performance, and volume fraction is also closest to the prescribed maximum material consumption 30%, and more iterations are required to meet the convergent criterion owing to the increasing of design variables. In terms of choosing the IGA mesh in the optimization, it is also a trade-off between the computational cost and numerical precision. In general, a mesh with 100×50 is a great choice.

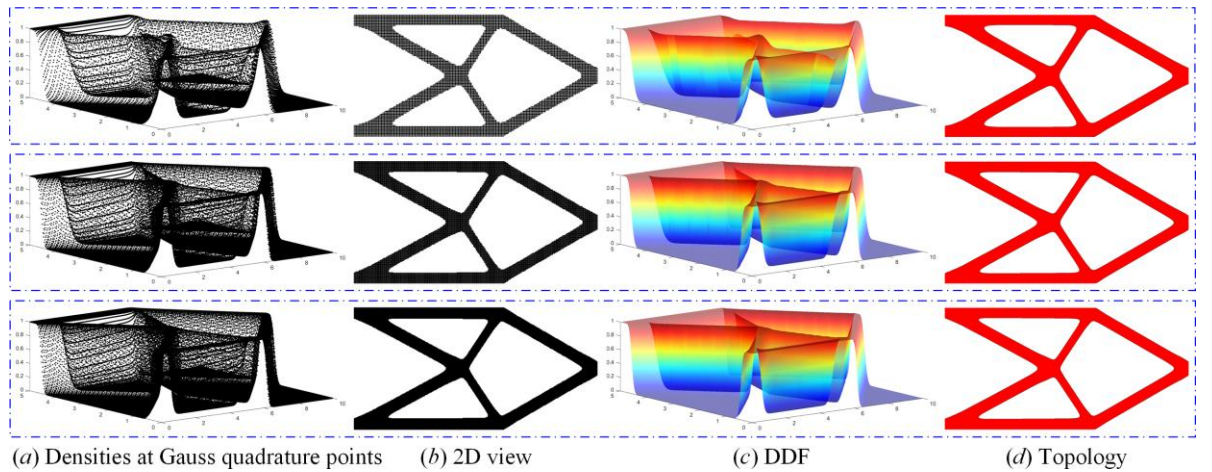


Figure 3-9 The optimized results in three cases

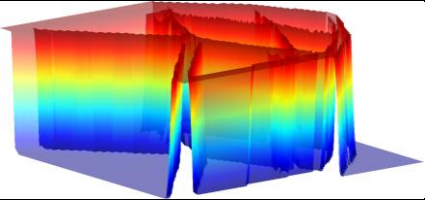
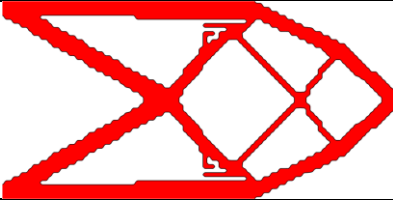
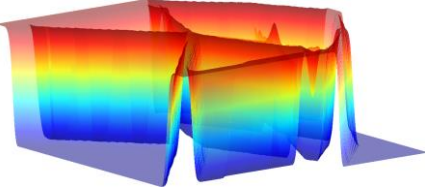

Table 3-3 The numerical results in three cases

Case 1 with a mesh 80×40			Case 2 with a mesh 120×60			Case 3 with a mesh 140×70		
<i>Obj</i>	<i>Num</i>	<i>Vol</i>	<i>Obj</i>	<i>Num</i>	<i>Vol</i>	<i>Obj</i>	<i>Num</i>	<i>Vol</i>
144.33	67	30.56%	122.08	86	30.16%	117.01	101	30.07%

3.5.1.2 Discussions of the Shepard function

In this subsection, two numerical cases are performed to address the influence of the Shepard function on the optimization, where the construction of the DDF does not employ the Shepard function to improve the smoothness of nodal densities. Two cases have different orders of NURBS basis functions, namely the 1-order basis functions in Case 1 and 3-order in Case 2. Other parameters are consistent with the first example, and the initial design of the cantilever beam in Figure 3-5 is utilized in two cases.

Table 3-4 The optimized results in two cases

Case 1 with 1-order		Obj	Num	Vol
DDF	Topology			
		111.86	None	30.88%
Case 2 with 3-order		Obj	Num	Vol
DDF	Topology			
		119.45	None	30.49%

The optimized results of two cases are provided in Table 3-4, including the DDF, the topology, the objective function, the total steps, and the volume fraction of the topology. It can be seen that the optimized results in Case 1 are featured with “islanding” or “layering” structures, “zig-zag” or wavy structural boundaries. However, the numerical issue of the “islanding” or “layering” structures is removed in the final topology of Case 2. In order to show the influence of the Shepard function and the order of basis functions on the “islanding” and “layering” numerical artifact in detail, the intermediate topologies in Cases 1 and 2 are presented in Figure 3-10, respectively. As we can see, the “islanding” and “layering” structures are easily

occurred during the optimization in Case 1, as shown in Figure 3-10 (ac), (ad) (ae) and (af). The NURBS filter is inactive in the elimination of the numerical issue, if the order is equal to 1 [96]. Elevating the order of the NURBS basis functions can increase the filter scale. As shown in Figure 3-10 (bd), the formed “islanding” and “layering” structures in Case 2 can be removed in the final topology.

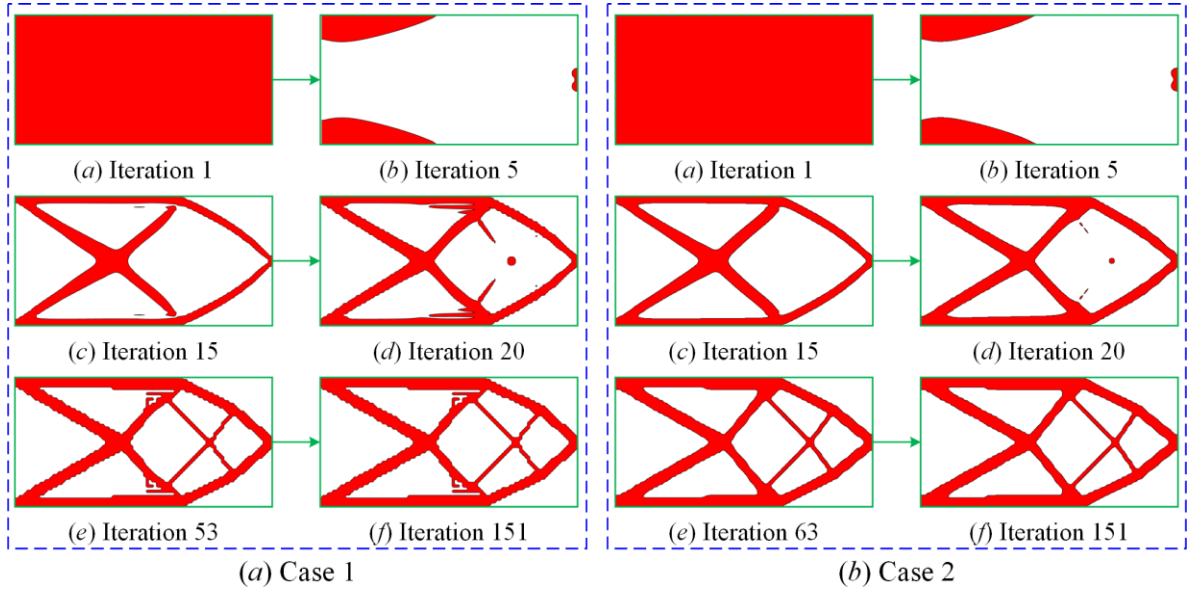


Figure 3-10 Intermediate topologies

As given in Table 3-4, the “zig-zag” or wavy structural boundaries are existed in the optimized topologies of Cases 1 and 2, which introduce some difficulties for the latter manufacturing. Similar to some results in [95] where densities at control points are applied to represent the structural topology, the wavy and blurry structural boundaries are also occurred, due to a fact that the overall smoothness of nodal densities is not improved. Meanwhile, the optimizations in two cases are not stable, and the final change of nodal densities between consecutive steps cannot satisfy the defined criterion. Hence, we can confirm that it is imperative to consider the Shepard function in the construction of the DDF, not only ensure the sufficient smoothness and continuity, but also improve the stability of the optimization.

3.5.1.3 Discussions of the initial design

In this subsection, the influence of the initial design on the optimization will be investigated in three cases, where three different initial designs of nodal densities are employed, as shown in Figure 3-11. As we can see, nodal densities are homogenously distributed and equal to 0.5 and 0.3, respectively. In the initial design 3, the definition of nodal densities is not uniformly configured in the structural design domain, with a part of nodal densities equal to 0. Other design parameters keep consistent with the first example, shown in Figure 3-4. The maximum material consumptions in three cases are equal to 30%.

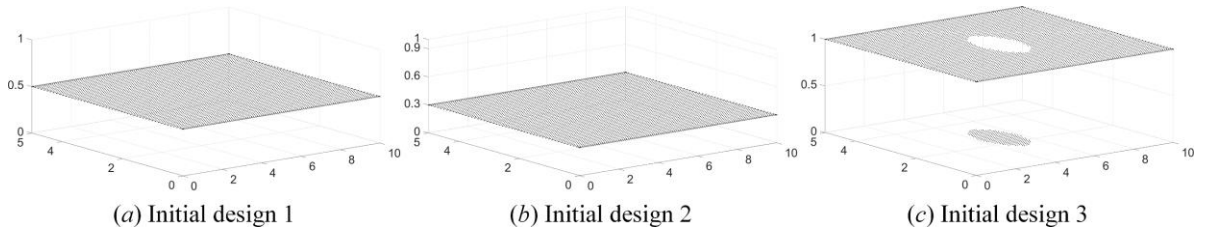


Figure 3-11 Nodal densities at control points in three cases

The optimized designs in three cases are displayed in Figure 3-12, including the optimized densities at Gauss points, the DDF and the topology. It can be easily seen that the optimized topologies are mostly identical in three cases, and only the topology in case 3 has the minor difference. The related numerical results of three cases are listed in Table 3-5, containing the optimized objective values, the total convergent steps and the volume fraction of the topology. As we can see, the objective functions in three cases are mostly identical, and only Case 3 has a larger structural mean compliance, namely 131.32. We can confirm that the initial design of nodal densities in a homogenous distribution has a negligible effect on the optimization, as shown in Table 3-1 and Figure 3-12. Moreover, the homogenous nodal densities are beneficial to the latter optimization of structures, and the non-uniform distributed nodal densities might lead to a local optimum.

Table 3-5 The numerical results in three cases

Case 1 with the initial design 1			Case 2 with the initial design 2			Case 3 with the initial design 3		
<i>Obj</i>	<i>Num</i>	<i>Vol</i>	<i>Obj</i>	<i>Num</i>	<i>Vol</i>	<i>Obj</i>	<i>Num</i>	<i>Vol</i>
130.15	72	30.12%	130.08	71	30.12%	131.32	82	30.54%

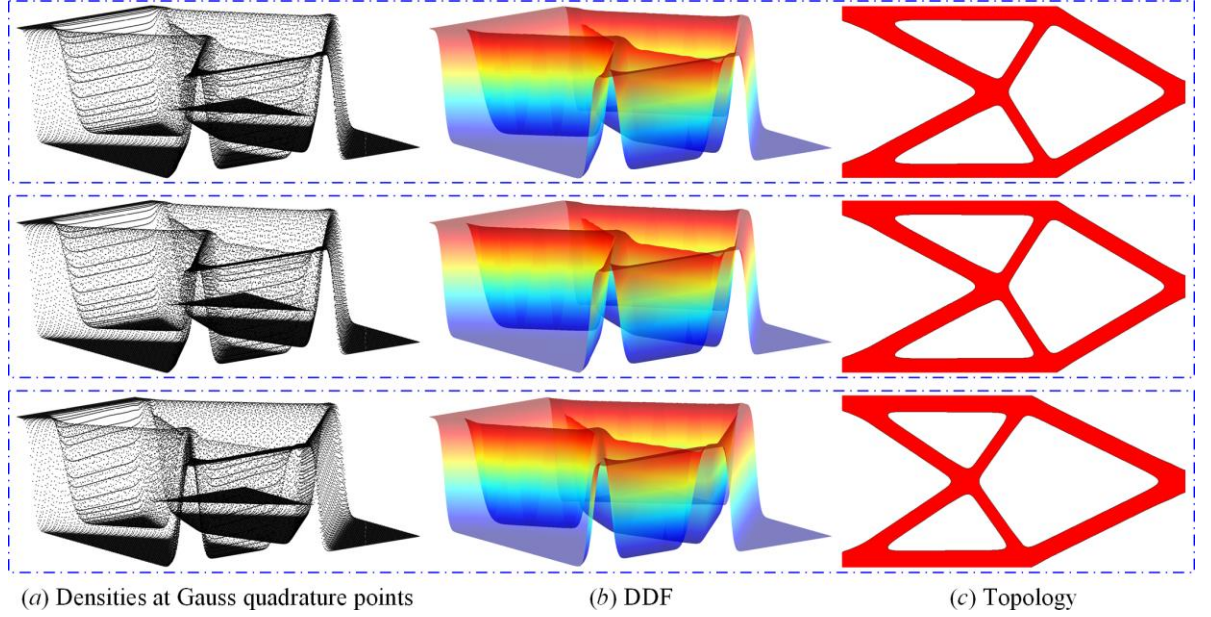


Figure 3-12 The optimized designs in three cases

3.5.2 Quarter annulus

In this subsection, a quarter annulus with the loads and boundary conditions is defined Figure 3-13 (a), and two indices r and R are set as 5 and 10, respectively. The NURBS surface with control points and the IGA mesh with Gauss quadrature points are shown in Figure 3-13 (b) and (c), respectively. The maximum material volume fraction is set as 40%. The initial design of the quarter annulus is shown in Figure 3-14.

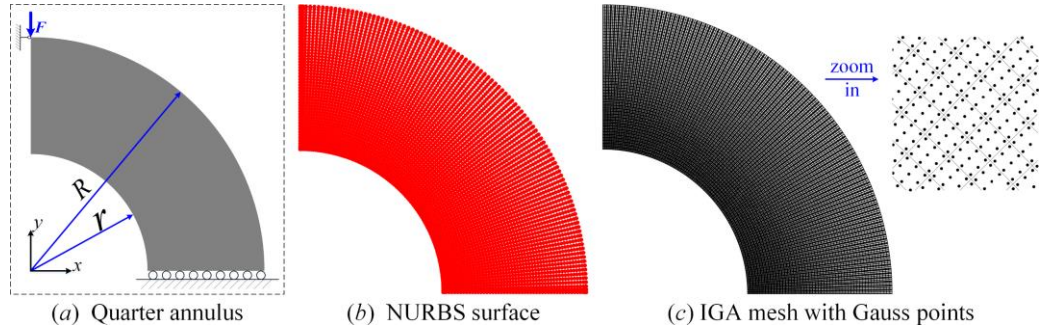


Figure 3-13 Quarter annulus

$$\Xi = \{0, 0, 0, 0, 0.01, \dots, 0.99, 1, 1, 1, 1\}, \mathcal{H} = \{0, 0, 0, 0, 0.02, \dots, 0.98, 1, 1, 1, 1\};$$

$$IGA \text{ elements } 100 \times 50 \quad p = 3, \quad q = 3;$$

The optimized designs, including the densities at Gauss quadrature points, the 2D view of densities larger than 0.5, the DDF and topology, are shown in Figure 3-15. Similar to Section 6.1, the optimized topology is featured with the smooth structural boundaries and the distinct interfaces between solids and voids. Meanwhile, the DDF is also featured with the sufficient smoothness and continuity, and the intermediate DDFs during the optimization are also shown in Figure 3-16. As we can see, the evolving of the DDF is featured with the high stability and can quickly reach the defined convergent criterion, which can demonstrate the effectiveness and efficiency of the proposed ITO method.

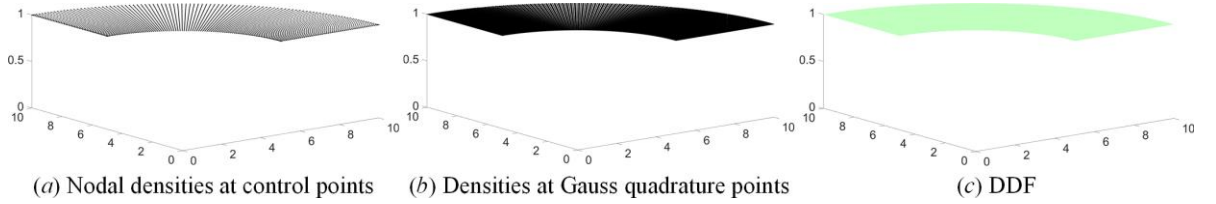


Figure 3-14 The initial design of quarter annulus

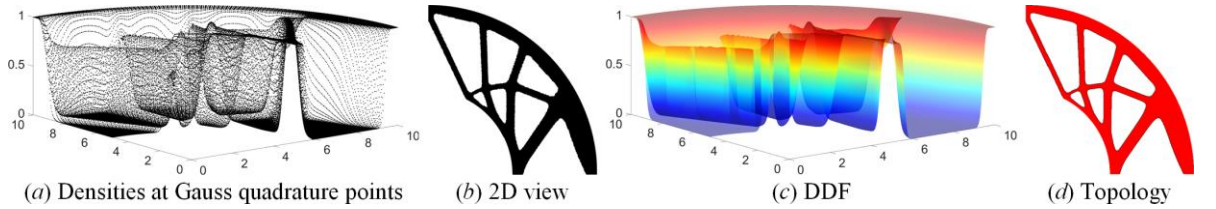


Figure 3-15 The optimized results of quarter annulus

Meanwhile, the iterative histories of the objective function and volume fraction of the DDF are also shown in Figure 3-17. It can be easily seen that the volume fraction of the DDF can quickly arrives at the prescribed maximum material consumption. Then, the DDF is gradually advanced to improve the structural stiffness performance. The major structural features are formed in the former iterations (nearly 30 steps) and more iterations are spent to slightly adjust the geometric details until the optimal design is found. Moreover, the intermediate topologies

are also attached with the display of the iterative curves, shown in Figure 3-17. The volume fraction of the final topology is also re-calculated, equal to 40.41%. Hence, we can confirm that the scheme to define the structural topology using the DDF is relatively applicable.

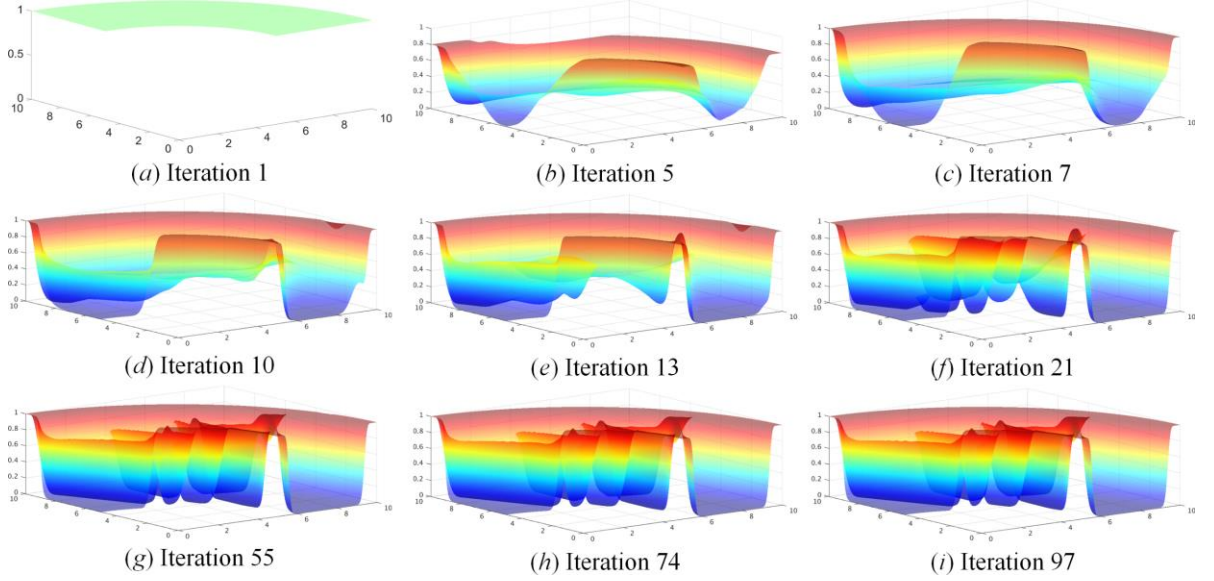


Figure 3-16 The intermediate DDFs

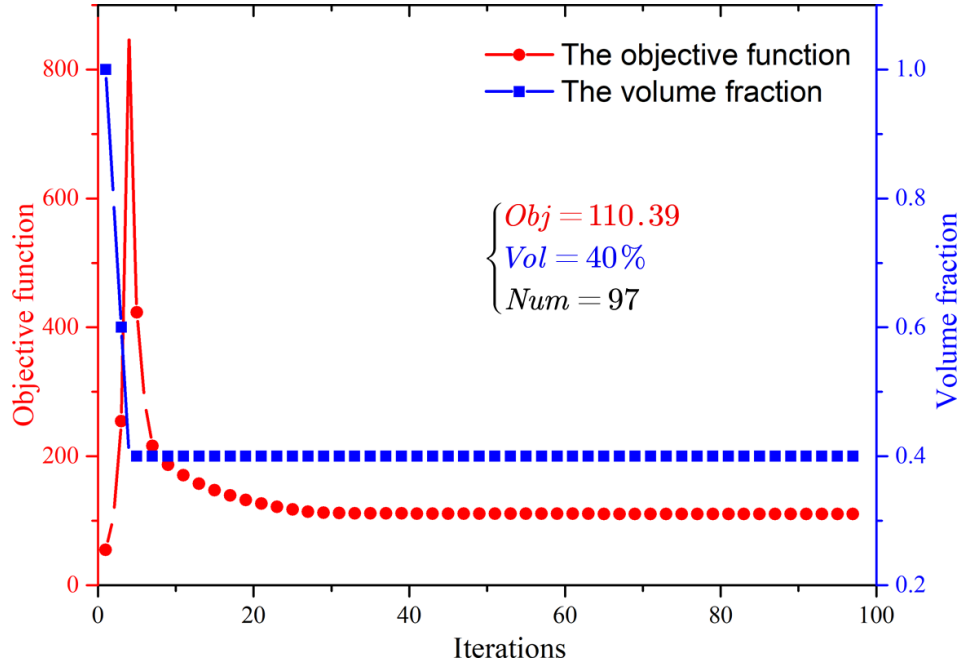


Figure 3-17 Convergent histories

3.5.2.1 Discussions of the order of NURBS basis functions

This subsection aims to address the influence of the order of NURBS basis functions on the optimization of the curved structures. The order of the NURBS basis functions is defined in three cases, namely 2, 3 and 4. The corresponding knot vectors are defined in Table 3-6. The maximum material consumptions in three cases are all defined as 40%. The initial values of nodal densities in three cases are all equal to 1.

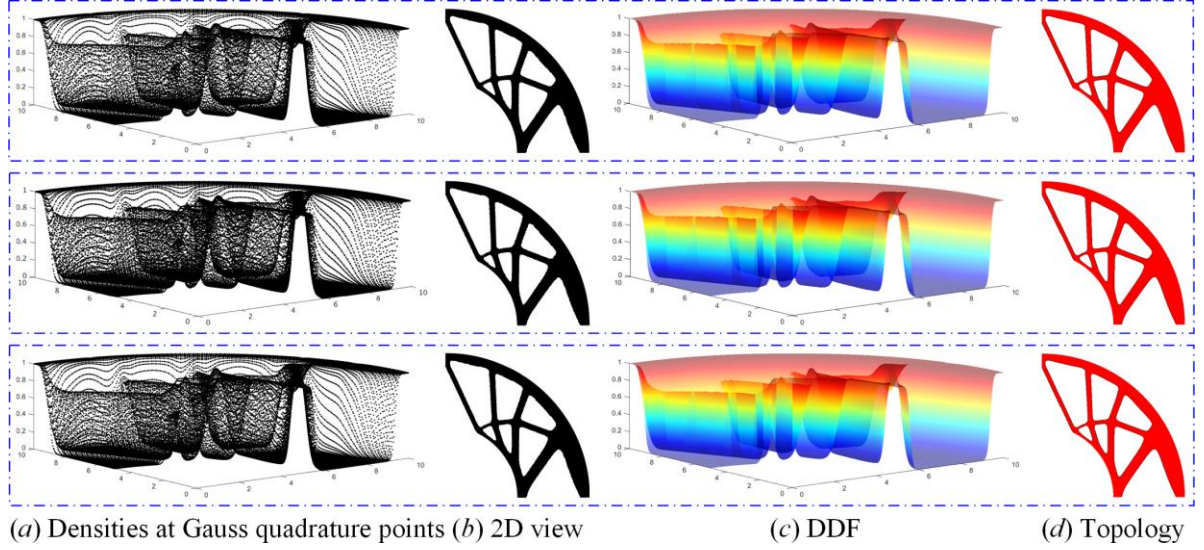
Table 3-6 Knot vectors in three cases

Case	Knot vectors
1	$\Xi = \{0, 0, 0, 0.01, \dots, 0.99, 1, 1\}, \mathcal{H} = \{0, 0, 0.02, \dots, 0.98, 1, 1\}.$
2	$\Xi = \{0, 0, 0, 0.01, \dots, 0.99, 1, 1, 1\}, \mathcal{H} = \{0, 0, 0, 0.02, \dots, 0.98, 1, 1, 1\}.$
3	$\Xi = \{0, 0, 0, 0, 0, 0.01, \dots, 0.99, 1, 1, 1, 1, 1\},$ $\mathcal{H} = \{0, 0, 0, 0, 0, 0.02, \dots, 0.98, 1, 1, 1, 1, 1\}.$

The optimized designs, including densities at Gauss quadrature points, 2D view of densities larger than 0.5, the DDF and topology in three cases are shown in Figure 3-18. The numerical results of three cases are all listed in Table 3-7, consisting of the optimized objective function, the total iterations and volume fraction of the final topology. It can be easily to find that the optimized topologies in three cases are nearly identical. As given in Table 3-7, the optimized objective functions in three cases increase with the elevation of the order of the NURBS basis functions, owing to the fact that the high-order IGA elements are usually softer than the lower-order ones [159]. Meanwhile, it is important to note that the total iterative steps are gradually decreased if the order is elevated. The reason is that the high-order NURBS basis functions cannot only exactly capture the geometry, but also ensure the computational precision, which can be beneficial to enhance the stability of the optimization. The iteration can quickly arrive at the convergent criterion. Additionally, the volume fractions of the optimized topologies in three cases are nearly equal to 40%.

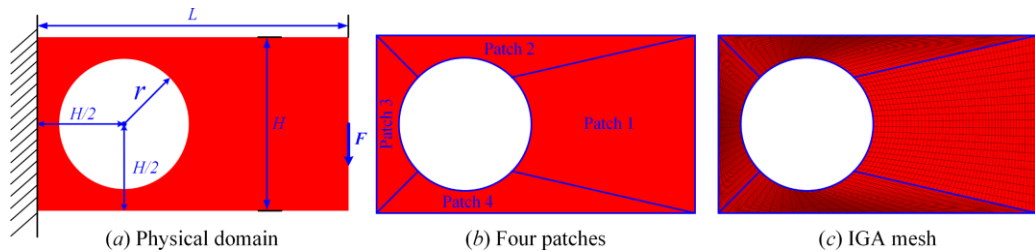
Table 3-7 The numerical results in three cases

Case 1 with 2-order			Case 2 with 3-order			Case 3 with 4-order		
<i>Obj</i>	<i>Num</i>	<i>Vol</i>	<i>Obj</i>	<i>Num</i>	<i>Vol</i>	<i>Obj</i>	<i>Num</i>	<i>Vol</i>
108.23	112	40.47%	110.39	97	40.41%	114.07	72	40.12%


Figure 3-18 The optimized designs in three cases

3.5.3 Complex structure

In this section, we present the ability of the developed ITO method to optimize the complex structure. It is difficult to use a single IGA patch to parametrize the geometry, and multiple patches are required. As shown in Figure 3-19 (a), a complex structure with the loads and boundary conditions is defined. The structural sizes are defined as: $L=9$, $H=5$ and $2r=3.75$. The corresponding IGA mesh with four patches is also displayed in Figure 3-19 (b). The maximum volume fraction is set to be 30%. The initial nodal densities at control points are defined to be 1. The details of the parametrization are listed below Figure 3-19.


Figure 3-19 The details of the complex structure

IGA elements 84×49 ; $\Xi = \{0, 0, 0, 0, 0.0476, \dots, 0.9524, 1, 1, 1, 1\}$,
 $\mathcal{H} = \{0, 0, 0, 0, 0.0204, \dots, 0.9796, 1, 1, 1, 1\}$; $p = 3$, $q = 3$;

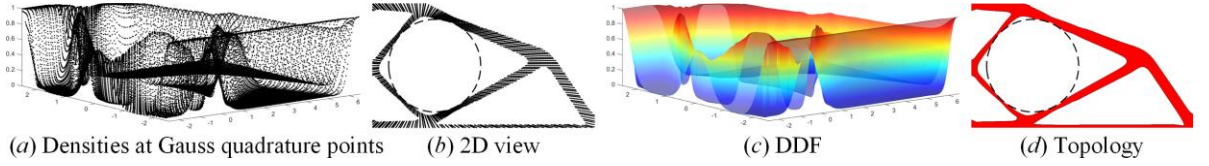


Figure 3-20 The optimized designs

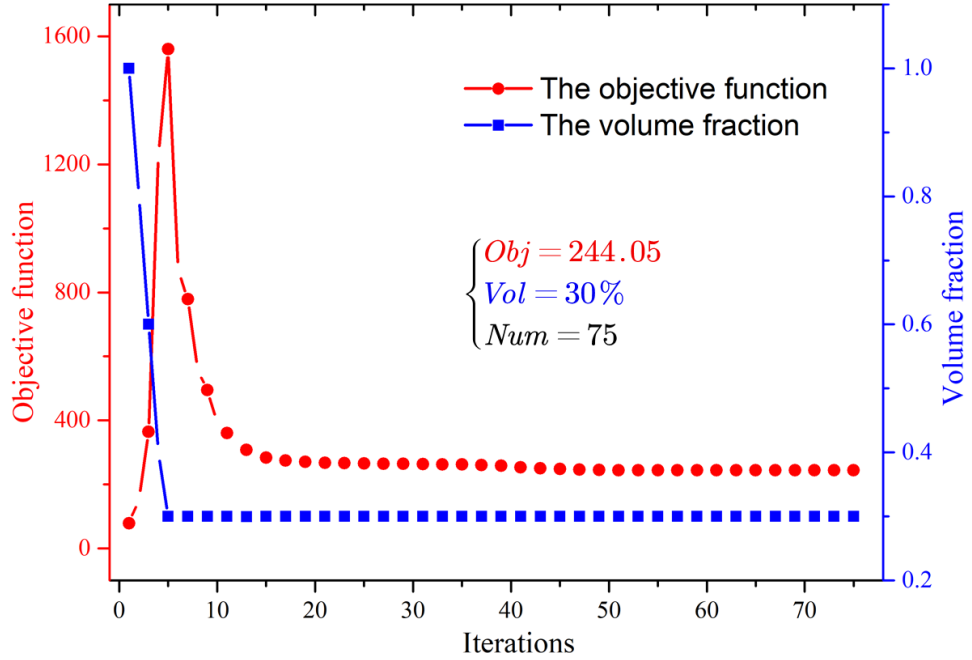


Figure 3-21 Convergent histories

As shown in Figure 3-20, the optimized designs are provided, including densities at Gauss quadrature points, the 2D view of densities larger than 0.5, the DDF and the final topology. The DDF is featured with the sufficiently smoothness and continuity, and the final topology has the smooth structural boundaries and distinct interfaces between the solids and voids. Meanwhile, the iterative histories of the objective and constraint functions are displayed in Figure 3-21. It can be easily found that the optimized topology with the maximum stiffness performance can be quickly found by the ITO method in 75 iterations. Hence, the ITO method for the structure parametrized by multiple patches is also featured with the high efficiency

and perfect stability. Additionally, the volume fraction of the topology is equal to 30.36%, also nearly equal to the prescribed value 30%, which displays the reasonability of the scheme in Eq. (3-38).

3.5.4 3D Michell structure

In this section, the ITO method is applied to optimize 3D structures to demonstrate its utility. As shown in Figure 3-22 (a), a 3D Michell structure with the loads and boundary conditions is defined, and the corresponding NURBS solid and the refined IGA mesh are displayed in Figure 3-22 (b) and (c), respectively. The maximum volume fraction V_0 is set as 15%, and the initial values of nodal densities are also defined to be 1.

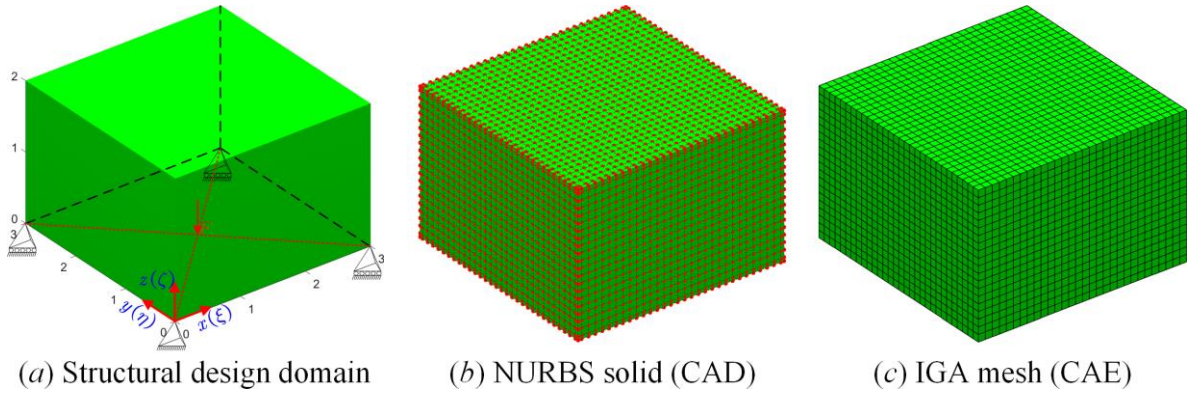


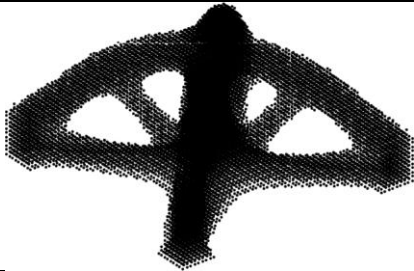
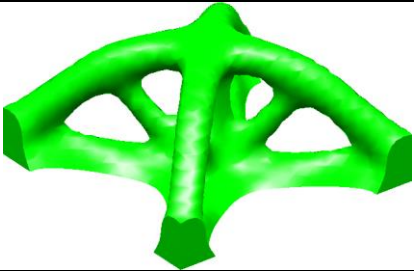
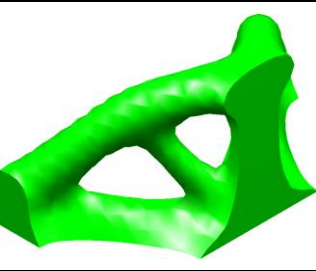
Figure 3-22 The details of 3D Michell structure

IGA elements $30 \times 30 \times 20$; $p = 2$, $q = 2$, $r = 2$; $\Xi = \{0, 0, 0, 0.0333, \dots, 0.9667, 1, 1, 1\}$,
 $\mathcal{H} = \{0, 0, 0, 0.0333, \dots, 0.9667, 1, 1, 1\}$, $\mathcal{Z} = \{0, 0, 0, 0.05, \dots, 0.95, 1, 1, 1\}$.

The optimized results of the 3D Michell structure are provided in Table 3-8. The 3D view of the densities at Gauss quadrature points with the values larger than 0.5 is given in the first column, and the optimized 3D topology is displayed in the second column. In order to display the interior details of the topology, a cross-sectional view of the optimized 3D topology is presented in the final column. It is easily to see the optimized 3D topology is still featured with the smooth structural boundaries and distinct interfaces between the solids and voids.

The iterative curves of the objective function, the volume fraction and the change are all shown in Figure 3-23. As we can see, the total iterations are equal to 34, which demonstrate the superior efficiency of the ITO method to seek the optimized 3D topology. Meanwhile, the advancing of the change of nodal densities between two consecutive iterations is very stable. The intermediate topologies of the 3D Michell structure are also presented in Figure 3-24. Additionally, the volume fraction of the final 3D topology is also calculated, equal to 15.31% (nearly 15%), which also shows the post-definition scheme is appropriate.

Table 3-8 The optimized results of 3D Michell structure

3D view of densities	Topology	Cross-sectional view
		

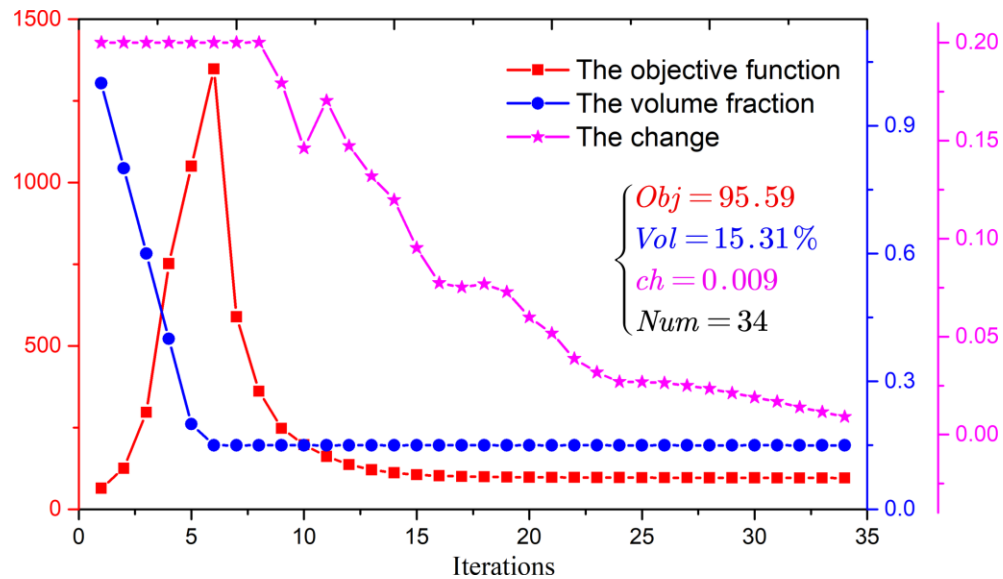


Figure 3-23 Convergent histories

Finally, the optimized topology of the 3D Michell structure can be directly outputted in a “STL.file” format and then additively fabricated by the STL technique. The 3D prototypes in

three different views are shown in Figure 3-25. Hence, a systematic procedure for continuum structures with the optimized stiffness performance from the conceptual design stage to the manufacturing phase is realized.

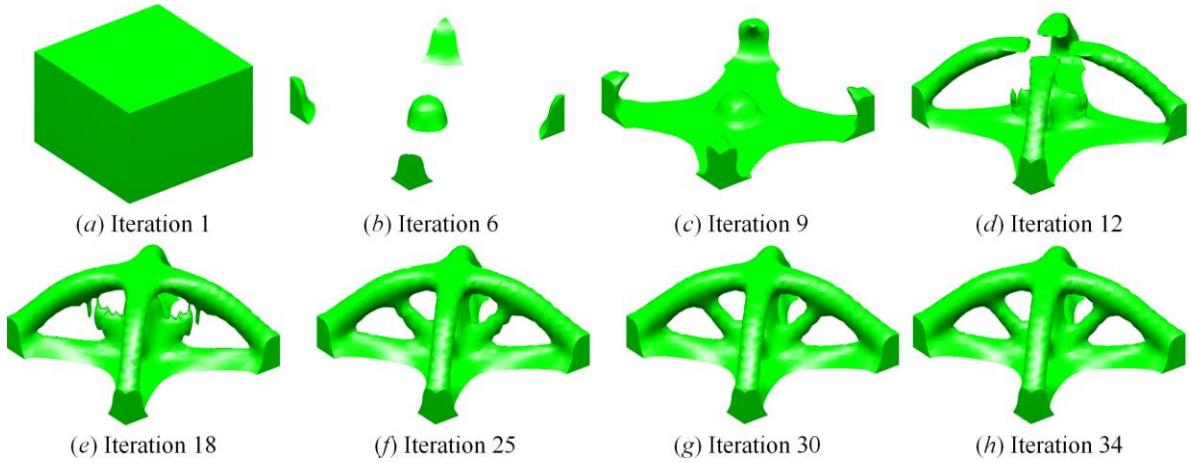


Figure 3-24 The intermediate topologies

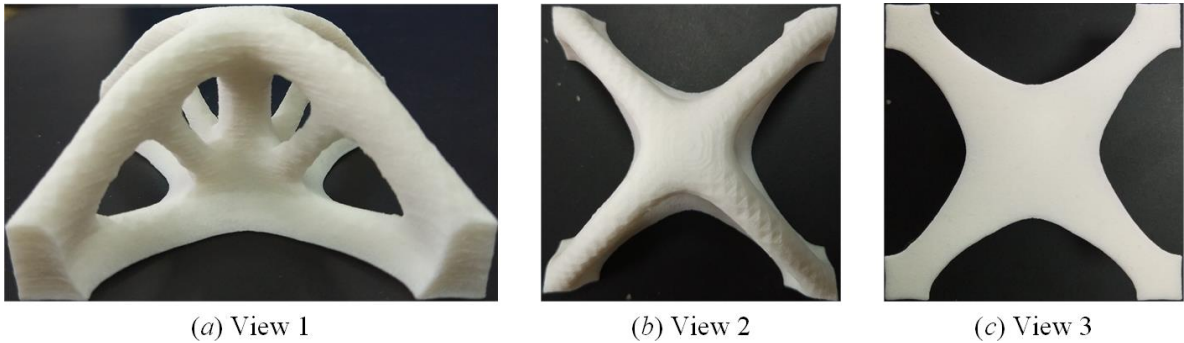


Figure 3-25 3D printing prototype of the 3D Michell structure

3.6 Conclusions

In this chapter, a more effective and efficient ITO method with the enhanced DDF that has desired smoothness and continuity is proposed for the design of continuum structures. Two procedures are mainly involved in the construction of the DDF, namely the improvement of the smoothness of nodal densities and the NURBS parametrization. The ITO formulation is developed for the minimization of the structural mean compliance.

Several numerical examples in 2D and 3D are tested to show the effectiveness and efficiency of the proposed ITO method. It can be found that the DDF with the desired smoothness and continuity has a significant influence on the optimization of 2D and 3D structures with the rectangular design domain, the curved shape and the complex geometry. Meanwhile, the final topologies are featured with smooth boundaries and distinct interfaces between the solids and voids. The optimization of 3D structures presents the effectiveness of the ITO method and the topologically optimized 3D designs are prototyped using the SLS technique.

Chapter 4 A multi-material ITO (M-ITO) method using a NURBS-based Multi-material Interpolation (N-MMI)

Overall speaking, the multi-material topology optimization problems pose more challenges than the single-material designs. The first work might go back to [164], which employed the homogenization technique to design a structure with one or two materials. A mixture rule for the interpolation of three-phase material properties was proposed in the framework of the SIMP method to design composites with extreme thermal expansion [165] and extreme bulk modulus [166], which has been applied to the optimization design of multiphysics actuators [167] and reinforced concrete structures [168]. Stegmann and Lund [169] proposed a discrete material optimization (DMO) to optimize composite laminate shell structures. Then, Gao and Zhang [170] extended the mixture rule and DMO to multi-material problems with the total mass constraint, where the recursive multiphase materials interpolation (RMMI) model and uniform multiphase materials interpolation (UMMI) model were studied. Later, many multi-material topology optimization methods were developed, like the peak function to decrease design variables [171], the ordered SIMP interpolation [172], and the alternating active-phase algorithm [173] to split the multi-material optimization into an array of the binary designs. [174] also developed a continuum topology optimization framework for the multi-material compliance minimization considering arbitrary volume and mass constraints. The LSMs also have been applied to solve several multi-material problems, such as a “color” level set [61] and the MM-LS topology description model [76] in a parametric LSM [175]. In the multi-material topology optimization, a critical ingredient lies in how to develop an effective multi-

material interpolation model. Several challenges will be involved: (1) How to exactly capture each distinct material in a designable element or point; (2) No overlaps: a designable element or point only has a unique phase; (3) No redundant phases: the design domain is occupied by all materials and the void phase. However, the developed multi-material interpolation models in the previously-mentioned works might not be effective in some problems. For instance, the RMMI model has no capability to ensure the multi-material optimization can seek the optimal design subject to the total mass constraint [170], where a set of design variables is defined to determine the existence of all materials and other sets work as topology variables to determine the selection of materials. In the UMMI model, each set of design variables can be regarded as the set of topology variables to determine the distribution of a unique material. In the above developed multi-material interpolation models, including the earlier mixture rule, the DMO scheme, the RMMI and UMMI models, a similar feature is existed, where the design variables and topology variables are expressed in coupled manner and evolved in a parallel mechanism in the optimization. The coupled expression and parallel evolving cause several numerical troubles in solving multi-material problems, like the unrealistic designs with the “mixed” material or a local optimal design [120,170]. Hence, we can find that numerical troubles of the multi-material interpolation models still affect the effectiveness of the optimization to some extent. It is of great importance to develop a more effective multi-material ITO method with the superior capability to seek the optimal layouts of multiple materials.

In this chapter, we intend to propose a Multi-Material Interpolation model using NURBS (N-MMI), and then apply it to develop a new multi-material isogeometric topology optimization (M-ITO) method, which has more effectiveness on solving the multi-material problems with both multiple volume constraints and total mass constraint. In the N-MMI model, two kinds

of variables are introduced, respectively, namely the Fields of Design Variables (DVs) and Fields of Topology Variables (TVFs), which are formulated in a manner of the decoupled expression and serial evolving, rather than the coupled and parallel manner. The decoupled expression and serial evolving of the DVs and TVFs can make sure all constraint functions are separate and linear with respect to TVFs, which can be beneficial to solve multi-material problems, particularly for the problem with the total mass constraint.

4.1 NURBS-based Multi-Material Interpolation (N-MMI)

The earlier works have developed many different multi-material interpolation models for solving problems, such as the mixture rule [165,166] and the DMO scheme [169]. The design variables and topology variables are coupled in a mathematical symbol, like \mathbf{x} , which makes design variables and topology variables to be evolved in the parallel mechanism. In the current work, the main intention of the proposed N-MMI model is to decouple the design variables and topology variables, which will be advanced in a serial manner.

In terms of the multi-material topology optimization problem, it is assumed that Θ distinct materials need to be distributed in the structural domain. we need to introduce Θ Fields of Topology Variables (TVFs) ϕ^ϑ ($\vartheta = 1, 2, \dots, \Theta$), each of field determines the distribution of a unique material. In order to define the TVFs, Θ Fields of Design Variables (DVs) \mathcal{X}^ϑ ($\vartheta = 1, 2, \dots, \Theta$) are introduced in the structural design domain, and each TVF is defined by a combination of all DVs.

4.1.1 The Field of Design Variables (DVF)

The DVs are used to construct the TVFs, and two basic requirements should be maintained to ensure the justified topology variables: 1) Nonnegativity; 2) Strict bounds. we can see that

two conditions are same as the introducing of the nodal densities to define the topology in some previous works, e.g. [98,100,102,104]. The construction of the DVF inherits the principle of NURBS, where the NURBS basis functions are linearly combined with the nodal design variables and each control point is assigned by a nodal design variable. As shown in Figure 4-1 (a), the control points are plotted by the red color. The nodal design variables assigned to control points are varied in a bound $[0, 1]$, displayed in Figure 4-1 (b), and the corresponding DVF for the design domain is shown in Figure 4-1 (c).

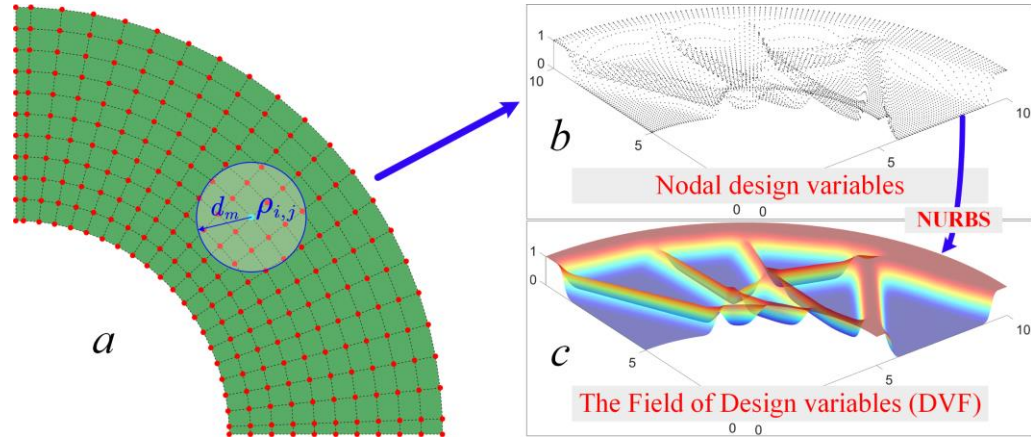


Figure 4-1 The construction of the DVF

4.1.1.1 Smooth nodal design variables using Shepard function

As discussed in [105,125], the smoothness mechanism of the DVF plays a significant but different role in the optimization compared to the filtering, such as the density and sensitivity filter [29]. The smoothness of the nodal design variables should be enhanced to ensure the DVF with the desired smoothness. The principle is that each nodal design variable is equal to the mean value of all design variables in the local support area of the current design variable, as shown in the circular area of Figure 4-1 (a), explicitly expressed as:

$$\mathcal{G}(\rho_{i,j}) = \sum_{i=1}^{\mathcal{N}} \sum_{j=1}^{\mathcal{M}} \psi(\rho_{i,j}) \rho_{i,j} \quad (4-1)$$

where $\mathcal{G}(\rho_{i,j})$ is the smoothed nodal design variable at the $(i,j)_{th}$ control point, and $\rho_{i,j}$ is the design variable which need to satisfy the nonnegative and range-bounded by 0 and 1. \mathcal{N} and \mathcal{M} are the numbers of design variables located at the local support area of the current $(i,j)_{th}$ design variable in two parametric directions, respectively. $\psi(\rho_{i,j})$ is the value of the Shepard function [160] at the $(i,j)_{th}$ design variable, and expressed by:

$$\psi(\rho_{i,j}) = \frac{w(\rho_{i,j})}{\sum_{\hat{i}=1}^{\mathcal{N}} \sum_{\hat{j}=1}^{\mathcal{M}} w(\rho_{\hat{i},\hat{j}})} \quad (4-2)$$

where $w(\rho_{i,j})$ is the weight function of the $(i,j)_{th}$ design variable. It can be defined by many functions, such as the inverse distance weighting function [160], the exponential cubic spline and radial basis functions (RBFs) [175]. Here, the CSRBFs with the C^4 continuity are used due to the compactly supported, high-order continuity and nonnegativity, as:

$$w(r) = (1-r)_+^6 (35r^2 + 18r + 3) \quad (4-3)$$

where $r = d/d_m$, and d is the Euclidean distance between the current design variable and the other nodal design variable in the local support area. d_m is the radius of the local domain.

4.1.1.2 Construction of the DVF

Based on the smoothed nodal design variables, the DVF is constructed by the linear combination of the NURBS basis functions with the smoothed nodal design variables. It is assumed that the DVF in the structural domain is denoted by $\mathcal{X}(\xi, \eta)$, and the mathematical form is defined as:

$$\mathcal{X}(\xi, \eta) = \sum_{i=1}^n \sum_{j=1}^m R_{i,j}^{p,q}(\xi, \eta) \mathcal{G}(\rho_{i,j}) \quad (4-4)$$

We can find that Eq. (4-4) for the DVF has the same form of NURBS surface. The difference lies in the physical meanings of control coefficients. The NURBS surface for the structure is transformed into the definition of the DVF for the design domain, and the properties 1 to 3 of NURBS basis functions can guarantee the DVF with the nonnegativity and Strict bounds from 0 to 1. The most important aspect is that the variation diminishing property of NURBS can ensure the non-oscillatory of the DVF [89,90].

4.1.2 The Field of Topology Variables (TVF)

As already pointed out, each TVS $\phi^\vartheta (\vartheta = 1, 2, \dots, \Theta)$ is formulated by a summation of all Θ DVFs \mathcal{X}^ϑ , which is applied to represent the layout of a unique material in the design domain, expressed as:

$$\phi^\vartheta = \prod_{\lambda=1}^{\vartheta} \mathcal{X}^\lambda \prod_{\lambda=\vartheta+1}^{\Theta} (1 - \mathcal{X}^\lambda) \quad (\vartheta = 1, 2, \dots, \Theta) \quad (4-5)$$

As the examples of $\Theta = 1, 2, 3$, the detailed forms in three cases are clearly defined as:

$$\begin{cases} \Theta = 1: \phi^1 = \mathcal{X}^1 \\ \Theta = 2: \phi^1 = \mathcal{X}^1(1 - \mathcal{X}^2); \phi^2 = \mathcal{X}^1 \mathcal{X}^2 \\ \Theta = 3: \begin{cases} \phi^1 = \mathcal{X}^1(1 - \mathcal{X}^2)(1 - \mathcal{X}^3); \\ \phi^2 = \mathcal{X}^1 \mathcal{X}^2(1 - \mathcal{X}^3); \phi^3 = \mathcal{X}^1 \mathcal{X}^2 \mathcal{X}^3 \end{cases} \end{cases} \quad (4-6)$$

A brief representation is shown in Figure 4-2, in which Θ DVFs are combined together to describe the distributions of Θ materials ($\Theta + 1$ phases: including void phase) in the design domain, and each unique material is plotted with a distinct color, namely material 1 with the black, material 2 with the red and material 3 with the green. Hence, each TVS for the distinct material is related to all the DVFs. we only need to change the values of a DVF every time to display the variation of the phase.

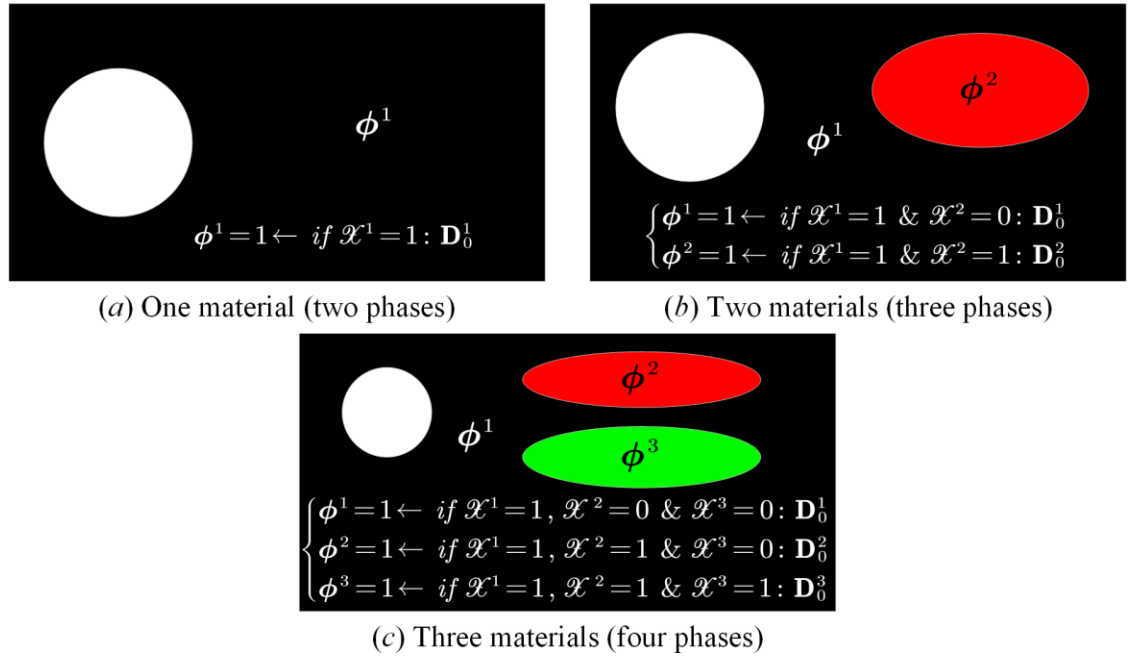


Figure 4-2 Multi-material topology description in the N-MMI model

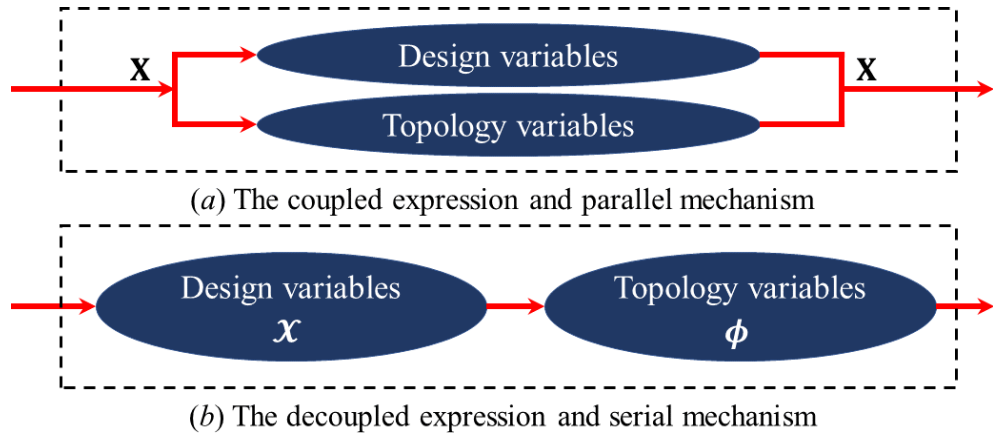


Figure 4-3 The expression and evolving mechanisms of design variables and topology variables

As shown in Figure 4-3, two different mechanisms of design variables and topology variables are given, namely the coupled expression and parallel mechanism, the decoupled expression and serial mechanism. The first mechanism has been extensively studied in many previous works [90,120,165,166,170]. Although the mathematical formula is simplified to describe design variables and topology variables, several numerical troubles are introduced in solving the multi-material topology optimization problems. Currently, the decoupled expression and

serial mechanism is constructed for two kinds of variables, which can lower the complexity of the numerical computations and offer more benefits for the multi-material optimization.

4.1.3 Multi-material interpolation

As already given in [105,125], the densities at Gauss quadrature points with a penalization parameter to form a power function are interpolated with material constitutive elastic tensor to compute the IGA element stiffness matrix. In the current construction of the TVFs for all materials, the TVFs with densities at any points in the design domain are iteratively evolved during the optimization. Based on material interpolation schemes [11], the Multi-Material Interpolation is expressed by a summation of all the interpolated functions of TVFs with the corresponding physical properties of materials, given by:

$$\mathbf{D} = \sum_{\vartheta=1}^{\Theta} (\phi^{\vartheta})^{\gamma} \mathbf{D}_0^{\vartheta} = \sum_{\vartheta=1}^{\Theta} \left(\prod_{\lambda=1}^{\vartheta} (\mathcal{X}^{\lambda})^{\gamma} \prod_{\lambda=\vartheta+1}^{\Theta} (1 - \mathcal{X}^{\lambda})^{\gamma} \right) \mathbf{D}_0^{\vartheta} \quad (4-7)$$

where \mathbf{D}_0^{ϑ} is the elastic tensor matrix of the ϑ_{th} distinct material. γ is the penalty parameter.

As we can see, the developed N-MMI model has the similar mathematical form of the UMMI model in the viewpoint of the TVSSs. Meanwhile, considering the DVFs, the mathematical equation of the N-MMI model is also analogous to the RMMI model. However, the most ingredient of the N-MMI model is the introducing of two mathematical forms for two kinds of variables in a decoupled expression. Here, the N-MMI model can exhibit the advantages: (1) A topology description model to exactly capture a distinct material; (2) No overlaps between multiple materials; (3) No redundant phases in the design domain; (4) No introducing a large number of additional constraints to ensure properties (1), (2) and (3); (5) An explicit mathematical form to ease the sensitivity analysis.

4.2 Multi-material Isogeometric topology optimization (M-ITO)

4.2.1 M-ITO formulation to minimize the structural mean compliance

The minimization of the structural mean compliance for the linearly elastic structures will be studied to show the effectiveness of the proposed N-MMI model, and the M-ITO formulation for the problem with multiple volume constraints can be stated as:

$$\left\{ \begin{array}{l} \text{Find: } \rho_{i,j}^{\vartheta} \quad (\vartheta = 1, 2, \dots, \Theta; \quad i = 1, 2, \dots, m; \quad j = 1, 2, \dots, n) \\ \text{Min: } J(\mathbf{u}, \boldsymbol{\phi}) = \frac{1}{2} \int_{\Omega} \mathbf{D}(\boldsymbol{\phi}(\rho_{i,j}^{\vartheta})) \boldsymbol{\varepsilon}(\mathbf{u}) \boldsymbol{\varepsilon}(\mathbf{u}) d\Omega \\ \text{S.t. } \left\{ \begin{array}{l} a(\mathbf{u}, \delta \mathbf{u}) = l(\delta \mathbf{u}), \quad \mathbf{u}|_{\Gamma_D} = \mathbf{g}, \quad \forall \delta \mathbf{u} \in H^1(\Omega) \\ G_v^{\hat{\vartheta}} = \frac{1}{|\Omega|} \int_{\Omega} \boldsymbol{\phi}^{\hat{\vartheta}}(\rho_{i,j}^{\vartheta}) v_0 d\Omega - V_0^{\hat{\vartheta}} \leq 0, \quad (\hat{\vartheta} = 1, 2, \dots, \Theta) \\ 0 \leq \rho_{i,j}^{\vartheta} \leq 1 \end{array} \right. \end{array} \right. \quad (4-8)$$

where $\rho_{i,j}^{\vartheta}$ is the $(i,j)_{th}$ nodal design variable for the ϑ_{th} DVF. J is the objective function. $G_v^{\hat{\vartheta}}$ ($\hat{\vartheta} = 1, 2, \dots, \Theta$) is the volume constraint for the $\hat{\vartheta}_{th}$ unique material, and $V_0^{\hat{\vartheta}}$ is the corresponding maximum consumption and v_0 is the volume fraction of the solid. We can find that all the volume constraints have the separable and linear form with respect to the corresponding TVS $\boldsymbol{\phi}^{\hat{\vartheta}}$. $\boldsymbol{\phi}^{\hat{\vartheta}}$ is the TVS to represent the distribution of the $\hat{\vartheta}_{th}$ material. \mathbf{u} is the displacement field in the domain Ω , and \mathbf{g} is the prescribed displacement vector on Γ_D , and $\delta \mathbf{u}$ is the virtual displacement field belonging to the space $H^1(\Omega)$. a and l are the bilinear energy and linear load functions, given as:

$$\left\{ \begin{array}{l} a(\mathbf{u}, \delta \mathbf{u}) = \int_{\Omega} \mathbf{D}(\boldsymbol{\phi}(\rho_{i,j}^{\vartheta})) \boldsymbol{\varepsilon}(\mathbf{u}) \boldsymbol{\varepsilon}(\delta \mathbf{u}) d\Omega \\ l(\delta \mathbf{u}) = \int_{\Omega} \mathbf{f} \delta \mathbf{u} d\Omega + \int_{\Gamma_N} \mathbf{h} \delta \mathbf{u} d\Gamma_N \end{array} \right. \quad (4-9)$$

where \mathbf{f} is the body force and \mathbf{h} is the boundary traction on Γ_N . In order to demonstrate the ability of the proposed M-ITO method to seek the optimum, a more practical problem with the total mass constraint should be studied, and the alternative formulation is written as:

$$\left\{ \begin{array}{l} \text{Find: } \rho_{i,j}^{\vartheta} \quad (\vartheta = 1, 2, \dots, \Theta; i = 1, 2, \dots, m; j = 1, 2, \dots, n) \\ \text{Min: } J(\mathbf{u}, \boldsymbol{\phi}) = \frac{1}{2} \int_{\Omega} \mathbf{D}(\boldsymbol{\phi}(\rho_{i,j}^{\vartheta})) \boldsymbol{\varepsilon}(\mathbf{u}) \boldsymbol{\varepsilon}(\mathbf{u}) d\Omega \\ \text{S.t.} \left\{ \begin{array}{l} a(\mathbf{u}, \delta \mathbf{u}) = l(\delta \mathbf{u}), \quad \mathbf{u}|_{\Gamma_D} = g, \quad \forall \delta \mathbf{u} \in H^1(\Omega) \\ G_m = \sum_{\hat{\vartheta}=1}^{\Theta} G_v^{\hat{\vartheta}} \Lambda_0^{\hat{\vartheta}} - M_0 \leq 0, \quad (\hat{\vartheta} = 1, 2, \dots, \Theta) \\ 0 \leq \rho_{i,j}^{\vartheta} \leq 1 \end{array} \right. \end{array} \right. \quad (4-10)$$

where $\Lambda_0^{\hat{\vartheta}}$ is the mass density of the $\hat{\vartheta}_{th}$ unique material and M_0 is the maximal value of the structural mass in the constraint G_m . Similar to volume constraints, the total mass constraint is also featured with a separable-linear form of the corresponding TVS $\boldsymbol{\phi}^{\hat{\vartheta}}$. As we can see, the formulation 2 in Eq. (4-10) can simultaneously consider the influence of volume fractions and structural mass on the selection of materials in the optimization. It should be noticed that multiple mass constraints are physically equivalent compared to the formulation 1 defined in Eq. (4-8), due to the fact that the volume constraint for each distinct material is separable and linear with respect to the TVS $\boldsymbol{\phi}^{\hat{\vartheta}}$ of the $\hat{\vartheta}_{th}$ material. Multiple volume constraints can be directly converted into mass constraints by multiplying the corresponding mass density on both sides. This positive feature can lower the numerical troubles in the optimization to a great extent, particularly for the formulation with the total mass constraint.

4.2.2 Sensitivity analysis of the objective function

In Eqs. (4-8) and (4-10), the objective function is the structural compliance. The first-order derivative of the structural compliance with respect to the TVS $\boldsymbol{\phi}^{\hat{\vartheta}}$ can be derived as:

$$\begin{cases} \frac{\partial J}{\partial \phi^{\hat{\vartheta}}} = \int_{\Omega} \mathbf{D}(\phi^{\hat{\vartheta}}) \boldsymbol{\varepsilon}(\dot{\mathbf{u}}) \boldsymbol{\varepsilon}(\mathbf{u}) d\Omega + \frac{1}{2} \int_{\Omega} \frac{\partial \mathbf{D}(\phi^{\hat{\vartheta}})}{\partial \phi^{\hat{\vartheta}}} \boldsymbol{\varepsilon}(\mathbf{u}) \boldsymbol{\varepsilon}(\mathbf{u}) d\Omega \\ (\hat{\vartheta} = 1, 2, \dots, \Theta) \end{cases} \quad (4-11)$$

where $\dot{\mathbf{u}}$ is the first-order derivative of the displacement field with respect to the TVS $\phi^{\hat{\vartheta}}$. Performing the first-order derivatives on both sides of the equilibrium state equation in Eq. (4-9), expressed by:

$$\begin{cases} \frac{\partial a}{\partial \phi^{\hat{\vartheta}}} = \begin{cases} \int_{\Omega} \mathbf{D} \boldsymbol{\varepsilon}(\dot{\mathbf{u}}) \boldsymbol{\varepsilon}(\delta \mathbf{u}) d\Omega + \int_{\Omega} \mathbf{D} \boldsymbol{\varepsilon}(\mathbf{u}) \boldsymbol{\varepsilon}(\delta \dot{\mathbf{u}}) d\Omega \\ + \int_{\Omega} \frac{\partial \mathbf{D}(\phi^{\hat{\vartheta}})}{\partial \phi^{\hat{\vartheta}}} \boldsymbol{\varepsilon}(\mathbf{u}) \boldsymbol{\varepsilon}(\delta \mathbf{u}) d\Omega \end{cases} \\ \frac{\partial l}{\partial \phi^{\hat{\vartheta}}} = \int_{\Omega} \mathbf{f} \delta \dot{\mathbf{u}} d\Omega + \int_{\Gamma_N} \mathbf{h} \delta \dot{\mathbf{u}} d\Gamma_N \end{cases} \quad (4-12)$$

where $\delta \dot{\mathbf{u}}$ is the derivative of the virtual displacement field with respect to the TVS $\phi^{\hat{\vartheta}}$. Considering that $\delta \dot{\mathbf{u}} \in H^1(\Omega)$, the equilibrium state equation is given as:

$$\int_{\Omega} \mathbf{D}(\phi^{\hat{\vartheta}}) \boldsymbol{\varepsilon}(\mathbf{u}) \boldsymbol{\varepsilon}(\delta \dot{\mathbf{u}}) d\Omega = \int_{\Omega} \mathbf{f} \delta \dot{\mathbf{u}} d\Omega + \int_{\Gamma_N} \mathbf{h} \delta \dot{\mathbf{u}} d\Gamma_N \quad (4-13)$$

Substituting Eq. (4-13) into Eq. (4-12) and removing all the terms containing $\delta \dot{\mathbf{u}}$, and a much more compact form of Eq. (4-12) can be obtained, as:

$$\int_{\Omega} \mathbf{D}(\phi^{\hat{\vartheta}}) \boldsymbol{\varepsilon}(\dot{\mathbf{u}}) \boldsymbol{\varepsilon}(\delta \mathbf{u}) d\Omega = - \int_{\Omega} \frac{\partial \mathbf{D}(\phi^{\hat{\vartheta}})}{\partial \phi^{\hat{\vartheta}}} \boldsymbol{\varepsilon}(\mathbf{u}) \boldsymbol{\varepsilon}(\delta \mathbf{u}) d\Omega \quad (4-14)$$

It is known that the static compliance problem is self-adjoint, and a new form is given by:

$$\int_{\Omega} \mathbf{D}(\phi^{\hat{\vartheta}}) \boldsymbol{\varepsilon}(\dot{\mathbf{u}}) \boldsymbol{\varepsilon}(\mathbf{u}) d\Omega = - \int_{\Omega} \frac{\partial \mathbf{D}(\phi^{\hat{\vartheta}})}{\partial \phi^{\hat{\vartheta}}} \boldsymbol{\varepsilon}(\mathbf{u}) \boldsymbol{\varepsilon}(\mathbf{u}) d\Omega \quad (4-15)$$

Substituting Eq. (4-15) into Eq. (4-11). The derivatives of the compliance with respect to the TVS $\phi^{\hat{\vartheta}}$ is obtained, explicitly expressed as:

$$\frac{\partial J}{\partial \phi^{\hat{\vartheta}}} = -\frac{1}{2} \int_{\Omega} \frac{\partial \mathbf{D}(\phi^{\hat{\vartheta}})}{\partial \phi^{\hat{\vartheta}}} \boldsymbol{\varepsilon}(\mathbf{u}) \boldsymbol{\varepsilon}(\mathbf{u}) d\Omega \quad (4-16)$$

Hence, the sensitivity of the objective function can be achieved by calculating the first-order derivative of the elastic tensor with respect to the VTS $\phi^{\hat{\vartheta}}$. According to the N-MMI model, the sensitivity analysis of the multi-material elastic tensor can be directly obtained, and a new form of Eq. (4-16) is given as:

$$\frac{\partial J}{\partial \phi^{\hat{\vartheta}}} = -\frac{1}{2} \int_{\Omega} \gamma(\phi^{\hat{\vartheta}})^{\gamma-1} \mathbf{D}_0^{\hat{\vartheta}} \boldsymbol{\varepsilon}(\mathbf{u}) \boldsymbol{\varepsilon}(\mathbf{u}) d\Omega \quad (4-17)$$

In Section 4.1, the VTS $\phi^{\hat{\vartheta}}$ to display the layout of the $\hat{\vartheta}$ unique material is expressed as a combination of all DVFs, and each DVF is developed by NURBS basis functions with the nodal design variables ρ^{ϑ} . we can firstly derive the derivative of the VTS $\phi^{\hat{\vartheta}}$ with respect to the DVF \mathcal{X}^{ϑ} , given as:

$$\frac{\partial \phi^{\hat{\vartheta}}}{\partial \mathcal{X}^{\vartheta}} = \begin{cases} \prod_{\lambda=1, \lambda \neq \vartheta}^{\hat{\vartheta}} \mathcal{X}^{\lambda} \prod_{\lambda=\hat{\vartheta}+1}^{\Theta} (1 - \mathcal{X}^{\lambda}) & \text{if } \vartheta \leq \hat{\vartheta} \\ -\prod_{\lambda=1}^{\hat{\vartheta}} \mathcal{X}^{\lambda} \prod_{\lambda=\hat{\vartheta}+1, \lambda \neq \vartheta}^{\Theta} (1 - \mathcal{X}^{\lambda}) & \text{if } \vartheta > \hat{\vartheta} \end{cases} \quad (\vartheta = 1, 2, \dots, \Theta) \quad (4-18)$$

Then, the derivative of the DVF with respect to the nodal design variables can be obtained by consecutively differentiating Eq. (4-4) and (4-1), given as:

$$\frac{\partial \mathcal{X}^{\vartheta}}{\partial \rho_{i,j}^{\vartheta}} = \frac{\partial \mathcal{X}^{\vartheta}}{\partial \mathcal{G}^{\vartheta}} \frac{\partial \mathcal{G}^{\vartheta}}{\partial \rho_{i,j}^{\vartheta}} = R_{i,j}^{p,q}(\xi, \eta) \psi(\rho_{i,j}^{\vartheta}) \quad (4-19)$$

where $R_{i,j}^{p,q}(\xi, \eta)$ is the NURBS basis function at the computational point (ξ, η) . $\psi(\rho_{i,j}^{\vartheta})$ is the Shepard function at the current control point (i, j) . It is important to note that the above computational point (ξ, η) is different from control point (i, j) . The computational points are Gauss quadrature points. The derivative of the structural compliance with respect to the nodal design variables can be derived, and the final form is given as:

$$\begin{aligned} \frac{\partial J}{\partial \rho_{i,j}^\vartheta} &= \frac{\partial J}{\partial \phi} \frac{\partial \phi}{\partial \mathcal{X}^\vartheta} \frac{\partial \mathcal{X}^\vartheta}{\partial \rho_{i,j}^\vartheta} = \sum_{\hat{\vartheta}=1}^{\Theta} \frac{\partial J}{\partial \phi} \frac{\partial \phi}{\partial \mathcal{X}^{\hat{\vartheta}}} \frac{\partial \mathcal{X}^{\hat{\vartheta}}}{\partial \rho_{i,j}^\vartheta} = \dots \\ &\sum_{\hat{\vartheta}=1}^{\Theta} \left\{ \begin{aligned} &\left\{ -\frac{1}{2} \int_{\Omega} \left(\gamma(\mathcal{X}^\vartheta)^{\gamma-1} \prod_{\lambda=1, \lambda \neq \vartheta}^{\hat{\vartheta}} (\mathcal{X}^\lambda)^\gamma \prod_{\lambda=\hat{\vartheta}+1}^{\Theta} (1-\mathcal{X}^\lambda)^\gamma \right) \mathbf{D}_0^{\hat{\vartheta}} \dots \right\} & \text{if } \vartheta \leq \hat{\vartheta} \\ &\left\{ R_{i,j}^{p,q}(\xi, \eta) \psi(\rho_{i,j}^\vartheta) \boldsymbol{\varepsilon}(\mathbf{u}) \boldsymbol{\varepsilon}(\mathbf{u}) d\Omega \right. \\ &\left. -\frac{1}{2} \int_{\Omega} \left(-\gamma(1-\mathcal{X}^\vartheta)^{\gamma-1} \prod_{\lambda=1}^{\hat{\vartheta}} (\mathcal{X}^\lambda)^\gamma \prod_{\lambda=\hat{\vartheta}+1, \lambda \neq \vartheta}^{\Theta} (1-\mathcal{X}^\lambda)^\gamma \right) \mathbf{D}_0^{\hat{\vartheta}} \dots \right\} & \text{if } \vartheta > \hat{\vartheta} \end{aligned} \right\} \end{aligned} \quad (4-20)$$

In Eq. (4-20), we can see that the sensitivity analysis of the objective function with respect to the nodal design variables consist of the DVFs, elastic tensors, NURBS basis functions and Shepard function. The NURBS basis functions keep unchanged and the Shepard function only depends on the spatial locations of the control points. They can be pre-stored without using additional storage space, so that the sensitivity analysis is also cost-effective.

4.2.3 Sensitivity analysis of constraint functions

In formulations 1 and 2, two different constraints are defined, containing multiple volume fractions and the total mass constraint. As far as multiple volume constraints, the derivatives of all volume constraints with respect to the nodal design variables can be derived, as:

$$\begin{aligned} \frac{\partial G_v^\vartheta}{\partial \rho_{i,j}^\vartheta} &= \frac{\partial G_v^\vartheta}{\partial \phi} \frac{\partial \phi}{\partial \mathcal{X}^\vartheta} \frac{\partial \mathcal{X}^\vartheta}{\partial \rho_{i,j}^\vartheta} = \dots \\ &\begin{cases} \left\{ \frac{1}{|\Omega|} \int_{\Omega} \left(\prod_{\lambda=1, \lambda \neq \vartheta}^{\hat{\vartheta}} \mathcal{X}^\lambda \prod_{\lambda=\hat{\vartheta}+1}^{\Theta} (1-\mathcal{X}^\lambda) R_{i,j}^{p,q} \psi(\rho_{ij}^\vartheta) \right) v_0 d\Omega \right\} & \text{if } \vartheta \leq \hat{\vartheta} \\ \left\{ -\frac{1}{|\Omega|} \int_{\Omega} \left(\prod_{\lambda=1}^{\hat{\vartheta}} \mathcal{X}^\lambda \prod_{\lambda=\hat{\vartheta}+1, \lambda \neq \vartheta}^{\Theta} (1-\mathcal{X}^\lambda) R_{i,j}^{p,q} \psi(\rho_{ij}^\vartheta) \right) v_0 d\Omega \right\} & \text{if } \vartheta > \hat{\vartheta} \end{cases} \end{aligned} \quad (4-21)$$

The first-order derivative of the total mass constraint in formulation 2 can be derived by the summation of all the derivatives of multiple volume constraints with mass densities, given as:

$$\frac{\partial G_m}{\partial \rho_{i,j}^{\vartheta}} = \sum_{\hat{\vartheta}=1}^{\Theta} \frac{\partial G_v^{\hat{\vartheta}}}{\partial \rho_{i,j}^{\hat{\vartheta}}} \Lambda_0^{\hat{\vartheta}} = \dots$$

$$\sum_{\hat{\vartheta}=1}^{\Theta} \left\{ \begin{aligned} & \frac{1}{|\Omega|} \int_{\Omega} \left(\prod_{\lambda=1, \lambda \neq \vartheta}^{\hat{\vartheta}} \mathcal{X}^{\lambda} \prod_{\lambda=\hat{\vartheta}+1}^{\Theta} (1 - \mathcal{X}^{\lambda}) R_{i,j}^{p,q} \psi(\rho_{ij}^{\hat{\vartheta}}) \right) \Lambda_0^{\hat{\vartheta}} v_0 d\Omega \quad \text{if } \vartheta \leq \hat{\vartheta} \\ & - \frac{1}{|\Omega|} \int_{\Omega} \left(\prod_{\lambda=1}^{\hat{\vartheta}} \mathcal{X}^{\lambda} \prod_{\lambda=\hat{\vartheta}+1, \lambda \neq \vartheta}^{\Theta} (1 - \mathcal{X}^{\lambda}) R_{i,j}^{p,q} \psi(\rho_{ij}^{\hat{\vartheta}}) \right) \Lambda_0^{\hat{\vartheta}} v_0 d\Omega \quad \text{if } \vartheta > \hat{\vartheta} \end{aligned} \right\} \quad (4-22)$$

Hereto, the sensitivity analysis for two formulations, including the objective and constraint functions, are derived in detail from Eqs. (4-11) to (4-22). In the M-ITO method, the nodal design variables will be optimized with a gradient-based optimization algorithm to solve the multi-material optimization formulations, and the method of moving asymptotes (MMA) [72] is used in the next numerical examples.

4.3 Numerical Examples

In this section, several numerical examples are performed to demonstrate the effectiveness of the proposed M-ITO method. All structures with the linear elasticity are considered, and 2D structures will be discretized with the IGA elements with unit edge thickness. In all examples, the magnitude of the loaded force is equal to unit, and 3×3 (2D) or $3 \times 3 \times 3$ (3D) Gauss quadrature points are chosen in solving the IGA element stiffness matrix. All the nodal design variables ρ^{ϑ} ($\vartheta = 1, 2, \dots, \Theta$) are defined as 0.5, and the penalty factor γ is set to be 3. The convergence will be terminated when the maximum change of the DVFs is lower than 1% within 300 iterations. Four “virtual” isotropic solid materials will be considered in examples, and the details are listed in Table 4-1, including the Young’s modulus, Poisson’s ratio, Mass density and the stiffness-to-mass ratio.

Table 4-1 Four “virtual” isotropic solid materials

i	Materials	Young’s modulus: E_0^i	Poisson’s ratio ν	Mass density: Λ_0^i	Stiffness-to-mass ratio: \mathcal{R}_o^i
-----	-----------	--------------------------	-----------------------	--------------------------------	---

1	M1	10	0.3	2	5
2	M2	10	0.3	5	2
3	M3	5	0.3	2	2.5
4	M4	3	0.3	2	1.5

4.3.1 Messerschmitt-Bolkow-Blohm (MBB) beam

The formulation 1 with multiple volume constraints is applied to optimize the MBB beam in this example. In Figure 4-4, the MBB beam with the loads and boundary conditions is defined, and two indices L and H are set as 18 and 3, respectively. The NURBS is used to parameterize the MBB beam. The details are listed below Figure 4-4, where the quadratic NURBS basis functions are used.

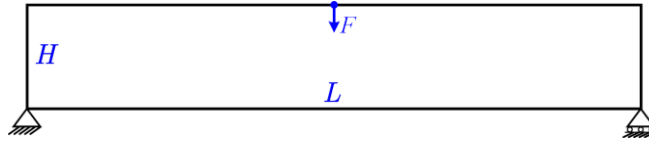


Figure 4-4 The details of MBB beam

IGA elements 180×30 ; $\Xi = \{0, 0, 0, 0, 0.00565, \dots, 0.99444, 1, 1, 1, 1\}$,
 $\mathcal{H} = \{0, 0, 0, 0, 0.0333, \dots, 0.9667, 1, 1, 1, 1\}$; $n = 183$, $m = 33$; $p = 3$, $q = 3$;

4.3.1.1 Two-material design

In this case, two distinct materials (**M2** and **M3**) are available in the optimization of the MBB beam. Two TVFs need to be defined for **M2** and **M3** materials, respectively, denoted by ϕ^1 and ϕ^2 . In Eq. (14), the allowable material volume fractions for **M2** and **M3** are defined as 20% and 8%, respectively. As discussed in Section 4.1, the Gauss quadrature points work as the computational points in solving the stiffness matrix. In numerical results, we firstly show the TVFs at the Gauss quadrature points (GQPs) and then display the TVFs of the design domain. As defined in Section 3.1, the DVF corresponds to a NURBS surface with the strict physical meanings (densities) for the design domain, and each TVF is a combination of all DVFs. Hence, a TVF can be viewed as a DDF to represent the distribution of each distinct

material in the design domain. Currently, the initial nodal densities are equal to 0.5, and the corresponding initial designs of the TVFs for two materials are shown in Figure 4-5, including the TVFs at the Gauss quadrature points and the TVFs in the design domain. It can be found that the TVFs at the Gauss quadrature points are the discretized distribution of densities, and the TVFs in the design domain are the continuous form of the density distribution.

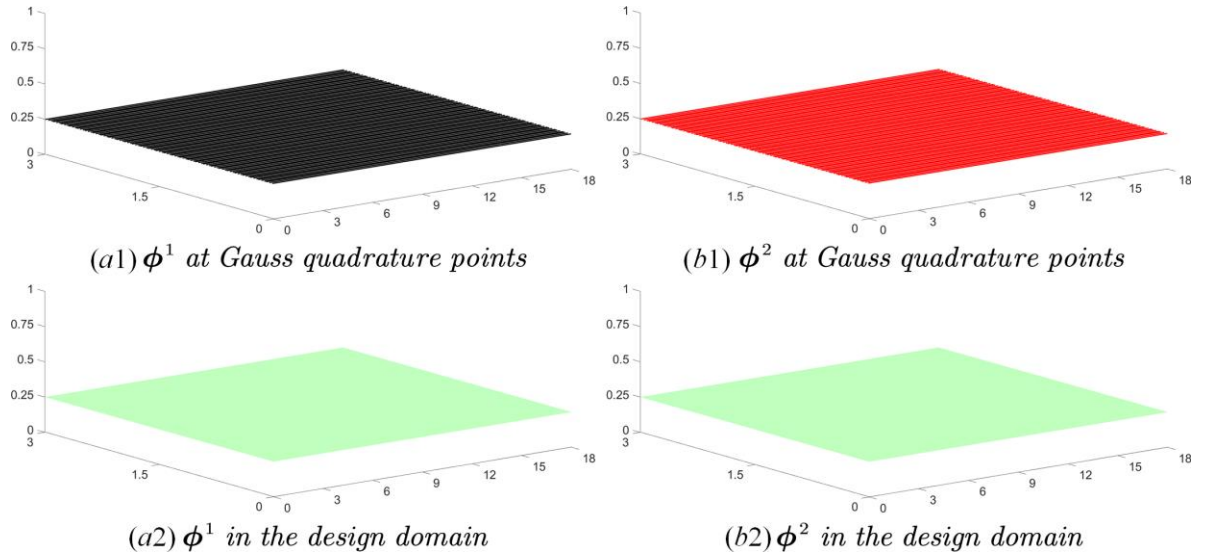


Figure 4-5 Initial design of the MBB beam

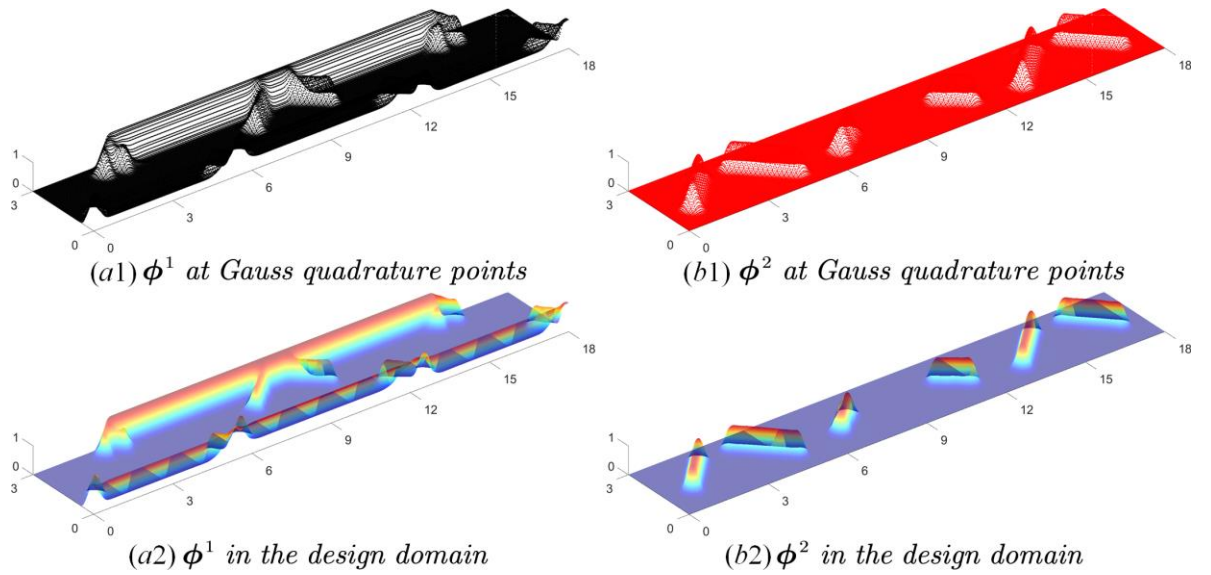


Figure 4-6 The optimized design of the MBB beam

As displayed in Figure 4-6, the optimized design of the MBB beam with two distinct materials (**M2** and **M3**) is provided, including the TVFs at the Gauss quadrature points and in the design domain. As we can see, the TVFs are featured with the sufficient smoothness and continuity, mainly resulting from the construction of DVFs using NURBS basis functions and Shepard function. The former can make sure the continuity, and the latter guarantees the smoothness. Moreover, it can easily be seen that the densities of the optimized TVFs in the design domain are mostly distributed nearly the lower and upper bounds.





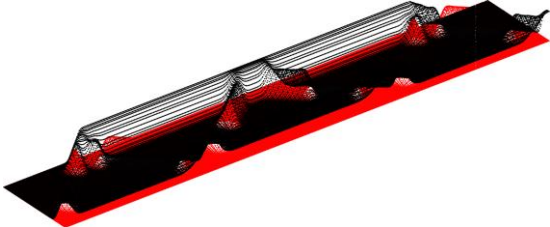
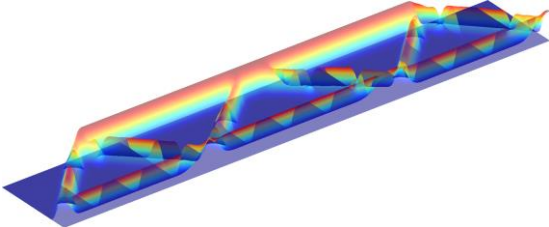
Based on the optimized design of the MBB beam shown in Figure 4-6, a simple but efficient heuristic scheme is introduced to define the topology, and the corresponding mathematical model is defined in Eq. (4-23), where ϕ_c is a constant. As we can see, the structural boundary of the MBB beam is expressed by the iso-contour of ϕ . ϕ with the values higher than ϕ_c represents the solids in the design domain, and the values lower than ϕ_c describes voids. Hence, this scheme is very analogous to the implicit representation model in the LSM [13–15]. However, it is important to note that the heuristic scheme is just a post-definition criterion to obtain the structural topology from the optimized TVFs.

$$\begin{cases} 0 \leq \phi(\xi, \eta) < \phi_c & \text{void} \\ \phi(\xi, \eta) = \phi_c & \text{boundary} \\ \phi_c < \phi(\xi, \eta) \leq 1 & \text{solid} \end{cases} \quad (4-23)$$

As discussed in [105,125] for the optimization of the single-material problems, the constant equal to 0.5 can ensure that the final volume fraction of the obtained topology is mostly identical to the prescribed allowable material consumption. In [105], the extensive discussions about the definition of the constant are performed. Here, the post-definition scheme is applied to define the topology for the multi-material problems from the TVFs. The constant should

be equal to 0.5 to guarantee no overlaps between different materials and no redundant phases in the N-MMI model. For example, if the constant ϕ_c is equal to 0.2, it means that the densities at the structural boundaries of **M2** and **M3** materials are both equal to 0.2, and the summation of them is equal to 0.4, which cannot satisfy the summation of the densities of all materials in each designable point is equal to 1. Hence, the constant ϕ_c must be equal to 0.5 to guarantee the reasonable physical meanings of the N-MMI model. As listed in Table 4-2, the optimized results of the MBB beam with two materials are provided, including the 2D-view of the TVF ϕ^1 with the higher values than ϕ_c at the Gauss Quadrature Points (GQPs), and the corresponding topology of **M2** material, the 2D-view of the TVF ϕ^2 with the higher values than ϕ_c at the GQPs, the topology of **M3** material, the TVFs ϕ^1 and ϕ^2 at the GQPs and in the design domain, the 2D-view of the TVFs ϕ^1 and ϕ^2 at the GQPs, and the topology of two materials in the design domain. The volume fraction of the topology of **M2** material is equal to 19.7% (nearly 20%), and the volume fraction of the topology of **M3** material is equal to 7.8% (nearly 8%). Hence, the volume fraction of the topology of two materials in the MBB beam is equal to 27.5% (also nearly 28%).

Table 4-2 The optimized results of the MBB beam with two materials

M2 material	2D-view of the TVS ϕ^1 at GQPs	The optimized topology
		
M3 material	2D-view of the TVS ϕ^2 at GQPs	The optimized topology
		
The TVSs ϕ^1 and ϕ^2 at GQPs		The TVSs ϕ^1 and ϕ^2 in the design domain
		

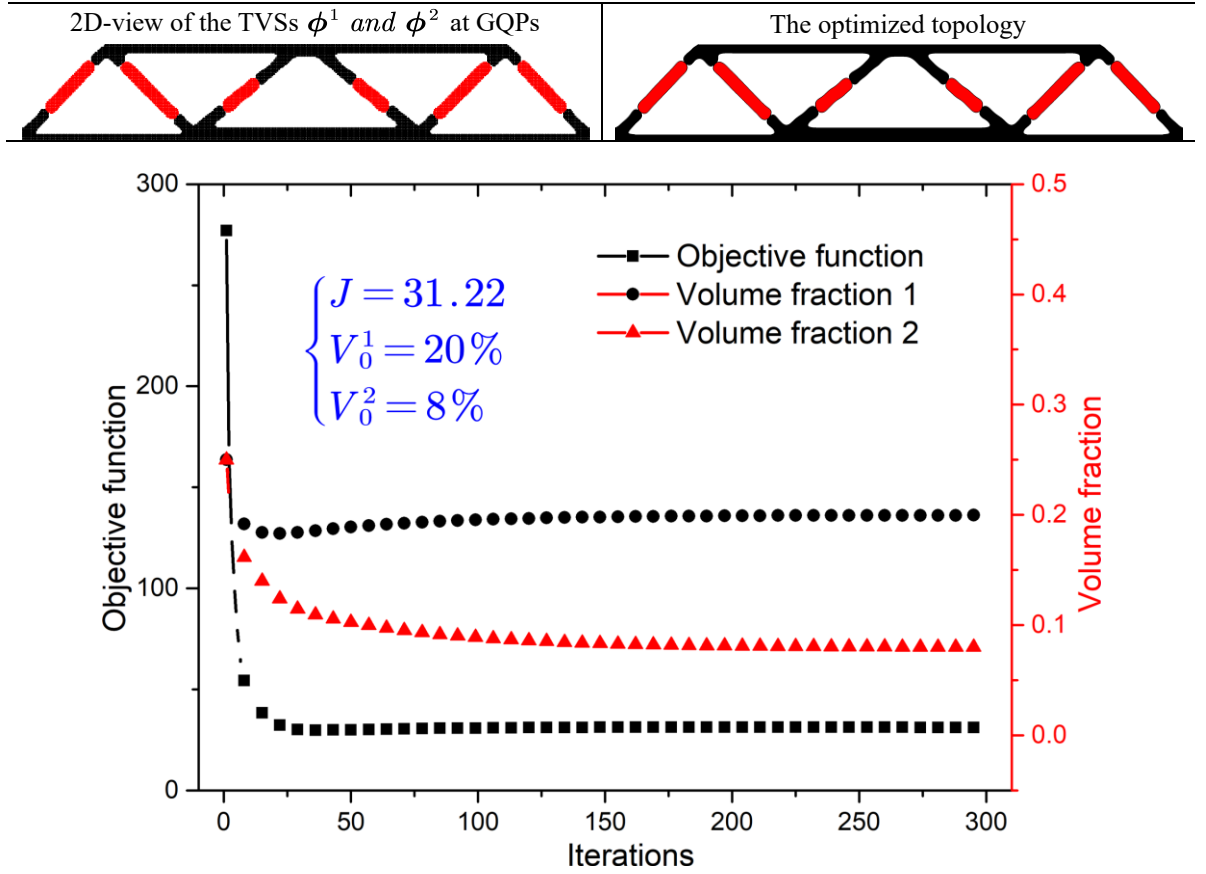


Figure 4-7 Convergent histories

Additionally, each distinct material in the final two-material design can form the independent load-bearing structural members, as displayed in Table 4-2, owing to a fact that the Young's modulus is comparable between two materials (**M2** with $E_0^2 = 10$ and **M3** with $E_0^3 = 5$), also given in [1,76]. To this end, the optimized design in this example can present the effectiveness of the developed M-ITO method in seeking the overall distribution of multiple materials in the design domain. Moreover, a pure design that each point only has one phase demonstrates the effectiveness of the proposed N-MMI model. Finally, the iterative curves for the objective function and two volume fractions are shown in Figure 4-7, which shows the stable iteration to arrive at the final design, and the volume fraction of each distinct material can be preserved. Moreover, it should be noted that the volume fractions in the iterative curves correspond to

the variations of the TVFs ϕ^1 and ϕ^2 for two materials. However, the volume fractions in Table 4-2 of the topologies for two materials are defined by TVFs with a slight modification, namely $\phi \leftarrow 1$ (if $\phi \geq \phi_c$) and $\phi \leftarrow 0$ (if $\phi < \phi_c$).

4.3.1.2 Three-material design

This case will consider the three-material topology optimization for the MBB beam, and **M2**, **M3** and **M4** materials will be available, and the corresponding volume fractions for three materials are set as 20%, 12% and 3%, respectively. The initial designs of the TVFs for **M2**, **M3** and **M4** materials are illustrated in Figure 4-8, including the TVFs at the GQPs and in the design domain.

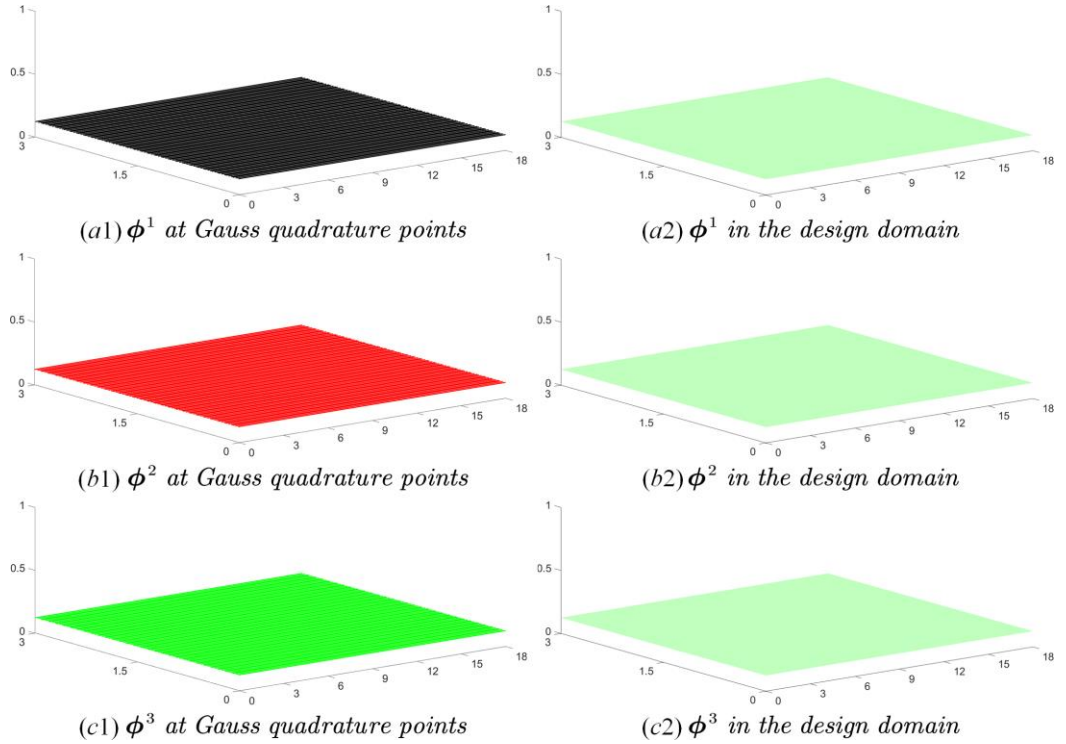


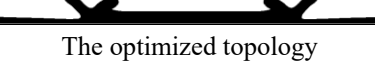


Figure 4-8 Initial design of the MBB beam

The optimized designs of the TVFs for three materials are displayed in Figure 4-9, consisting of the discretized distributions of the TVFs at the GQPs, and the continuous distributions of the TVFs in the design domain. It can be easily seen that three continuous distributions of the

TVFs are featured with the enough continuity and smoothness. The heuristic scheme in Eq. (29) is employed here to define the structural topology of the MBB beam with three materials from the optimized TVFs shown in Figure 4-9, and the constant ϕ_c is still defined as 0.5. The numerical results of three materials in the MBB beam are listed in Table 4-3, including the 2D-views of the TVFs at the GQPs with the values higher than 0.5, and the topologies of three materials in the design domain. We can easily see that the three-material topology of the MBB beam is characterized with the distinct interfaces between multiple materials and voids. The necessary requirements studied in Section 3 can be perfectly maintained in the final three-material topology, like no overlaps, no redundant phases and so on. Hence, the effectiveness of the proposed N-MMI model in the optimization can be demonstrated clearly. Moreover, each distinct material is formed into the independent members to afford the load transmission in the design domain, due to the comparable values of the Young's modulus of three materials. Additionally, the convergent histories of the objective function and volume fractions for three materials are displayed in Figure 4-10. It can be easily seen that all the iterative curves are very smooth and the optimization for three materials is featured with the high stability. The volume fractions of three TVFs can quickly arrive at the prescribed values, namely 20%, 12% and 3%. The corresponding volume fractions of the achieved topologies in Table 4-3 are equal to 20.13%, 11.5% and 2.98%, respectively. Hence, we can confirm that the M-ITO method has the capability to seek the optimized distributions of three materials.

Table 4-3 The optimized results of the MBB beam with three materials

M2 material	2D-view of the TVS ϕ^1 at GQPs	The optimized topology
	2D-view of the TVS ϕ^2 at GQPs	The optimized topology
		
		

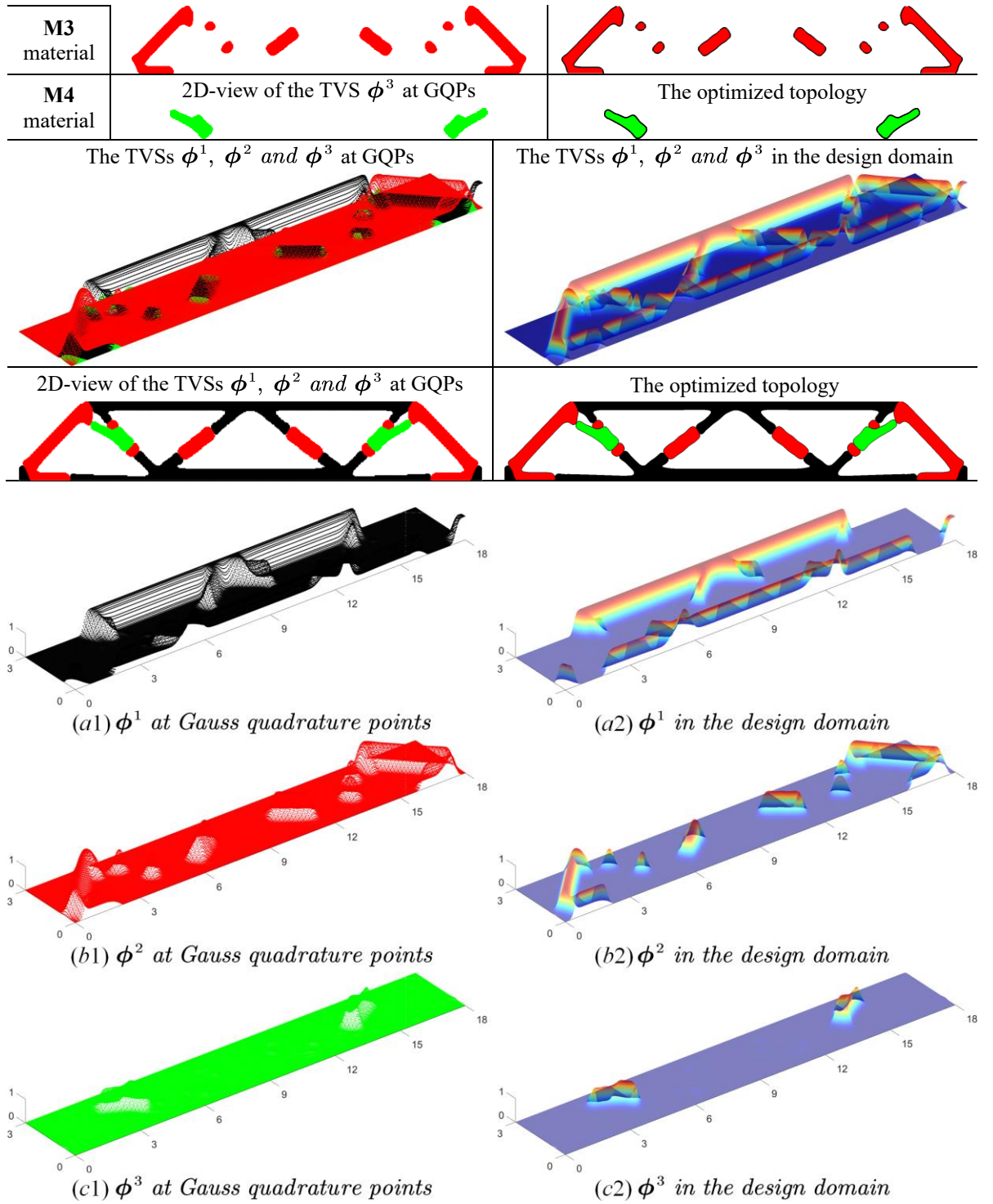


Figure 4-9 The optimized design of the MBB beam

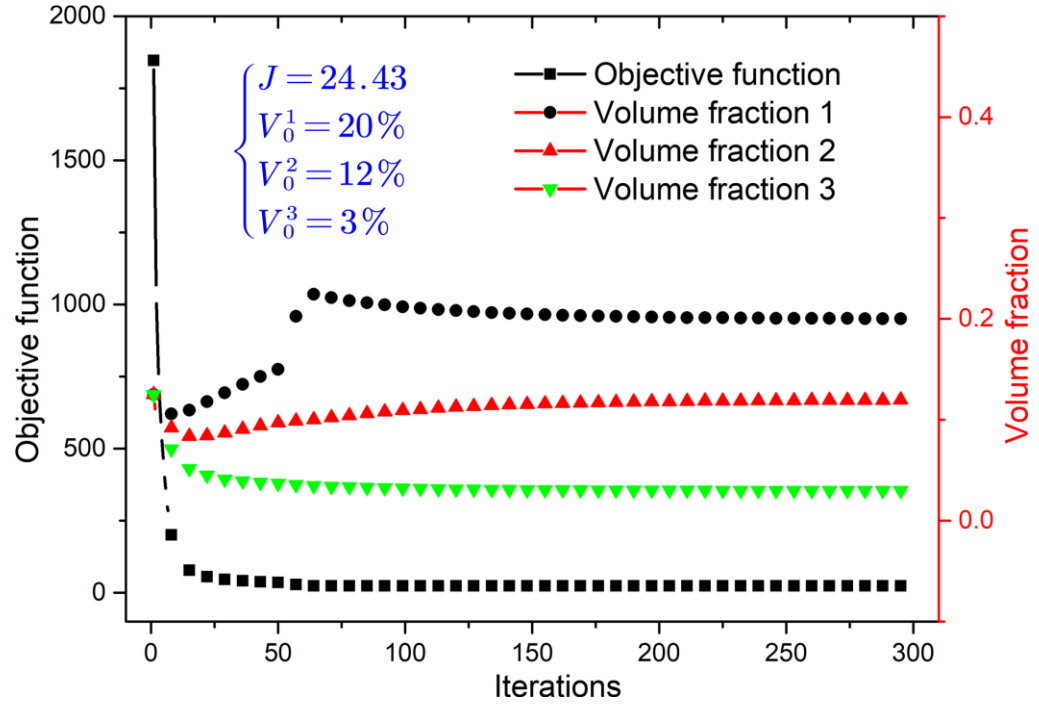


Figure 4-10 Convergent histories

4.3.2 Cantilever beam

In this section, the cantilever beam is optimized by formulation 2 to study the effectiveness of the N-MMI model on the multi-material problem with the mass constraint. The structural design domain with the loads and boundary conditions is defined in Figure 4-11, where the scales in two directions are 10 (L) and 5 (H), respectively. The beam is parametrized by the NURBS surface, and the corresponding numerical details are listed below Figure 4-11.

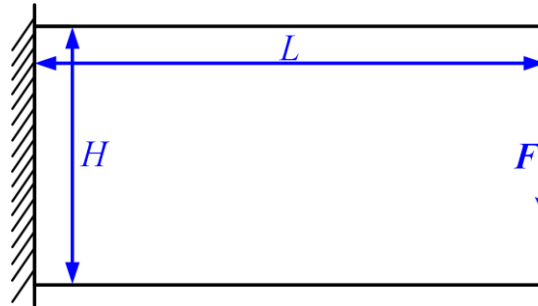


Figure 4-11 The details of Cantilever beam

IGA elements 100×50 ; $\Xi = \{0, 0, 0, 0.01, \dots, 0.99, 1, 1, 1\}$,
 $\mathcal{H} = \{0, 0, 0, 0.02, \dots, 0.98, 1, 1, 1\}$; $n = 102$, $m = 52$; $p = 2$, $q = 2$;

4.3.2.1 Two-material design

Two distinct materials (**M2** and **M3**) will be considered in the optimization of the cantilever beam. As defined in Table 4-1, **M2** material has the larger Young's modulus $E_0^2 = 10$, but with a lower Stiffness-to-mass ratio $\mathcal{R}_o^2 = 2$, compared with **M3** material with $E_0^3 = 5$ and $\mathcal{R}_o^3 = 2.5$ presented in Table 4-1. In formulation 2, the maximum consumption of the total mass G_m is set to be 30. Similar to Section 5.2, two different colors (the black and red) are used to describe the overall distributions of **M2** and **M3** materials within the optimized design, respectively. Meanwhile, the initial designs of TVFs for two materials has the same densities in the initial designs shown in Figure 4-5.

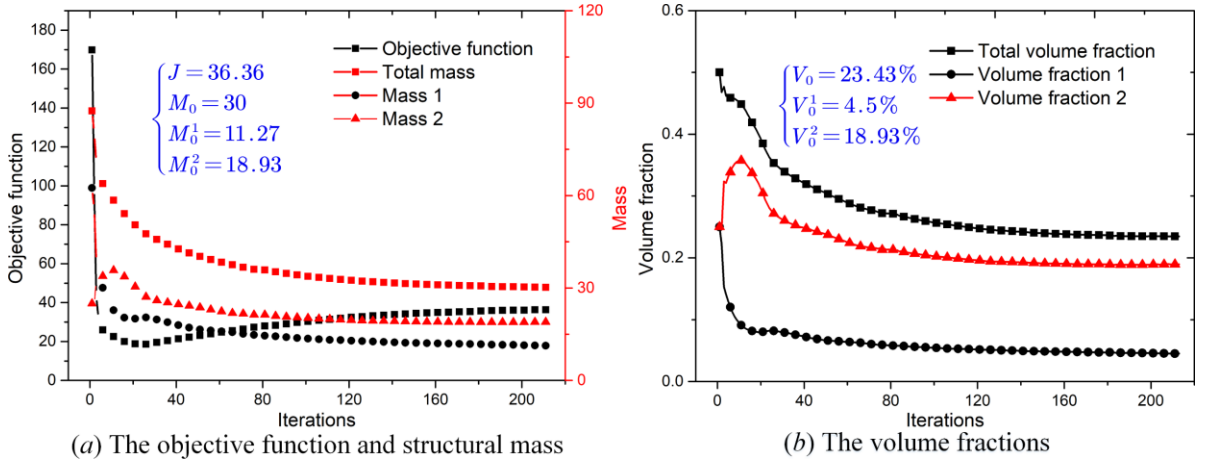


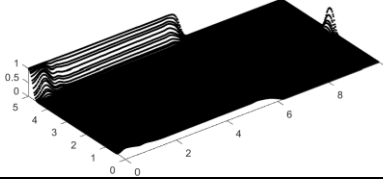
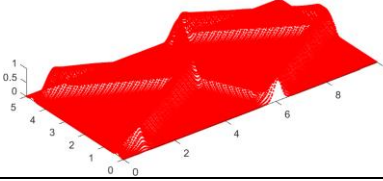
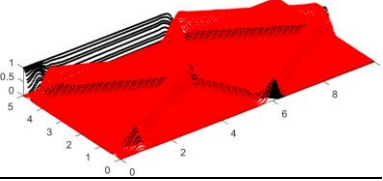

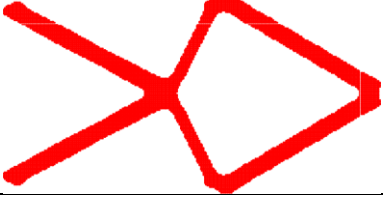
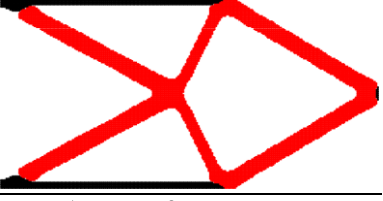
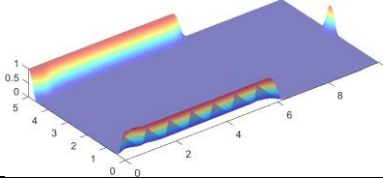
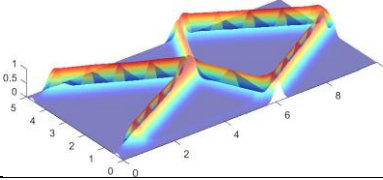
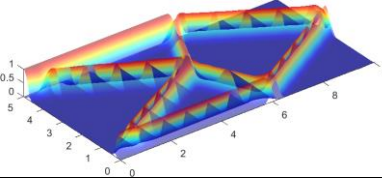
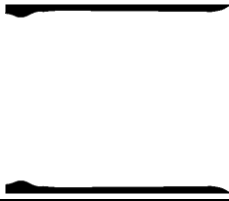
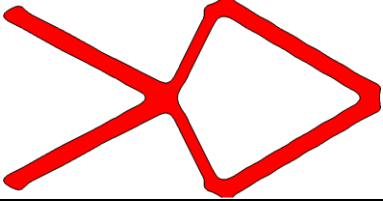
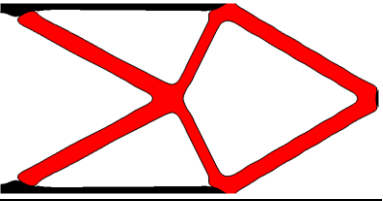
Figure 4-12 Convergent histories

The optimized results of the cantilever beam with **M2** and **M3** materials are listed in Table 4-4. Firstly, the discretized and continuous distributions of the TVFs at the GQPs and in the design domain are illustrated in the second and sixth rows of Table 4-4, respectively. Similar to the above example in Section 4.3.1 for MBB beam, the distributions of the TVFs are also featured with the sufficient smoothness and continuity, which are beneficial to the latter definition of the structural topology. The heuristic scheme defined in Eq. (29) is applied to

define the structural topology for multiple materials, where the constant is still set as 0.5. Hence, the 2D-views of the TVFs at the GQPs with values higher than 0.5 are displayed in the fourth row of Table 4-4, and the topologies for two materials are listed in the last row of Table 4-4. As shown in the last row and column of Table 4-4 for the optimized topology of multiple materials in the cantilever beam, we can observe that the optimized distributions for two materials have the distinct interfaces and smooth boundaries between the solids and voids. Hence, we can confirm that the N-MMI model is effective on the optimization of multi-material structures with the total mass constraint.

Meanwhile, **M2** and **M3** materials are formed into different structural members in the final topology to afford the loads, such as the black part filled with the strong **M2** material and the color area occupied by the weak **M3** material. Moreover, **M2** material is mainly filled in the areas having the stress concentration, in order to provide the higher stiffness for the beam. However, the weak material **M3** is dominant in the overall distribution, because the material has a larger stiffness-to-mass ratio. Hence, the formulation 2 with the total mass constraint improves the structural performance considering two components, namely the stiffness and mass, simultaneously. Finally, the iterative histories of the structural compliance, the total mass and mass of each material are shown in Figure 4-12 (a). Meanwhile, the iterative curves of the total volume fraction and the volume fraction for each material are displayed in Figure 4-12 (b). It can be easily seen that the optimization with the total mass constraint for multiple materials is featured with the superior stability to seek the distributions of multiple materials in the design domain. Moreover, the mass of each material has been gradually adjusted during the optimization to enhance the structural performance as much as possible, rather than in a monotonous way of the single-material optimization.

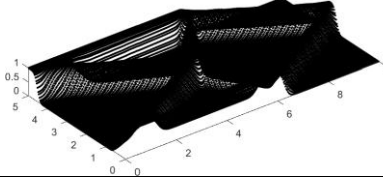
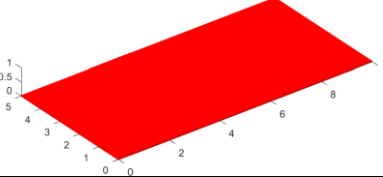
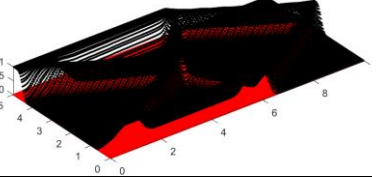
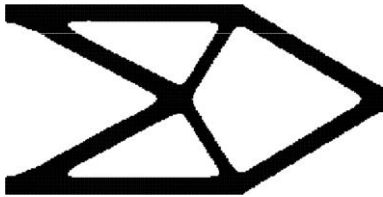

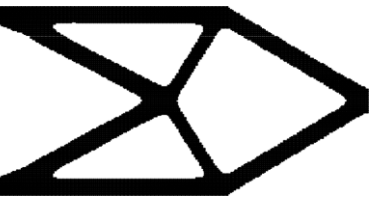
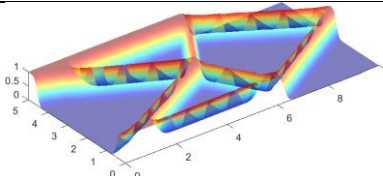
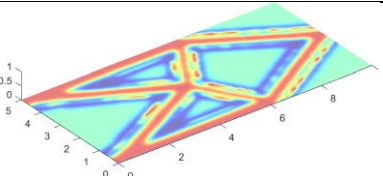
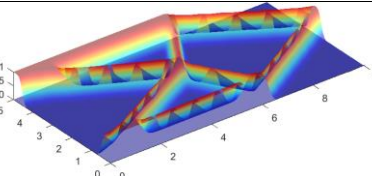
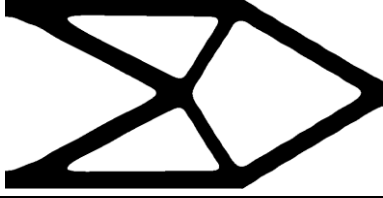

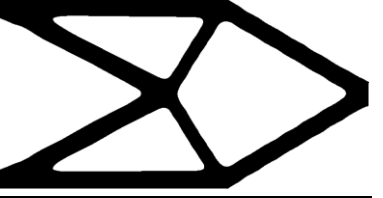
Table 4-4 The optimized results of cantilever beam with two materials

ϕ^1 at GQPs	ϕ^2 at GQPs	ϕ^1 and ϕ^2 at GQPs
		
2D-view of ϕ^1 at GQPs	2D-view of ϕ^2 at GQPs	2D-view of ϕ^1 and ϕ^2 at GQPs
		
ϕ^1 in the design domain	ϕ^2 in the design domain	ϕ^1 and ϕ^2 in the design domain
		
The topology of M2 material	The topology of M3 material	The topology of cantilever beam
		

4.3.2.2 Influence of the stiffness-to-mass ratio

In order to present the effect of the stiffness-to-mass ratio on the multi-material optimization, **M1** and **M3** materials are available in this case. The Young's modulus $E_0^1 = 10$ and stiffness-to-mass ratio $\mathcal{R}_o^1 = 5$ of **M1** material are both larger than **M3** material having $E_0^3 = 5$ and $\mathcal{R}_o^3 = 2.5$. The total mass consumption is same as Section 4.1.1, namely $G_m = 30$. **M1** and **M3** materials are respectively plotted with the black and red. The initial designs of the TVSSs for **M1** and **M3** materials are also consistent with Section 4.1.1, and with same densities shown in Figure 4-5.

Table 4-5 The optimized results of cantilever beam with two materials

ϕ^1 at GQPs	ϕ^2 at GQPs	ϕ^1 and ϕ^2 at GQPs
		
2D-view of ϕ^1 at GQPs	2D-view of ϕ^2 at GQPs	2D-view of ϕ^1 and ϕ^2 at GQPs
		
ϕ^1 in the design domain	ϕ^2 in the design domain	ϕ^1 and ϕ^2 in the design domain
		
The topology of M1 material	The topology of M3 material	The topology of cantilever beam
		

As listed in Table 4-5, the optimized results of the cantilever beam with **M1** and **M3** materials are provided, also including the TVSs at the GQPs and in the design domain in the second and sixth rows, respectively, the 2D-views of the TVSs at the GQPs with the higher values than 0.5 in the fourth row, and the topologies of **M1**, **M3** materials and the cantilever beam obtained by the heuristic scheme with the constant 0.5. As we can see, the optimized topology of the cantilever beam with **M1** and **M3** materials is completely different from the design in Section 4.3.1. In the current design, the cantilever beam only consists of **M1** material, even if **M3** material is available during the optimization. As clearly shown in the convergent curves in Figure 4-13, the mass of **M3** material gradually decreases within the optimization, until it

arrives at zero. Meanwhile, the mass of **M1** material is equal to the total mass, and their convergent curves coincide together. Hence, we can confirm that the multi-material topology optimization formulation with the total mass constraint is more prone to choose the material with both the larger Young's modulus and stiffness-to-mass ratio, to improve the structural performance. Meanwhile, it also reveals that the developed M-ITO method with the N-MMI model has the capability to find the design only with one material, if the Young's modulus and stiffness-to-mass ratio are both larger compared with other available materials. In the viewpoint of the authors', the main reason is that the total mass constraint in formulation 2 is separate and linear with respect to topology variables, which can be beneficial to lower the numerical difficulties to find the design solution with the optimized performance. Moreover, the designs of the cantilever beam in above examples, including Figure 4-9, Table 4-2 to 4-5, do not have the "mixture" materials, namely unrealistic designs.

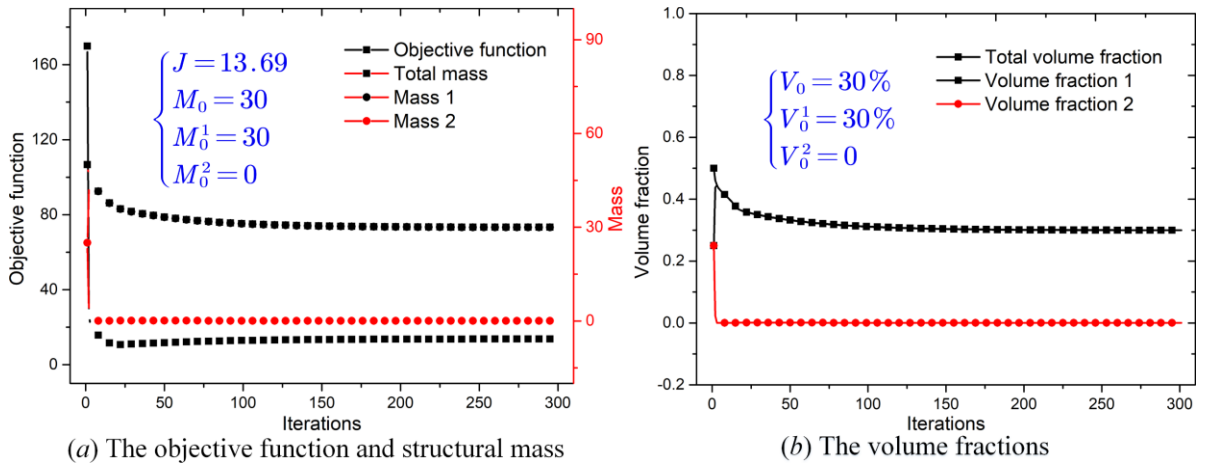


Figure 4-13 Convergent histories

4.3.2.3 Three-material design

In this sub section, we will present the effectiveness of the formulation 2 to seek the three-material design of the cantilever beam (**M2**, **M3** and **M4**). In Table 4-1, **M2** material has the

larger Young's modulus and a larger Stiffness-to-mass ratio is featured by **M3** material. Three materials (**M2**, **M3** and **M4**) will be plotted with different colors, namely the black, red and green colors, respectively, in the optimized distributions. The maximum value of the total mass constraint is defined as 35. The initial designs of the TVFs for three materials have the same densities of the TVFs shown in Figure 4-9.

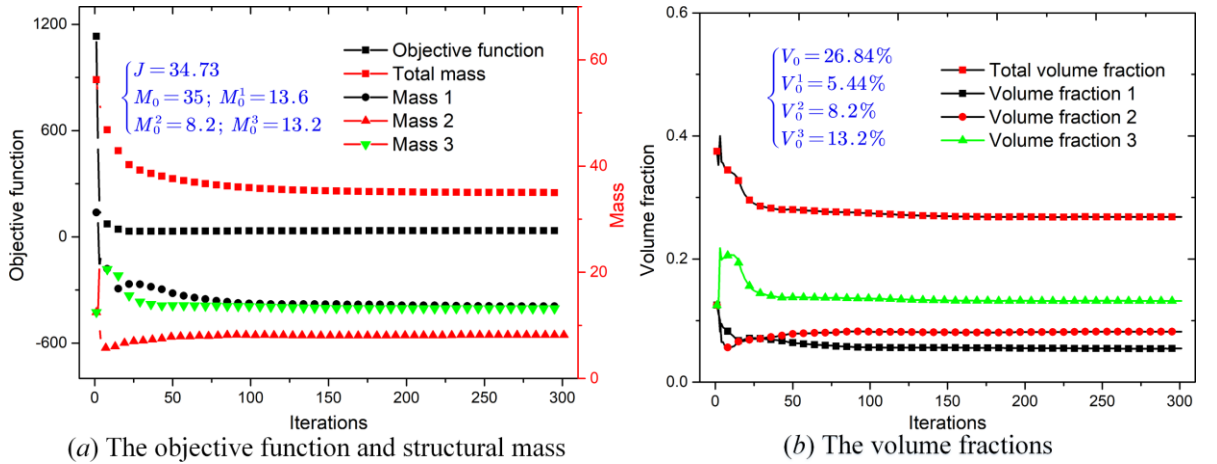


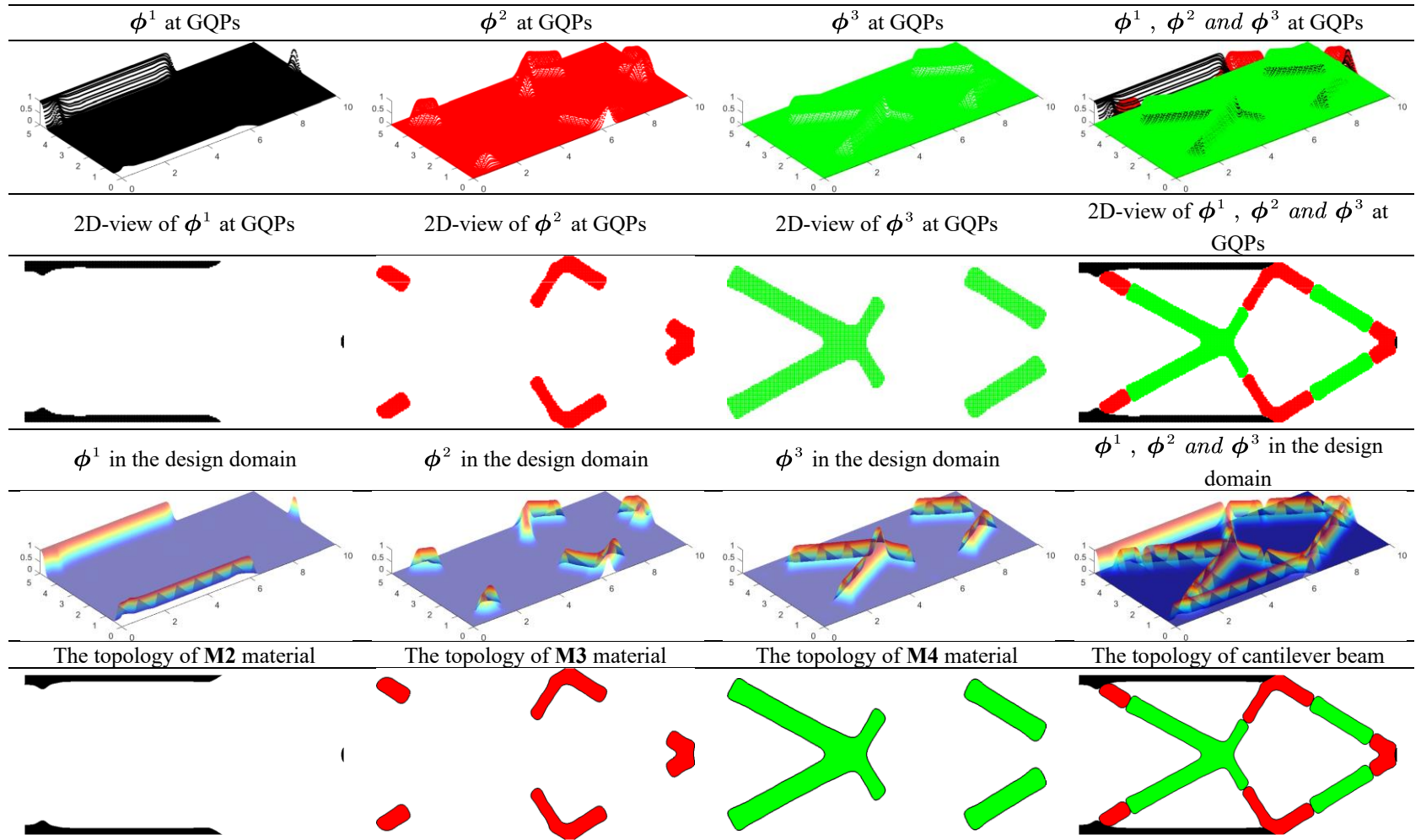
Figure 4-14 Convergent histories

The optimized results of the cantilever beam with three materials considering the total mass constraint are provided in Table 4-6. Similar to Sections 4.3.1 and 4.3.2, the optimized layouts of the TVFs at GQPs are listed in the second row of Table 4-6, and the corresponding 2D-views of the TVFs at GQPs with the higher values than 0.5 are given in the fourth row of Table 4-6. The continuous distributions of the TVFs in the design domain are provided in the sixth row of Table 4-6. Based on the heuristic scheme in Eq. (4-23), the topologies of three materials and the topology of the cantilever beam with three materials are provided in the last row of Table 4-6. It can be easily seen that the optimized topology of the cantilever beam is featured with the smooth boundaries and distinct interfaces between solids and voids. Each material can constitute the independent structural members in the optimized design to afford

the imposed loads and boundary conditions, which can reveal the effectiveness of the M-ITO method on solving the multi-material problems with the total mass constraint. **M2** material is also mainly filled in some regions with the occurrence of the stress concentration.

Finally, the iterative histories of the objective function, the total mass and mass of each material are shown in Figure 4-14 (a), and Figure 4-14 (b) displays the iterations for the total volume fraction and the volume fraction of each distinct material. We can find that the masses for **M2**, **M3** and **M3** materials are equal to 13.6, 8.2 and 13.2, respectively. Observed from the iterative curves, all the masses and volume fractions for three materials are changed in a non-monotonous manner, and each of them is evolved to seek for an appropriate value in the optimization process, until the objective function arrives at $J = 34.73$.

Table 4-6 The optimized results of cantilever beam with three materials



4.3.3 Quarter annulus

In this section, we intend to show the utility of the M-ITO formulation with multiple volume constraints on the optimization of the curved structures. As clearly illustrated in Figure 4-15, a quarter annulus with the loads and boundary conditions is defined, and two indices r and R are defined as 5 and 10, respectively. NURBS is used to construct the geometrical model and numerical analysis model of the quarter annulus. The detailed information is listed below Figure 4-15. It should be noted that this example employs the cubic NURBS basis functions to model the structural geometry and construct the solution space in the finite element analysis, which is more beneficial to improve the numerical precision during the optimization [105]. In term of the design domain with the rectangular shape, like Sections 5.1 and 5.2, the NURBS basis functions with the quadratic are enough to ensure the numerical precision and save the computational cost in the optimization [105]. Meanwhile, this example will be studied in two cases. Case 1 performs the two-material design (**M2** and **M3**) and case 2 considers three materials (**M2**, **M3** and **M4**). In case 1, the maximum volume fractions for **M2** and **M3** materials are defined as 25% and 12%, respectively. In case 2, the maximum consumptions of **M2**, **M3** and **M4** materials are respectively set to be 25%, 10% and 5%. Three materials are plotted with the black, red and green colors, respectively, in the optimized designs. The initial designs of cases 1 and 2 have the same densities of the TVFs shown in Figure 4-5 and Figure 4-8, respectively.

The optimized results of the quarter annulus with **M2** and **M3** materials in case 1 are listed in Table 4-7, and Table 4-8 provides the optimized results of the quarter annulus with **M2**, **M3** and **M4** materials. which both include the distributions of the TVFs for multiple materials at

the GQPs and in the design domain, the 2D-views of the TVFs at the GQPs, and the topologies for multiple materials and the quarter annulus. As we can see, the optimized topologies of the quarter annulus in cases 1 and 2 are both featured with the smooth structural boundaries and distinct interfaces between solids and voids. No overlaps between these materials are occurred in the optimized topologies of the quarter annulus, which presents the effectiveness of the N-MMI model. Additionally, multiple materials can be formed into the independent parts of the topologies to play the respective roles to afford the imposed loads. The appropriate layouts of the distinct materials can demonstrate the effectiveness and utility of the developed M-ITO method on the optimization of the curved structures with multiple materials.

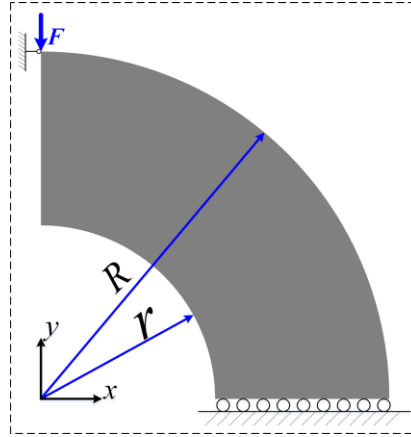


Figure 4-15 The details of quarter annulus

$IGA\ elements\ 100 \times 50; \Xi = \{0, 0, 0, 0, 0.01, \dots, 0.99, 1, 1, 1, 1\},$
 $\mathcal{H} = \{0, 0, 0, 0, 0.02, \dots, 0.98, 1, 1, 1, 1\}; p = 3, q = 3;$

Table 4-7 The optimized results of quarter annulus with M2 and M3 materials

ϕ^1 at GQPs	2D-view of ϕ^1	ϕ^1 in the design domain	The topology of M2
ϕ^2 at GQPs	2D-view of ϕ^2	ϕ^2 in the design domain	The topology of M3

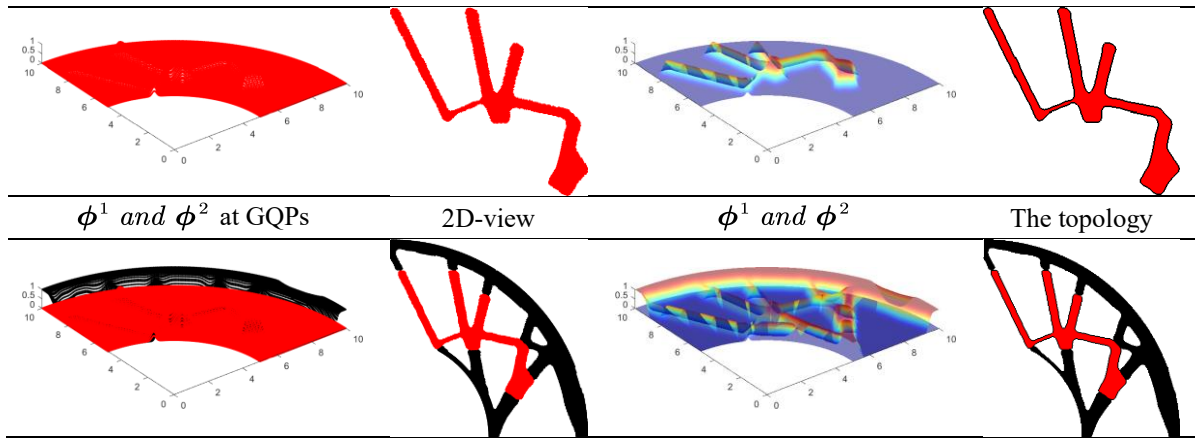
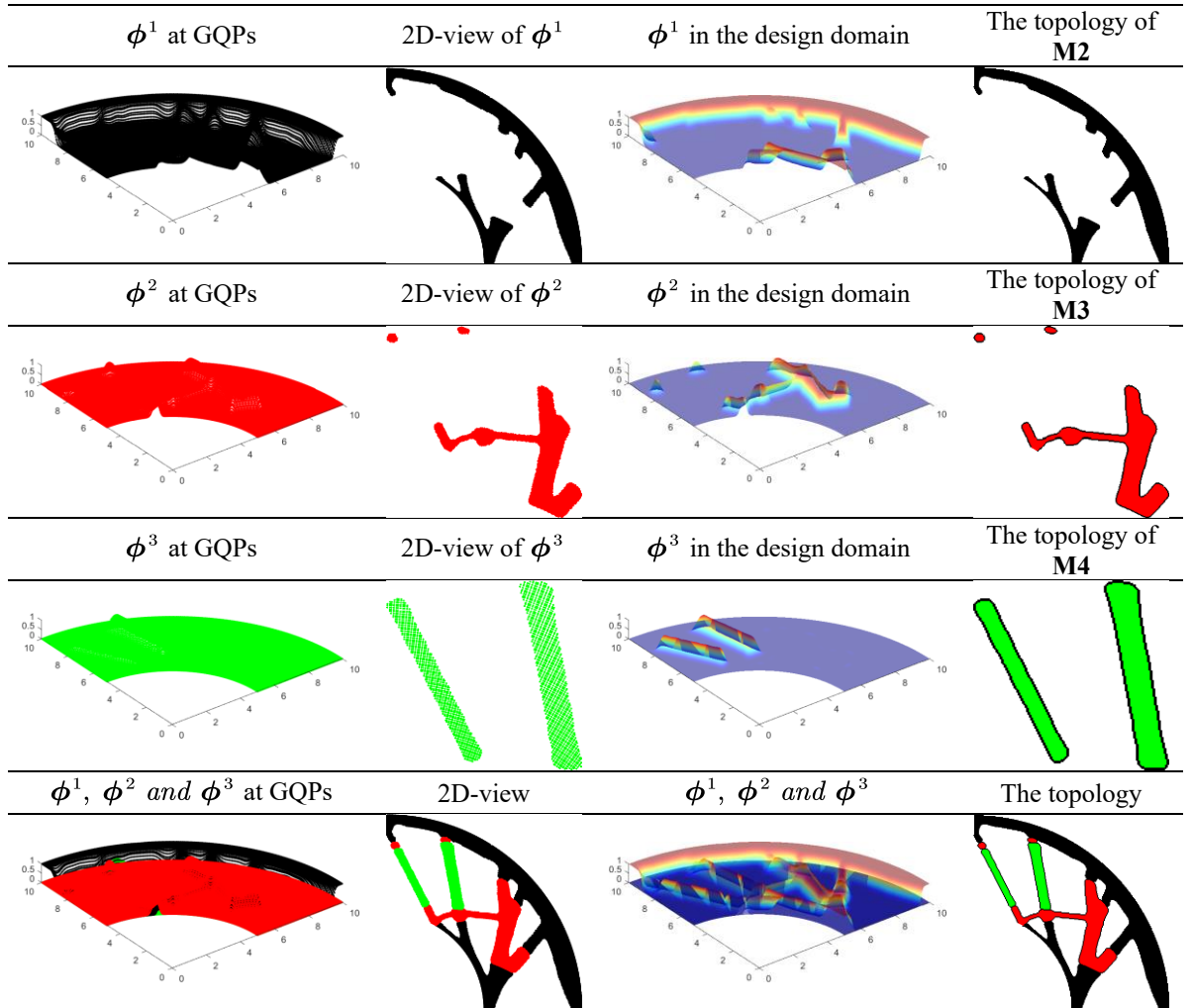


Table 4-8 The optimized results of quarter annulus with M2, M3 and M4 materials



4.3.4 3D Michell structure

This section will discuss the effectiveness of the M-ITO method on the optimization of 3D structures with multiple materials. As displayed in Figure 4-16, a 3D Michell structure with the loads and boundary conditions is defined. The quadratic NURBS basis functions are used to construct the NURBS solid and the numerical analysis model for the 3D Michell structure. The knot vectors and IGA elements are listed below Figure 4-16. Meanwhile, this example will be also studied in two cases, in which case 1 considers the optimization of two materials (**M2** and **M3** materials are available) in the design domain and case 2 intends to optimize the 3D Michell structure with **M2**, **M3** and **M4** materials. In case 1, the allowable material volume fractions for **M2** and **M3** are defined as 14% and 6%, respectively. The maximum volume fractions of **M2**, **M3** and **M4** materials in case 2 are set as 16%, 3.5% and 2.5%, respectively. **M2**, **M3** and **M4** materials are also shown with the black, red and green colors, respectively. Additionally, the initial designs of cases 1 and 2 have the same densities of the TVFs shown in Figure 4-5 and Figure 4-8, respectively.

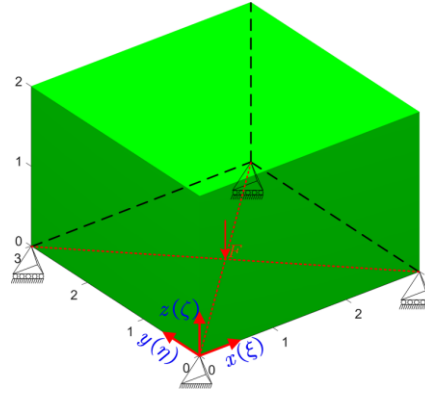
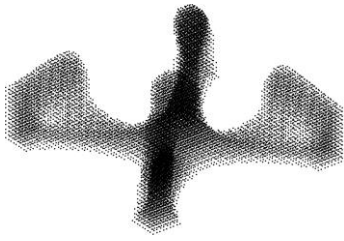

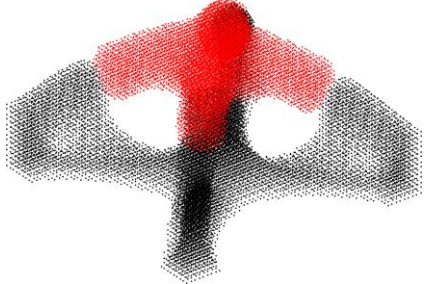





Figure 4-16 The details of 3D Michell structure
 IGA elements $30 \times 30 \times 18$; $p = 2$, $q = 2$, $r = 2$;
 $\Xi = \{0, 0, 0, 0.0333, \dots, 0.9667, 1, 1, 1\}$,
 $\mathcal{H} = \{0, 0, 0, 0.0333, \dots, 0.9667, 1, 1, 1\}$,
 $\mathcal{Z} = \{0, 0, 0, 0.0556, \dots, 0.9444, 1, 1, 1\}$.

In Table 4-9, the optimized results of the 3D Michell structure with **M2** and **M3** materials are provided, and the optimized results of the 3D Michell structure with three materials (**M2**, **M3** and **M4**) are provided in Table 4-10. As far as the 3D optimization, the DVFs and the TVFs correspond to the 4D functions, and it is hard to display the 4D data in a figure. Hence, we present the 3D-view of the TVFs with the higher values than the constant 0.5 at the GQPs for three materials, and the corresponding topologies of **M2**, **M3** and **M4** materials. It can be easily seen that the optimized topologies of the 3D Michell structure with two materials and three materials are both featured with the smooth structural boundaries and distinct interfaces between different materials and void phases. Meanwhile, the appropriate distributions of **M2**, **M3** and **M4** materials can be beneficial to afford the imposed loads and boundary conditions, which constitute the independent structural members in the design domain. Additionally, we also provided different views for the optimized topologies in two cases to more clearly present the geometrical features.

Table 4-9 The optimized results of 3D Michell structure with M2 and M3 materials

3D-view of ϕ^1 at GQPs	3D-view of ϕ^2	3D-view of ϕ^1 and ϕ^2
		
M2 material	M3 material	The topology
		

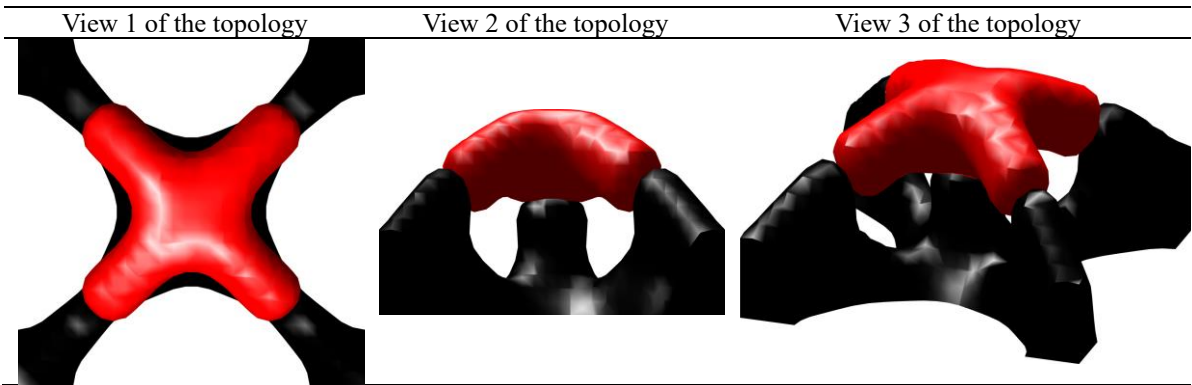
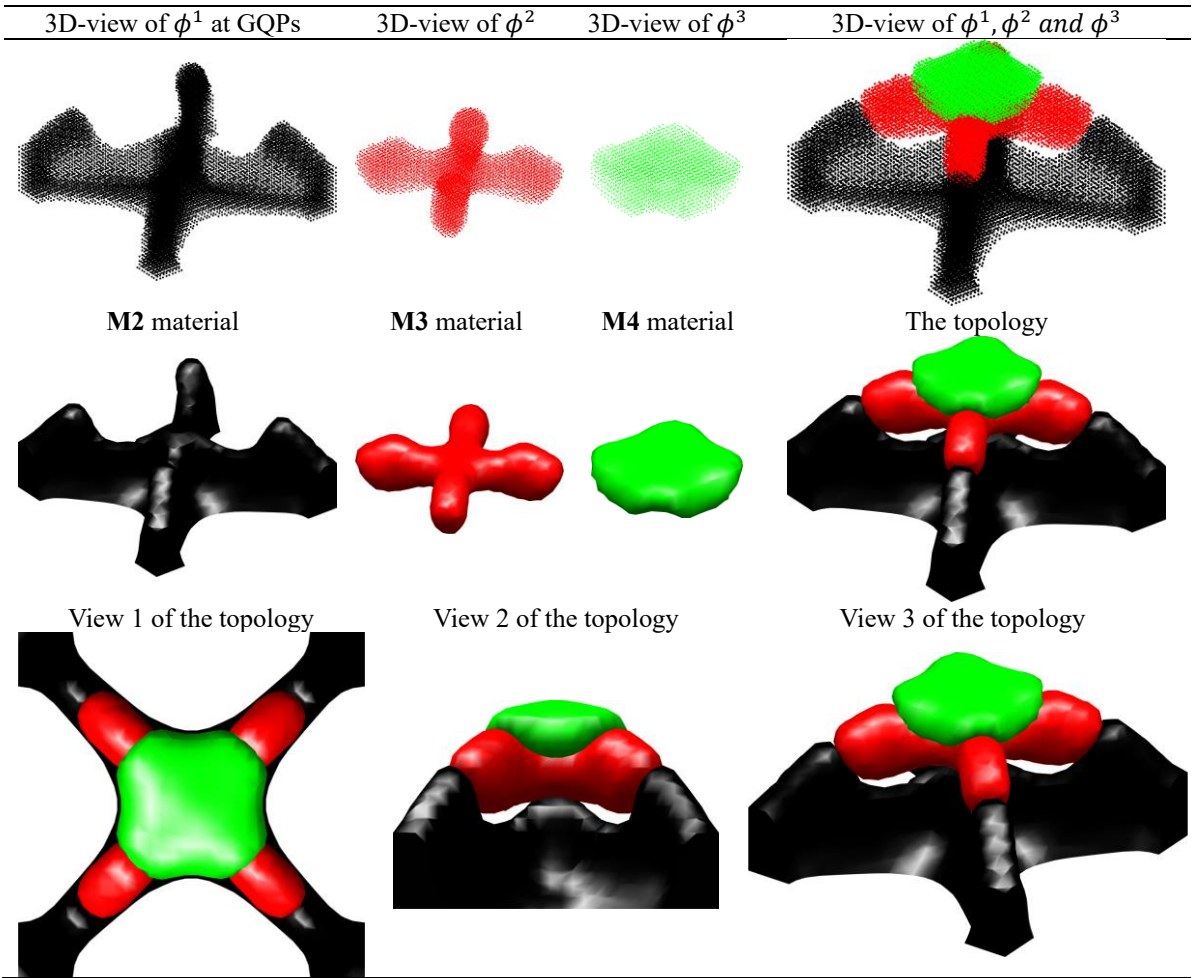


Table 4-10 The optimized results of 3D Michell structure with M2, M3 and M4 materials



4.4 Conclusions

In this chapter, a more effective M-ITO method with a N-MMI model is proposed for the optimization of multiple materials in structures. Firstly, the N-MMI model with the decoupled expression and serial evolving for the design variables and topology variables is developed using NURBS, mainly involving three components, including the DVFs, the TVFs and the multi-material interpolation. Secondly, two M-ITO formulations are developed using the N-MMI model for both multiple volume constraints and the total mass constraint, respectively, where IGA is applied to solve the structural responses.

Several numerical examples are performed to demonstrate the effectiveness of the M-ITO method with the N-MMI model. Firstly, the formulation 1 with multiple volume constraints is studied on the optimization of MBB beam with two materials and three materials. Later, the formulation 2 with the total mass constraint is discussed for the effectiveness of the M-ITO method on the multi-material optimization, and the effect of the properties of materials is also addressed. Finally, the effectiveness and utility of the M-ITO method on the curved structures and 3D structures is also presented. Additionally, the effectiveness of the decoupled expression and evolving mechanism of the DVFs and TVFs on removing the numerical troubles can also be demonstrated.

Chapter 5 Rational design of auxetic metamaterials using ITO method

In this chapter, the main intention is to develop a more effective and efficient isogeometric topology optimization (ITO) method for the design of auxetic metamaterials, particularly 3D material microstructures. It should be noted that the current work in this chapter comes from the published paper [125]. In the proposed ITO method, a DDF with the sufficient smoothness and continuity is firstly constructed to represent the evolving of the structural topology. Later, the homogenization is numerically implemented by the IGA to evaluate macroscopic effective properties, with the imposing of the periodic boundary formulation. An ITO formulation for 2D and 3D auxetic metamaterials is developed using the DDF, and the homogenized elastic tensor is applied to develop the objective function.

5.1 IGA-based EBHM

The principle of the homogenization is that the macroscopic effective properties of the bulk material are determined by using the information from material microstructure [20]. There are two basic requirements to be maintained in the homogenization: (1) the dimensions of the microstructure are much smaller than that of the bulk material, and (2) material microstructure needs to be periodically distributed in the bulk material. An example of the bulk material with only a kind of material microstructure is displayed in Figure 5-1, in which the microstructure is described in the coordinate system \mathbf{y} .

Considering the linear elasticity, the displacement field $\mathbf{u}^\epsilon(\mathbf{x})$ at the bulk material can be characterized by the asymptotic expansion theory, expressed as:

$$\mathbf{u}^\epsilon(\mathbf{x}) = \mathbf{u}_0(\mathbf{x}, \mathbf{y}) + \epsilon \mathbf{u}_1(\mathbf{x}, \mathbf{y}) + \epsilon^2 \mathbf{u}_2(\mathbf{x}, \mathbf{y}) + \dots \quad (5-1)$$

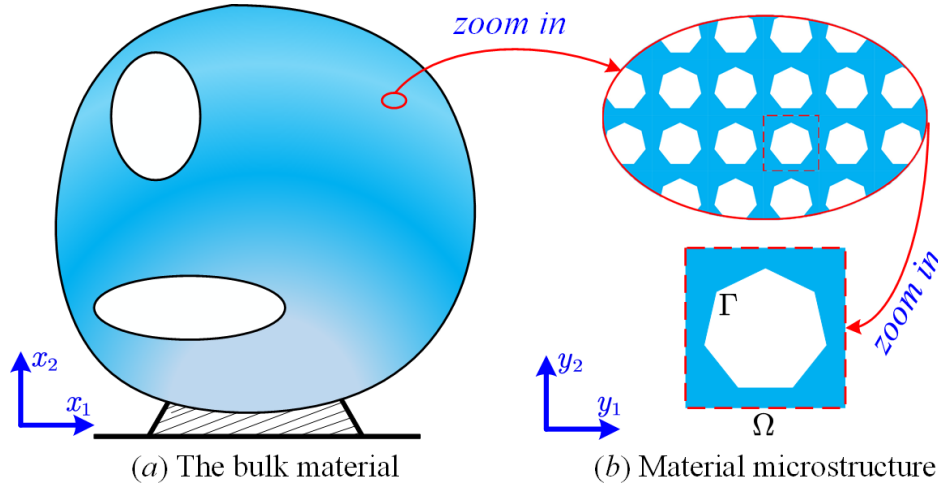


Figure 5-1 The bulk material composed of a kind of material microstructure

where ϵ is the aspect ratio between the scales of the microstructure and the bulk material, which is far less than 1. For numerical simplicity, only the first-order variation term with respect to the parameter expansion ϵ is considered. The effective elastic tensor of the bulk material D_{ijkl}^H can be computed as:

$$D_{ijkl}^H = \frac{1}{|\Omega|} \int_{\Omega} (\varepsilon_{pq}^{0(ij)} - \varepsilon_{pq}(u^{ij})) D_{pqrs} (\varepsilon_{rs}^{0(kl)} - \varepsilon_{rs}(u^{kl})) d\Omega \quad (5-2)$$

where $|\Omega|$ is the area (2D) or volume (3D) of the microstructure, and D_{pqrs} is the locally varying elastic property. $\varepsilon_{pq}^{0(ij)}$ is the linearly independent unit test strain field, containing three components in 2D and six in 3D. $\varepsilon_{pq}(u^{ij})$ denotes the unknown strain field in the microstructure, which is solved by the following linear elasticity equilibrium equation with \mathbf{y} -periodic boundary conditions (PBCs):

$$\int_{\Omega} \varepsilon_{pq}(u^{ij}) D_{pqrs} \varepsilon_{rs}(\delta u^{ij}) d\Omega = \int_{\Omega} \varepsilon_{pq}^{0(ij)} D_{pqrs} \varepsilon_{rs}(\delta u^{ij}) d\Omega, \quad \forall \delta u \in H_{per}(\Omega, \mathbb{R}^d) \quad (5-3)$$

where δu is the virtual displacement in the microstructure belonging to the admissible displacement space H_{per} with \mathbf{y} -periodicity, and d is the dimension of the microstructure. The

homogenization is performed numerically by discretizing and solving Eq. (5-3) using the finite element method (FEM), namely numerical homogenization [176], where the utmost importance is the imposing of the PBCs on the microstructure. As an alternative method, the energy-based homogenization (EBHM) with the simplified periodic boundary formulation [79,140,146] is developed. In this study, the numerical analysis of material microstructure is performed by IGA, with the use of the periodic boundary formulation developed in the EBHM. In IGA, the displacement field in material microstructure is approximately expressed by a combination of the NURBS basis functions with the displacements at control points:

$$\mathbf{u} = \sum_{i=1}^n \sum_{j=1}^m R_{i,j}^{p,q}(\xi, \eta) \mathbf{u}_{i,j} \quad (5-4)$$

where $\mathbf{u}_{i,j}$ denote the displacements of the $(i,j)_{th}$ control point. As we can see, NURBS basis functions are employed to approximate the displacement field in material microstructure by linearly combining with nodal displacements. In the application of the EBHM to predict the macroscopic effective properties of the microstructure, the displacement field in material microstructure needs to satisfy the PBCs, and a general form is expressed as:

$$\mathbf{u}_k^+ - \mathbf{u}_k^- = \varepsilon(\mathbf{u}_0) \Delta k \quad (5-5)$$

where k is the normal direction of the structural boundary. \mathbf{u}_k^+ indicate the displacements of points at the structural boundary with the normal direction k , and the normal direction is in the positive direction of the coordinate axis. \mathbf{u}_k^- correspond to the displacements of points at the opposite structural boundary. Δk is the scale of the material microstructure along the direction of k . The expressions of the boundary constraint equations in PBCs in detail can refer to [146] for 2D and [79] for 3D.

5.2 Isogeometric topology optimization (ITO)

As already pointed out in Section 2, the physical coordinates of control points act as control coefficients in parametrizing of the structural geometry. If each control point is assigned to a nodal density, the NURBS response corresponds to a field of density in the structural domain, namely density distribution function (DDF). The topology optimization formulation to obtain auxetic metamaterials can be developed with the use of the DDF, where IGA is applied to solve structural responses in material microstructure.

5.2.1 Density distribution function (DDF)

Before developing the DDF, the definition of nodal densities assigned to control points needs to satisfy two basic conditions [98,100,103,104]: (1) non-negativity; and (2) the strict bounds ranging from 0 to 1. Meanwhile, the Shepard function is firstly used to improve the overall smoothness of nodal densities, to make sure the smoothness of the DDF. The corresponding mathematical model is given as:

$$\mathcal{G}(\rho_{i,j}) = \sum_{i=1}^{\mathcal{N}} \sum_{j=1}^{\mathcal{M}} \psi(\rho_{i,j}) \rho_{i,j} = \sum_{i=1}^{\mathcal{N}} \sum_{j=1}^{\mathcal{M}} \left(w(\rho_{i,j}) / \sum_{\hat{i}=1}^{\mathcal{N}} \sum_{\hat{j}=1}^{\mathcal{M}} w(\rho_{\hat{i},\hat{j}}) \right) \rho_{i,j} \quad (5-6)$$

where $\mathcal{G}(\rho_{i,j})$ is the smoothed nodal density assigned to the $(i,j)_{th}$ control point, and $\rho_{i,j}$ is the initial defined nodal density. \mathcal{N} and \mathcal{M} are the numbers of the nodal densities located at the local support area of the current nodal density in two parametric directions respectively, as shown in the sub area bounded by the blue circle in Figure 5-2. Hence, the key idea of the current smoothing scheme for the nodal densities is that each nodal density is equal to the mean value of all the nodal densities in the local area of the current nodal density. $\psi(\rho_{i,j})$ is the Shepard function [160] of the $(i,j)_{th}$ nodal density. w is the weight function of the

nodal density of the $(i,j)_{th}$ control point. The CSRBFs with the C^4 continuity [161] are used in this work due to the compactly supported, the high-order continuity and the nonnegativity over the local domain, by:

$$w(r) = (1-r)_+^6 (35r^2 + 18r + 3) \quad (5-7)$$

where $r = d/d_m$, and d is the Euclidean distance between the current nodal density and the other nodal density in the support domain. d_m is the radius of this domain shown in Figure 5-2. It can be seen that the smoothed nodal densities can still maintain the necessary conditions for a physically meaningful material density [98,100,101,103,104]. Assuming that the DDF in the structural domain is denoted by \mathcal{X} , the DDF is constructed by the NURBS basis functions with a linear combination of the smoothed nodal densities, given as:

$$\mathcal{X}(\xi, \eta) = \sum_{i=1}^n \sum_{j=1}^m R_{i,j}^{p,q}(\xi, \eta) \mathcal{G}(\rho_{i,j}) \quad (5-8)$$

It can be seen that Eq. (5-9) for the DDF has the same mathematical formula for NURBS. The key difference is the physical meaning of control coefficients. The initial NURBS-based geometrical model for the domain has been converted into a representation of the DDF. Eq. (5-9) is the global form, which can be expanded as a local form depended on the local area of $(\xi, \eta) \in [\xi_i, \xi_{i+1}] \times [\eta_j, \eta_{j+1}]$, that

$$\mathcal{X}(\xi, \eta) = \sum_{e=i-p}^i \sum_{f=j-q}^j R_{e,f}^{p,q}(\xi, \eta) \mathcal{G}(\rho_{e,f}) \quad (5-9)$$

By virtue of the properties of NURBS, the current developed DDF is also featured with the non-negativity and strict-bounds. Hence, the DDF can guarantee the strict physical meaning of the material density for structural domain in the next optimization formulation. The non-interpolant of NURBS has no influence on the DDF, originating from that the control points

are not necessarily on the structural domain. Moreover, the variation diminishing property of NURBS can make sure the non-oscillatory of the DDF, even if the higher-order NURBS basis functions are used [89,90].

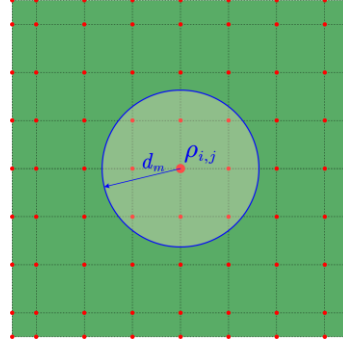


Figure 5-2 Nodal densities assigned to control points

5.2.2 ITO formulation for auxetic metamaterials

The Poisson's ratio of materials is equal to the aspect ratio of the transverse contraction strain to longitudinal extension strain in the direction of stretching force. Considering the material elastic tensor, Poisson's ratios in two directions of 2D materials can be defined by $v_{12} = D_{1122}/D_{1111}$ and $v_{21} = D_{1122}/D_{2222}$. In order to generate materials with the NPR property, several different objective functions are developed, such as the minimization of the weighted square difference between the expected elastic tensor and the evaluated elastic tensor [142–144,149], the minimization of the difference between the predicted NPR and its target [147], minimizing the combination of the elastic tensor [75,146] and so on [148].

Here, the objective function of the optimization of auxetic metamaterials is expressed by a combination of the homogenized elastic tensor. It is known that the occurrence of the auxetic behavior is highly related to the rotating effect of mechanisms in microstructures [75,140]. As defined in Eq. (16), minimizing the term $\sum_{i,j=1,i=j}^d D_{ii}^H$ can guarantee the generation of

the mechanism-type layouts, which is beneficial to facilitate microstructures with the auxetic behavior. Meanwhile, the term $\sum_{i,j=1,i \neq j}^d D_{iijj}^H$ can prevent mechanism-type topologies when its value is smaller than 0. In the defined optimization formulation, the optimizer tends to maximize the second term $\sum_{i,j=1,i=j}^d D_{iijj}^H$ and minimize the first term $\sum_{i,j=1,i \neq j}^d D_{iijj}^H$, so that the objective function can be gradually minimized and materials can be featured with the auxetic behavior in all directions.

$$\left\{ \begin{array}{l} \text{Find: } \boldsymbol{\rho} \{ [\rho_{i,j}]_{2D} \quad [\rho_{i,j,k}]_{3D} \} \\ \text{Min: } J(\mathbf{u}, \mathcal{X}) = \sum_{\hat{i}, \hat{j}=1, \hat{i} \neq \hat{j}}^d D_{iijj}^H(\mathbf{u}, \mathcal{X}) - \beta \left\{ \sum_{\hat{i}, \hat{j}=1, \hat{i}=\hat{j}}^d D_{iijj}^H(\mathbf{u}, \mathcal{X}) \right\} \\ \text{S.t: } \left\{ \begin{array}{l} G(\mathcal{X}) = \frac{1}{|\Omega|} \int_{\Omega} \mathcal{X}(\boldsymbol{\rho}) v_0 d\Omega - V_0 \leq 0 \\ a(\mathbf{u}, \delta \mathbf{u}) = l(\delta \mathbf{u}), \quad \forall \delta \mathbf{u} \in H_{per}(\Omega, \mathbb{R}^d) \\ 0 < \rho_{\min} \leq \boldsymbol{\rho} \leq 1, \quad (i = 1, 2, \dots, n; j = 1, 2, \dots, m; k = 1, 2, \dots, l) \end{array} \right. \end{array} \right. \quad (5-10)$$

where $\boldsymbol{\rho}$ denote the nodal densities assigned to the control points, working as the design variables. J is the objective function. As we can see, the optimization formulation intends to minimize $D_{iijj}^H (\hat{i} \neq \hat{j})$ and maximize $D_{iijj}^H (\hat{i} = \hat{j})$ simultaneously, which can facilitate the generation of materials with the NPR in all directions. Hence, the objective function can be applicable not only for the isotropic, but also for the orthotropic materials. β is a weighting parameter to claim the importance of the corresponding terms. d is the spatial dimension of materials. G is the volume constraint, in which V_0 is the maximum value and v_0 is the volume fraction of the solid. \mathcal{X} is the DDF in Eq. (5-9). \mathbf{u} is the displacement field in the material microstructure, which have to satisfy the PBCs given in Eq. (5-5). $\delta \mathbf{u}$ is the virtual displacement field belonging to the admissible displacement space H_{per} with \mathbf{y} -periodicity, which is calculated by the elastic equilibrium equation. a and l are the bilinear energy and

linear load functions, as:

$$\begin{cases} a(\mathbf{u}, \delta \mathbf{u}) = \int_{\Omega} (\mathcal{X}(\boldsymbol{\rho}))^\gamma \mathbf{D}_0 \boldsymbol{\varepsilon}(\mathbf{u}) \boldsymbol{\varepsilon}(\delta \mathbf{u}) d\Omega \\ l(\delta \mathbf{u}) = \int_{\Omega} (\mathcal{X}(\boldsymbol{\rho}))^\gamma \mathbf{D}_0 \boldsymbol{\varepsilon}^0 \boldsymbol{\varepsilon}(\delta \mathbf{u}) d\Omega \end{cases} \quad (5-11)$$

It should be noted that the elastic tensor is assumed to be an exponential function with respect to the DDF, and γ is the penalization parameter. \mathbf{D}_0 is the constitutive elastic tensor of the basic material.

5.2.3 Design Sensitivity analysis

In Eq. (5-11), the ITO formulation for auxetics are developed using the DDF, and which is expressed by the linear combination of the nodal densities and NURBS basis functions. Moreover, the nodal densities are the design variables. Hence, we firstly derive the first-order derivative of the objective function with respect to the DDF before obtaining the sensitivity analysis with respect to the design variables, as:

$$\frac{\partial J}{\partial \mathcal{X}} = \sum_{\hat{i}, \hat{j}=1, \hat{i} \neq \hat{j}}^d \frac{\partial D_{\hat{i}\hat{j}\hat{j}\hat{j}}^H}{\partial \mathcal{X}} - \beta \left\{ \sum_{\hat{i}, \hat{j}=1, \hat{i} = \hat{j}}^d \frac{\partial D_{\hat{i}\hat{j}\hat{j}\hat{j}}^H}{\partial \mathcal{X}} \right\} \quad (5-12)$$

As we can see, the core of the derivative of the objective function with respect to the DDF is located at the computation of the derivative of the homogenized elastic tensor $D_{\hat{i}\hat{j}\hat{j}\hat{j}}^H$. The derivations for the first-order derivative of the homogenized stiffness tensor in detail can refer to [75,79,143,151], and the final form is given by:

$$\frac{\partial D_{\hat{i}\hat{j}\hat{j}\hat{j}}^H}{\partial \mathcal{X}} = \frac{1}{|\Omega|} \int_{\Omega} \left(\varepsilon_{pq}^{0(\hat{i}\hat{i})} - \varepsilon_{pq}(u^{\hat{i}\hat{i}}) \right) \gamma (\mathcal{X})^{\gamma-1} D_{pqrs}^0 \left(\varepsilon_{rs}^{0(\hat{j}\hat{j})} - \varepsilon_{rs}(u^{\hat{j}\hat{j}}) \right) d\Omega \quad (5-13)$$

As pointed out in Section 5.2.1, the DDF is constructed by a linear combination of the NURBS basis functions with the smoothed nodal densities, and which are obtained by the Shepard

function to process the nodal densities. The first-order derivatives of the DDF with respect to the nodal densities of the control points can be derived by:

$$\frac{\partial \mathcal{X}(\xi, \eta)}{\partial \rho_{i,j}} = \frac{\partial \mathcal{X}(\xi, \eta)}{\partial \mathcal{G}(\rho_{i,j})} \frac{\partial \mathcal{G}(\rho_{i,j})}{\partial \rho_{i,j}} = R_{i,j}^{p,q}(\xi, \eta) \psi(\rho_{i,j}) \quad (5-14)$$

where $R_{i,j}^{p,q}(\xi, \eta)$ is the NURBS basis function at the computational point (ξ, η) . $\psi(\rho_{i,j})$ is the value of the Shepard function at the control point (i, j) . It is important to note that the above computational point (ξ, η) is different from the control point (i, j) . In Eq. (5-11), the computational points are Gauss quadrature points. According to the chain rule, the final form of the derivative of the homogenized elastic tensor with respect to the initial nodal densities can be computed by:

$$\frac{\partial D_{ijj}^H}{\partial \mathcal{X}} = \frac{1}{|\Omega|} \int_{\Omega} \left(\varepsilon_{pq}^{0(i\ddot{i})} - \varepsilon_{pq}(u^{\ddot{i}}) \right) \gamma(\mathcal{X})^{\gamma-1} D_{pqrs}^0 \left(\varepsilon_{rs}^{0(j\ddot{j})} - \varepsilon_{rs}(u^{\ddot{j}}) \right) R_{i,j}^{p,q}(\xi, \eta) \psi(\rho_{i,j}) d\Omega \quad (5-15)$$

Hence, the first-order derivative of the objective function J with respect to design variables can be obtained based on Eq. (5-16). Similarly, the derivatives of the volume constraint with respect to the design variables are given by:

$$\frac{\partial G}{\partial \rho_{i,j}} = \frac{1}{|\Omega|} \int_{\Omega} R_{i,j}^{p,q}(\xi, \eta) \psi(\rho_{i,j}) v_0 d\Omega \quad (5-16)$$

According to Eqs. (5-13), (5-16) and (5-17), the first-order derivatives of the objective and constraint functions are strongly dependent on NURBS basis functions at Gauss quadrature points and Shepard function at the control points. In the optimization process, the NURBS basis functions and Shepard function keep unchanged, and they can be pre-stored. Hence, the sensitivity analysis can save the computational cost in the optimization. Meanwhile, it should be noted that the above derivations are developed for 2D materials, which can be directly

extended to 3D scenario.

5.3 A relaxed OC method

It is known that the OC method [162] has been widely employed in structural optimization problems [1] in which a large number of design variables but only with a single constraint. Moreover, the objective and constraint functions should satisfy the monotonicity properties. However, the positive and negative sensitivities of the objective function with respect to the design variables can appear in the optimization of auxetic metamaterials considering the above formulation. In previous works [146], the damping factor has been eliminated, leading to a result that the volume fraction is inactive in the optimization process. Here, a relaxed OC method [177] is applied to update the design variables, and the corresponding update scheme is expressed as:

$$\rho_{i,j,k}^{(\kappa+1)} = \left\{ \begin{array}{ll} \max\{(\rho_{i,j,k}^{(\kappa)} - m), \rho_{min}\} & \text{if } \left\{ \begin{array}{l} (\Pi_{i,j,k}^{(\kappa)})^\zeta \rho_{i,j,k}^{(\kappa)} \leq \\ \max\{(\rho_{i,j,k}^{(\kappa)} - m), \rho_{min}\} \end{array} \right\} \\ (\Pi_{i,j,k}^{(\kappa)})^\zeta \rho_{i,j,k}^{(\kappa)} & \text{if } \left\{ \begin{array}{l} \max\{(\rho_{i,j,k}^{(\kappa)} - m), \rho_{min}\} \\ < (\Pi_{i,j,k}^{(\kappa)})^\zeta \rho_{i,j,k}^{(\kappa)} \\ < \min\{(\rho_{i,j,k}^{(\kappa)} + m), \rho_{max}\} \end{array} \right\} \\ \min\{(\rho_{i,j,k}^{(\kappa)} + m), \rho_{max}\} & \text{if } \left\{ \begin{array}{l} \min\{(\rho_{i,j,k}^{(\kappa)} + m), \rho_{max}\} \\ \leq (\Pi_{i,j,k}^{(\kappa)})^\zeta \rho_{i,j,k}^{(\kappa)} \end{array} \right\} \end{array} \right\} \quad (5-17)$$

where m , ζ are the move limit and the damping factor, respectively. The Lagrange multiplier $\Lambda^{(\kappa)}$ at the κ^{th} iteration step can be advanced by a bi-sectioning algorithm [1]. The updating factor $\Pi_{i,j}^{(\kappa)}$ for the design variable at the κ^{th} iteration step can be defined as:

$$\Pi_{i,j}^{(\kappa)} = \frac{1}{\Lambda^{(\kappa)} + \mu^{(\kappa)}} \left(\mu^{(\kappa)} - \frac{\partial J}{\partial \rho_{i,j}^{(\kappa)}} / \max\left(\Delta, \frac{\partial G}{\partial \rho_{i,j}^{(\kappa)}}\right) \right) \quad (5-18)$$

where Δ is a small positive constant to avoid the fraction with a form of $0/0$. The updating

factor $\Pi_{i,j}^{(\kappa)}$ can be positive in the optimization, by choosing an appropriate value of the shift parameter $\mu^{(\kappa)}$, namely:

$$\mu^{(\kappa)} \geq \max \left\{ \frac{\partial J}{\partial \rho_{i,j}^{(\kappa)}} / \max \left(\Delta, \frac{\partial G}{\partial \rho_{i,j}^{(\kappa)}} \right) \right\} \quad (i = 1, 2, \dots, n; j = 1, 2, \dots, m) \quad (5-19)$$

A systematic flowchart of the ITO formulation for auxetic metamaterials is shown in Figure 5-3, and the detailed steps are listed as follows:

- Step 01:** Input initial parameters: structural sizes, NURBS basis functions; knot vector and so on;
- Step 02:** Construct geometrical model (CAD) of the structure by NURBS;
- Step 03:** Construct numerical analysis model (CAE) of the structure, namely IGA mesh;
- Step 04:** Construct the initial DDF by NURBS basis functions and Shepard function;
- Step 05:** Impose PBCs on the microstructure and apply IGA to solve the displacement field;
- Step 06:** IGA-based EBHM to evaluate the homogenized elastic tensor;
- Step 07:** Calculate the objective function and volume fraction;
- Step 08:** Calculate the derivatives of the objective and constraint functions;
- Step 09:** Update the design variables and DDF by the relaxed OC method;
- Step 10:** Check convergence; if not, go back to **Step 05**; if yes, go to **Step 11**;
- Step 11:** End and Output auxetic metamaterials.

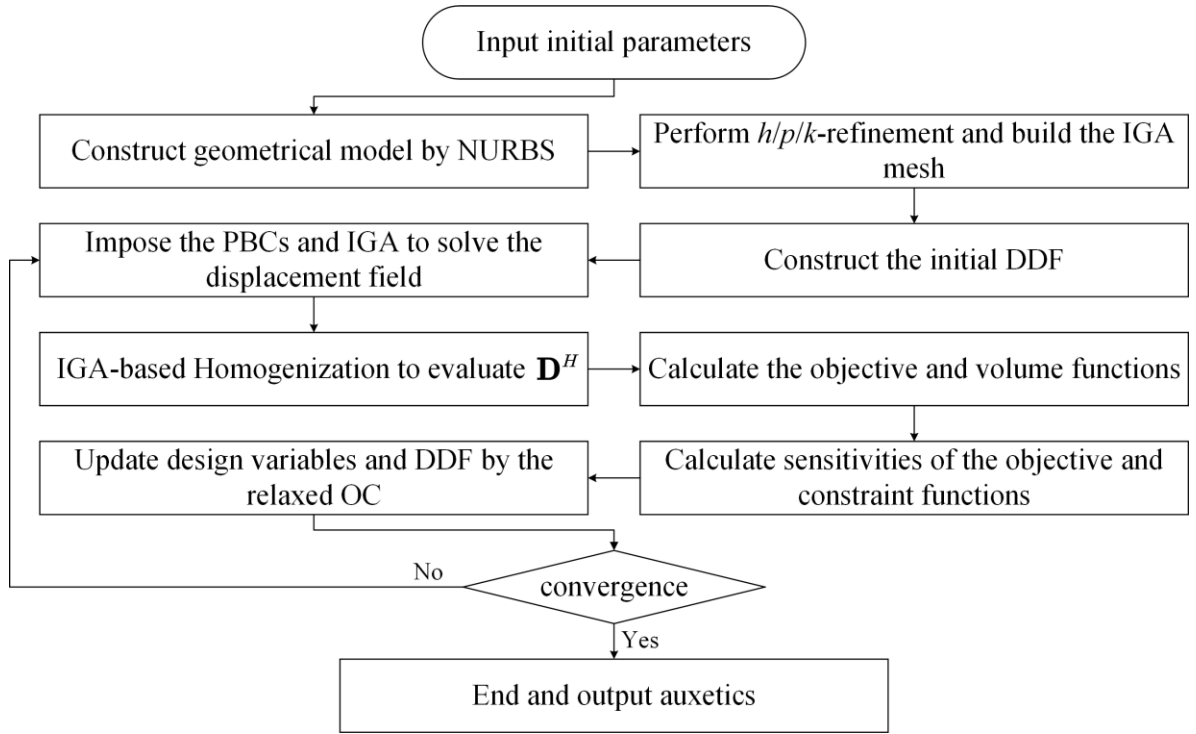


Figure 5-3 The flowchart of the ITO formulation for auxetic metamaterials

5.4 Numerical Examples

In this section, several numerical examples are provided to demonstrate the effectiveness and merits of the ITO formulation for auxetic metamaterials. Only the linearly elastic materials are considered, and 2D microstructures will be discretized with the plane stress elements. In all example, the Young's moduli E_0 and Poisson's ratio ν_0 for the basis material are defined as 1 and 0.3, respectively. In the numerical analysis, 3×3 (2D) or $3 \times 3 \times 3$ (3D) Gauss quadrature points are chosen in each IGA element. For numerical simplicity, the dimensions of material microstructures in all directions are set to be 1. The penalty parameter in Section 4.2 is set as 3. The constant parameter β in all numerical examples is set as 0.003. The terminal criterion is that the L_∞ norm of the difference of the nodal densities between two consecutive iterations is less than 1% or the maximum 100 iteration steps are reached.

5.4.1 2D auxetic metamaterials

Considering 2D materials, the structural design domain is a square with 1×1 , shown in Figure 5-4 (a). Here, NURBS surface is used to parametrize the design domain, where the quadratic NURBS are chosen and the knot vectors are: $\Xi = \mathcal{H} = \{0,0,0,0.01, \dots, 0.99,1,1,1\}$. The IGA mesh for the design domain has 100×100 elements, and 101×101 (10202) control points are contained in the NURBS surface. The maximum material consumption V_0 is defined as 30%. The weight parameter β is equal to 0.03. As already described in Section 5.2, the developed ITO method aims to optimize the densities in the DDF to represent the evolving of the structural topology, until auxetic microstructures can be achieved. As given in Eq. (5-9), the DDF is constructed by the NURBS, which can be viewed as a density response surface in space for nodal densities. The initial design of material microstructure is displayed in Figure 5-4, including the nodal densities at control points in Figure 5-4 (a), densities at Gauss quadrature points in Figure 5-4 (b) and the density response surface of the DDF in Figure 5-4 (c). It should be noted that the height direction denotes the density value in Figure 5-4. It can be found that the initial design of material microstructure is homogenously occupied with some holes to avoid the uniformly distributed sensitivity field, owing to the imposing of the periodic boundary conditions on material microstructure.

As displayed in Figure 5-5, the optimized designs of material microstructure are provided, including the optimized densities at Gauss quadrature points in Figure 5-5 (a) and the density response surface of the DDF in Figure 5-5 (b). It can be found that the optimized densities at Gauss quadrature points and the optimized density response are featured with the sufficient smoothness and continuity. The main cause is that the Shepard function and NURBS basis

functions are considered in the DDF. The former can guarantee the smoothness of the DDF by improving the overall smoothness of nodal densities, and the latter ensure its continuity. In order to show the details of the optimization of the DDF, we provide a series of intermediate density response surfaces of the DDF during the process. As shown in Figure 5-4 (c) and Figure 5-6 (a), the initial density response surface has a break from 0 to 1. In the optimization, the smoothness is gradually improved with the consideration of the Shepard function in the construction of the DDF, explicitly represented by the transition part of the surface from 0 to 1. Additionally, the optimized densities of the DDF in material microstructure are distributed nearly 0 and 1, due to the penalty parameter, and the key principle of the penalty mechanism in topology optimization can refer to [11].

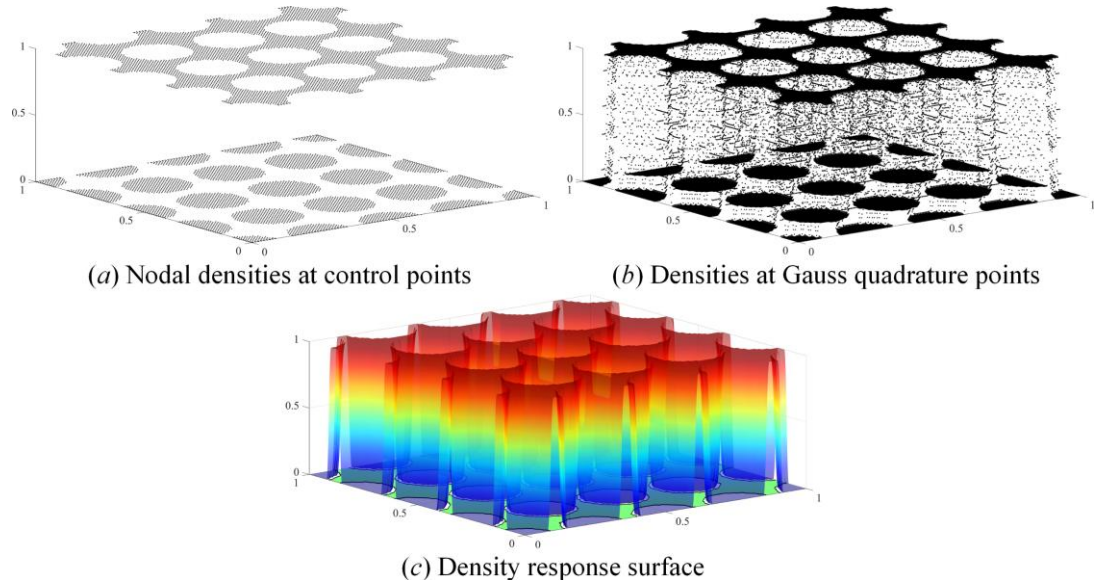


Figure 5-4 The initial design of material microstructure

As shown in Figure 5-6, the advancing of the DDF represent the topological changes in the optimization. In order to obtain an appropriate configuration of material microstructure using the DDF, a heuristic scheme is introduced to define the structure topology. The mathematical model is defined in Eq. (5-21), where \mathcal{X}_c is a constant, expressed as:

$$\begin{cases} 0 \leq \mathcal{X}(\xi, \eta) < \mathcal{X}_c & \text{void} \\ \mathcal{X}(\xi, \eta) = \mathcal{X}_c & \text{boundary} \\ \mathcal{X}_c < \mathcal{X}(\xi, \eta) \leq 1 & \text{solid} \end{cases} \quad (5-20)$$

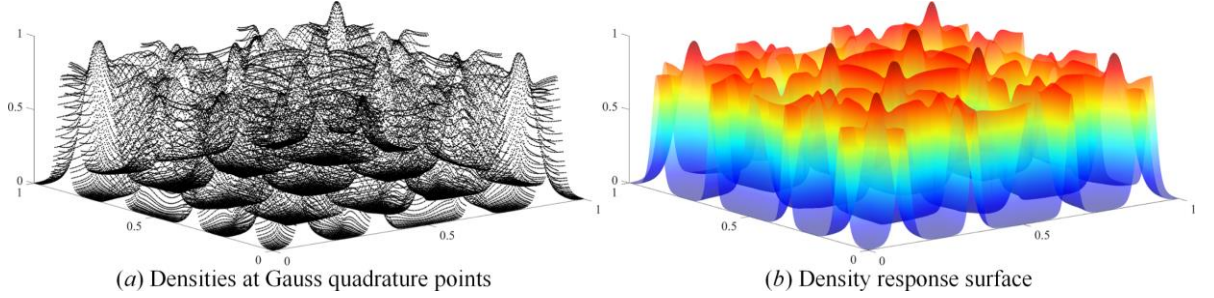


Figure 5-5 The optimized designs of material microstructure

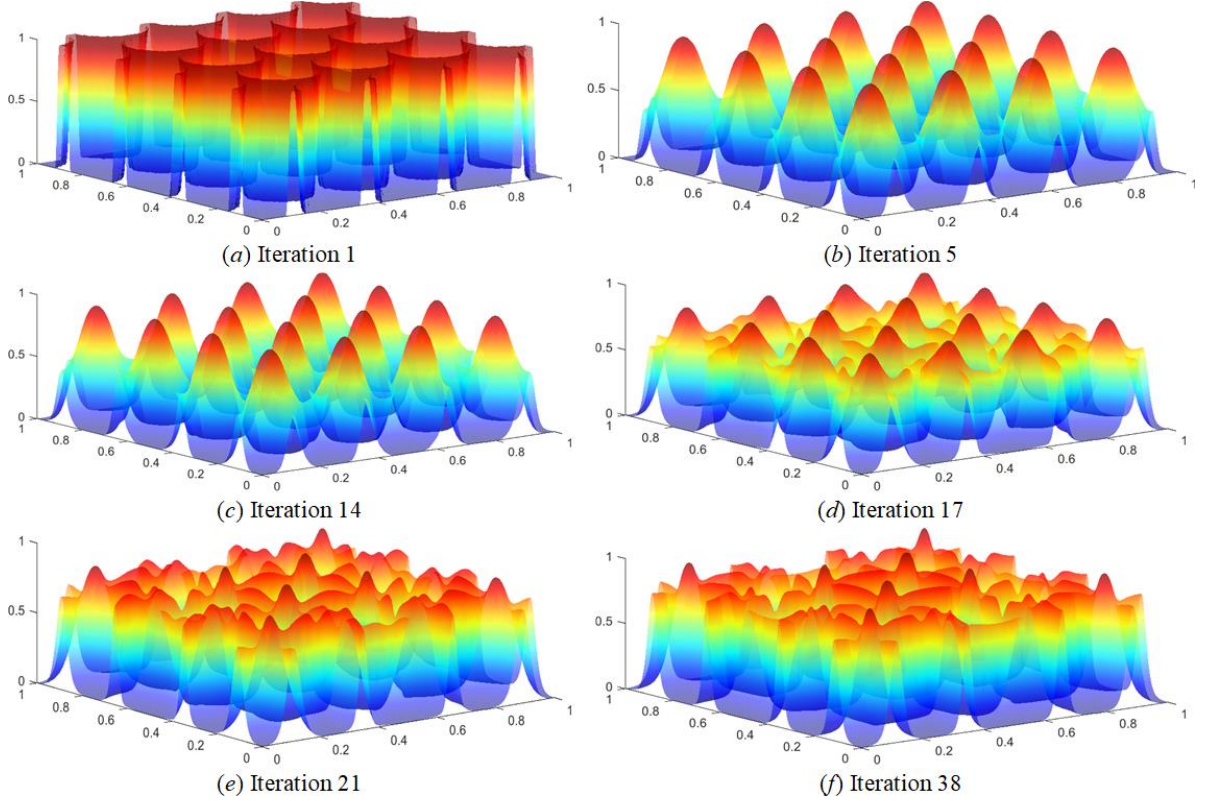
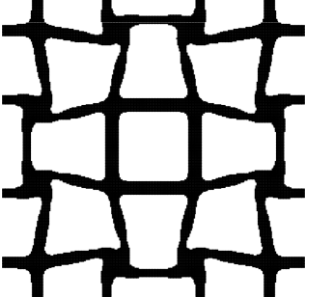
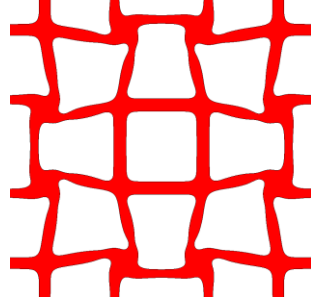


Figure 5-6 Intermediate density response surfaces of the DDF

As we can see, the structural boundaries of material microstructure are expressed by the iso-contour of the DDF. The DDF with the densities higher than \mathcal{X}_c describes solids in the structural design domain, and the densities lower than \mathcal{X}_c is used to present voids. We can find that the current scheme to define the structural topology using the DDF is analogous to

the implicit boundary representation model in the LSM [13–15]. However, it is important to notice that the ITO method for auxetic metamaterials is not developed in a framework of the Hamilton-Jacobi partial differential equation to track the advancing of the structural boundary. Eq. (5-20) can be just viewed as a post-processing mechanism to define the topology using the DDF, and the key of the ITO method for auxetic metamaterials is the optimization of the DDF to represent the topological changes.

Table 5-1 The optimized 2D auxetic metamaterial

DGQP	Topology	\mathbf{D}^H	ν	V_f
		$\begin{bmatrix} 8.8 & -5.4 & 0 \\ -5.4 & 8.8 & 0 \\ 0 & 0 & 0.27 \end{bmatrix} e^{-2}$	-0.61	29.88%

In the work, the constant \mathcal{X}_c is set to be 0.5. According to Figure 5-5, we can see that the 0.5 is a relatively suitable value to define the topology, due to a phenomenon that most densities are distributed nearly 0 or 1 ($[0, 0.2]$ and $[0.8, 1]$). The corresponding numerical results of material microstructure are listed in Table 5-1, including the 2D view of densities at Gauss quadrature points but with only higher than 0.5, the optimized topology, the homogenized elastic tensor \mathbf{D}^H , the corresponding negative Poisson's ratio $\nu = -0.61$ and the volume fraction of the optimized topology $V_f = 29.88\%$. The volume fraction of the final topology is mostly close to the prescribed volume fraction 30%, which shows the appropriateness of the threshold value 0.5 to define the topology using the DDF. The topologically-optimized design of microstructure with the negative Poisson ratio -0.61 shows the effectiveness of the

current ITO method on seeking for 2D auxetic metamaterials.

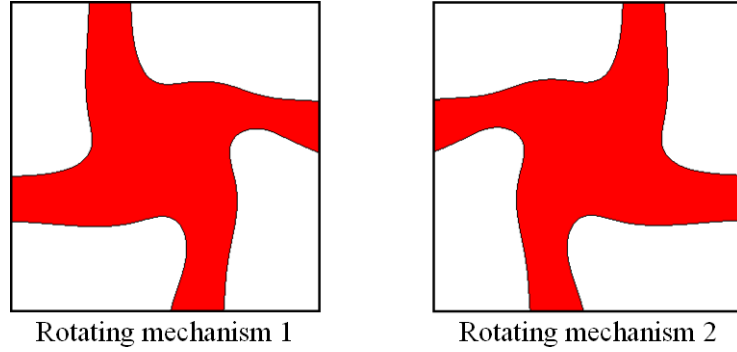


Figure 5-7 Rotating mechanisms in the optimized 2D auxetic metamaterial

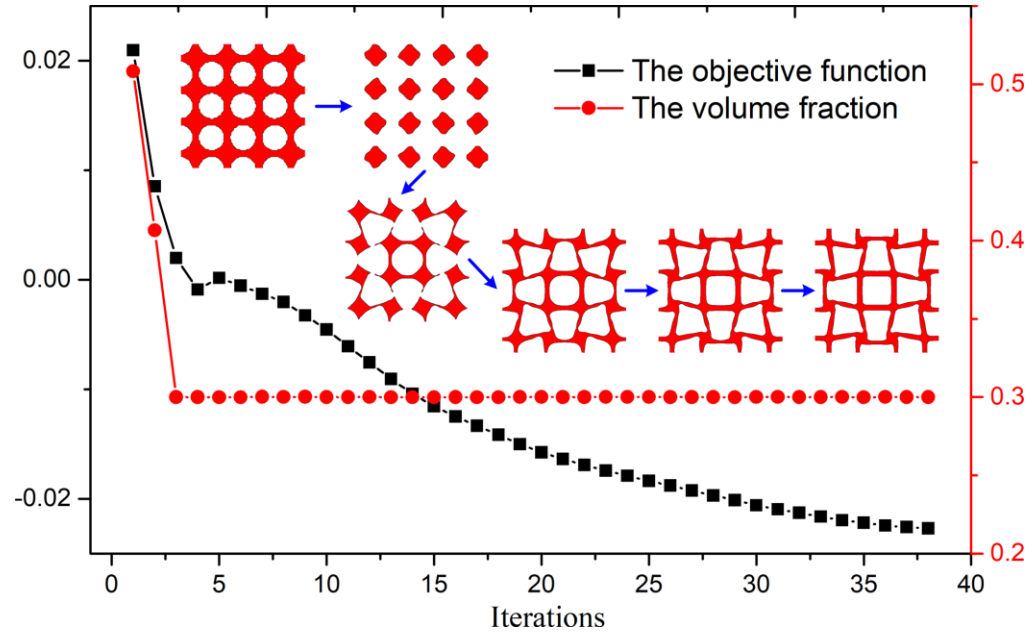


Figure 5-8 Iterative curves of 2D auxetic metamaterial

Additionally, it can be easily found that the optimized topology is featured with the smooth boundaries and clear interfaces between solids and voids owing to the DDF with the sufficient smoothness and continuity, which can be beneficial to lower the difficulties for the latter manufacturing. Although the ITO method for auxetic metamaterials is developed on the basis of the conception of material densities, the key intention of the ITO formulation is to seek for the optimal DDF with the auxetic characteristic. Finally, the iterative curves of the objective

function and volume fraction of the DDF are shown in Figure 5-8, with the intermediate topologies of 2D auxetic microstructure. It can be easily found that the iterative histories are very smooth, and the optimization can quickly arrive at the prescribed convergent condition within 38 steps, which presents the perfect stability of the proposed ITO method on the optimization of 2D auxetics.

5.4.2 Discussions of the weight parameter

In this section, we study the effect of the weight parameter β in the objective function on the optimization of auxetic metamaterials. The weight parameter β will be discussed with 15 cases, namely 0.03 (Section 6.1), 0.04, 0.05, 0.06, 0.07, 0.08, 0.09, 0.10, 0.15, 0.20, 0.25, 0.30, 0.0001, 0.0005, 0.02. The related design parameters are consistent with Section 6.1, like the NURBS details, the maximum material consumption, the initial design and etc.

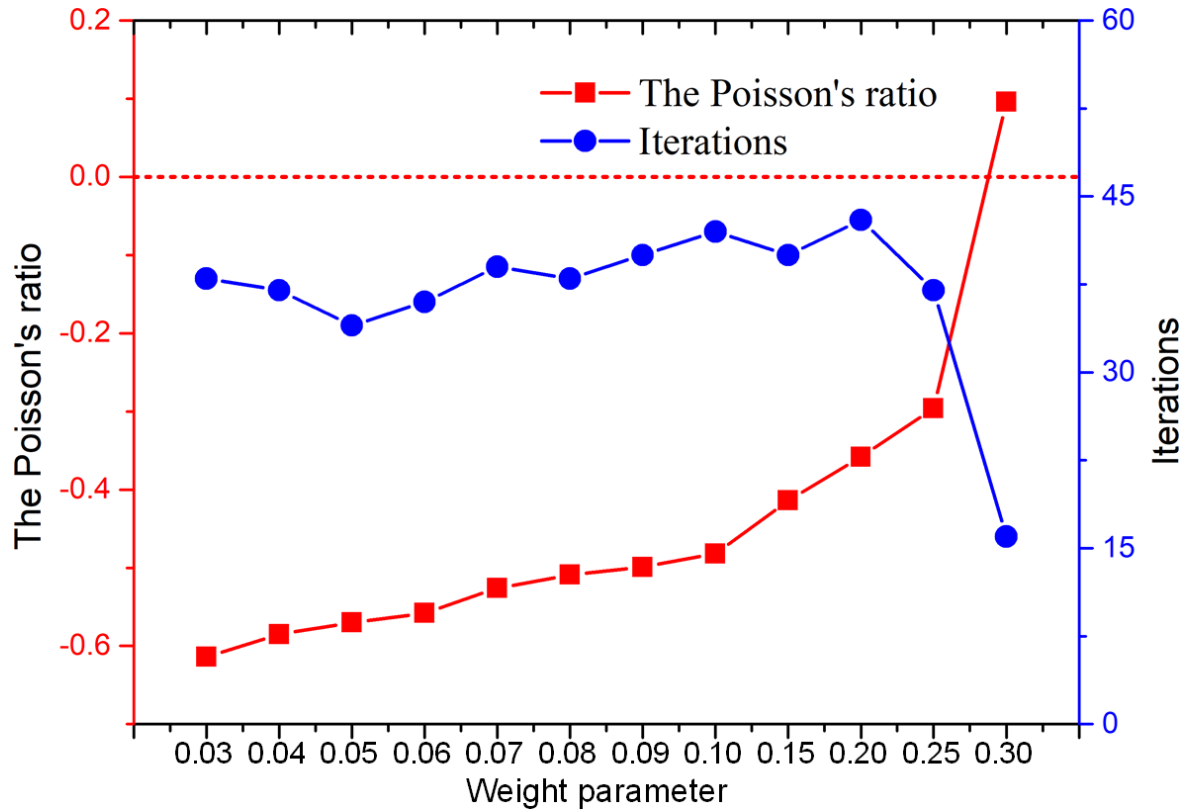


Figure 5-9 Numerical results of the former twelve cases

As shown in Figure 5-9, the corresponding numerical results of the former twelve cases from 0.03 to 0.30 are firstly provided. It can be found that the values of the Poisson's ratio in twelve cases are increased with the increasing of the weight parameter. The corresponding auxetic microstructures in twelve cases are shown in Figure 5-10. The auxetic behavior is becoming smaller and smaller with the increasing of the weight parameter. When the weight parameter is equal to 0.3, the optimized microstructure is not featured with the negative Poisson's ratio. Meanwhile, the first case with the weight parameter 0.03 can obtain auxetic microstructure with the negative Poisson's ratio -0.614 in the similar iterative steps when compared to other cases. Three numerical cases with the weight parameter equal to 0.02, 0.005 and 0.0001, respectively, are provided in Table 5-2. If the weight parameter is decreased, the optimizer intends to minimize the negative Poisson's ratio in one direction. As listed in the third row of Table 5-2, namely $\beta = 0.0005$, the v_{21} is smaller than the v_{12} , and the auxetic microstructure is the orthotropic. However, if the weight parameter is very small, equal to 0.0001, the final auxetic metamaterial is the anisotropic. The auxetic behavior of the design results from the chiral deformation mechanism. The above phenomenon mainly stems from a fact that the weight parameter controls the influence degree of the term $\sum_{i,j=1,l=j}^d D_{ijl}^H$ in the objective function. Additionally, as provided in the last column of Table 5-2, we can confirm that an increasing number of iterations are required to arrive at the convergent criterion, with the decreasing of the weight parameter. Hence, as far as finding auxetic microstructures with the identical negative Poisson's ratios in two directions, the weight parameter 0.03 is a relatively appropriate value for the ITO method. It should be noted that the discussion for the weight parameter is just suitable for the current ITO method.

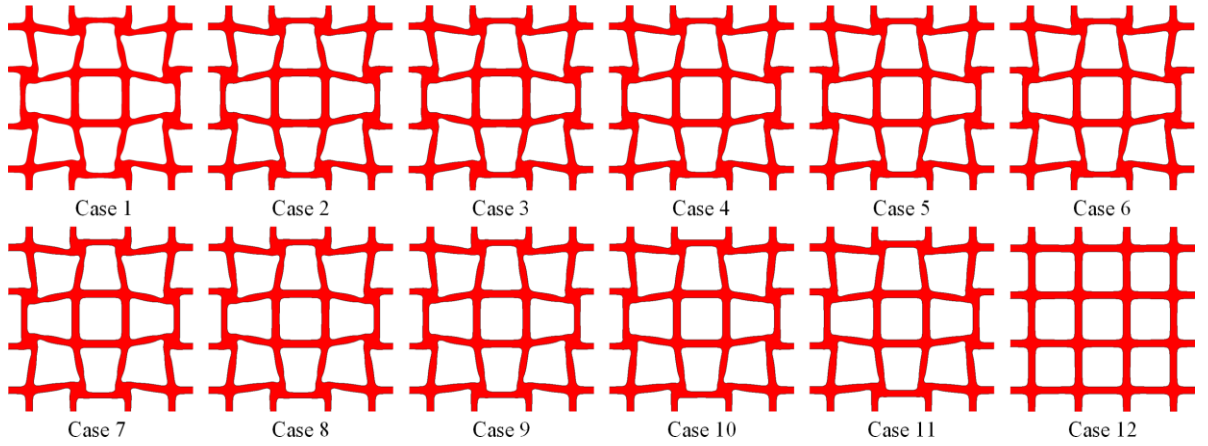
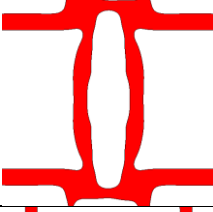
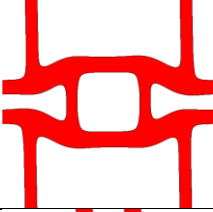



Figure 5-10 Auxetic microstructures in twelve cases

Table 5-2 Numerical results of three cases

β	Topology	Homogenized elastic tensor \mathbf{D}^H	ν	Iterations
0.02		$\begin{bmatrix} 0.0762 & -0.038 & 0 \\ -0.038 & 0.0702 & 0 \\ 0 & 0 & 0.0008 \end{bmatrix}$	$\begin{cases} \nu_{12} = -0.498 \\ \nu_{21} = -0.541 \end{cases}$	117
0.0005		$\begin{bmatrix} 0.1204 & -0.053 & 0 \\ -0.053 & 0.0392 & 0 \\ 0 & 0 & 0.0011 \end{bmatrix}$	$\begin{cases} \nu_{12} = -0.442 \\ \nu_{21} = -1.352 \end{cases}$	101
0.0001		$\begin{bmatrix} 0.084 & -0.057 & 0.013 \\ -0.057 & 0.085 & -0.013 \\ 0.013 & -0.013 & 0.0028 \end{bmatrix}$	$\begin{cases} \nu_{12} = -0.678 \\ \nu_{21} = -0.671 \end{cases}$	157

5.4.3 3D auxetic metamaterials

In this section, the optimization of 3D auxetic metamaterials is studied to present the superior effectiveness of the developed ITO method. As far as 3D material microstructure, the design domain is a cubic with $1 \times 1 \times 1$, as shown in Figure 5-11 (a). The structural design domain is parameterized by the NURBS solid, where the quadratic NURBS basis functions are used and knot vectors in parametric directions are $\Xi = \mathcal{H} = \mathcal{Z} = \{0, 0, 0, 0.0417, \dots, 0.9583, 1, 1, 1\}$.

The NURBS solid and the IGA mesh for the design domain are displayed in Figure 5-11 (b) and (c), respectively. The IGA mesh has $24 \times 24 \times 24$ elements, and $26 \times 26 \times 26$ control points are included in the NURBS solid. The total number of design variables is equal to $26 \times 26 \times 26$. An IGA element contains $3 \times 3 \times 3$ Gauss quadrature points, and the total number of Gauss quadrature points is equal to $72 \times 72 \times 72$. In this section, four different initial designs of 3D material microstructure are defined and four cases will be discussed. As far as 3D material microstructure, it is difficult to plot the 4D density response surface. We only display the corresponding iso-contours of four initial material microstructures, as given in Figure 5-12, where \mathcal{X}_c is still set to be 0.5.

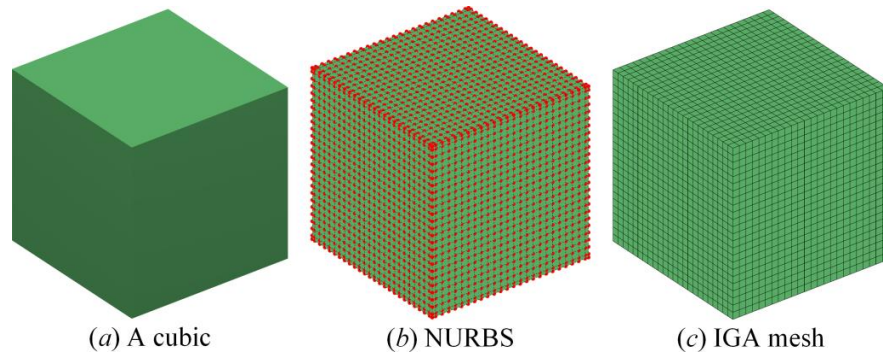


Figure 5-11 3D material microstructure

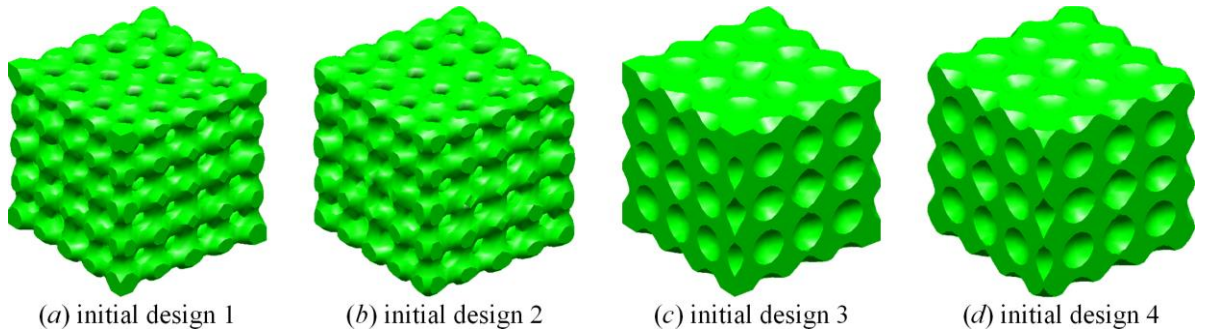


Figure 5-12 Four initial designs for 3D material microstructure

The initial design 1 shown in Figure 5-11 (a) is considered in Case 1, where the maximum material consumption is set to be 30%. As clearly displayed in Figure 5-12 (a), the optimized

topology of 3D material microstructure with the auxetic behavior is provided. In order to observe the interior configuration of the optimized design, the middle cross-sectional view of 3D auxetic microstructure is shown in Figure 5-12 (b). Meanwhile, a 3D auxetic metamaterial with $3 \times 3 \times 3$ repetitive microstructures is shown in Figure 5-12 (c). It can be easily seen that the optimized 3D auxetic microstructure is characterized with the smooth boundaries and distinct interfaces between the solids and voids, originating from the constructed DDF with the desired smoothness and continuity. Meanwhile, it can be observed that the 3D material microstructure shown in Figure 5-12 (a) can exhibit the counterintuitive dilatational behavior, when a load is imposed on one direction of this structure. As provided in Table 5-3, the homogenized elastic tensor of the 3D material microstructure in Figure 5-12 (a) is given and the corresponding Poisson's ratio is equal to -0.047. Hence, the auxetic behavior of the 3D microstructure 1 can be confirmed from not only the qualitative analysis, but also quantitative calculation.

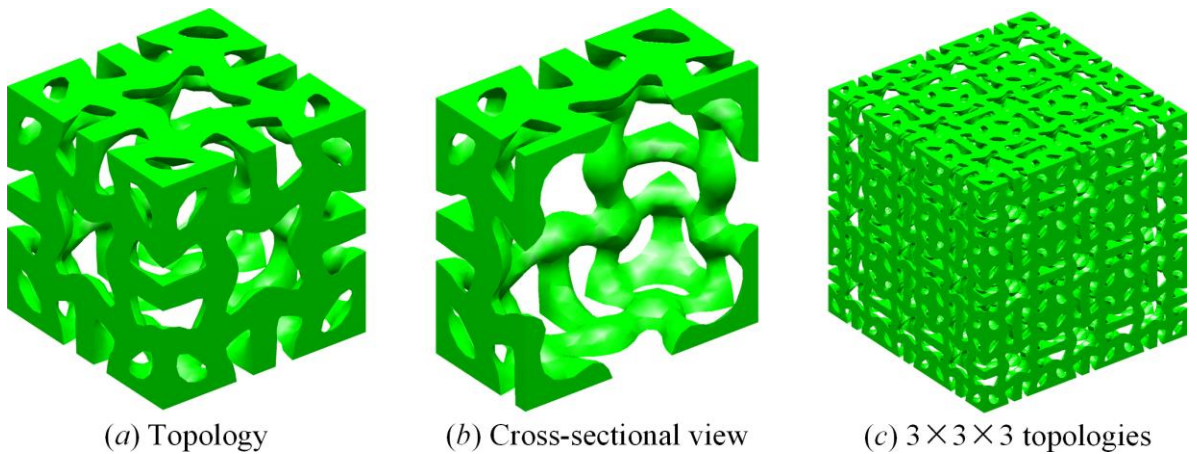


Figure 5-13 3D auxetic microstructure No. 1

Similarly, Case 2 is performed with the maximum volume fraction 30%, starting from the initial design 2, shown in Figure 5-11 (b). The initial design 3, illustrated in Figure 5-11 (c),

is considered in Case 3 with the maximum material consumption 30%, and Case 4 optimizes the 3D microstructure starting from the initial design 4 displayed in Figure 5-11 (d), but with the maximum volume fraction 24%. The optimized results in Cases 2, 3 and 4 are displayed in Figure 5-13, 5-14 and 5-15, respectively, also including the optimized topology, the cross-sectional view of the topology to illustrate the interior information and $3 \times 3 \times 3$ repetitive distributed microstructures. The homogenized elastic tensors of 3D auxetic microstructures 2, 3 and 4 are listed in Table 5-3, where the corresponding Poisson's ratio are also computed, namely -0.082, -0.12, -0.11. Thereby, the capability of the ITO method to seek for 3D auxetic metamaterials can be presented.

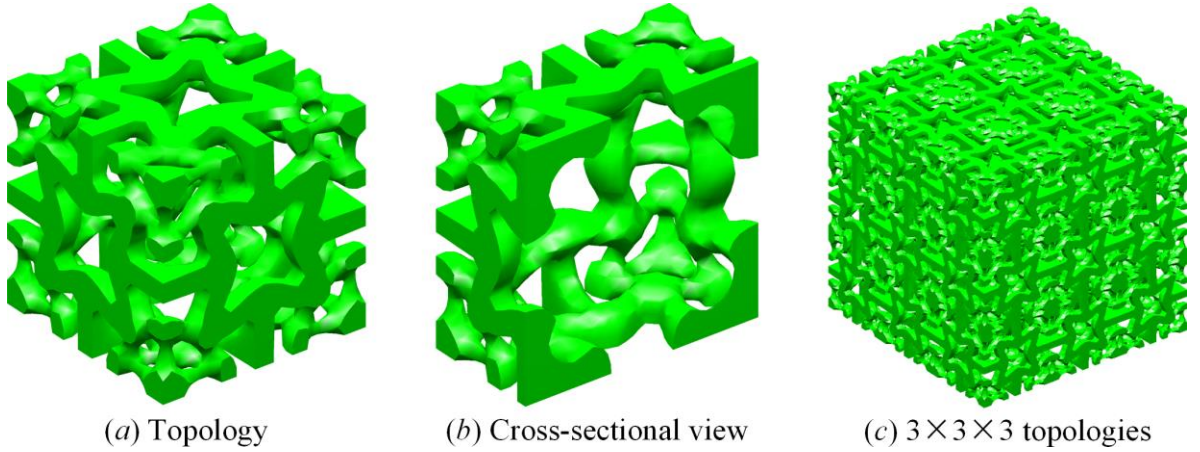


Figure 5-14 3D auxetic microstructure No. 2

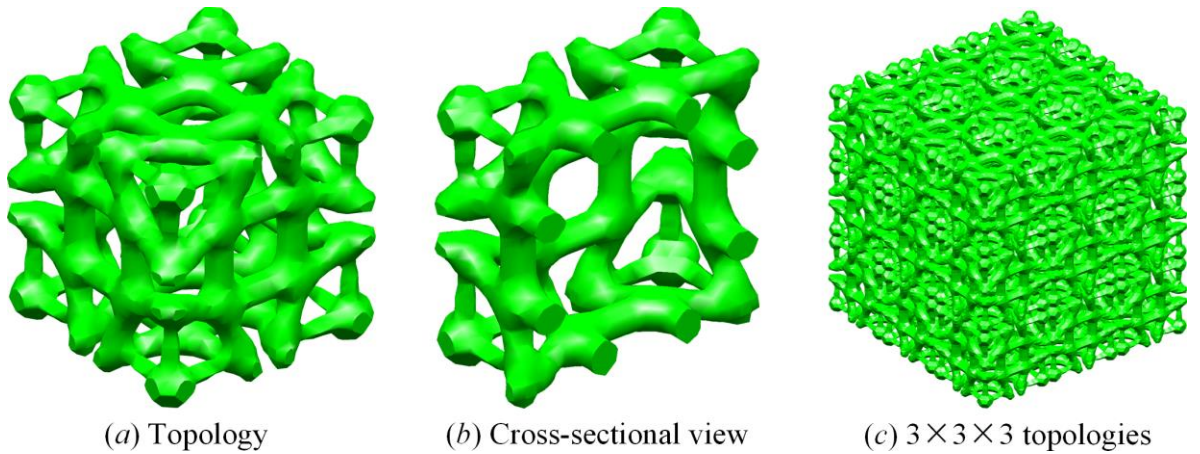


Figure 5-15 3D auxetic microstructure No. 3

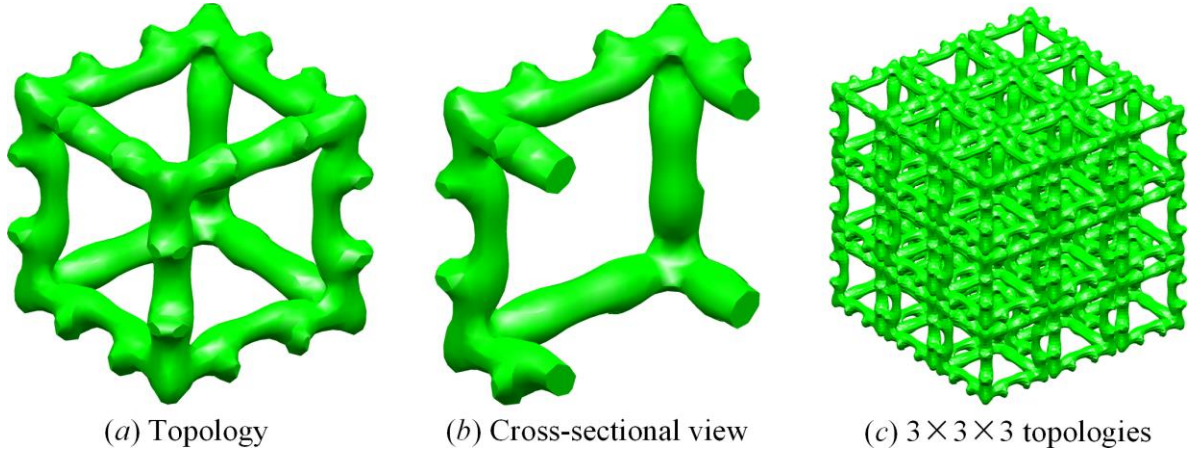


Figure 5-16 3D auxetic microstructure No. 4

Table 5-3 The homogenized elastic tensors of four 3D auxetic microstructures

3D auxetic microstructure 1						3D auxetic microstructure 2					
$\begin{bmatrix} 4.5 & -0.21 & -0.21 & 0 & 0 & 0 \\ -0.21 & 4.5 & -0.04 & 0 & 0 & 0 \\ -0.21 & -0.21 & 4.5 & 0 & 0 & 0 \\ 0 & 0 & 0 & 0.31 & 0 & 0 \\ 0 & 0 & 0 & 0 & 0.31 & 0 \\ 0 & 0 & 0 & 0 & 0 & 0.31 \end{bmatrix} e^{-2}$						$\begin{bmatrix} 7.88 & -0.65 & -0.65 & 0 & 0 & 0 \\ -0.65 & 7.88 & -0.65 & 0 & 0 & 0 \\ -0.65 & -0.65 & 7.88 & 0 & 0 & 0 \\ 0 & 0 & 0 & 0.52 & 0 & 0 \\ 0 & 0 & 0 & 0 & 0.52 & 0 \\ 0 & 0 & 0 & 0 & 0 & 0.52 \end{bmatrix} e^{-2}$					
$\nu = -0.047$						$\nu = -0.082$					
3D auxetic microstructure 3						3D auxetic microstructure 4					
$\begin{bmatrix} 7.89 & -0.94 & -0.94 & 0 & 0 & 0 \\ -0.94 & 7.89 & -0.94 & 0 & 0 & 0 \\ -0.94 & -0.94 & 7.89 & 0 & 0 & 0 \\ 0 & 0 & 0 & 0.6 & 0 & 0 \\ 0 & 0 & 0 & 0 & 0.6 & 0 \\ 0 & 0 & 0 & 0 & 0 & 0.6 \end{bmatrix} e^{-2}$						$\begin{bmatrix} 3.31 & -0.38 & -0.38 & 0 & 0 & 0 \\ -0.38 & 3.31 & -0.38 & 0 & 0 & 0 \\ -0.38 & -0.38 & 3.31 & 0 & 0 & 0 \\ 0 & 0 & 0 & 0.24 & 0 & 0 \\ 0 & 0 & 0 & 0 & 0.24 & 0 \\ 0 & 0 & 0 & 0 & 0 & 0.24 \end{bmatrix} e^{-2}$					
$\nu = -0.12$						$\nu = -0.11$					

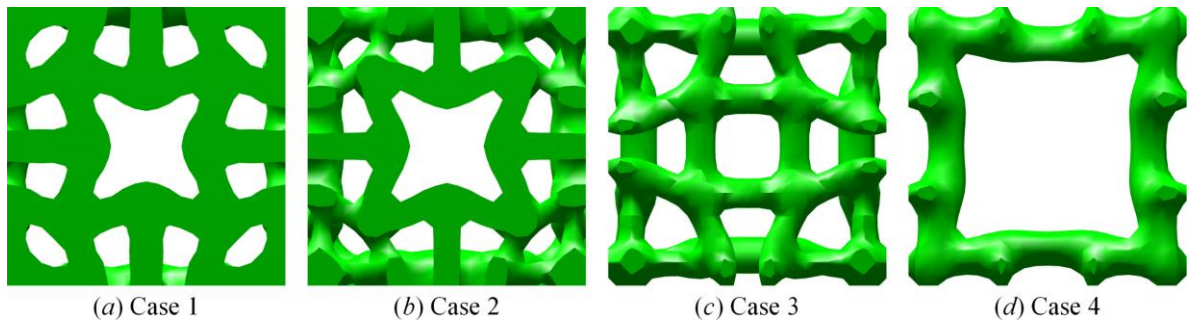


Figure 5-17 The 2D-views for four auxetic microstructures

As shown in Figure 5-17, the 2D views of the optimized 3D auxetic microstructures are provided, which are analogous to the reported 2D auxetic microstructures in previous works [143,146]. However, it is not straight to extend the optimization for 2D auxetic metamaterials to 3D scenario. The convergent curves of the objective function, the volume fraction of the DDF and the topological change between two adjacent iterations in Cases 1 and 2 are shown in Figure 5-18. It can be easily found that the iterative histories in two cases are very smooth and quickly arrive at the prescribed convergent criterion, only 34 steps in Case 1 and 51 steps in Case 2. The intermediate topologies of the 3D auxetic microstructures in Case 1 and 2 are also displayed in Figure 5-19 and 5-20, respectively. Hence, the effectiveness and efficiency of the ITO method on the optimization of 3D auxetic metamaterials can be demonstrated. Meanwhile, the pre-defined geometrical symmetries are not considered in the optimization to allow more freedoms to seek for the novel 3D auxetic microstructures. As shown in Figure 5-13 to 5-14, a series of interesting 3D auxetic microstructures can be achieved in the current work. However, the negative Poisson's ratios of the optimized 3D auxetic microstructures are larger than the reported designs [142,148,149]. The negative Poisson's ratio of the auxetic microstructure strongly depends on the objective function. In Eq. (16), the objective function is expressed by a combination of the homogenized elastic tensor, which can only provide a reasonable search direction for the optimizer to find auxetic metamaterials. It is difficult to arrive at the expected negative Poisson's ratio. It should be noted that this phenomenon has a negligible influence on the latter applications of the ITO method, owing to the fact that the proposed ITO method can achieve topological design of auxetic metamaterials in a more effective and efficient manner. Based on the skeleton of the current topologically optimized designs (Figure 5-13 to 5-14), the auxetic metamaterials with any given negative Poisson's

ratio can be achieved by further using shape optimization, similar to [148].

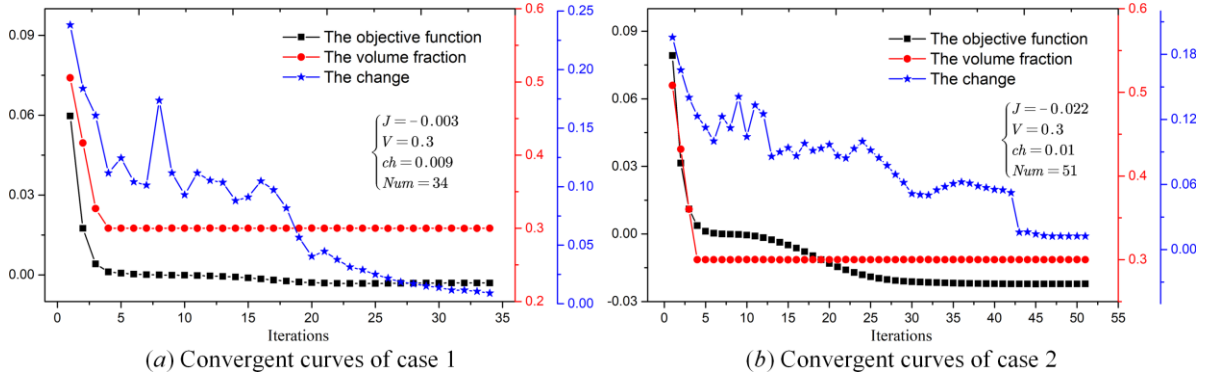


Figure 5-18 Convergent histories of Cases 1 and 2

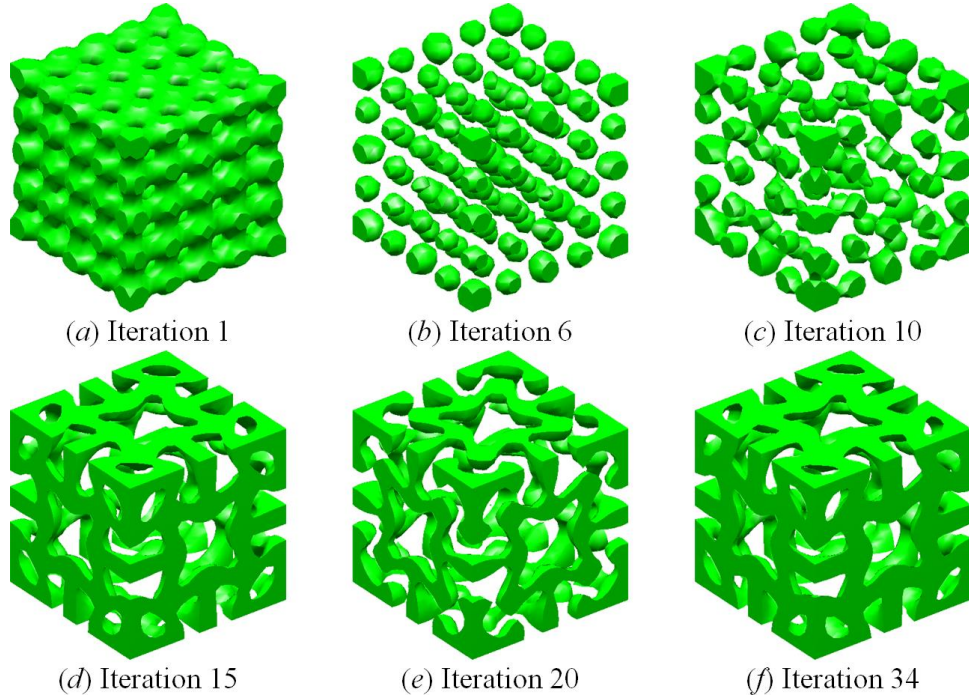


Figure 5-19 Intermediate results of Case 1

According to the discussion about the weight parameter in Section 6.2, two different cases with $\beta = 0.02$ and 0.0001 for 3D auxetic metamaterials are discussed, respectively. The optimized 3D auxetic designs in two cases are shown in Figure 5-21, including the optimized topologies and the cross-sectional views of the topologies. It can be seen that the 3D auxetic microstructure 5 in Figure 5-21 (a) is similar to the reported microstructure in [149]. The 3D

auxetic microstructure No. 6 with the anisotropic is a new finding with the chiral deformation mechanism to form the auxetic behavior. The homogenized elastic tensors of two 3D auxetic microstructures are listed in Table 5-4, and the minimum Poisson's ratios of two cases are equal to -0.257 and -0.188, respectively.

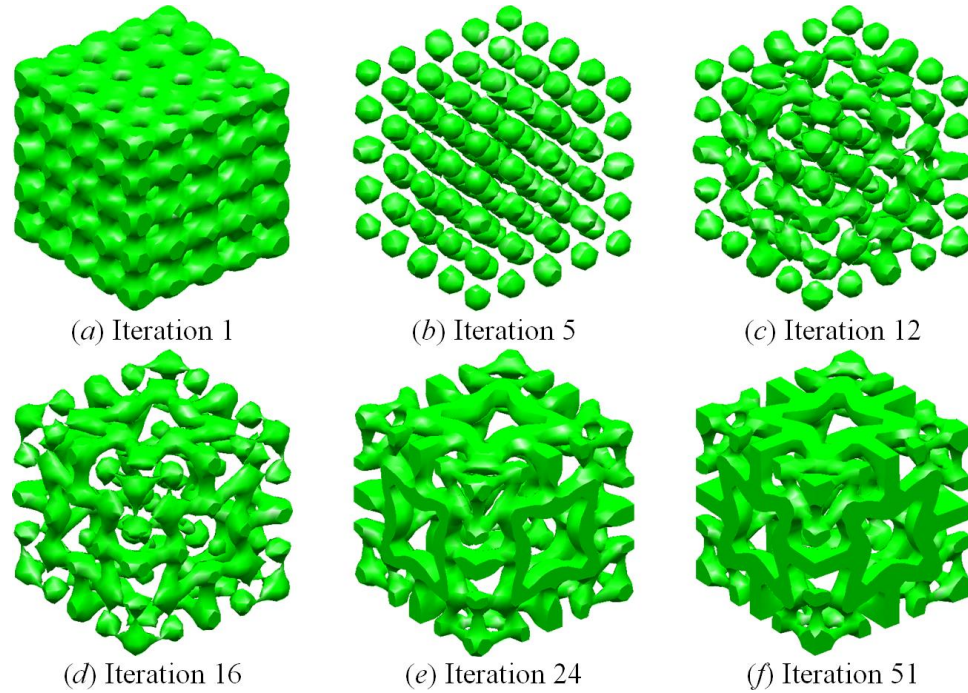


Figure 5-20 Intermediate results of Case 2

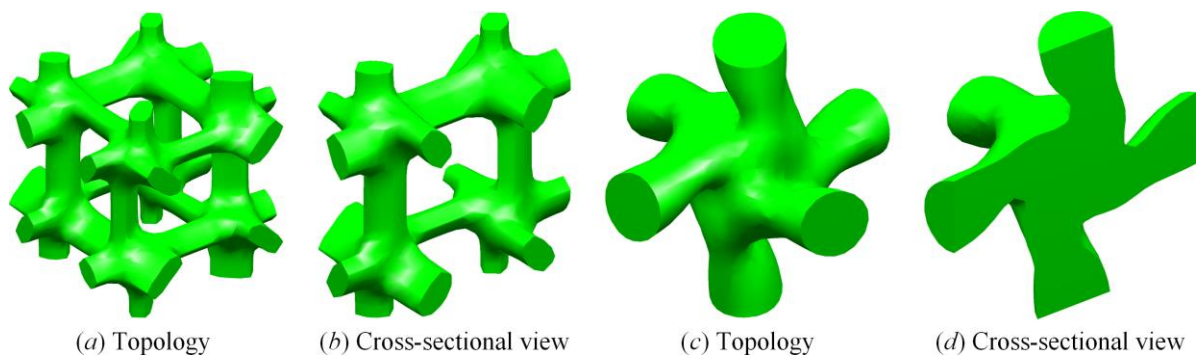


Figure 5-21 3D auxetic microstructures No. 5 and No.6

Table 5-4 Homogenized elastic tensors of 3D auxetic microstructures No. 5 and 6

3D auxetic microstructure 5	3D auxetic microstructure 6
-----------------------------	-----------------------------

$$\begin{bmatrix} 0.0483 & -0.0124 & -0.0049 & 0 & 0 & 0 \\ -0.0124 & 0.0633 & -0.0122 & 0 & 0 & 0 \\ -0.0049 & -0.0122 & 0.0505 & 0 & 0 & 0 \\ 0 & 0 & 0 & 0.0047 & 0 & 0 \\ 0 & 0 & 0 & 0 & 0.0048 & 0 \\ 0 & 0 & 0 & 0 & 0 & 0.0047 \end{bmatrix} \begin{bmatrix} 0.0457 & -0.0028 & -0.008 & 0.0031 & 0.0009 & 0.0067 \\ -0.0028 & 0.0426 & -0.0062 & -0.0032 & -0.0062 & -0.0004 \\ -0.008 & -0.0062 & 0.053 & -0.0003 & 0.0045 & -0.0053 \\ 0.0031 & -0.0032 & -0.0003 & 0.004 & -0.0002 & -0.0002 \\ 0.0009 & -0.0062 & 0.0045 & -0.0002 & 0.0038 & 0.0004 \\ 0.0067 & -0.0004 & -0.0053 & -0.0002 & 0.0004 & 0.0038 \end{bmatrix}$$

$v_{min} = -0.257$
 $v_{min} = -0.188$

5.4.4 Simulating validation based on ANSYS

In this section, the numerical verification of the above optimized auxetic microstructures is performed using ANSYS, and the auxetic microstructure No. 1 is considered. The “STL” file of the auxetic microstructure No. 1, as displayed in Figure 5-22 (a), is firstly exported from Matlab and then imported into ANSYS. The “STL” file needs to be slightly modified in the SpaceClaim of ANSYS and converted into the solid geometry with $1\text{cm} \times 1\text{cm} \times 1\text{cm}$, given in Figure 5-22 (b). The volume fraction of the “STL” file for 3D auxetic microstructure 1 is equal to 29.65% (nearly 30%) and the volume fraction 29.73% of the modified solid geometry is also mostly identical to 30%. In order to test the negative Poisson’s ratio with a much higher accuracy, an auxetic metamaterial with $5 \times 5 \times 5$ auxetic microstructures No. 1 is considered in the latter simulation, as shown in Figure 5-23 (a), and the corresponding mesh is also shown in Figure 5-23 (b) with 19763500 finite elements.

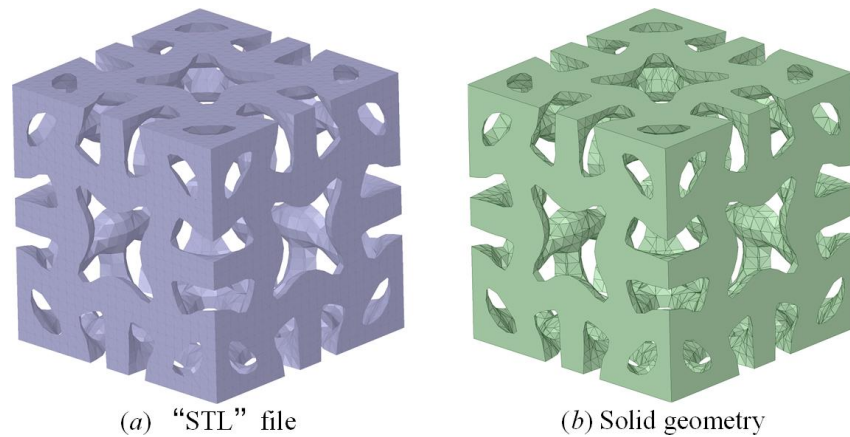


Figure 5-22 3D auxetic microstructure No. 1

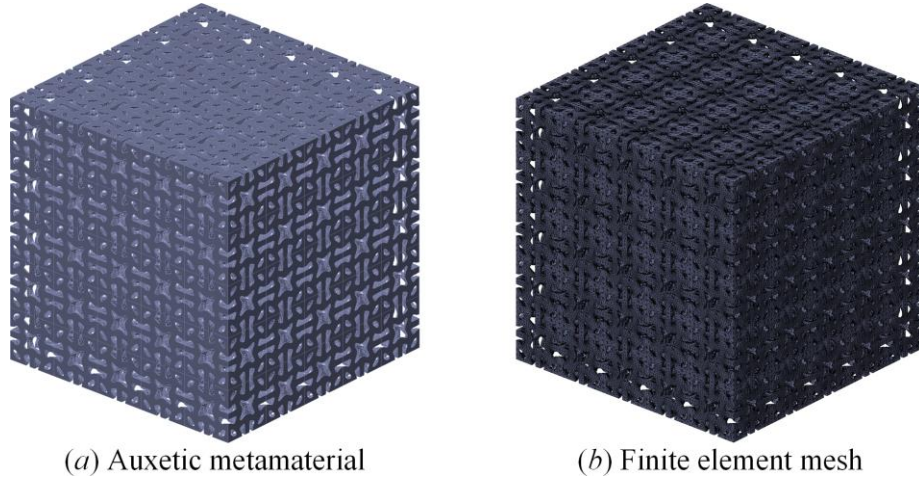


Figure 5-23 Auxetic metamaterial and its finite element mesh

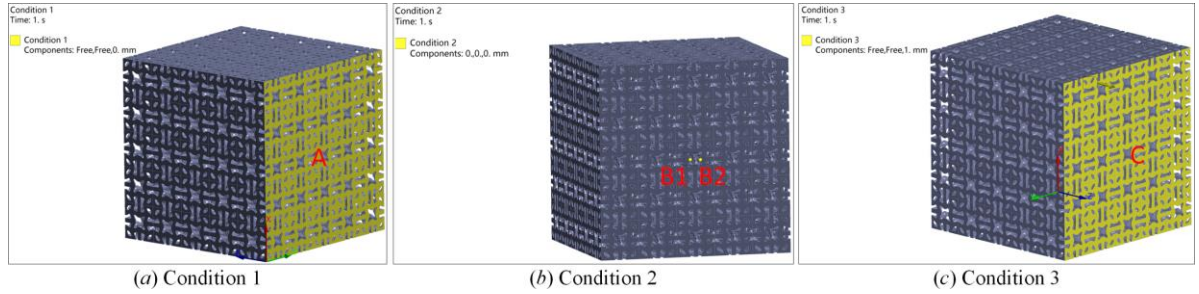


Figure 5-24 Boundary conditions imposed on the auxetic metamaterial

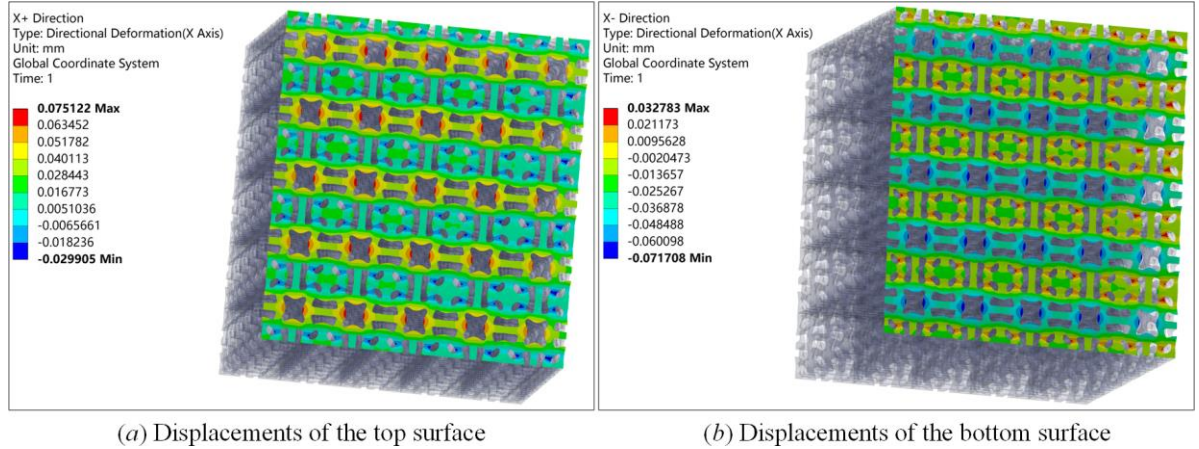


Figure 5-25 Displacement responses of auxetic metamaterial

In Figure 5-24, three boundary conditions are imposed on the auxetic metamaterial. Condition 1, shown in Figure 5-24 (a), fixes the Z-direction displacements of the surface A with the normal direction Z-. In the Condition 2, two points at the middle of the surface A are fixed to avoid the rotation of the auxetic metamaterial, given in Figure 5-24 (b). As shown in Figure

5-24 (c), a displacement with 1 mm in Z direction is homogenously imposed on the surface C with the normal direction Z+ in Condition 3. It should be noted that the surfaces A and C are opposite along Z direction. The deformations of the top and bottom surfaces in X direction of the auxetic metamaterial are displayed in Figure 5-25. In order to obtain a more accurate value, the difference of the average displacements on the top and bottom surfaces is viewed as the deformation degree of auxetic metamaterial 1 in the X direction. The displacement mean on the top surface is equal to 0.0239 mm, and the mean on the bottom surface is -0.0227 mm. The deformation of auxetic metamaterial in X direction is equal to $\Delta x = 0.0466\text{mm}$. The negative Poisson's ratio is defined by $\nu = -\Delta x/\Delta z = -0.0466$. We consider different displacements imposed on the Surface C, ranging from 0.1mm to 1mm, and the corresponding negative Poisson's ratios in different cases are all equal to -0.0466, shown in Figure 5-26. The simulated values are mostly identical to the result calculated by the homogenization.

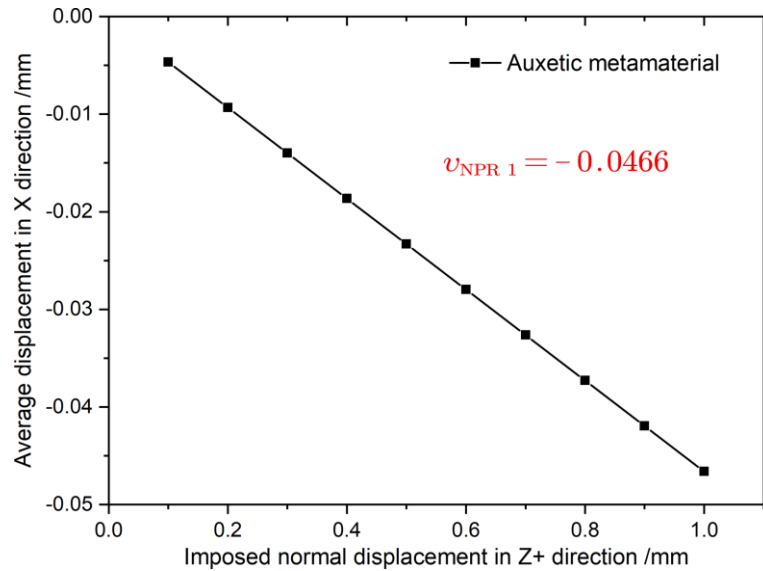


Figure 5-26 Mechanical responses of auxetic metamaterial

Finally, all 3D printing prototypes for the topologically optimized 3D auxetic microstructures No. 1 to 6 are fabricated using the SLS technique, displayed in Figure 5-27, respectively.



(a) Auxetic microstructure No.1



(b) Auxetic microstructure No.2



(c) Auxetic microstructure No.3



(d) Auxetic microstructure No.4



(e) Auxetic microstructure No.5



(f) Auxetic microstructure No.6

Figure 5-27 3D printing samples for six auxetic microstructures

5.5 Conclusions

In this chapter, we present an effective and efficient ITO method for the optimization of 2D and 3D auxetic metamaterials, where an enough smooth and continuous DDF is constructed to represent the structural topology and IGA is applied to solve the displacement responses in microstructures. The homogenization to predict the effective material properties is numerical implemented by IGA. A relaxed form of the OC method is employed to derive the advancing of the structural topology.

In numerical examples, 2D and 3D auxetic microstructures are discussed to demonstrate the effectiveness and efficiency of the ITO method. As we can see, the key characteristic of the current method is to optimize the DDF for material microstructures with the auxetic behavior, rather than the spatial arrangements of element densities. Moreover, the optimized topologies of auxetics have smooth boundaries and distinct interfaces, which is beneficial to the latter manufacturing. Additionally, the ITO method is featured with the higher efficiency for the optimization of 3D auxetic microstructures, only 37 steps for the auxetic microstructure No.1 and 52 iterations for the auxetic microstructure No.2. A series of new and interesting auxetic microstructures can be achieved. The proposed ITO method is general, and in the future, it can be extended to other more advanced topological design problems, like the nonlinear and multifunctional material microstructures.

Chapter 6 Rational design of auxetic composites using M-ITO method

In this chapter, the main intention is to develop an effective and efficient ITO method for the systematic design and realization of auxetic composites with not only the negative Poisson's ratio, but also the improving stiffness to some extent. Firstly, the homogenization to evaluate macroscopic effective properties is numerically implemented by IGA, with the imposing of a rational periodic boundary formulation on microstructures. Secondly, a NURBS-based multi-material interpolation (N-MMI) model is developed, where two kinds of variables are defined, namely design variables and topology variables, to represent the advancing of multiple phases in the design domain. The field of design variables is constructed by the non-uniform rational B-splines (NURBS) and Shepard function to enhance the overall smoothness of nodal design variables. Multiple sets of topology variables are defined by a combination of all fields of design variables, and each of them is applied to represent the evolvement of one material in the optimization. Thirdly, the ITO formulation for the design of 2D and 3D auxetic composites is developed using the homogenization and the N-MMI model, in which IGA is adopted to solve the structural responses and the objective function is expressed by a combination of the effective elastic tensor. We can see that NURBS integrates the N-MMI model and IGA into a unified mathematical formula for the topology optimization of auxetic composites.

Finally, a series of novel and interesting auxetic composites can be achieved in numerical examples to demonstrate the effectiveness of the proposed ITO method.

6.1 IGA-based Homogenization

The homogenization [20] is applied to predict macroscopic effective properties of materials considering the micro information. Noting that two basic requirements should be maintained in the homogenization: (1) the scales of microstructures are much smaller than that of the bulk material, and (2) material microstructure, working as a unit cell, is periodically distributed in the bulk material. As displayed in Figure 6-1, the bulk material is configured by an identical material microstructure with two materials (three phases), where material cell is depicted in the coordinate system $o - y_1 y_2$.

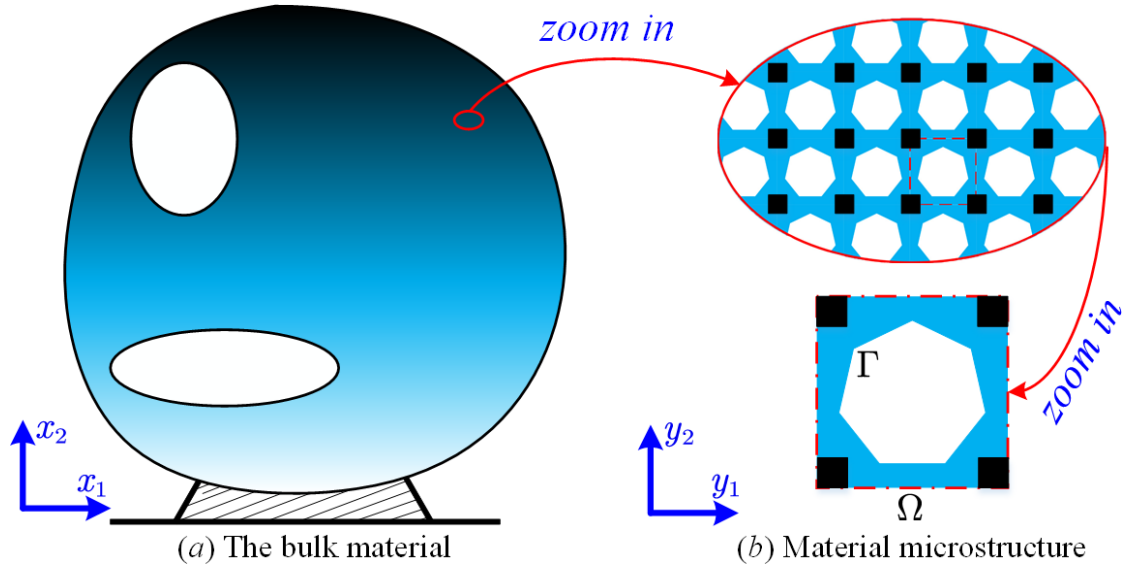


Figure 6-1 The bulk material composed of a kind of material microstructure

For the linearly elastic material, the displacement field $\mathbf{u}^\epsilon(\mathbf{x})$ at the bulk material can be characterized by the asymptotic expansion theory, expressed as:

$$\mathbf{u}^\epsilon(\mathbf{x}) = \mathbf{u}_0(\mathbf{x}, \mathbf{y}) + \epsilon \mathbf{u}_1(\mathbf{x}, \mathbf{y}) + \epsilon^2 \mathbf{u}_2(\mathbf{x}, \mathbf{y}) + \dots \quad (6-1)$$

where ϵ is the aspect ratio between the scales of the microstructure and the bulk material, which is far less than 1. For numerical simplicity, only the first-order variation term. The macroscopic effective tensor of the bulk material D_{ijkl}^H can be expressed by:

$$D_{ijkl}^H = \frac{1}{|\Omega|} \int_{\Omega} D_{pqrs} (\varepsilon_{pq}^{0(ij)} - \varepsilon_{pq}(u^{ij})) (\varepsilon_{rs}^{0(kl)} - \varepsilon_{rs}(u^{kl})) d\Omega \quad (6-2)$$

where $|\Omega|$ is the area (2D) or volume (3D) of the microstructure, and D_{pqrs} is the locally varying elastic property. $\varepsilon_{pq}^{0(ij)}$ is the linearly independent unit test strain field, containing three components in 2D and six in 3D. $\varepsilon_{pq}(u^{ij})$ denotes the unknown strain field in the microstructure, which is solved by the following linear elasticity equilibrium equation with \mathbf{y} -periodic boundary conditions:

$$\int_{\Omega} D_{pqrs} \varepsilon_{pq}(u^{ij}) \varepsilon_{rs}(\delta u^{ij}) d\Omega = \int_{\Omega} D_{pqrs} \varepsilon_{pq}^{0(ij)} \varepsilon_{rs}(\delta u^{ij}) d\Omega, \quad \forall \delta u \in H_{per}(\Omega, \mathbb{R}^d) \quad (6-3)$$

where δu is the virtual displacement in material microstructure belonging to the admissible displacement space H_{per} with \mathbf{y} -periodicity, and d denotes the dimension of microstructure. In IGA, the NURBS basis functions are firstly applied to parametrize the structural geometry, and then construct the approximate space for the unknown structural response. For the latter, the key principle is that the continuous solution space is developed by a linear combination of the NURBS basis functions with structural responses on control points. The mathematical formula of the solution space is consistent with the geometrical model, but control coefficients are the responses of control points, for example nodal displacements, rather than the physical coordinates for the geometrical model, given as:

$$\mathbf{u}(\xi, \eta, \zeta) = \sum_{i=1}^n \sum_{j=1}^m \sum_{k=1}^l R_{i,j,k}^{p,q,r}(\xi, \eta, \zeta) \mathbf{u}_{i,j,k} \quad (6-4)$$

where \mathbf{u} is the field of the structural responses in design domain, and $\mathbf{u}_{i,j,k}$ are the responses on control points. Considering the linear elasticity in the IGA, the system stiffness matrix is assembled by the element stiffness matrices. The IGA element stiffness matrix is solved by

the Gauss quadrature method, and the iso-parametric formulation is applied to calculate the element stiffness matrix:

$$\mathbf{K}_e = \sum_{i=1}^3 \sum_{j=1}^3 \sum_{k=1}^3 \{ \mathbf{B}^T(\xi_i, \eta_j, \zeta_k) \mathbf{D} \mathbf{B}(\xi_i, \eta_j, \zeta_k) | \mathbf{J}_1(\xi_i, \eta_j, \zeta_k) | | \mathbf{J}_2 | w_i w_j w_k \} \quad (6-5)$$

where \mathbf{D} is the material elastic tensor, and (ξ_i, η_j, ζ_k) denotes the chosen Gauss quadrature point. In the current work, $3 \times 3 \times 3$ Gauss quadrature points in each IGA element are adopted to calculate stiffness matrix. w_i , w_j and w_k are the weights for the Gauss quadrature point (ξ_i, η_j, ζ_k) in three parametric directions, respectively. \mathbf{B} is the strain-displacement matrix calculated by the partial derivatives of the NURBS basis functions with respect to the parametric coordinates. In the iso-parametric formulation, two mappings have to be defined. As shown in Figure 6-2 for a cross-sectional view of the cubic in ζ direction, $\mathbf{X}: \hat{\Omega}_e \rightarrow \Omega_e$ is the mapping from the parametric space to the physical space; and $\mathbf{Y}: \tilde{\Omega}_e \rightarrow \hat{\Omega}_e$ maps the bi-unit parent element into the parametric element. \mathbf{J}_1 and \mathbf{J}_2 are the Jacobi matrices of two mappings, respectively. The details for the derivations of them can refer to [89].

In the numerical implementation of the homogenization to evaluate the homogenized elastic tensor D_{ijkl}^H , IGA is employed to calculate the structural responses. Meanwhile, the periodic boundary conditions should be imposed on material microstructure in order to guarantee two basic requirements. In the implementation, an energy-based homogenization method (EBHM) [79,140,146] with a simple periodic boundary formulation is developed. Hence, the numerical analysis of material microstructure is implemented by IGA, with the imposing of the periodic boundary formulation developed in the EBHM. In Eq. (6-4), the displacement field in material microstructure is approximately constructed by the nodal displacements on control points

with NURBS basis functions. Moreover, the displacement field needs to satisfy the periodic boundary conditions, and a general form is expressed by:

$$\mathbf{u}_k^+ - \mathbf{u}_k^- = \varepsilon(\mathbf{u}_0) \triangle k \quad (6-6)$$

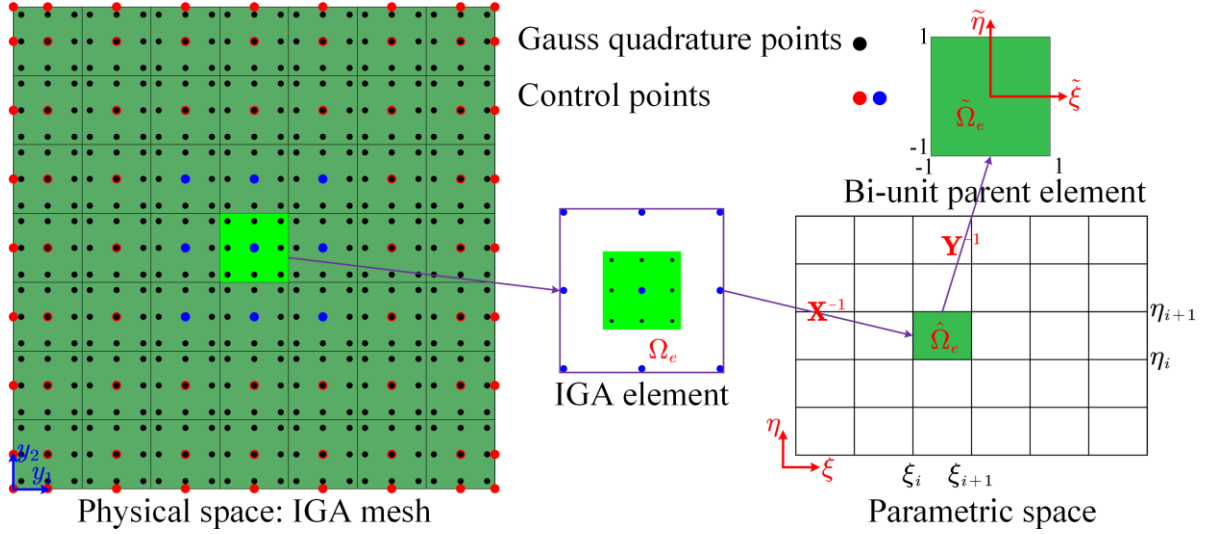


Figure 6-2 IGA mesh with Gauss quadrature points

where k denotes the normal direction of boundary, and \mathbf{u}_k^+ indicates the displacements of points at the structural boundary with the normal direction k , and the normal direction is in the positive direction of the coordinate axis. \mathbf{u}_k^- corresponds to the displacements of points at the opposite structural boundary. $\triangle k$ is the scale of material microstructure in the normal direction k . Hence, control points at structural boundary should be appropriately classified to develop periodic boundary conditions. The details can refer to [146] for 2D and [79] for 3D.

6.2 Isogeometric topology optimization (ITO) for auxetic composites

6.2.1 ITO formulation

It is known that the physical meaning of the Poisson's ratio corresponds to the deformation

mechanism of the bulk material, which is defined by the aspect ratio of the transverse contraction strain to the longitudinal extension strain in the direction of stretching force. In the existed works for the design of auxetic materials, several objective functions are defined to generate material microstructures with the auxetic behavior, such as the minimization of the weighted square difference between the effective elastic tensor and the expected elastic [143,150], or the minimization of the combination of the effective elastic tensor [75,146]. Comparatively speaking, the latter form of the definition is more stable and efficient in the optimization of auxetic materials with the negative Poisson's ratio [75,146].

The current work aims to develop a systematic design method for the optimization of auxetic composites with not only the negative Poisson's ratio, but also a stiffer structure, by virtue of the superior features of the composites with the enhanced properties from different materials. The combination of the homogenized elastic tensor of the composite microstructure works as the objective function of the optimization, and the ITO formulation can be expressed by:

$$\left\{ \begin{array}{l} \text{Find: } \boldsymbol{\rho}^\vartheta \{ \rho_{i,j}^\vartheta \rho_{i,j,k}^\vartheta \} \\ \text{Min: } J(\mathbf{u}, \boldsymbol{\phi}) = \left\{ \begin{array}{l} -\beta \left\{ \sum_{\hat{i}, \hat{j}=1, \hat{i}=\hat{j}}^d D_{\hat{i}\hat{i}\hat{j}\hat{j}}^H(\mathbf{u}, \boldsymbol{\phi}(\boldsymbol{\rho}^\vartheta)) \right\} \\ \sum_{\hat{i}, \hat{j}=1, \hat{i} \neq \hat{j}}^d D_{\hat{i}\hat{i}\hat{j}\hat{j}}^H(\mathbf{u}, \boldsymbol{\phi}(\boldsymbol{\rho}^\vartheta)) \end{array} \right\} \\ \text{S.t. } \left\{ \begin{array}{l} a(\mathbf{u}, \delta \mathbf{u}) = l(\delta \mathbf{u}), \quad \forall \delta \mathbf{u} \in H^1(\Omega) \\ G_v^\vartheta = \frac{1}{|\Omega|} \int_{\Omega} \boldsymbol{\phi}^\vartheta v_0 d\Omega - V_0^\vartheta \leq 0, \quad (\vartheta = 1, 2, \dots, \Theta) \\ 0 < \rho_{\min} \leq \boldsymbol{\rho}^\vartheta \leq 1 \\ \vartheta = 1, 2, \dots, \Theta; \quad i = 1, 2, \dots, m; \quad j = 1, 2, \dots, n; \quad k = 1, 2, \dots, l \end{array} \right. \end{array} \right. \quad (6-7)$$

where $\boldsymbol{\rho}^\vartheta$ denotes the design variables of the ϑ_{th} set, including $\rho_{i,j}^\vartheta$ for the 2D and $\rho_{i,j,k}^\vartheta$ for the 3D. J is the objective function, defined by the combination of the effective elastic tensor,

where the first term is beneficial to the generation of the mechanism-type structures to form the auxetic behavior and the second term can prevent the generation of the mechanism-type topologies. It can be easily seen that the current objective function cannot only facilitate the generation of composites with the negative Poisson's ratio, but also keep a reasonable topology during the optimization. β is a weighting parameter to claim the importance of the corresponding terms. d is the spatial dimension of composites. $G_v^{\hat{\vartheta}}$ is the volume constraint for the $\hat{\vartheta}_{th}$ distinct material, where $V_0^{\hat{\vartheta}}$ is the maximum material consumption and v_0 is the volume fraction of the solids. We can find that all the volume constraints have the separable and linear form with respect to the topology variables. $\phi^{\hat{\vartheta}}$ is the set of the topology variables to represent $\hat{\vartheta}_{th}$ unique material. \mathbf{u} is the displacement field in material microstructure, which should meet the periodic boundary conditions. $\delta\mathbf{u}$ denotes the virtual displacement field belonging to the admissible space H_{per} with \mathbf{y} -periodicity, which is calculated by the linearly elastic equilibrium equation. a and l correspond to the bilinear energy function and the linear load function, respectively, given as:

$$\begin{cases} a(\mathbf{u}, \delta\mathbf{u}) = \int_{\Omega} \mathbf{D}(\phi(\boldsymbol{\rho}^{\hat{\vartheta}})) \boldsymbol{\varepsilon}(\mathbf{u}) \boldsymbol{\varepsilon}(\delta\mathbf{u}) d\Omega \\ l(\delta\mathbf{u}) = \int_{\Omega} \mathbf{D}(\phi(\boldsymbol{\rho}^{\hat{\vartheta}})) \boldsymbol{\varepsilon}^0 \boldsymbol{\varepsilon}(\delta\mathbf{u}) d\Omega \end{cases} \quad (6-8)$$

where \mathbf{D} is the constituent elastic tensor of composites defined by the N-MMI model.

6.2.2 Design Sensitivity analysis

In Eq. (6-7), the ITO formulation is developed for the optimization of auxetic composites, with the design variable $\boldsymbol{\rho}^{\hat{\vartheta}}$. Firstly, we derive the first-order derivative of the objective function with respect to the set of topology variables $\phi^{\hat{\vartheta}}$, expressed by:

$$\frac{\partial J}{\partial \phi^{\hat{\vartheta}}} = -\beta \left\{ \sum_{\hat{i}, \hat{j}=1, \hat{i}=\hat{j}}^d \frac{\partial D_{\hat{i}\hat{j}\hat{j}\hat{j}}^H}{\partial \phi^{\hat{\vartheta}}} \right\} + \left\{ \sum_{\hat{i}, \hat{j}=1, \hat{i} \neq \hat{j}}^d \frac{\partial D_{\hat{i}\hat{j}\hat{j}\hat{j}}^H}{\partial \phi^{\hat{\vartheta}}} \right\} \quad (\hat{\vartheta} = 1, 2, \dots, \Theta) \quad (6-9)$$

It can be easily seen that the core of the first-order derivative of the objective function with respect to the set of topology variables is located at the calculation of the derivatives of the effective elastic tensor $D_{\hat{i}\hat{j}\hat{j}\hat{j}}^H$ with respect to the set of topology variables $\phi^{\hat{\vartheta}}$. The detailed derivations for the derivatives of the effective stiffness tensor can refer to [75,143,151], and the final form is expressed by:

$$\frac{\partial D_{\hat{i}\hat{j}\hat{j}\hat{j}}^H}{\partial \phi^{\hat{\vartheta}}} = \frac{1}{|\Omega|} \int_{\Omega} \gamma(\phi^{\hat{\vartheta}})^{\gamma-1} D_{0,pqrs}^{\hat{\vartheta}} \left(\varepsilon_{pq}^{0(\hat{i}\hat{i})} - \varepsilon_{pq}(u^{\hat{i}\hat{i}}) \right) \left(\varepsilon_{rs}^{0(\hat{j}\hat{j})} - \varepsilon_{rs}(u^{\hat{j}\hat{j}}) \right) d\Omega \quad (6-10)$$

As already defined, $\phi^{\hat{\vartheta}}$ to represent the distribution of the $\hat{\vartheta}$ unique material is defined by a combination of all the fields of design variables. Each field of design variables is constructed by NURBS basis functions with the nodal design variables ρ^{ϑ} . we can derive the first-order derivative of the set of topology variables $\phi^{\hat{\vartheta}}$ with respect to the field of design variables \mathcal{X}^{ϑ} , given as:

$$\frac{\partial \phi^{\hat{\vartheta}}}{\partial \mathcal{X}^{\vartheta}} = \begin{cases} \prod_{\lambda=1, \lambda \neq \vartheta}^{\hat{\vartheta}} \mathcal{X}^{\lambda} \prod_{\lambda=\hat{\vartheta}+1}^{\Theta} (1 - \mathcal{X}^{\lambda}) & \text{if } \vartheta \leq \hat{\vartheta} \\ - \prod_{\lambda=1}^{\hat{\vartheta}} \mathcal{X}^{\lambda} \prod_{\lambda=\hat{\vartheta}+1, \lambda \neq \vartheta}^{\Theta} (1 - \mathcal{X}^{\lambda}) & \text{if } \vartheta > \hat{\vartheta} \end{cases} \quad (\vartheta = 1, 2, \dots, \Theta) \quad (6-11)$$

Then, the derivative of the field of design variables with respect to the nodal design variables ρ^{ϑ} can be achieved by consecutively differentiating them, and a detailed form for the 3D composites with the nodal design variables $\rho_{i,j,k}^{\vartheta}$ is expressed by:

$$\frac{\partial \mathcal{X}^{\vartheta}}{\partial \rho_{i,j,k}^{\vartheta}} = \frac{\partial \mathcal{X}^{\vartheta}}{\partial \mathcal{G}^{\vartheta}} \frac{\partial \mathcal{G}^{\vartheta}}{\partial \rho_{i,j,k}^{\vartheta}} = R_{i,j,k}^{p,q,r}(\xi, \eta, \zeta) \psi(\rho_{i,j,k}^{\vartheta}) \quad (6-12)$$

where $R_{i,j,k}^{p,q,r}(\xi, \eta, \zeta)$ denotes the NURBS basis function at the computational point (ξ, η, ζ) .

$\psi(\rho_{i,j,k}^\vartheta)$ is the Shepard function at the current control point (i,j,k) . It is important to notice that the above computational point (ξ,η,ζ) is different from the control point (i,j,k) . The former corresponds to the Gauss quadrature points, which is located at the structural domain. However, the lattice of the control points forms a polygon in spatial which contain the structural geometry, and the control points might not on the structural geometry. Finally, the derivatives of the homogenized elastic tensor with respect to the nodal design variables can be derived, and the final form is explicitly expressed as:

$$\begin{aligned} \frac{\partial D_{ijj}^H}{\partial \rho_{i,j,k}^\vartheta} &= \frac{\partial D_{ijj}^H}{\partial \phi} \frac{\partial \phi}{\partial \mathcal{X}^\vartheta} \frac{\partial \mathcal{X}^\vartheta}{\partial \rho_{i,j,k}^\vartheta} = \sum_{\hat{\vartheta}=1}^{\Theta} \frac{\partial D_{ijj}^H}{\partial \phi^{\hat{\vartheta}}} \frac{\partial \phi^{\hat{\vartheta}}}{\partial \mathcal{X}^\vartheta} \frac{\partial \mathcal{X}^\vartheta}{\partial \rho_{i,j,k}^\vartheta} = \dots \\ &\sum_{\hat{\vartheta}=1}^{\Theta} \left\{ \begin{aligned} &\left\{ \frac{1}{|\Omega|} \int_{\Omega} \left(\gamma(\mathcal{X}^\vartheta)^{\gamma-1} \prod_{\lambda=1, \lambda \neq \vartheta}^{\hat{\vartheta}} (\mathcal{X}^\lambda)^\gamma \prod_{\lambda=\hat{\vartheta}+1}^{\Theta} (1-\mathcal{X}^\lambda)^\gamma \right) D_{0,pqrs}^{\hat{\vartheta}} \dots \right\} & \text{if } \vartheta \leq \hat{\vartheta} \\ &R_{i,j,k}^{p,q,r}(\xi,\eta,\zeta) \psi(\rho_{i,j,k}^\vartheta) \left(\varepsilon_{pq}^{0(\ddot{ii})} - \varepsilon_{pq}(u^{\ddot{ii}}) \right) \left(\varepsilon_{rs}^{0(\ddot{jj})} - \varepsilon_{rs}(u^{\ddot{jj}}) \right) d\Omega \\ &\left\{ \frac{1}{|\Omega|} \int_{\Omega} \left(-\gamma(1-\mathcal{X}^\vartheta)^{\gamma-1} \prod_{\lambda=1}^{\hat{\vartheta}} (\mathcal{X}^\lambda)^\gamma \prod_{\lambda=\hat{\vartheta}+1, \lambda \neq \vartheta}^{\Theta} (1-\mathcal{X}^\lambda)^\gamma \right) D_{0,pqrs}^{\hat{\vartheta}} \dots \right\} & \text{if } \vartheta > \hat{\vartheta} \\ &R_{i,j,k}^{p,q,r}(\xi,\eta,\zeta) \psi(\rho_{i,j,k}^\vartheta) \left(\varepsilon_{pq}^{0(\ddot{ii})} - \varepsilon_{pq}(u^{\ddot{ii}}) \right) \left(\varepsilon_{rs}^{0(\ddot{jj})} - \varepsilon_{rs}(u^{\ddot{jj}}) \right) d\Omega \end{aligned} \right\} \end{aligned} \quad (6-13)$$

Hence, the sensitivity analysis of the objective function with respect to the design variables can be obtained. Similarly, the derivatives of the volume constraint with respect to the design variables can be expressed by:

$$\begin{aligned} \frac{\partial G_v^{\hat{\vartheta}}}{\partial \rho_{i,j,k}^\vartheta} &= \frac{\partial G_v^{\hat{\vartheta}}}{\partial \phi^{\hat{\vartheta}}} \frac{\partial \phi^{\hat{\vartheta}}}{\partial \mathcal{X}^\vartheta} \frac{\partial \mathcal{X}^\vartheta}{\partial \rho_{i,j,k}^\vartheta} = \dots \\ &\begin{cases} \frac{1}{|\Omega|} \int_{\Omega} \left(\prod_{\lambda=1, \lambda \neq \vartheta}^{\hat{\vartheta}} \mathcal{X}^\lambda \prod_{\lambda=\hat{\vartheta}+1}^{\Theta} (1-\mathcal{X}^\lambda) R_{i,j,k}^{p,q,r}(\xi,\eta,\zeta) \psi(\rho_{i,j,k}^\vartheta) \right) v_0 d\Omega & \text{if } \vartheta \leq \hat{\vartheta} \\ -\frac{1}{|\Omega|} \int_{\Omega} \left(\prod_{\lambda=1}^{\hat{\vartheta}} \mathcal{X}^\lambda \prod_{\lambda=\hat{\vartheta}+1, \lambda \neq \vartheta}^{\Theta} (1-\mathcal{X}^\lambda) R_{i,j,k}^{p,q,r}(\xi,\eta,\zeta) \psi(\rho_{i,j,k}^\vartheta) \right) v_0 d\Omega & \text{if } \vartheta > \hat{\vartheta} \end{cases} \end{aligned} \quad (6-14)$$

It can be seen that the first-order derivatives of the objective and constraint functions are strongly dependent on the NURBS basis functions at the Gauss quadrature points and the Shepard function at the control points. The NURBS basis functions and Shepard function only depend on the spatial locations of the corresponding points and keep unchanged during the optimization. Hence, they can be pre-stored without using additional storage space, and the sensitivity analysis of the objective is cost-effective. The method of moving asymptotes (MMA) [72] is used to evolve design variables in the next numerical examples.

6.3 Numerical implementations

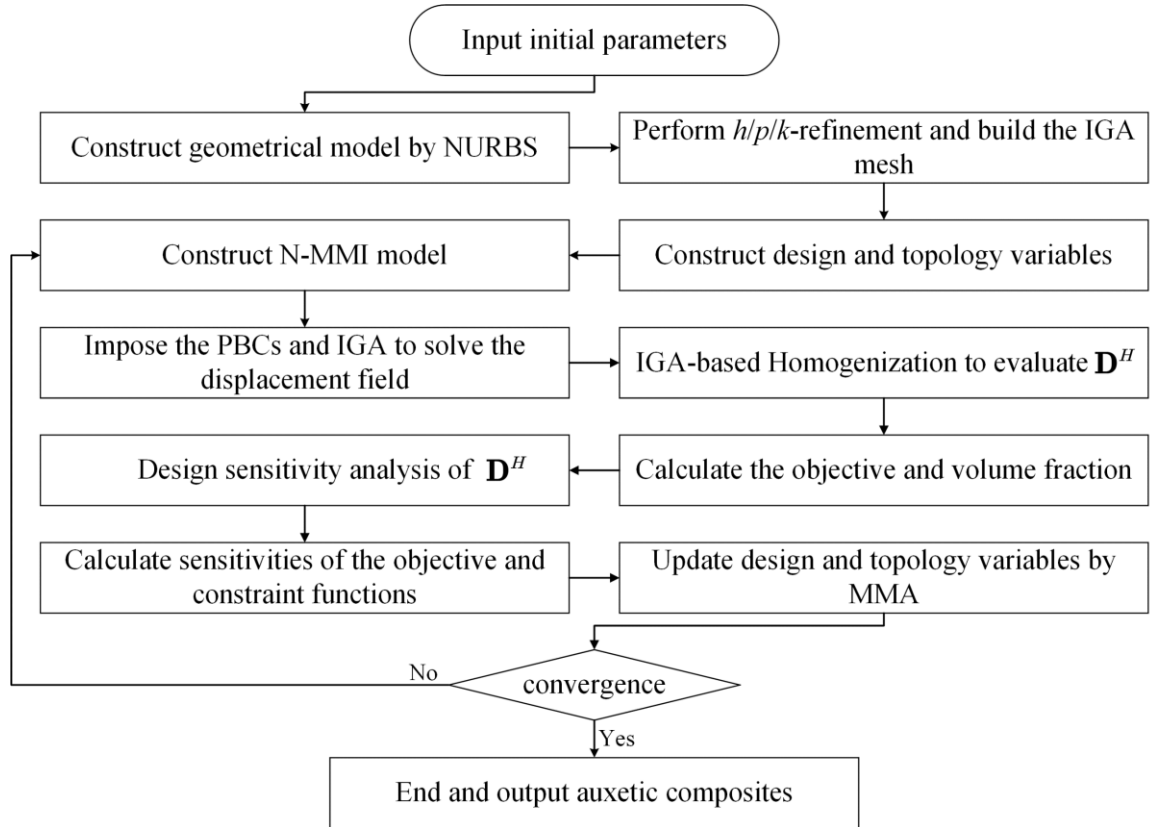


Figure 6-3 The flowchart of the ITO formulation for auxetic composites

As shown in Figure 6-3, a flowchart in detail of the ITO formulation for the optimization of auxetic composites is provided, and the key steps of the optimization are involved into the

following components: the geometry parametrization and then discretization, respectively, the construction of the fields of design variables and the sets of topology variables for multiple materials, the imposing of the periodic boundary conditions and the homogenization to predict the effective elastic tensor, the calculation of the objective function and volume fractions of all materials, the design sensitivity analysis and the evolving of design and topology variables.

6.4 Numerical Examples

In this section, several numerical examples are provided to demonstrate the effectiveness and efficiency of the ITO method for auxetic composites. Firstly, the discussions of 2D auxetic composites with two different materials are performed to show the basic features of the ITO method. Secondly, the ITO method is applied to optimize 2D auxetic composites with three distinct materials to demonstrate its superior effectiveness on the problem with multiple materials. Thirdly, the optimization of 3D auxetic composites are performed by the current ITO method to seek the novel 3D auxetic composite microstructures. Finally, the optimized 2D and 3D auxetic composites are simulated in the software ANSYS to show their auxetic behavior. In the numerical analysis, 3×3 (2D) or $3 \times 3 \times 3$ (3D) Gauss quadrature points are chosen in each IGA element. The dimensions of material microstructures in all directions are set to be 1. The penalty parameter γ is set to be 3. The constant parameter β in all numerical examples is equal to 0.03. Three “virtual” isotropic solid materials will be considered in next examples, and the related details are defined in Table 6-1.

Table 6-1 Three “virtual” isotropic solid materials

i	Materials	Young's modulus: E_0^i	Poisson's ratio ν
1	M1	10	0.3
2	M2	5	0.3
3	M3	3	0.3

6.4.1 2D auxetic composites

2D auxetic composites with two-material and three-material microstructures are considered, respectively. In the optimization of 2D auxetic composites, the design domain is a square with 1×1 . The NURBS surface is applied to parametrize the design domain, where the quadratic NURBS are chosen and the knot vectors are: $\Xi = \mathcal{H} = \{0, 0, 0, 0.01, \dots, 0.99, 1, 1, 1\}$. The corresponding IGA mesh for the design domain has 100×100 elements, and 101×101 (10202) control points are contained in the NURBS surface.

6.4.1.1 Auxetic composite microstructure with two materials

In this case, two distinct materials (**M1** and **M2**) are considered in the optimization of auxetic composites. The allowable volume fractions $V_0^{\vartheta} \left(\hat{\vartheta} = 1, 2 \right)$ for **M1** and **M2** materials are defined as 20% and 20%, respectively. Two kinds of variables should be defined in the N-MMI model, namely design variables $\mathcal{X}^{\vartheta} (\vartheta = 1, 2)$ and topology variables $\phi^{\vartheta} (\vartheta = 1, 2)$. It can be seen that each field of design variables is constructed by NURBS basis functions with the nodal design variables, which can be viewed as a response surface for nodal design variables in the domain. Moreover, a set of topology variables is expressed by a combination of all fields of design variables, which corresponds to a combination of all response surfaces. As shown in Figure 6-4 (a1) and (a2), the initial designs of the nodal design variables for two fields are defined, respectively, and the height direction shows the value of the nodal design variables. That is, $\mathcal{X}^{\vartheta} (\vartheta = 1, 2)$ at the control points. Based on the initial definition of the nodal design variables, the topology variables for two materials (**M1** and **M2**) at the Gauss quadrature points are shown in Figure 6-4 (b1) and (b2), respectively, namely $\phi^{\vartheta} (\vartheta = 1, 2)$ at the Gauss quadrature points. As already pointed out in the above section, the set of topology

variables is expressed by a combination of all response surfaces of the nodal design variables, and the corresponding surfaces of the sets of topology variables for two materials (**M1** and **M2**) are shown in Figure 6-4 (c1) and (c2), respectively, namely ϕ^ϑ ($\vartheta = 1, 2$) in the design domain. It should be noticed that the height direction in Figure 6-4 indicates the value of the corresponding variables.

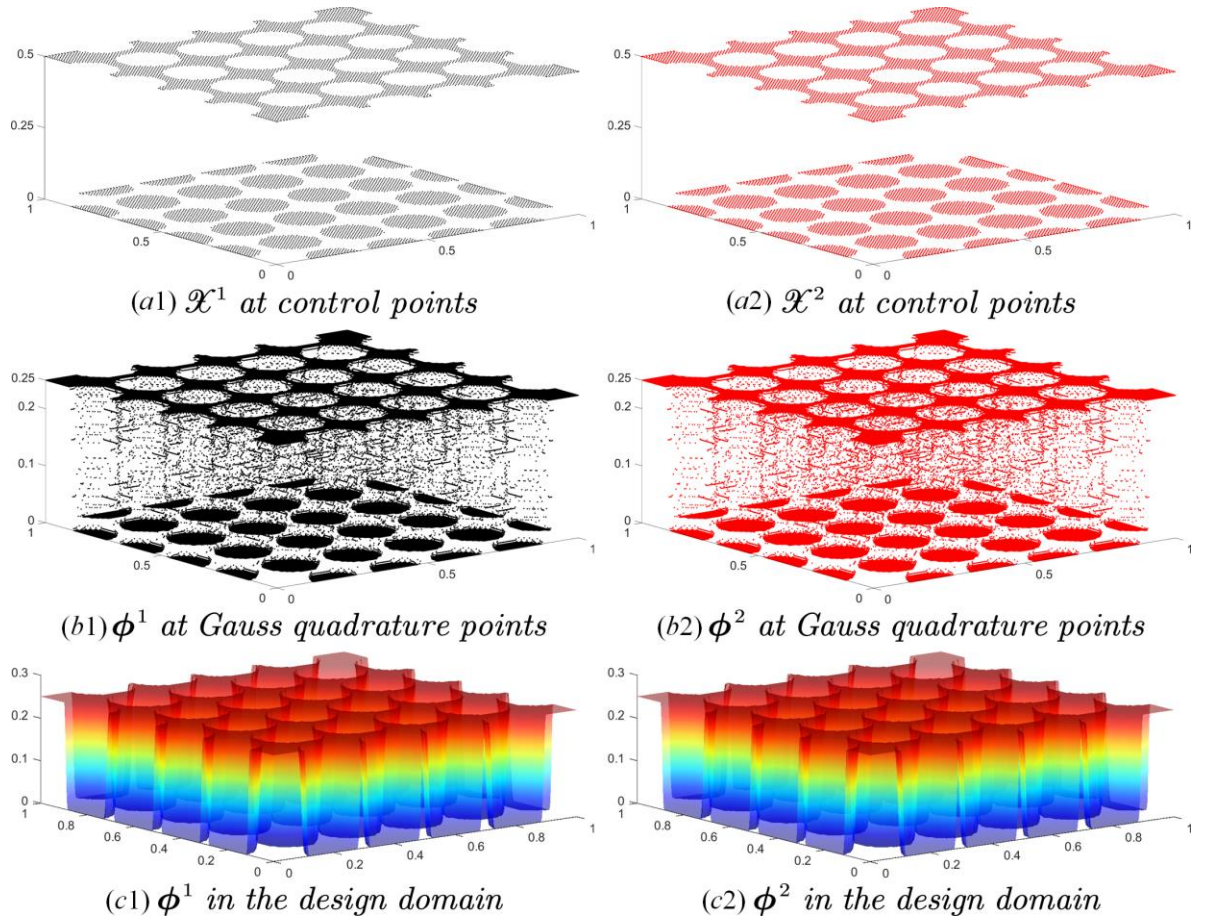


Figure 6-4 Initial design of the two-material microstructure

As shown in Figure 6-5, the optimized designs of ϕ^ϑ ($\vartheta = 1, 2$) for the overall layouts of **M1** and **M2** materials in the design domain are provided, including ϕ^ϑ ($\vartheta = 1, 2$) at the Gauss quadrature points in Figure 6-5 (a1) and (a2), respectively, and ϕ^ϑ ($\vartheta = 1, 2$) in the design domain shown in Figure 6-5 (b1) and (b2), respectively. It can be easily seen that the

optimized distributions of ϕ^ϑ ($\vartheta = 1, 2$) in the design domain are characterized with the desired smoothness and continuity, which offers more benefits to represent the evolution of the topologies for two materials. Meanwhile, it can be easily seen that the optimized values in the overall layouts of ϕ^ϑ ($\vartheta = 1, 2$) in the design domain are mostly identical to 0 or 1.

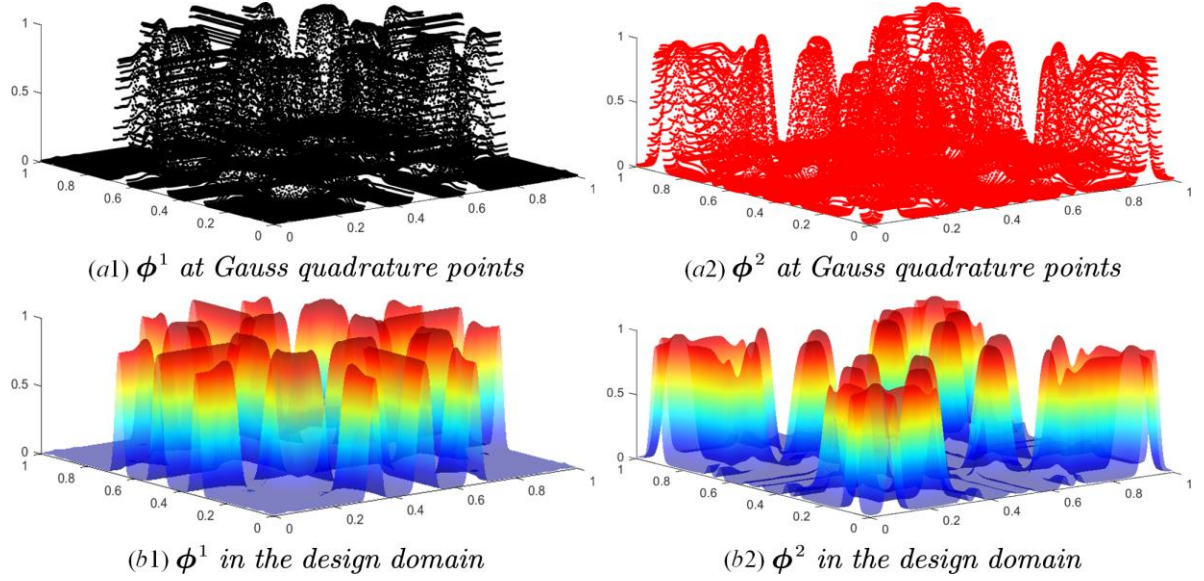


Figure 6-5 The optimized designs

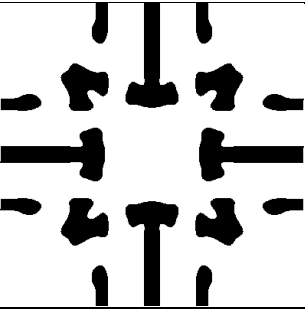
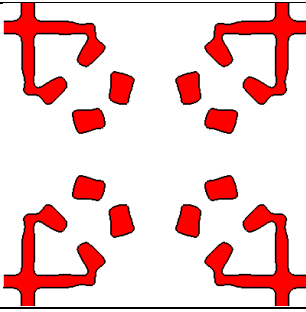
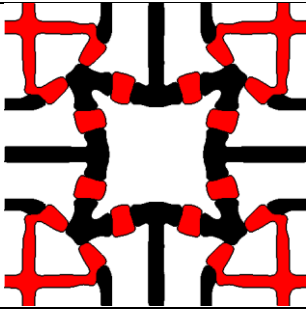
According to the optimized distributions of ϕ^ϑ ($\vartheta = 1, 2$) in the design domain shown in Figure 6-5 (b1) and (b2), a simple but efficient heuristic criterion is introduced to define the structural topology. The mathematical formula is defined, where ϕ_c is a constant. As we can see, the current heuristic scheme inherited the basic idea of the implicit boundary description model in LSM [14,15]. The structural boundary of the optimized composite microstructure is expressed by the iso-contour ϕ_c of ϕ^ϑ . ϕ^ϑ with the values higher than ϕ_c denotes the solids in the topology, and the values smaller than ϕ_c describes the voids. However, it should be noted that the current heuristic criterion is just a post-definition scheme to define the topology for the composite microstructure using the optimized distributions of ϕ^ϑ

($\vartheta = 1, 2$). The core of the proposed ITO method for auxetic composites is to seek the optimized ϕ^ϑ in the design domain, so that the composite microstructure can be featured with the auxetic behavior. Moreover, ϕ^ϑ ($\vartheta = 1, 2$) represents the distributions of materials in the design domain, which has the strict physical meanings in the optimization. This is the key difference between the current ITO method and the LSM.

$$\begin{cases} 0 \leq \phi(\xi, \eta) < \phi_c & \text{void} \\ \phi(\xi, \eta) = \phi_c & \text{boundary} \\ \phi_c < \phi(\xi, \eta) \leq 1 & \text{solid} \end{cases} \quad (6-15)$$

In the current work, the constant ϕ_c is set as 0.5, due to a basic fact that the values of ϕ^ϑ ($\vartheta = 1, 2$) in the design domain are mostly identical to 0 or 1, nearly ranging in two intervals $[0, 0.1]$ and $[0.9, 1]$. The optimized results of the auxetic composite microstructure are listed in Table 6-2, including the layouts of **M1** and **M2** materials, respectively, the topology of the auxetic composite microstructure, the effective elastic tensor, the corresponding volume fractions of **M1**, **M2** materials and the final topology and the final negative Poisson's ratio. As we can see, the total volume fraction of the topology is equal to 39.4%, almost nearly 40%. Hence, 0.5 is a relatively appropriate value to determine the topology of the auxetic composite microstructure. Meanwhile, the corresponding Poisson's ratio is equal to -0.606. As also clearly shown by the topology, the re-entrant mechanism is existed and formed by **M1** and **M2** materials, which can generate the auxetic behavior with the imposing of a load on the composite microstructure. Meanwhile, **M1** material with the larger Young's modulus can guarantee the auxetic composite microstructure with the much stiffer to afford the load. Hence, the auxetic composite can be featured with the multi-functional properties, which can offer more benefits for the applications in the engineering.

Table 6-2 The optimized 2D auxetic composite microstructure

M1 material	M2 material	The topology	\mathbf{D}^H
			$\begin{bmatrix} 0.66 & -0.40 & 0 \\ -0.40 & 0.66 & 0 \\ 0 & 0 & 0.0202 \end{bmatrix}$
V_0^1	V_0^2	V_0	ν
19.6%	19.8%	39.4%	-0.606

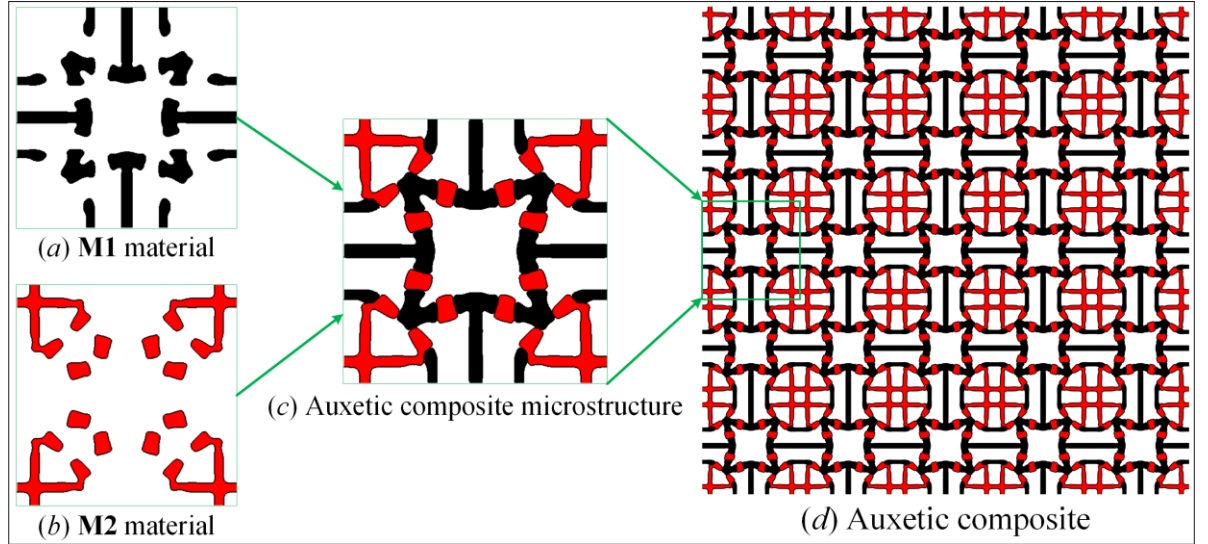


Figure 6-6 The optimized auxetic composite with two materials

Additionally, a systematic representation for the auxetic composite is also shown in Figure 6-6, where the 5×5 repetitive auxetic composite microstructures briefly describe the bulk auxetic composite. According to the auxetic composite in Figure 6-6 (d), the axial bars can be formed by **M1** and **M2** materials, which coincide with the initial observation of the auxetic composite with the more stiffness to afford the imposed force. Hence, we can confirm the superior effectiveness of the proposed ITO on seeking for auxetic composites.

Finally, the topology of the auxetic composite microstructure in Figure 6-6 has the smooth

structural boundaries and distinct interfaces between solids and voids, which might lower the numerical difficulties for the latter manufacturing phase. Moreover, several intermediate results of a combined distribution of ϕ^ϑ ($\vartheta = 1, 2$) in the design domain are shown in Figure 6-7. It can be easily seen that the proposed ITO method with the great effectiveness and efficiency to find the 2D auxetic composites with two materials. Meanwhile, the convergent histories of the objective function and volume fractions of two materials are shown in Figure 6-8, which shows the high stability and superior efficiency to find the optimized design.

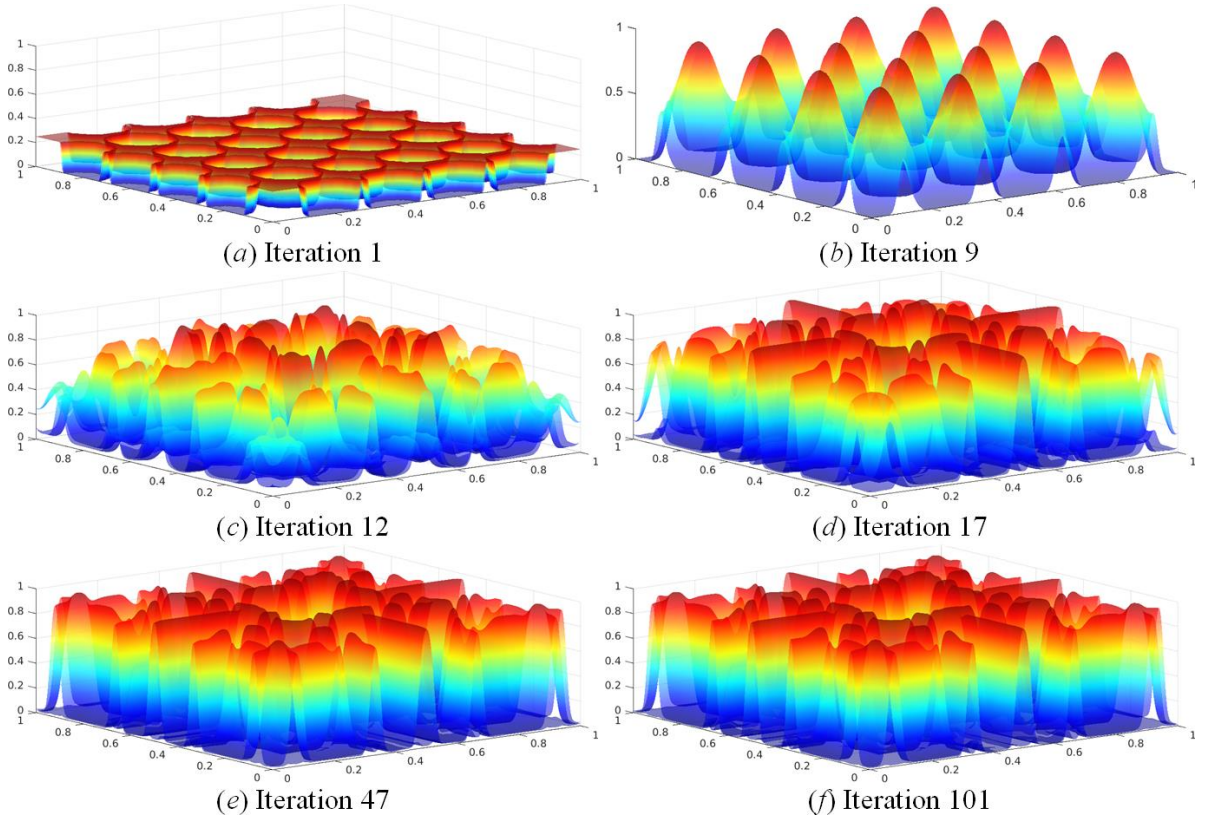


Figure 6-7 Intermediate results of the combined distributions

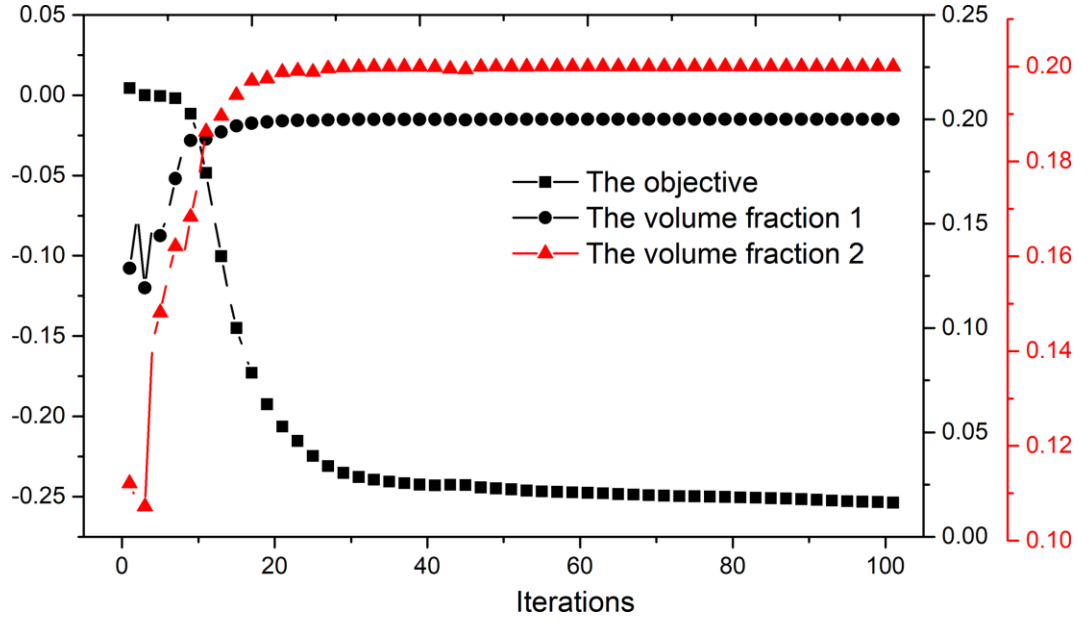


Figure 6-8 Convergent histories of the objective function and volume fractions

6.4.1.2 Auxetic composite microstructure with three materials

In this case, three distinct materials (**M1**, **M2** and **M3**) are considered in the optimization to show the ability of the proposed ITO method for auxetic composites with multiple materials, where the allowable volume fractions $V_0^{\hat{\vartheta}}$ ($\hat{\vartheta} = 1, 2, 3$) are defined as 15%, 15% and 10%, respectively. Three fields of design variables \mathcal{X}^{ϑ} ($\vartheta = 1, 2, 3$) and three sets of topology variables ϕ^{ϑ} ($\vartheta = 1, 2, 3$) for **M1**, **M2** and **M3** materials should be introduced, where the initial designs of the nodal design variables for **M1**, **M2** and **M3** materials are consistent with Figure 6-4 (*a1* and *a2*). **M3** material will be plotted with the green color in the final design.

The optimized designs of ϕ^{ϑ} ($\vartheta = 1, 2$ and 3) to represent the overall distributions of **M1**, **M2** and **M3** materials are displayed in Figure 6-9, including ϕ^{ϑ} ($\vartheta = 1, 2$ and 3) at the Gauss quadrature points and the surface of ϕ^{ϑ} ($\vartheta = 1, 2$ and 3) in the design domain, where the height direction denotes the values of the topology variables. Similarly, the overall distributions of ϕ^{ϑ} ($\vartheta = 1, 2$ and 3) are both featured with the sufficient smoothness and

continuity, which can provide more benefits for representing the topology in the latter and lower the numerical difficulties for the latter simulation. Moreover, the values of the topology variables are mostly distributed the lower and upper bounds, nearly 0 and 1.

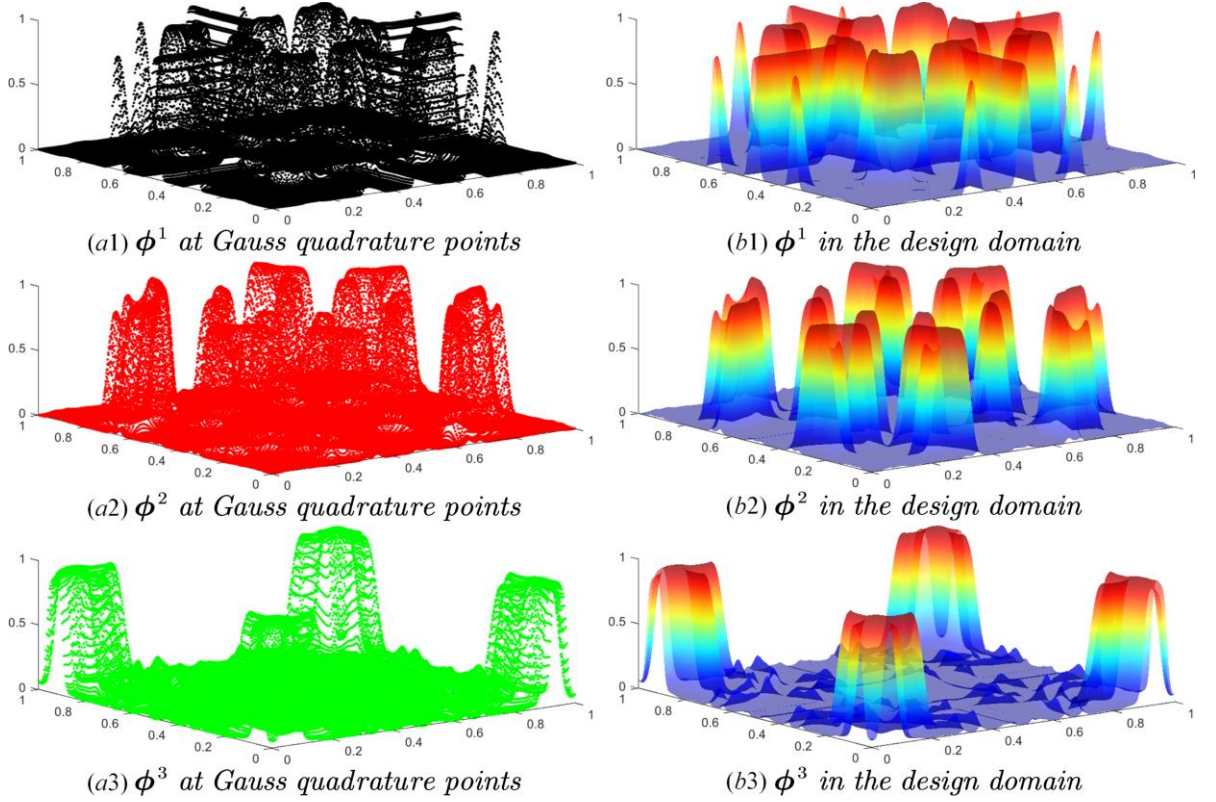


Figure 6-9 The optimized designs

The heuristic scheme to define the topology using the optimized designs of ϕ^ϑ ($\vartheta = 1, 2, 3$), given in Eq. (6-15), is also used here, where the iso-value of the surface ϕ^ϑ ($\vartheta = 1, 2, 3$) in the design domain is still set to be 0.5. As clearly listed in Table 6-3, the final topologies of **M1**, **M2**, **M3** materials and the design domain are included, and also the corresponding volume fractions are also provided. It can be easily found that the volume fractions of **M1**, **M2**, **M3** materials and the topology are mostly identical to the prescribed volume constraint, which presents the appropriateness of the choice for the constant ϕ_c . Meanwhile, the

effective elastic tensor of the final topology with three materials is given, and the negative Poisson's ratio is equal to -0.65. We can easily see that the auxetic composite with three materials in Table 6-3 has the lower negative Poisson ratio, and the composite will have the stronger auxetic behavior. According to the details of **M1**, **M2**, **M3** materials given in Table 6-1, **M3** material has the smallest Young's modulus, and it is much softer than both **M1** and **M2** materials. Introducing the softer material in the design of auxetic composites can be beneficial to improve the degree of the auxetic behavior. However, the stiffness performance of the auxetic design will be reduced to some extent, directly observing from the homogenized elastic tensor (the elements in diagonal are smaller than the corresponding value in Table 6-2: $0.534 < 0.66$). The overall layouts of **M1**, **M2**, **M3** materials in the final topology can also display this characteristic, where the axial bars to mainly afford the load have the M3 material compared to the auxetic composite in Figure 6-6. Additionally, it can be easily seen that the final topology of the auxetic composite microstructure has the smooth structural boundaries and distinct interfaces between solids and voids. Hence, we can confirm that the ITO method has the superior capability to optimize the auxetic composites with multiple materials.

Moreover, we also provide a systematic description about the auxetic composite, shown in Figure 6-10, where the 5×5 repetitive auxetic microstructures briefly represent the auxetic composite. Based on the periodic layout of the auxetic composite microstructure shown in Figure 6-10 (c), we can randomly extract any types of auxetic composite microstructures with different topologies, shown in Figure 6-10 (e). It is noted that all extracted microstructures have the same effective elastic tensor of the auxetic composite microstructure, displayed in Figure 6-10 (c).

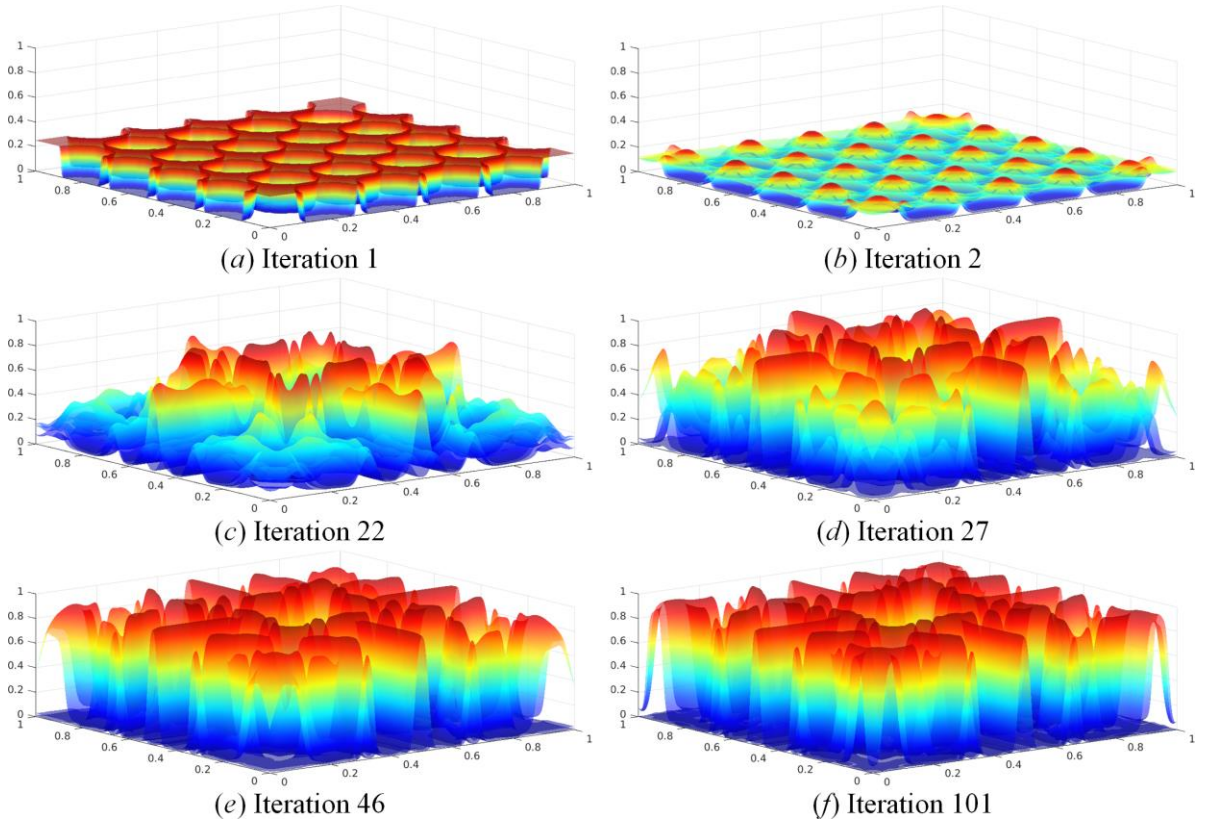


Figure 6-12 Intermediate results of the combined distributions

Additionally, the convergent histories of the objective function and volume fractions of three materials are shown in Figure 6-11, and the intermediate results of the combined distribution of all ϕ^ϑ ($\vartheta = 1, 2$ and 3) are also provided to show the details of the convergence. As we can see, the optimization for the auxetic composite with three materials is very stable and smooth, the optimized distributions of ϕ^ϑ for **M1**, **M2** and **M3** materials can be quickly found using the proposed ITO method, which can demonstrate its superior effectiveness and efficiency on the optimization of auxetic composites.

6.4.2 3D auxetic composite

In this section, the optimization of 3D auxetic composites with two materials is considered using the ITO method, where **M1** and **M2** distinct materials are available in the current

example. The allowable volume fractions of **M1** and **M2** materials are defined to be 25% and 20%, respectively. As far as 3D microstructure, the design domain is a cubic with the size $1 \times 1 \times 1$, as shown in Figure 6-13 (a). The NURBS solid is used to parametrize the design domain, and the quadratic NURBS basis functions are adopted, and the knot vectors in three parametric directions are defined as $\Xi = \mathcal{H} = \mathcal{Z} = \{0, 0, 0, 0.417, \dots, 0.9583, 1, 1, 1\}$. The solid and IGA mesh are shown in Figure 6-13 (b) and (c), respectively. The IGA mesh for the design domain has $24 \times 24 \times 24$ elements, and $26 \times 26 \times 26$ control points are included in the NURBS solid. In the IGA, an element will contain $3 \times 3 \times 3$ Gauss quadrature points, and the total number of the Gauss quadrature points is equal to $72 \times 72 \times 72$. It is hard to display the 4D response surface of ϕ^ϑ ($\vartheta = 1, 2$ and 3) in spatial. Currently, we only display the corresponding iso-surfaces, and the iso-value ϕ_e is still equal to 0.5. The initial nodal densities $\rho_{i,j,k}^\vartheta$ are all defined as 0.5, and with a series of homogeneously distributed holes in the design domain.

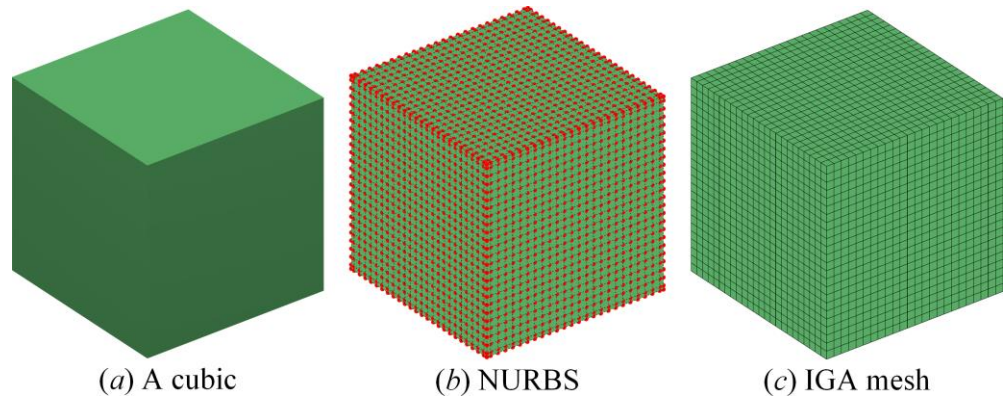
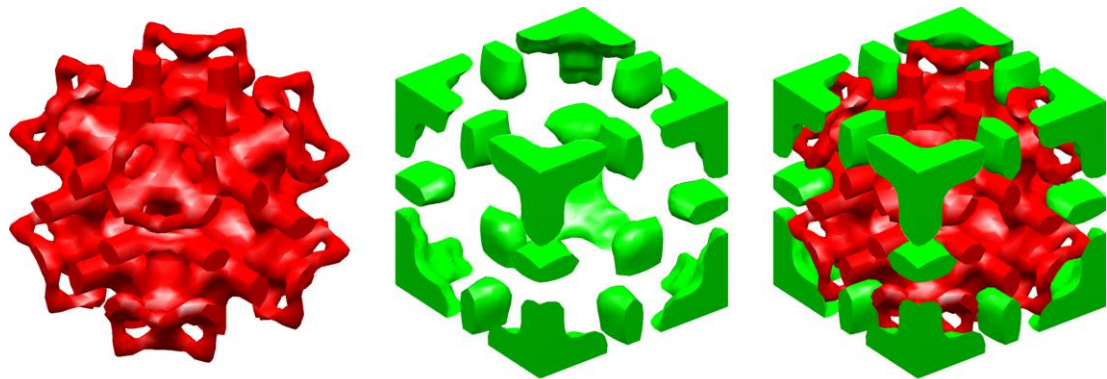


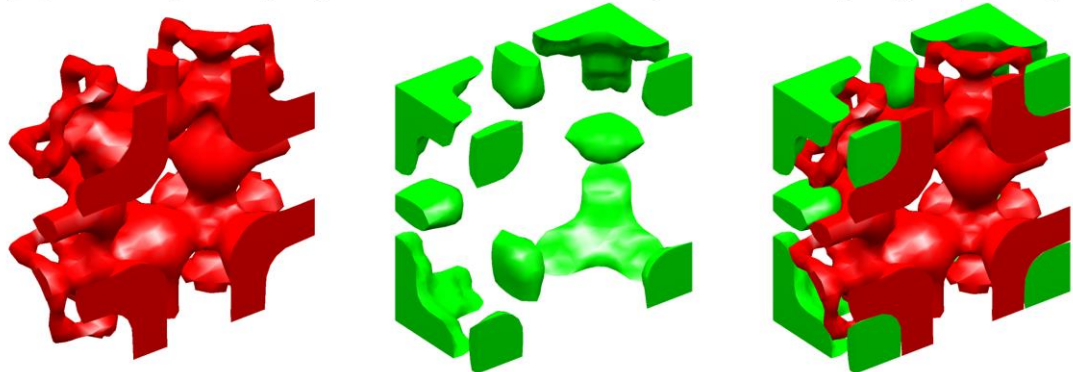
Figure 6-13 The 3D material microstructure

As shown in Figure 6-14, a 3D auxetic composite microstructure with **M1** and **M2** materials is provided, where the topologies of **M1** and **M2** materials, the corresponding cross-sectional views of them, the final topology of the 3D auxetic composite microstructure and its

corresponding cross-sectional view. As we can see, the optimized topology of the 3D auxetic composite microstructure is characterized with the smooth structural boundaries and distinct interfaces between the solids and voids, also existed in different phases. Meanwhile, the $3 \times 3 \times 3$ material microstructures briefly represent a 3D auxetic composite with the periodicity of material microstructures. In order to show the interior information, its cross-sectional view is also displayed in Figure 6-15, with the smooth and continuous boundaries. Based on the details to represent the 3D auxetic composite microstructure in Figure 6-14 and Figure 6-15, an auxetic deformation mechanism is formed by the distribution of **M1** material (red color in Figure 6-14 and Figure 6-15), and the **M2** material provides the stiffness for the whole 3D auxetic composite microstructure. Based on the qualitative analysis, a 3D auxetic composite with the negative Poisson's ratio and stiffness can be effectively obtained by the ITO method.



(a1, a2 and a3) The topologies of **M1** and **M2** materials, and the final topology respectively.



(b1, b2 and b3) Cross-sectional views of (a1, a2 and a3), respectively.

Figure 6-14 The optimized topology of 3D auxetic composite 1 with two materials

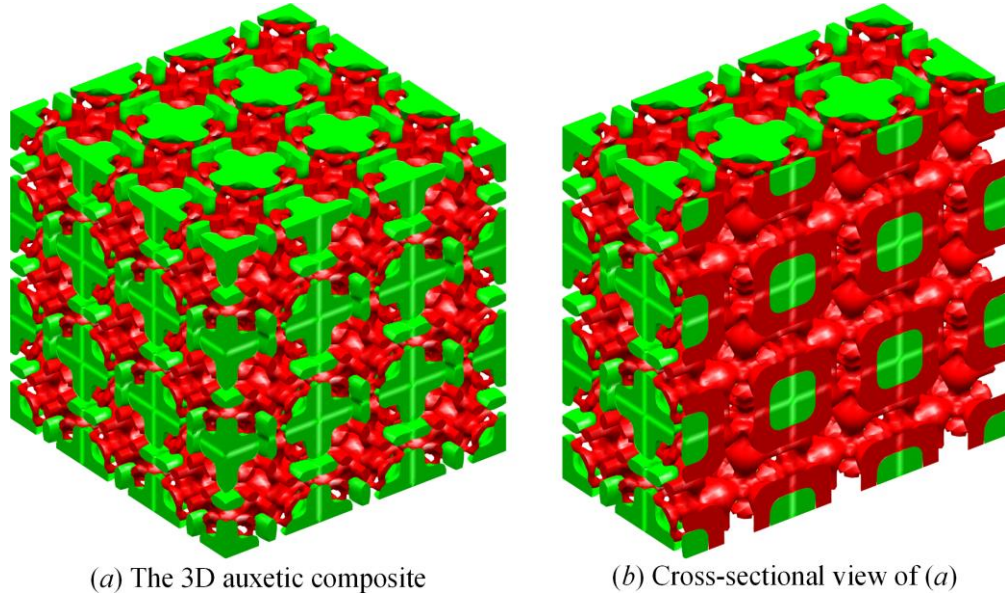


Figure 6-15 The details of the 3D auxetic composite No.1 with $3 \times 3 \times 3$ microstructures

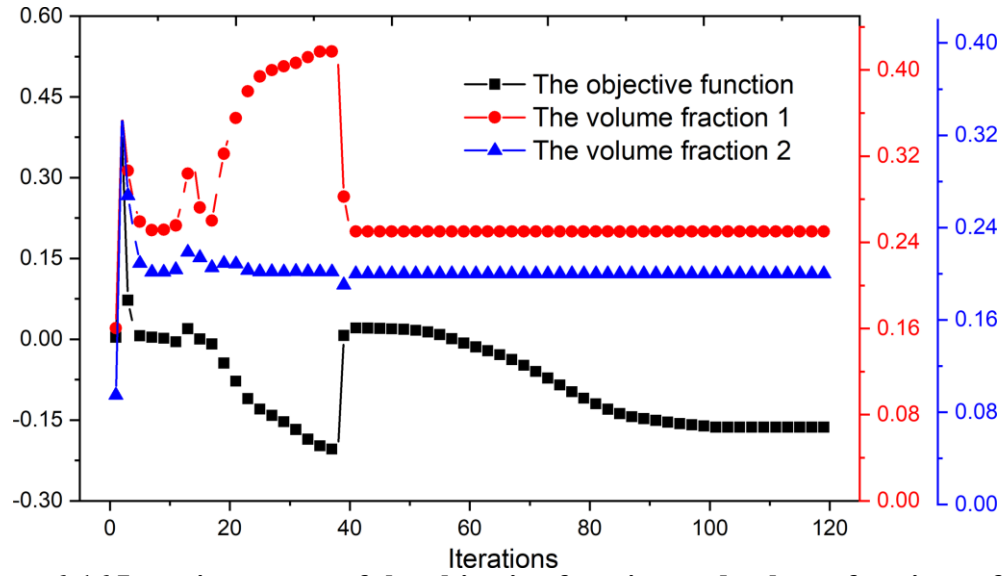


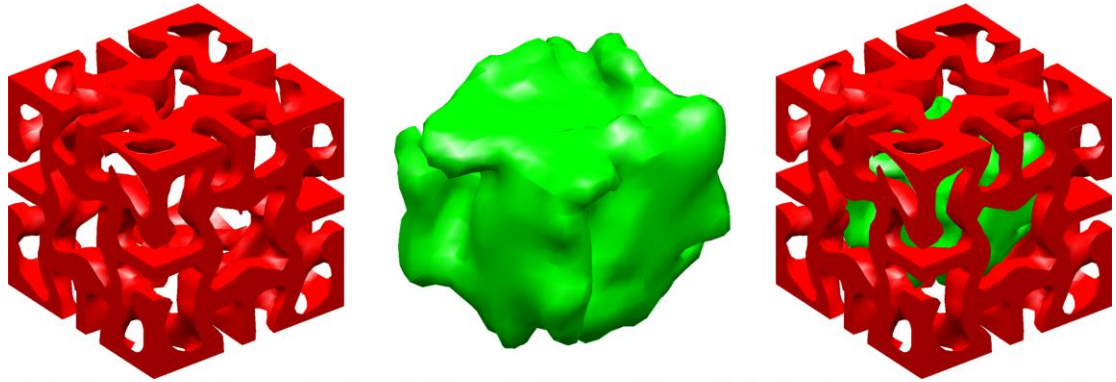
Figure 6-16 Iterative curves of the objective function and volume fractions of two materials

Meanwhile, we also provide the convergent histories of the objective function and volume fractions of two materials, shown in Figure 6-16. As we can see, the optimization of the 3D auxetic composite microstructure is much more difficult than 2D optimization, particularly in the former iterations, mainly due to an increasing number of design freedoms for 3D problem. It can be easily seen that the former iterations (nearly 40 steps) intends to find a 3D auxetic

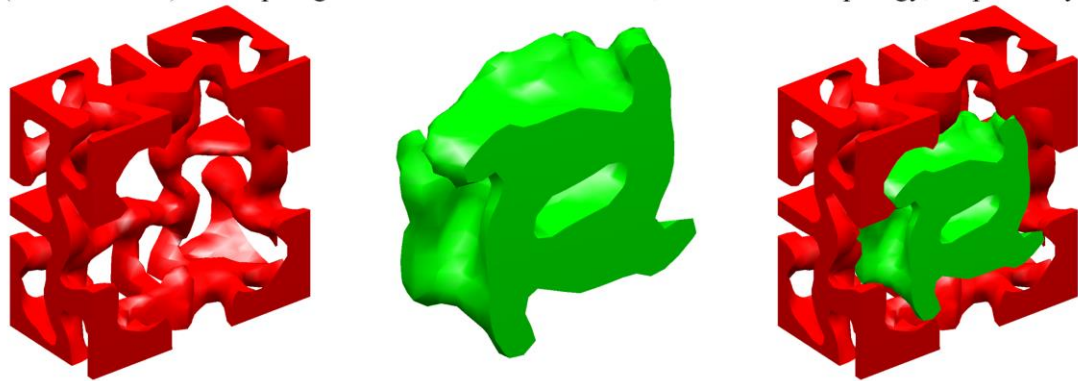
microstructure, but cannot maintain the prescribed volume constraint. After the 3D auxetic composite microstructure is obtained, the volume constraints of two materials quickly reach the prescribed values (25% and 20%), respectively, and the latter process of the objective and constraint functions is very stable. Hence, we can confirm that the proposed ITO method is effective and efficient on the optimization of the 3D auxetic composite with two materials.

The homogenized elastic tensor of the 3D auxetic composite microstructure is listed in the second row and the first column of Table 6-4, and its corresponding negative Poisson's ratio is equal to -0.0852. Hence, the optimized 3D composite microstructure shown in Figure 6-14 and Figure 6-15 is featured with the auxetic behavior based on the quantitative computation. Additionally, it is known that the micro-structured materials design is extensively dependent on the design parameters, like the initial design of the parameters in the optimization and etc., due to the non-uniqueness of the micro-architected materials design [79,140,146]. Here, in order to seek for many novel 3D auxetic composites, we have performed other three cases. As shown in Figure 6-17 to Figure 6-22, the optimized auxetic composites No.2 to No. 4 are provided, respectively, where the auxetic composite No. 2 is shown in Figure 6-17 and Figure 6-18, and the auxetic composite No. 3 is given in Figure 6-19 and Figure 6-20, and the auxetic composite No. 4 is presented in Figure 6-21 and Figure 6-22. In all numerical results, the topologies of all materials and their cross-sectional views, the topology of the 3D auxetic composite microstructure and its cross-sectional view, the topology of 3D auxetic composite with $3 \times 3 \times 3$ microstructures and its cross-sectional view are all provided. The corresponding homogenized elastic tensors of four auxetic composites are also listed in Table 6-4, where the Poisson's ratio of the 3D auxetic composites No.3 and No.4 are equal to -0.078 and -0.076, respectively. The auxetic composite No. 3 is periodically generated by an anisotropic material

microstructure, where the auxetic composite microstructure has different negative Poisson's ratio in different axial directions. Hence, a series of novel auxetic composites can be achieved using the proposed ITO method, which can perfectly present its effectiveness and efficiency on solving the 3D problem to seek for 3D auxetic composite microstructures.

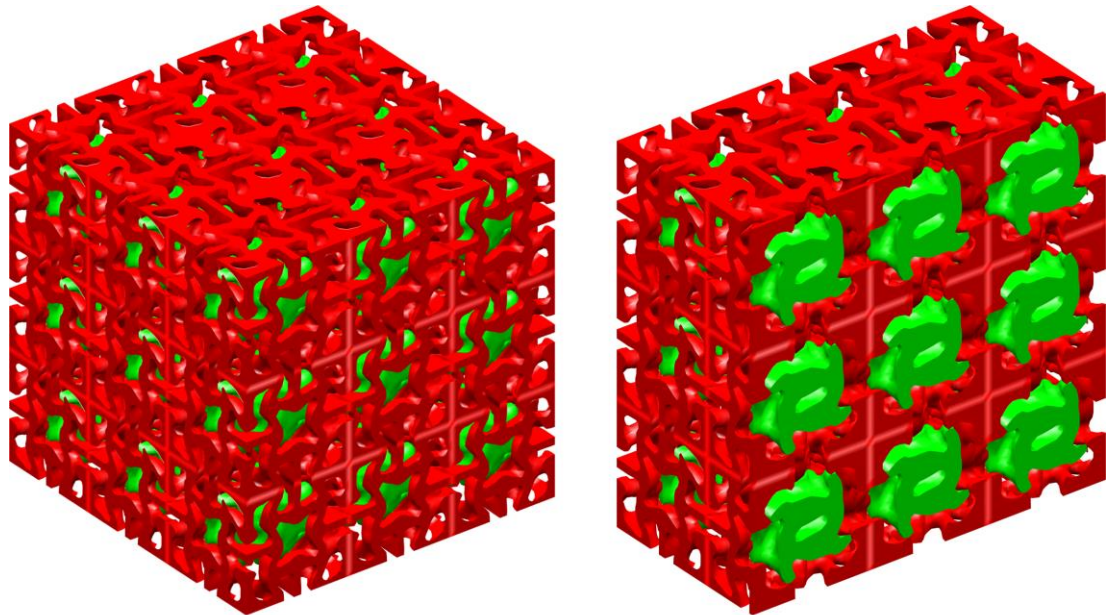


(a_1 , a_2 and a_3) The topologies of **M1** and **M2** materials, and the final topology, respectively.



(b_1 , b_2 and b_3) Cross-sectional views of (a_1 , a_2 and a_3), respectively.

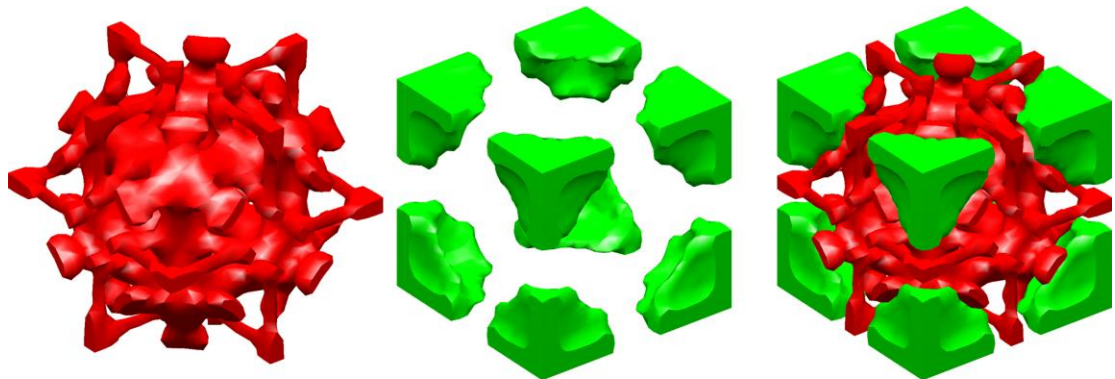
Figure 6-17 The optimized topology of 3D auxetic composite 2 with two materials



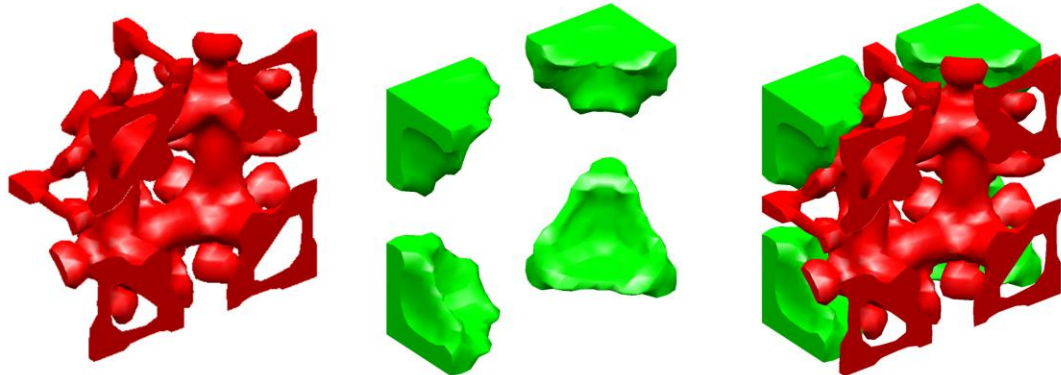
(a) The 3D auxetic composite

(b) Cross-sectional view of (a)

Figure 6-18 The details of the 3D auxetic composite No.2 with $3 \times 3 \times 3$ microstructures

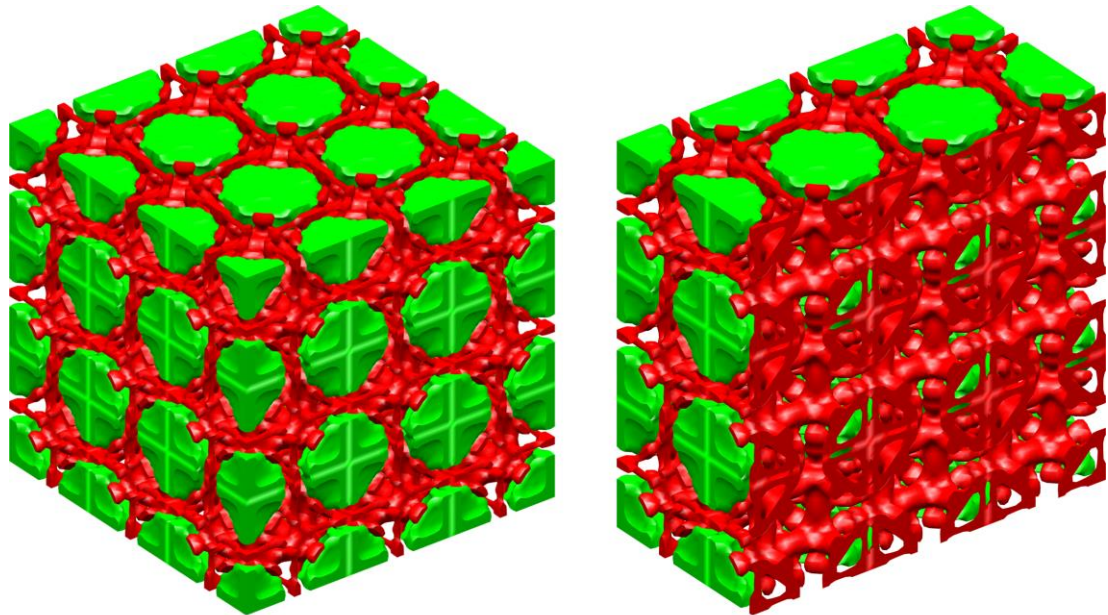


(a1, a2 and a3) The topologies of **M1** and **M2** materials, and the final topology respectively.



(b1, b2 and b3) Cross-sectional views of (a1, a2 and a3), respectively.

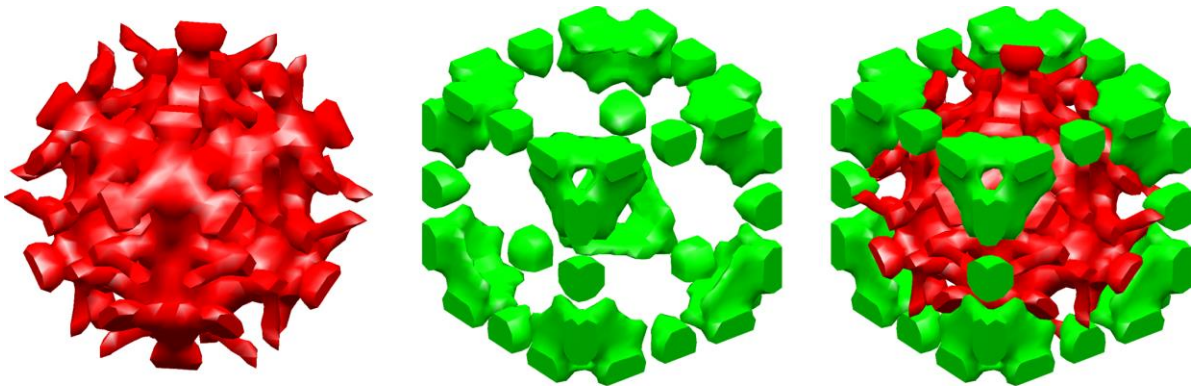
Figure 6-19 The optimized topology of 3D auxetic composite No.3 with two materials



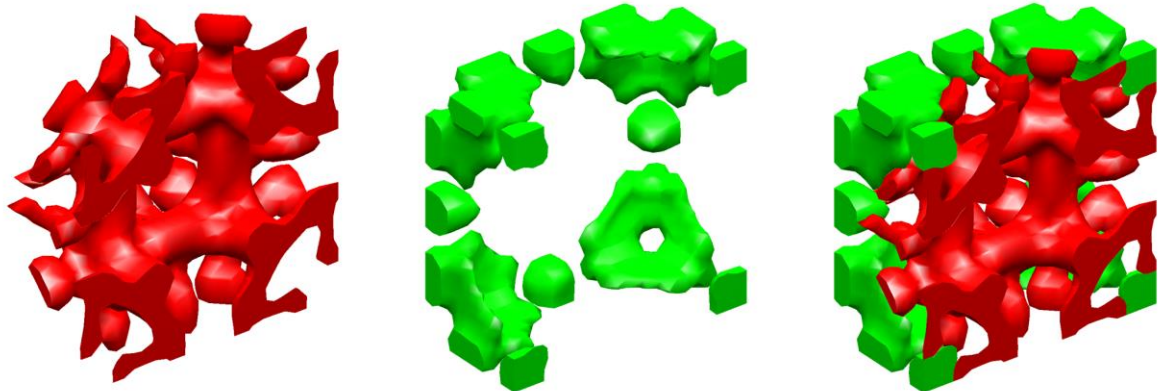
(a) The 3D auxetic composite

(b) Cross-sectional view of (a)

Figure 6-20 The details of the 3D auxetic composite No.3 with $3 \times 3 \times 3$ microstructures

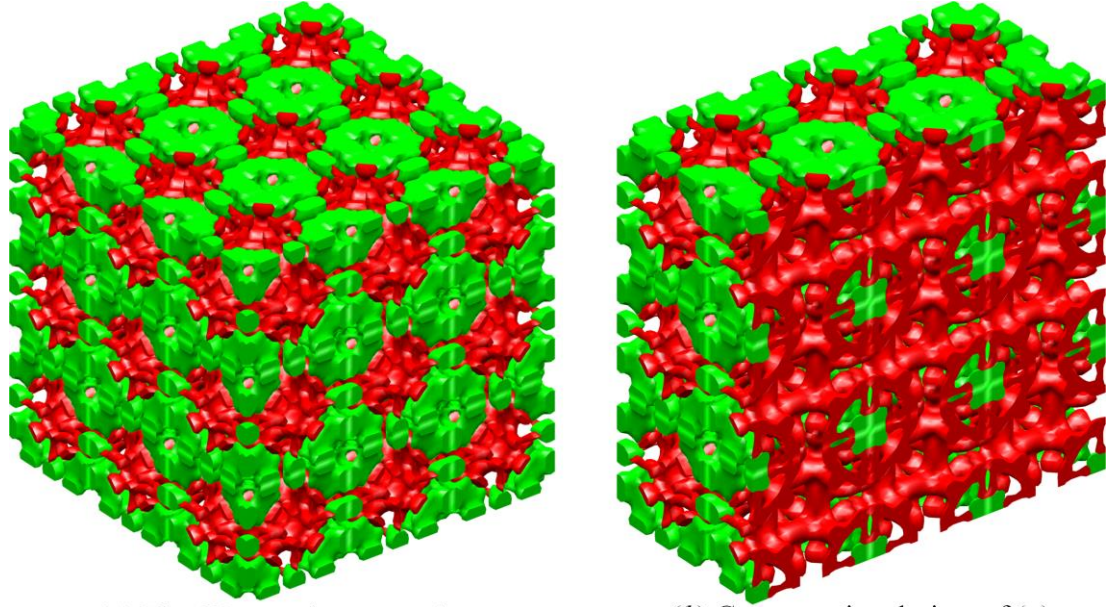


(a1, a2 and a3) The topologies of **M1** and **M2** materials, and the final topology respectively.



(b1, b2 and b3) Cross-sectional views of (a1, a2 and a3), respectively.

Figure 6-21 The optimized topology of 3D auxetic composite No.4 with two materials



(a) The 3D auxetic composite

(b) Cross-sectional view of (a)

Figure 6-22 The details of the 3D auxetic composite No.4 with 3×3×3 microstructures

Table 6-4 Homogenized elastic tensors of four auxetic composites

3D Auxetic composite No. 1						3D Auxetic composite No. 2					
0.3192	-0.0272	-0.0272	0	0	0	0.3953	-0.112	-0.575	-0.0138	-0.0007	-0.0028
-0.0272	0.3192	-0.0272	0	0	0	-0.1112	0.382	-0.0481	0.0215	0.0019	-0.0031
-0.0272	-0.0272	0.3192	0	0	0	-0.0575	-0.048	0.4360	-0.005	0.003	0.0124
0	0	0	0.024	0	0	-0.0138	0.0215	-0.005	0.0752	0.0018	-0.0026
0	0	0	0	0.024	0	-0.0007	0.002	0.0003	0.0018	0.0728	0.001
0	0	0	0	0	0.024	-0.0028	-0.003	0.0124	-0.0026	0.001	0.0757
3D Auxetic composite No. 3						3D Auxetic composite No. 4					
0.422	-0.033	-0.033	0	0	0	0.496	-0.038	-0.038	0	0	0
-0.033	0.422	-0.033	0	0	0	-0.038	0.496	-0.038	0	0	0
-0.033	-0.033	0.422	0	0	0	-0.038	-0.038	0.496	0	0	0
0	0	0	0.034	0	0	0	0	0	0.0318	0	0
0	0	0	0	0.034	0	0	0	0	0	0.0318	0
0	0	0	0	0	0.034	0	0	0	0	0	0.0318

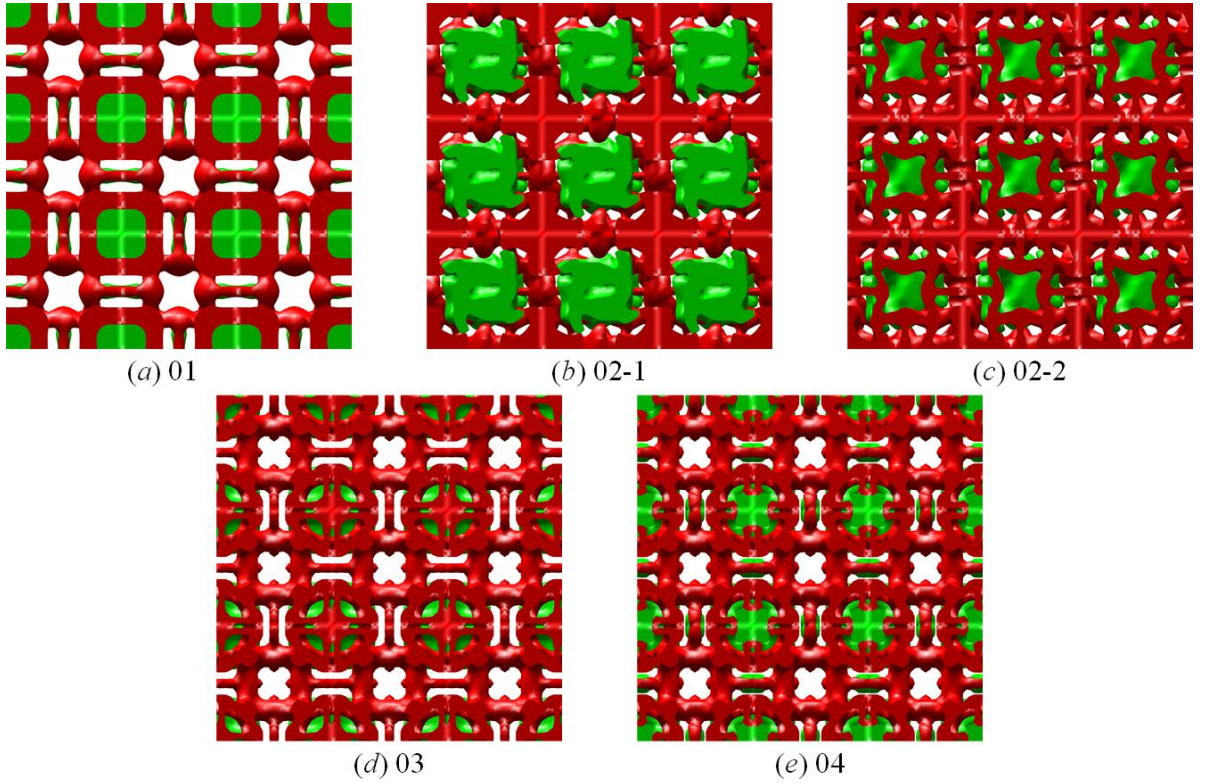


Figure 6-23 The deformation mechanisms of four auxetic composites

Finally, the deformation mechanisms of four 3D auxetic composites from No.1 to No. 4 are displayed in Figure 6-23. As we can see, the auxetic composites No. 1, No. 3 and No.4 can be classified into a same branch, where the auxetic behavior originates from the re-entrant deformation. However, the 3D auxetic composite has two different deformation mechanisms, shown in Figure 6-23 (b) and (c), respectively. The auxetic behavior is a combination of two deformation mechanisms, namely the re-entrant and chiral mechanisms. Moreover, the re-entrant type of deformation mechanism is formed by **M1** material and **M2** material forms the chiral deformation mechanism. The combination of both **M1** and **M2** materials can realize a reasonable loading transmission path in the topology of 3D auxetic composite No. 3. Hence, the effectiveness and efficiency of the proposed ITO method on the optimization of auxetic composites can be perfectly demonstrated.

6.4.3 Simulating validation based on ANSYS

In this section, the optimized auxetic composites in 2D and 3D are both simulated to validate the negative Poisson's ratio characteristic using the software ANSYS.

6.4.3.1 Simulation for 2D Auxetic composite

The optimized 2D auxetic composite with two materials, shown in Figure 6-6, is considered in this example. In Figure 6-24, the "STL.file" of the 2D auxetic composite microstructure in Figure 6-6 is firstly outputted from the Matlab software and then imported into the software ANSYS, which is converted into the solid geometry with the size of $10\text{cm} \times 10\text{cm} \times 0.1\text{cm}$ in the modeling module of ANSYS "SpaceClaim" and then distributed in spatial with a 5×5 periodicity. The periodic repetitive composite microstructures act as the auxetic composite in the latter simulation. The corresponding finite element mesh of the auxetic composite with the local view is also shown in Figure 6-24 (c).

As shown in Figure 6-25, four different boundary conditions are imposed on the 2D auxetic composite, namely Conditions 1 to 4. In Condition 1, the X-direction and Z-direction displacements of the left edge are fixed, respectively, namely the displacements equal to 0, shown in Figure 6-25 (a). Figure 6-25 (b) fixes the displacements of two points (plotted with the yellow color) located at the middle of the auxetic composite in all directions, which intends to avoid the rotation of the 2D auxetic composite with the imposing of the load. Condition 3 controls the displacements of the 2D auxetic composite in Z-direction, equal to 0, in order to make sure the deformation will be generated in the X-Y plane, shown in Figure 6-25 (c). Condition 4 is defined in Figure 6-25 (d), where a displacement 1mm along X^+ -direction is homogeneously imposed on the right edge.

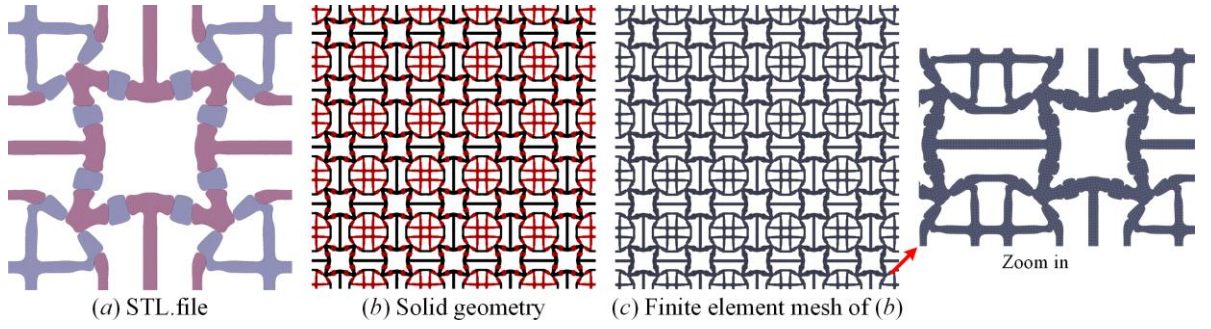


Figure 6-24 The details of the 2D auxetic composite

As displayed in Figure 6-26 (a) and (b), the displacements of the top and bottom edges are represented, respectively. The different of the average displacements on the top and bottom edges represents the deformation degree of the 2D auxetic composite, when a homogenous displacement is imposed on the edge. The mean value of the displacements on the top edge is equal to 0.302mm, and the average displacement of the bottom edge is equal to -0.302. Hence, the deformation of the 2D auxetic composite in Y direction is equal to 0.604mm. Based on the definition of the Poisson's ratio, and the Poisson's ratio of the 2D auxetic composite is equal to -0.604, which is identical to the value predicted by the IGA-based homogenization (-0.606). Meanwhile, the total deformation of the 2D auxetic composite is shown in Figure 6-26 (c), and the final view of the deformed auxetic composite is also displayed in Figure 6-26 (d), which can show the auxetic behavior of the optimized 2D auxetic composite.

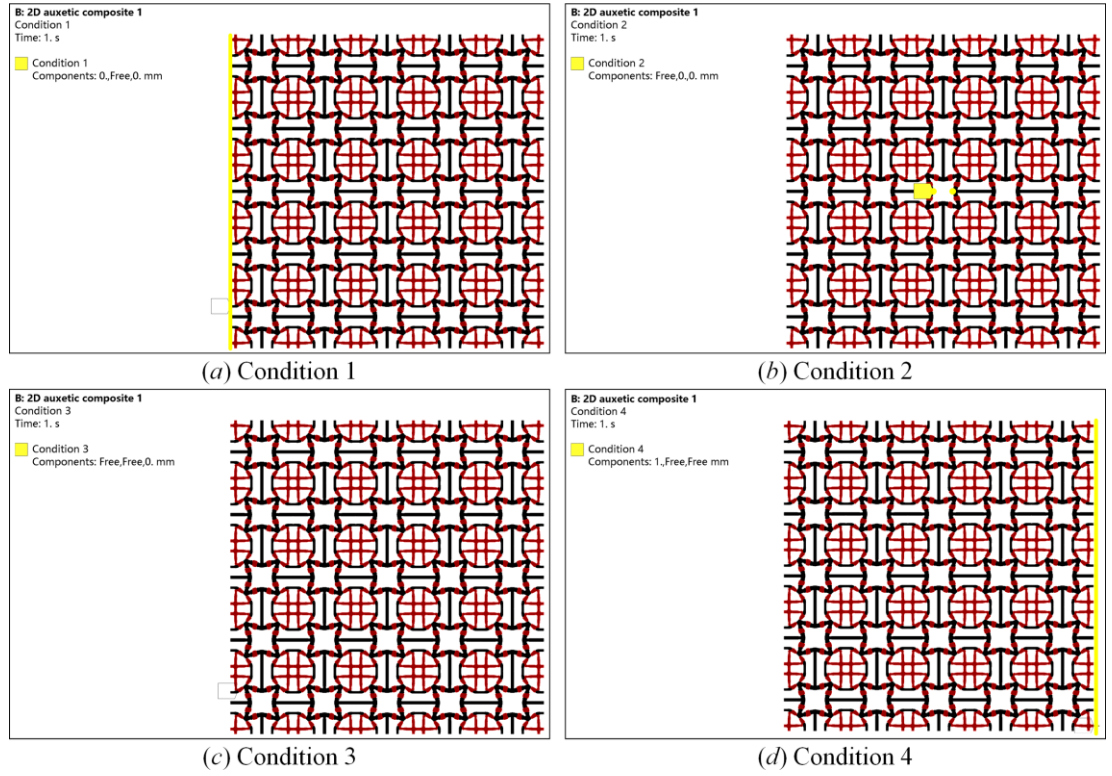


Figure 6-25 Boundary conditions imposed on the 2D auxetic composite

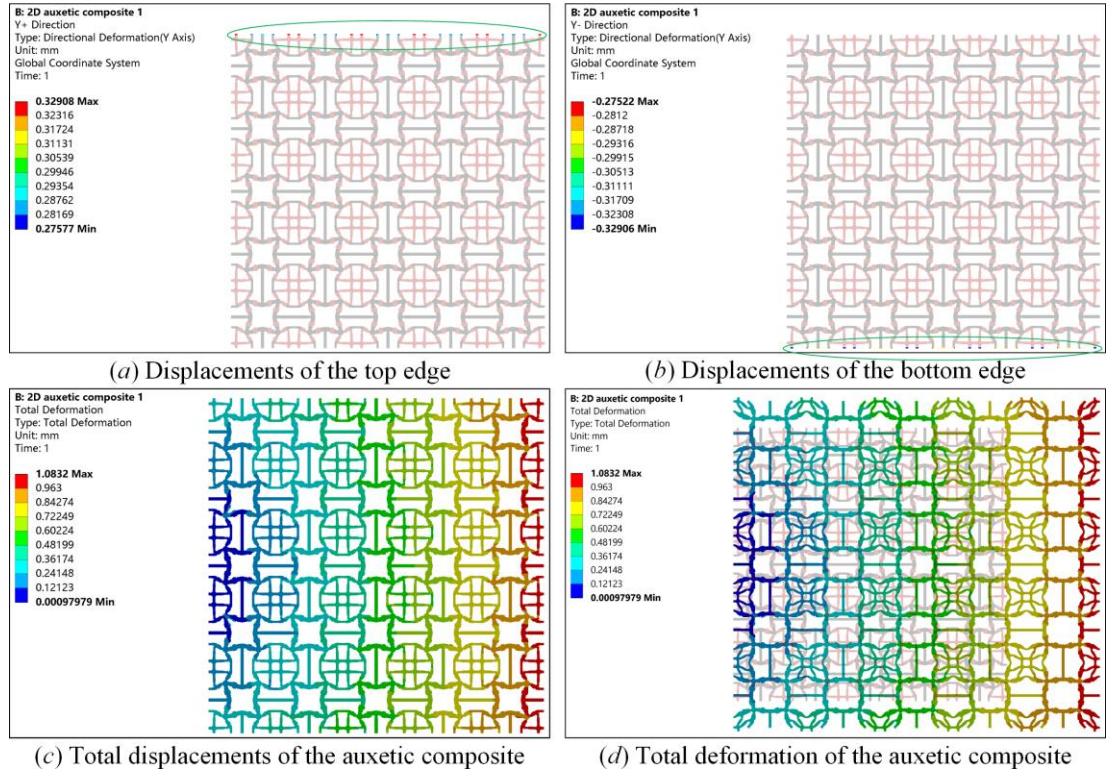


Figure 6-26 Displacement responses of the 2D auxetic composite

6.4.3.2 Simulation for the 3D Auxetic composite No.1

In this section, the numerical verification is performed for the 3D auxetic composite No.1 shown in Figure 6-15 using ANSYS platform. Based on the optimized result in Section 6.2, the STL files of the auxetic composite microstructure 1 is firstly outputted from the Matlab software, shown in Figure 6-27 (a) and then imported into the commercial software ANSYS. The STL files for the 3D auxetic composite microstructure 1 should be slightly modified in the modeling software SpaceClaim of ANSYS and converted into the solid geometries with $10 \times 10 \times 10 \text{ cm}$, displayed in Figure 6-27 (b). The 3D auxetic composite No.1 with the $3 \times 3 \times 3$ repetitive material microstructures will be considered in the simulation, and the corresponding solid geometry is shown in Figure 6-28 (a), and its finite element mesh with an enlarged view is given in Figure 6-28 (b).

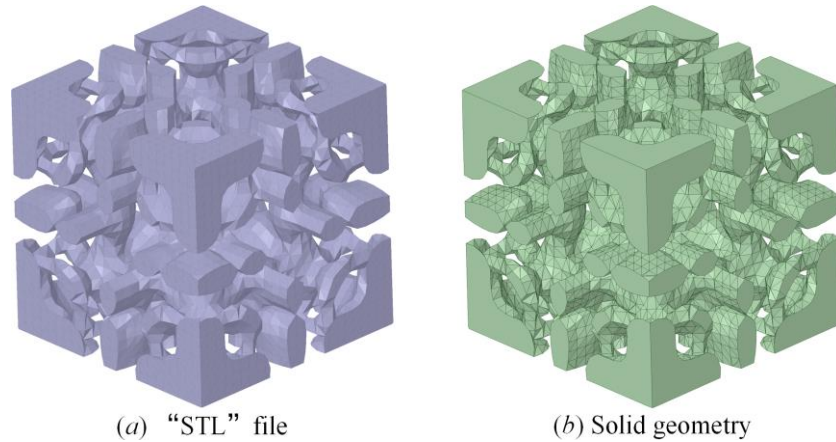


Figure 6-27 3D auxetic composite microstructure No.1

In the simulation, three different boundary conditions are imposed on 3D auxetic composite No.1. As shown in Figure 6-29 (a), the displacements of the surface A along Z-direction are fixed, and Condition 2 fixed two points located at the middle of the surface A to avoid the rotation of the auxetic composite No.1, given in Figure 6-29 (b). The displacement with 1mm

along Z direction is homogeneously imposed on the surface C in Condition 3, shown in Figure 6-29 (c). It should be noted that Surfaces A and C are opposite along Z direction. As shown in Figure 6-30, the displacements of the top and bottom surfaces in X direction are both provided. The difference of the average displacements at the top and bottom surfaces can be viewed as the deformation degree of the 3D auxetic composite No.1 in X direction. The average displacement on the bottom surface is equal to -0.0458mm , and the mean value of the displacements on the top surface is equal to $+0.0379\text{mm}$. Hence, the deformation of the auxetic composite No.1 in X direction is 0.0837 . According to the definition of the Poisson's ratio, the value is equal to -0.0837 . Hence, the simulated negative Poisson's ratio is mostly identical to the value evaluated by the IGA-based homogenization.

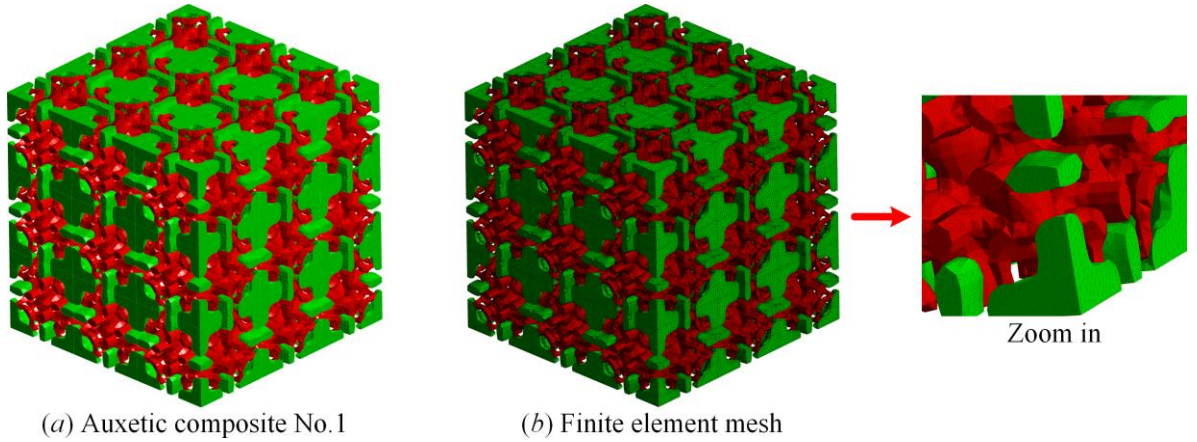


Figure 6-28 Auxetic composite No.1 and its finite element mesh with an enlarged view

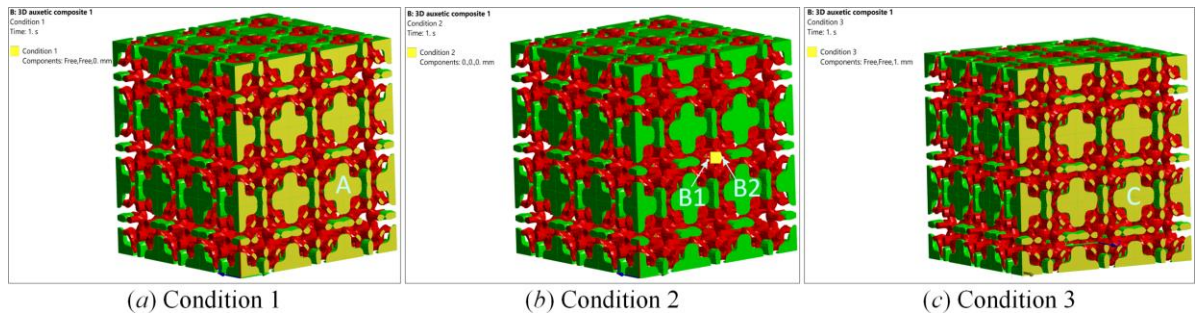
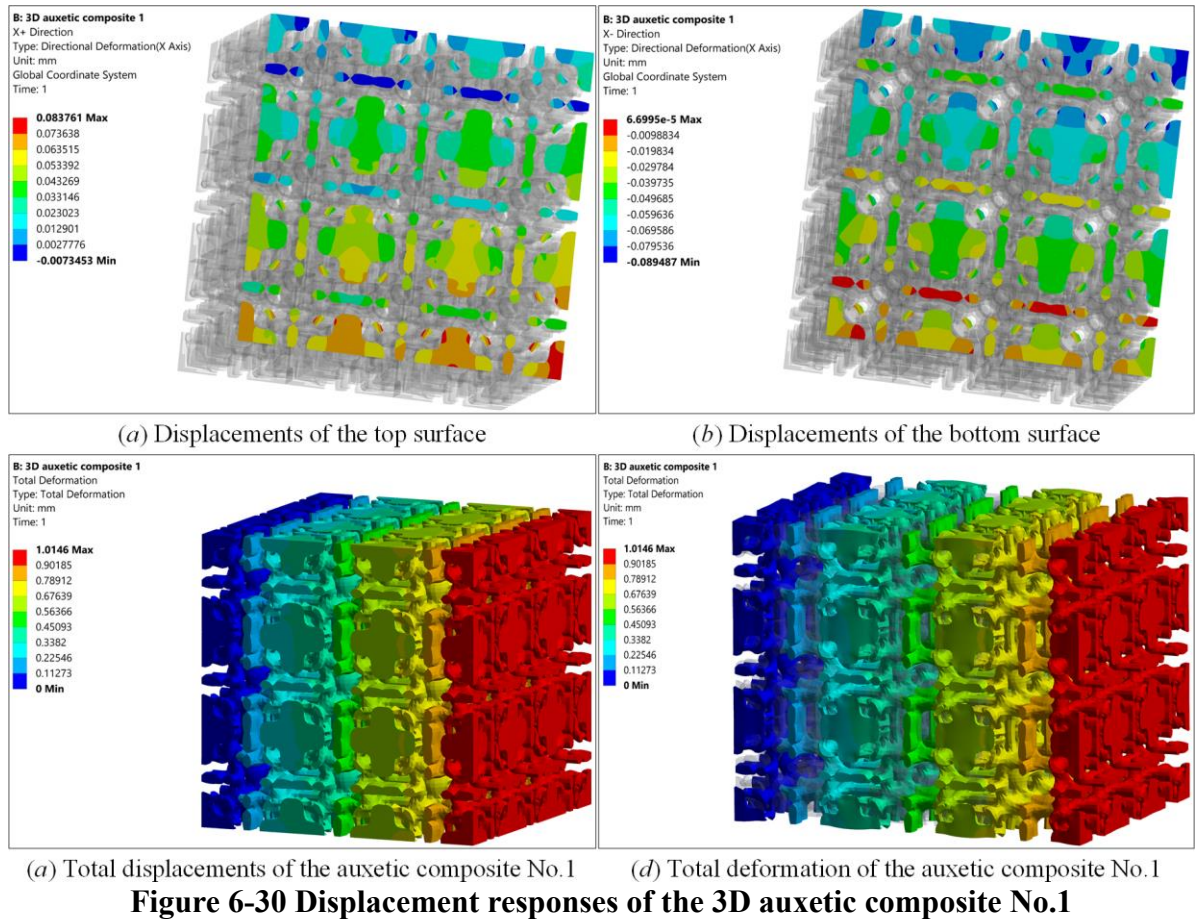


Figure 6-29 Boundary conditions imposed on the 3D auxetic composite No.1



6.5 Conclusions

In this chapter, an effective and efficient isogeometric topology optimization (ITO) method is proposed for the systematic design of auxetic composites, including 2D and 3D composite microstructures. In ITO method, an IGA-based EBHM is firstly developed, with the imposing of the periodic boundary formulation. Secondly, a N-MMI model is established to represent the evolving of multi-material topology. Finally, an ITO formulation is developed to optimize auxetic composites, where the objective is expressed as a combination of the homogenized elastic tensor. Several numerical examples are tested to show the effectiveness and efficiency of the ITO method. Firstly, a series of novel and interesting auxetic composites with properties in 2D and 3D can be achieved, which can present the superior capability of the ITO method. Secondly, the optimized auxetic composites are simulated in the software ANSYS to test the negative Poisson's ratio and show the auxetic behavior resulting from the re-entrant and chiral deformation mechanisms, respectively. Finally, the ITO method with the superior features might be naturally extended to other advanced problems, like micro-architected composites with multi-physical properties and novel findings in creating novel properties for artificial materials.

Chapter 7 Summary and prospects

7.1 Summary

In the current work, a novel Isogeometric Topology Optimization (ITO) method is proposed for the single-material structures with the more effectiveness and efficiency, and then a new Multi-material Isogeometric Topology Optimization (M-ITO) method with the effective N-MMI model is developed for the multi-material structures. Meanwhile, the currently proposed ITO and M-ITO methods are used to implement the rational design of auxetic metamaterials and auxetic composites, respectively.

In Chapter 2, we firstly provide a comprehensive review of several topology optimization methods and discuss the corresponding features of methods, also of the isogeometric topology optimization and address the existed research works for it, also of the ration design of auxetic metamaterials and composites with the brief descriptions about the multi-material topology optimization. The review shows that there are some important problems not well solved. For example, (1) several numerical artifacts are still existed in the current topology optimization works, like the zigzag and wavy boundaries, checkerboards, the local optimal designs and etc. These numerical issues will introduce several problems in the optimization and also the latter manufacturing; (2) The positive features of IGA has not been sufficiently used in material description models, like the representation of structural topology; (3) the lack of an effective topology optimization method for the rational design of auxetic metamaterials; (4) the lack of an effective topology optimization method for the rational design and realization of auxetic composites in 2D and 3D.

In Chapter 3, the development of a new ITO method for the optimization of the classic static compliance problems has been addressed, and several positive features are presented. several numerical examples in 2D and 3D are tested to demonstrate the effectiveness and efficiency of the proposed ITO method. It can be easily found that the DDF with the desired smoothness and continuity has a significant influence on the optimization of 2D and 3D structures with the rectangular design domain, the curved shape and the complex geometry. Meanwhile, the final topologies in all numerical examples are featured with smooth boundaries and distinct interfaces between solids and voids. The example for 3D structures can show the effectiveness of the ITO method and the topologically optimized 3D designs are prototyped using the SLS technique.

In Chapter 4, an efficient N-MMI model is developed for the representation of multiple materials and the computation of the multi-material properties, and then incorporated into the ITO to develop the M-ITO method for the structures with multiple materials. Several 2D and 3D numerical examples are performed to demonstrate the effectiveness of the M-ITO method with the N-MMI model. The formulation with multiple volume constraints is studied on the optimization of MBB beam with two materials and three materials. The formulation with the total mass constraint is studied to show the effectiveness of the M-ITO method on the multi-material optimization, and the effect of the properties of materials is also addressed. Finally, the effectiveness and utility of the M-ITO method on the curved structures and 3D structures is also presented.

In Chapter 5, the ITO method combined with the homogenization numerically implemented in the framework of IGA is employed to optimize auxetic metamaterials in both 2D and 3D,

and several novel and interesting auxetic microstructures can be found. As we can see, the key feature of the method is to optimize the DDF for microstructures with auxetic behavior, rather than the spatial arrangements of element densities. The optimized auxetics have smooth boundaries and distinct interfaces, which is beneficial to the manufacturing. Additionally, the ITO method is featured with the higher efficiency for 3D auxetic microstructures. A series of new and interesting auxetic microstructures can be achieved.

In Chapter 6, the M-ITO method is employed to discuss the topology optimization of auxetic composites and the IGA-based EBHM is applied to evaluate macroscopic effective properties of auxetic composites. A series of new and interesting auxetic composites microstructures in 2D and 3D can be achieved, which can present the superior capability of the ITO method. Secondly, the topologically optimized auxetic composites are simulated in the ANSYS to test the negative Poisson's ratio and show the auxetic behavior resulting from the re-entrant and chiral deformation mechanisms.

7.2 Prospects in future works

The future works need to be studied are outlined as follows:

Firstly, the effectiveness of the ITO method is discussed on the conventional static problems, namely the minimization of the structural mean compliance. The static compliance is an easy but classic problem to present the effectiveness of the ITO method. In the future works, the effectiveness of the ITO method on several different problems should be discussed, like the dynamic problems with the considerations of the frequency responses, the thermal problems, the nonlinear geometries, the nonlinear mechanics, the acoustics, the electromagnetics, also the fluids, and etc.

Secondly, IGA has more positive features in several problems, like the analysis of structural interface, the contact problem. Hence, it is more meaningful to apply for the ITO method to discuss the topology optimization considering the structural interface behaviors, and also the contact topology optimization problems. Additionally, the fracture resistance is also a critical problem and the ITO method might have several positive features on this problem.

Thirdly, additive manufacturing has obtained great promotion in recent years, due to its merits on solving the existed problems that conventional manufacturing cannot solved. On the other side, the technology of additive manufacturing also introduces some problems, for instance the overhang angles in the pre-printed structures, the minimum sizes of the structures and etc. Hence, how to consider the additive manufacturing constraints in the ITO method is also an important problem in the future work.

Finally, materials design is not only located at auxetic metamaterials. The current ITO method should be extended to other physical fields, such as the electromagnetic metamaterials, the acoustic metamaterials and also mechanical metamaterials. The capability of the ITO method on other metamaterials should be also addressed.

References

- [1] Bendsøe MP, Sigmund O. *Topology Optimization: Theory, Methods and Applications* 2003.
- [2] Bendsøe MP, Kikuchi N. Generating optimal topologies in structural design using a homogenization method. *Comput Methods Appl Mech Eng* 1988;71:197–224.
- [3] Sigmund O, Maute K. Topology optimization approaches. *Struct Multidiscip Optim* 2013;48:1031–55.
- [4] Rozvany GIN. A critical review of established methods of structural topology optimization. *Struct Multidiscip Optim* 2009;37:217–37.
- [5] van Dijk NP, Maute K, Langelaar M, van Keulen F. Level-set methods for structural topology optimization: a review. *Struct Multidiscip Optim* 2013;48:437–72.
- [6] Schmueser D, Goelke M. *Innovative Engineering Curricula and University Design Competition Applications of Altair OptiStruct and HyperStudy Structural Optimization CAE Tools*, Altair Engineering; 2013, p. 2013.
- [7] Michell AGM. The limits of economy of material in frame-structures. *London, Edinburgh, Dublin Philos Mag J Sci* 1904;8:589–97.
- [8] Cheng K-T, Olhoff N. An investigation concerning optimal design of solid elastic plates. *Int J Solids Struct* 1981;17:305–23. doi:10.1016/0020-7683(81)90065-2.
- [9] Keno-Tung C, Olhoff N. Regularized formulation for optimal design of axisymmetric plates. *Int J Solids Struct* 1982;18:153–69. doi:10.1016/0020-7683(82)90023-3.
- [10] Zhou M, Rozvany GIN. The COC algorithm, Part II: Topological, geometrical and generalized shape optimization. *Comput Methods Appl Mech Eng* 1991;89:309–36.
- [11] Bendsøe MP, Sigmund O. Material interpolation schemes in topology optimization. *Arch Appl Mech* 1999;69:635–54.
- [12] Xie YM, Steven GP. A simple evolutionary procedure for structural optimization. *Comput Struct* 1993;49:885–969.
- [13] Sethian JA, Wiegmann A. Structural Boundary Design via Level Set and Immersed Interface Methods. *J Comput Phys* 2000;163:489–528.
- [14] Wang MY, Wang X, Guo D. A level set method for structural topology optimization. *Comput Methods Appl Mech Eng* 2003;192:227–46.
- [15] Allaire G, Jouve F, Toader AM. Structural optimization using sensitivity analysis and a level-set method. *J Comput Phys* 2004;194:363–93.
- [16] Wang MY, Zhou S. Phase field: a variational method for structural topology optimization. *Comput Model Eng Sci* 2004;6:547–66.
- [17] Takezawa A, Nishiwaki S, Kitamura M. Shape and topology optimization based on the phase field method and sensitivity analysis. *J Comput Phys* 2010;229:2697–718.
- [18] Guo X, Zhang W, Zhong W. Doing Topology Optimization Explicitly and Geometrically—A New Moving Morphable Components Based Framework. *J Appl Mech* 2014;81:081009.
- [19] Guo X, Zhang W, Zhang J, Yuan J. Explicit structural topology optimization based on moving morphable components (MMC) with curved skeletons. *Comput Methods Appl Mech Eng* 2016;310:711–48.
- [20] Guedes MJ, Kikuchi N. Preprocessing and Postprocessing for Materials Based on the Homogenization Method With Adaptive Finite Element Methods. *Comput Methods Appl Mech Eng* 1990;83:143–98.
- [21] Torquato S. *Random heterogeneous materials: microstructure and macroscopic properties*. vol. 16. 2013.

-
- [22] Suzuki K, Kikuchi N. A homogenization method for shape and topology optimization. *Comput Methods Appl Mech Eng* 1991;93:291–318.
- [23] Díaz AR, Kikuchi N. Solutions to shape and topology eigenvalue optimization problems using a homogenization method. *Int J Numer Methods Eng* 1992;35:1487–502. doi:10.1002/nme.1620350707.
- [24] Díaz AR, Bendsøe MP. Shape optimization of structures for multiple loading conditions using a homogenization method. *Struct Optim* 1992;4:17–22. doi:10.1007/BF01894077.
- [25] Hassani B, Hinton E. A review of homogenization and topology optimization I—homogenization theory for media with periodic structure. *Comput Struct* 1998;69:707–17.
- [26] Hassani B, Hinton E. A review of homogenization and topology optimization II—analytical and numerical solution of homogenization equations. *Comput Struct* 1998;69:719–38.
- [27] Hassani B, Hinton E. A review of homogenization and topology optimization III—topology optimization using optimality criteria. *Comput Struct* 1998;69:739–56. doi:10.1016/S0045-7949(98)00133-3.
- [28] Sigmund O, Petersson J. Numerical instabilities in topology optimization: A survey on procedures dealing with checkerboards, mesh-dependencies and local minima. *Struct Optim* 1998;16:68–75.
- [29] Sigmund O. Morphology-based black and white filters for topology optimization. *Struct Multidiscip Optim* 2007;33:401–24.
- [30] Wang F, Lazarov BS, Sigmund O. On projection methods, convergence and robust formulations in topology optimization. *Struct Multidiscip Optim* 2011;43:767–84.
- [31] Du J, Olhoff N. Topological design of freely vibrating continuum structures for maximum values of simple and multiple eigenfrequencies and frequency gaps. *Struct Multidiscip Optim* 2007;34:91–110.
- [32] Du J, Olhoff N. Minimization of sound radiation from vibrating bi-material structures using topology optimization. *Struct Multidiscip Optim* 2007;33:305–21. doi:10.1007/s00158-006-0088-9.
- [33] Yoon GH. Structural topology optimization for frequency response problem using model reduction schemes. *Comput Methods Appl Mech Eng* 2010;199:1744–63. doi:https://doi.org/10.1016/j.cma.2010.02.002.
- [34] Yin L, Ananthasuresh GK. Topology optimization of compliant mechanisms with multiple materials using a peak function material interpolation scheme. *Struct Multidiscip Optim* 2001;23:49–62. doi:10.1007/s00158-001-0165-z.
- [35] Lin J, Luo Z, Tong L. A new multi-objective programming scheme for topology optimization of compliant mechanisms. *Struct Multidiscip Optim* 2010;40:241–55. doi:10.1007/s00158-008-0355-z.
- [36] Kiziltas G, Kikuchi N, Volakis JL, Halloran J. Topology optimization of dielectric substrates for filters and antennas using SIMP. *Arch Comput Methods Eng* 2004;11:355–88. doi:10.1007/BF02736229.
- [37] Choi JS, Yoo J. Simultaneous structural topology optimization of electromagnetic sources and ferromagnetic materials. *Comput Methods Appl Mech Eng* 2009;198:2111–21. doi:10.1016/J.CMA.2009.02.015.
- [38] Yoon GH, Jensen JS, Sigmund O. Topology optimization of acoustic–structure interaction problems using a mixed finite element formulation. *Int J Numer Methods Eng* 2007;70:1049–75. doi:10.1002/nme.1900.
- [39] Yoon GH. Acoustic topology optimization of fibrous material with Delany–Bazley empirical material formulation. *J Sound Vib* 2013;332:1172–87. doi:10.1016/J.JSV.2012.10.018.
-

-
- [40] Yoon GH, Kim YY. Element connectivity parameterization for topology optimization of geometrically nonlinear structures. *Int J Solids Struct* 2005;42:1983–2009. doi:10.1016/J.IJSOLSTR.2004.09.005.
- [41] Buhl T, Pedersen CBW, Sigmund O. Stiffness design of geometrically nonlinear structures using topology optimization. *Struct Multidiscip Optim* 2000;19:93–104. doi:10.1007/s001580050089.
- [42] Kang Z, Luo Y. Non-probabilistic reliability-based topology optimization of geometrically nonlinear structures using convex models. *Comput Methods Appl Mech Eng* 2009;198:3228–38. doi:10.1016/J.CMA.2009.06.001.
- [43] Kharmanda G, Olhoff N, Mohamed A, Lemaire M. Reliability-based topology optimization. *Struct Multidiscip Optim* 2004;26:295–307. doi:10.1007/s00158-003-0322-7.
- [44] Zheng B, Chang C-J, Gea HC. Topology optimization of energy harvesting devices using piezoelectric materials. *Struct Multidiscip Optim* 2009;38:17–23. doi:10.1007/s00158-008-0265-0.
- [45] Kim JE, Kim DS, Ma PS, Kim YY. Multi-physics interpolation for the topology optimization of piezoelectric systems. *Comput Methods Appl Mech Eng* 2010;199:3153–68. doi:10.1016/J.CMA.2010.06.021.
- [46] Huang X, Xie YM. Bi-directional evolutionary topology optimization of continuum structures with one or multiple materials. *Comput Mech* 2009;43:393–401. doi:10.1007/s00466-008-0312-0.
- [47] Huang X, Xie Y-MM. A further review of ESO type methods for topology optimization. *Struct Multidiscip Optim* 2010;41:671–83. doi:10.1007/s00158-010-0487-9.
- [48] Xie YM, Steven GP. Evolutionary structural optimization for dynamic problems. *Comput Struct* 1996;58:1067–73. doi:10.1016/0045-7949(95)00235-9.
- [49] Liu J, Chen T, Zhang Y, Wen G, Qing Q, Wang H, et al. On sound insulation of pyramidal lattice sandwich structure. *Compos Struct* 2019;208:385–94. doi:10.1016/J.COMPSTRUCT.2018.10.013.
- [50] Zhao Z-L, Zhou S, Feng X-Q, Xie YM. On the internal architecture of emergent plants. *J Mech Phys Solids* 2018;119:224–39. doi:10.1016/J.JMPS.2018.06.014.
- [51] Radman A, Huang X, Xie YM. Topology optimization of functionally graded cellular materials. *J Mater Sci* 2012;48:1503–10. doi:10.1007/s10853-012-6905-1.
- [52] Huang X, Radman A, Xie YM. Topological design of microstructures of cellular materials for maximum bulk or shear modulus. *Comput Mater Sci* 2011;50:1861–70.
- [53] Radman A, Huang X, Xie YMM. Topological optimization for the design of microstructures of isotropic cellular materials. *Eng Optim* 2013;45:1331–48.
- [54] Xia L, Breitkopf P. A reduced multiscale model for nonlinear structural topology optimization. *Comput Methods Appl Mech Eng* 2014;280:117–34. doi:10.1016/J.CMA.2014.07.024.
- [55] Xia L, Breitkopf P. Multiscale structural topology optimization with an approximate constitutive model for local material microstructure. *Comput Methods Appl Mech Eng* 2015;286:147–67.
- [56] Xia L, Breitkopf P. Recent Advances on Topology Optimization of Multiscale Nonlinear Structures. *Arch Comput Methods Eng* 2017;24:227–49.
- [57] Xia L, Xia Q, Huang X, Xie YM. Bi-directional Evolutionary Structural Optimization on Advanced Structures and Materials: A Comprehensive Review. *Arch Comput Methods Eng* 2018;25:437–78. doi:10.1007/s11831-016-9203-2.
- [58] Li C, Xu C, Gui C, Fox MD. Level set evolution without re-initialization: a new variational formulation. 2005 IEEE Comput. Soc. Conf. Comput. Vis. Pattern Recognit., vol. 1, 2005, p. 430–6 vol. 1. doi:10.1109/CVPR.2005.213.
-

-
- [59] Li C, Xu C, Gui C, Fox MD. Distance Regularized Level Set Evolution and Its Application to Image Segmentation. *IEEE Trans Image Process* 2010;19:3243–54. doi:10.1109/TIP.2010.2069690.
- [60] Osher SJ, Santosa F. Level Set Methods for Optimization Problems Involving Geometry and Constraints: I. Frequencies of a Two-Density Inhomogeneous Drum. *J Comput Phys* 2001;171:272–88. doi:https://doi.org/10.1006/jcph.2001.6789.
- [61] Wang MY, Wang X. “Color” level sets: A multi-phase method for structural topology optimization with multiple materials. *Comput Methods Appl Mech Eng* 2004;193:469–96.
- [62] Allaire G, Jouve F. A level-set method for vibration and multiple loads structural optimization. *Comput Methods Appl Mech Eng* 2005;194:3269–90. doi:https://doi.org/10.1016/j.cma.2004.12.018.
- [63] Shu L, Wang MY, Fang Z, Ma Z, Wei P. Level set based structural topology optimization for minimizing frequency response. *J Sound Vib* 2011;330:5820–34. doi:https://doi.org/10.1016/j.jsv.2011.07.026.
- [64] Allaire G, Jouve F. Minimum stress optimal design with the level set method. *Eng Anal Bound Elem* 2008;32:909–18. doi:https://doi.org/10.1016/j.enganabound.2007.05.007.
- [65] Guo X, Zhang WS, Wang MY, Wei P. Stress-related topology optimization via level set approach. *Comput Methods Appl Mech Eng* 2011;200:3439–52. doi:https://doi.org/10.1016/j.cma.2011.08.016.
- [66] Wang MY, Chen S, Wang X, Mei Y. Design of Multimaterial Compliant Mechanisms Using Level-Set Methods. *J Mech Des* 2005;127:941–56.
- [67] Luo Z, Tong L. A level set method for shape and topology optimization of large-displacement compliant mechanisms. *Int J Numer Methods Eng* 2008;76:862–92. doi:10.1002/nme.2352.
- [68] Burger M, Hackl B, Ring W. Incorporating topological derivatives into level set methods. *J Comput Phys* 2004;194:344–62. doi:https://doi.org/10.1016/j.jcp.2003.09.033.
- [69] Xia Q, Wang MY, Wang S, Chen S. Semi-Lagrange method for level-set-based structural topology and shape optimization. *Struct Multidiscip Optim* 2006;31:419–29.
- [70] Wang S, Wang MY. Radial basis functions and level set method for structural topology optimization. *Int J Numer Methods Eng* 2006;65:2060–90.
- [71] Luo Z, Wang MY, Wang S, Wei P. A level set-based parameterization method for structural shape and topology optimization. *Int J Numer Methods Eng* 2008;76:1–26.
- [72] Svanberg K. The method of moving asymptotes - a new method for structural optimization. *Int J Numer Methods Eng* 1987;24:359–73.
- [73] Li H, Li P, Gao L, Zhang L, Wu T. A level set method for topological shape optimization of 3D structures with extrusion constraints. *Comput Methods Appl Mech Eng* 2015;283:615–35.
- [74] Li H, Luo Z, Zhang N, Gao L, Brown T. Integrated design of cellular composites using a level-set topology optimization method. *Comput Methods Appl Mech Eng* 2016;309:453–75.
- [75] Li H, Luo Z, Gao L, Walker P. Topology optimization for functionally graded cellular composites with metamaterials by level sets. *Comput Methods Appl Mech Eng* 2018;328:340–64.
- [76] Wang Y, Luo Z, Kang Z, Zhang N. A multi-material level set-based topology and shape optimization method. *Comput Methods Appl Mech Eng* 2015;283:1570–86.
- [77] Zheng J, Luo Z, Jiang C, Gao J. Robust topology optimization for concurrent design of dynamic structures under hybrid uncertainties. *Mech Syst Signal Process* 2019;120:540–59.
- [78] Gao J, Li H, Luo Z, Gao L, Li P. Topology optimization of micro-structured materials featured with the specific mechanical properties. *Int J Comput Methods* 2020;17:1850144. doi:10.1142/S021987621850144X.
-

-
- [79] Gao J, Li H, Gao L, Xiao M. Topological shape optimization of 3D micro-structured materials using energy-based homogenization method. *Adv Eng Softw* 2018;116:89–102.
 - [80] Wang Y, Gao J, Luo Z, Brown T, Zhang N. Level-set topology optimization for multimaterial and multifunctional mechanical metamaterials. *Eng Optim* 2017;49:22–42.
 - [81] Fu J, Li H, Xiao M, Gao L, Chu S. Topology optimization of shell-infill structures using a distance regularized parametric level-set method. *Struct Multidiscip Optim* 2018:1–14. doi:10.1007/s00158-018-2064-6.
 - [82] Zhang Y, Li H, Xiao M, Gao L, Chu S, Zhang J. Concurrent topology optimization for cellular structures with nonuniform microstructures based on the kriging metamodel. *Struct Multidiscip Optim* 2018:1–27.
 - [83] Gao J, Luo Z, Li H, Gao L. Topology optimization for multiscale design of porous composites with multi-domain microstructures. *Comput Methods Appl Mech Eng* 2019;344:451–76.
 - [84] Gao J, Luo Z, Li H, Li P, Gao L. Dynamic multiscale topology optimization for multi-regional micro-structured cellular composites. *Compos Struct* 2019;211:401–17.
 - [85] Li H, Luo Z, Gao L, Wu J. An improved parametric level set method for structural frequency response optimization problems. *Adv Eng Softw* 2018;126:75–89.
 - [86] Jiang L, Chen S. Parametric structural shape & topology optimization with a variational distance-regularized level set method. *Comput Methods Appl Mech Eng* 2017;321:316–36. doi:10.1016/J.CMA.2017.03.044.
 - [87] Jiang L, Chen S, Jiao X. Parametric shape and topology optimization: A new level set approach based on cardinal basis functions. *Int J Numer Methods Eng* 2018;114:66–87. doi:10.1002/nme.5733.
 - [88] Fu J, Li H, Xiao M, Gao L, Chu S. Topology optimization of shell-infill structures using a distance regularized parametric level-set method. *Struct Multidiscip Optim* 2019;59:249–62.
 - [89] Cottrell JA, Hughes TJR, Bazilevs Y. *Isogeometric Analysis: Toward Integration of CAD and FEA*. 2009.
 - [90] Hughes TJR, Cottrell JAA, Bazilevs Y. Isogeometric analysis: CAD, finite elements, NURBS, exact geometry and mesh refinement. *Comput Methods Appl Mech Eng* 2005;194:4135–95.
 - [91] de Boor C. A practical guide to splines. *Math Comput* 1980;34:325.
 - [92] Piegl L, Tiller W. *The NURBS book*. Springer Science & Business Media; 2012.
 - [93] Cottrell JA, Evans JA, Lipton S, Scott MA, Sederberg TW. Isogeometric analysis using T-splines. *Comput Methods Appl Mech Eng* 2010;199:229–63. doi:10.1016/J.CMA.2009.02.036.
 - [94] Seo Y-D, Kim H-J, Youn S-K. Isogeometric topology optimization using trimmed spline surfaces. *Comput Methods Appl Mech Eng* 2010;199:3270–96.
 - [95] Hassani B, Khanzadi M, Tavakkoli SM. An isogeometrical approach to structural topology optimization by optimality criteria. *Struct Multidiscip Optim* 2012;45:223–33.
 - [96] Qian X. Topology optimization in B-spline space. *Comput Methods Appl Mech Eng* 2013;265:15–35.
 - [97] Yin L, Zhang F, Deng X, Wu P, Zeng H, Liu M. Isogeometric Bi-Directional Evolutionary Structural Optimization. *IEEE Access* 2019;7:91134–45.
 - [98] Matsui K, Terada K. Continuous approximation of material distribution for topology optimization. *Int J Numer Methods Eng* 2004;59:1925–44.
 - [99] Rahmatalla SF, C.C. S. A Q4/Q4 continuum structural topology optimization implementation. *Struct Multidiscip Optim* 2004;27:130–5.
 - [100] Paulino GH, Le CH. A modified Q4/Q4 element for topology optimization. *Struct Multidiscip Optim* 2009;37:255–64.
-

-
- [101] Guest JK, Prévost JH, Belytschko T. Achieving minimum length scale in topology optimization using nodal design variables and projection functions. *Int J Numer Methods Eng* 2004;61:238–54.
- [102] Kang Z, Wang Y. Structural topology optimization based on non-local Shepard interpolation of density field. *Comput Methods Appl Mech Eng* 2011;200:3515–25.
- [103] Kang Z, Wang Y. A nodal variable method of structural topology optimization based on Shepard interpolant. *Int J Numer Methods Eng* 2012;90:329–42.
- [104] Luo Z, Zhang N, Wang Y, Gao W. Topology optimization of structures using meshless density variable approximants. *Int J Numer Methods Eng* 2013;93:443–64.
- [105] Gao J, Gao L, Luo Z, Li P. Isogeometric topology optimization for continuum structures using density distribution function. *Int J Numer Methods Eng* 2019;119:991–1017.
- [106] Dedè L, Borden MJ, Hughes TJR. Isogeometric Analysis for Topology Optimization with a Phase Field Model. *Arch Comput Methods Eng* 2012;19:427–65.
- [107] Wang Y, Benson DJ. Isogeometric analysis for parameterized LSM-based structural topology optimization. *Comput Mech* 2016;57:19–35.
- [108] Wang Y, Benson DJ. Geometrically constrained isogeometric parameterized level-set based topology optimization via trimmed elements. *Front Mech Eng* 2016;11:328–43. doi:10.1007/s11465-016-0403-0.
- [109] Kang P, Youn S-K. Isogeometric topology optimization of shell structures using trimmed NURBS surfaces. *Finite Elem Anal Des* 2016;120:18–40.
- [110] Ghasemi H, Park HS, Rabczuk T. A level-set based IGA formulation for topology optimization of flexoelectric materials. *Comput Methods Appl Mech Eng* 2017;313:239–58.
- [111] Xie X, Wang S, Xu M, Wang Y. A new isogeometric topology optimization using moving morphable components based on R-functions and collocation schemes. *Comput Methods Appl Mech Eng* 2018;339:61–90.
- [112] Hou W, Gai Y, Zhu X, Wang X, Zhao C, Xu L, et al. Explicit isogeometric topology optimization using moving morphable components. *Comput Methods Appl Mech Eng* 2017;326:694–712.
- [113] Shojaei S, Mohamadianb M, Valizadeh N. Composition of isogeometric analysis with level set method for structural topology optimization. *Iran Univ Sci Technol* 2012;2:47–70.
- [114] Jahangiry HA, Tavakkoli SM. An isogeometrical approach to structural level set topology optimization. *Comput Methods Appl Mech Eng* 2017;319:240–57.
- [115] Taheri AH, Hassani B. Simultaneous isogeometrical shape and material design of functionally graded structures for optimal eigenfrequencies. *Comput Methods Appl Mech Eng* 2014;277:46–80. doi:10.1016/J.CMA.2014.04.014.
- [116] Taheri AH, Abolbashari MH, Hassani B. Free vibration characteristics of functionally graded structures by an isogeometrical analysis approach. *Proc Inst Mech Eng Part C J Mech Eng Sci* 2014;228:1512–30. doi:10.1177/0954406213508757.
- [117] Lieu QX, Lee J. Multiresolution topology optimization using isogeometric analysis. *Int J Numer Methods Eng* 2017;112:2025–47.
- [118] Lieu QX, Lee J. A multi-resolution approach for multi-material topology optimization based on isogeometric analysis. *Comput Methods Appl Mech Eng* 2017;323:272–302.
- [119] Lieu QX, Lee J. An isogeometric multimesh design approach for size and shape optimization of multidirectional functionally graded plates. *Comput Methods Appl Mech Eng* 2019;343:407–37. doi:10.1016/J.CMA.2018.08.017.
- [120] Taheri AH, Suresh K. An isogeometric approach to topology optimization of multi-material and functionally graded structures. *Int J Numer Methods Eng* 2017;109:668–96.
-

-
- [121] Costa G, Montemurro M, Pailhès J. A 2D topology optimisation algorithm in NURBS framework with geometric constraints. *Int J Mech Mater Des* 2018;14:669–96. doi:10.1007/s10999-017-9396-z.
 - [122] Liu H, Yang D, Hao P, Zhu X. Isogeometric analysis based topology optimization design with global stress constraint. *Comput Methods Appl Mech Eng* 2018;342:625–52.
 - [123] Lee S-W, Yoon M, Cho S. Isogeometric topological shape optimization using dual evolution with boundary integral equation and level sets. *Comput Des* 2017;82:88–99. doi:10.1016/J.CAD.2016.08.004.
 - [124] Wang Z-P, Poh LH, Dirrenberger J, Zhu Y, Forest S. Isogeometric shape optimization of smoothed petal auxetic structures via computational periodic homogenization. *Comput Methods Appl Mech Eng* 2017;323:250–71. doi:10.1016/J.CMA.2017.05.013.
 - [125] Gao J, Xue H, Gao L, Luo Z. Topology optimization for auxetic metamaterials based on isogeometric analysis. *Comput Methods Appl Mech Eng* 2019;352:211–36.
 - [126] Wang Y, Xu H, Pasini D. Multiscale isogeometric topology optimization for lattice materials. *Comput Methods Appl Mech Eng* 2017;316:568–85. doi:10.1016/J.CMA.2016.08.015.
 - [127] Lakes R. Foam structures with a negative Poisson's ratio. *Science* (80-) 1987;235:1038–41.
 - [128] Huang C, Chen L. Negative Poisson's Ratio in Modern Functional Materials. *Adv Mater* 2016;28:8079–96.
 - [129] Baughman RH. Auxetic materials: Avoiding the shrink. *Nat* 2003 4256959 2003;425:667–667.
 - [130] Smith C., Grima J., Evans K. A novel mechanism for generating auxetic behaviour in reticulated foams: missing rib foam model. *Acta Mater* 2000;48:4349–56.
 - [131] Spadoni A, Ruzzene M. Elasto-static micropolar behavior of a chiral auxetic lattice. *J Mech Phys Solids* 2012;60:156–71.
 - [132] Pasternak E, Dyskin AV. Materials and structures with macroscopic negative Poisson's ratio. *Int J Eng Sci* 2012;52:103–14.
 - [133] Babae S, Shim J, Weaver JC, Chen ER, Patel N, Bertoldi K. 3D soft metamaterials with negative Poisson's ratio. *Adv Mater* 2013;25:5044–9.
 - [134] Masters IG, Evans KE. Models for the elastic deformation of honeycombs. *Compos Struct* 1996;35:403–22.
 - [135] Frenzel T, Kadic M, Wegener M. Three-dimensional mechanical metamaterials with a twist. *Science* (80-) 2017;358:1072–4.
 - [136] Fu M, Liu F, Hu L. A novel category of 3D chiral material with negative Poisson's ratio. *Compos Sci Technol* 2018;160:111–8.
 - [137] Grima JN, Evans KE. Auxetic behavior from rotating squares. *Springer* 2000;19:1563–5.
 - [138] Saxena KK, Das R, Calius EP. Three Decades of Auxetics Research – Materials with Negative Poisson's Ratio: A Review. *Adv Eng Mater* 2016;18:1847–70.
 - [139] Ren X, Das R, Tran P, Ngo TD, Xie YM. Auxetic metamaterials and structures: a review. *Smart Mater Struct* 2018;27:23001.
 - [140] Sigmund O. Materials with prescribed constitutive parameters: An inverse homogenization problem. *Int J Solids Struct* 1994;31:2313–29.
 - [141] Osanov M, Guest JK. Topology optimization for architected materials design. *Annu Rev Mater Res* 2016;46:211–33.
 - [142] Andreassen E, Lazarov BS, Sigmund O. Design of manufacturable 3D extremal elastic microstructure. *Mech Mater* 2014;69:1–10.
 - [143] Wang Y, Luo Z, Zhang N, Kang Z. Topological shape optimization of microstructural metamaterials using a level set method. *Comput Mater Sci* 2014;87:178–86.
 - [144] Wang F, Sigmund O, Jensen JS. Design of materials with prescribed nonlinear properties. *J Mech Phys Solids* 2014;69:156–74.
-

-
- [145] Kaminakis NT, Drosopoulos GA, Stavroulakis GE. Design and verification of auxetic microstructures using topology optimization and homogenization. *Arch Appl Mech* 2015;85:1289–306. doi:10.1007/s00419-014-0970-7.
- [146] Xia L, Breitkopf P. Design of materials using topology optimization and energy-based homogenization approach in Matlab. *Struct Multidiscip Optim* 2015;52:1229–41.
- [147] Wu J, Luo Z, Li H, Zhang N. Level-set topology optimization for mechanical metamaterials under hybrid uncertainties. *Comput Methods Appl Mech Eng* 2017;319:414–41.
- [148] Wang F. Systematic design of 3D auxetic lattice materials with programmable Poisson's ratio for finite strains. *J Mech Phys Solids* 2018;114:303–18.
- [149] Zong H, Zhang H, Wang Y, Wang MY, Fuh JYH. On two-step design of microstructure with desired Poisson's ratio for AM. *Mater Des* 2018;159:90–102.
- [150] Schwerdtfeger J, Wein F, Leugering G, Singer RF, Körner C, Stingl M, et al. Design of auxetic structures via mathematical optimization. *Adv Mater* 2011;23:2650–4.
- [151] Zhang H, Luo Y, Kang Z. Bi-material microstructural design of chiral auxetic metamaterials using topology optimization. *Compos Struct* 2018;195:232–48.
- [152] de Lima CR, Paulino GH. Auxetic structure design using compliant mechanisms: A topology optimization approach with polygonal finite elements. *Adv Eng Softw* 2019;129:69–80.
- [153] Clausen A, Wang F, Jensen JS, Sigmund O, Lewis JA. Topology Optimized Architectures with Programmable Poisson's Ratio over Large Deformations. *Adv Mater* 2015;27:5523–7.
- [154] Jones RM, Bert CW. *Mechanics of composite materials* 1975.
- [155] Hou X, Hu H, Silberschmidt V. A novel concept to develop composite structures with isotropic negative Poisson's ratio: Effects of random inclusions. *Compos Sci Technol* 2012;72:1848–54.
- [156] Wang X-T, Wang B, Wen Z-H, Ma L. Fabrication and mechanical properties of CFRP composite three-dimensional double-arrow-head auxetic structures. *Compos Sci Technol* 2018;164:92–102.
- [157] Shufrin I, Pasternak E, Dyskin A V. Hybrid materials with negative Poisson's ratio inclusions. *Int J Eng Sci* 2015;89:100–20.
- [158] Vogiatzis P, Chen S, Wang X, Li T, Wang L. Topology optimization of multi-material negative Poisson's ratio metamaterials using a reconciled level set method. *Comput Des* 2017;83:15–32.
- [159] Hughes TJR. *The finite element method: linear static and dynamic finite element analysis*. Courier Corporation; 2012.
- [160] Shepard D. A two-dimensional interpolation function for irregularly-spaced data. *Proc. 1968 23rd ACM Natl. Conf., ACM*; 1968, p. 517–24.
- [161] Wendland H. Piecewise polynomial, positive definite and compactly supported radial functions of minimal degree. *Adv Comput Math* 1995;4:389–96.
- [162] Rozvany GIN, Bendsøe MP, Kirsch U. Layout optimization of structures. *Appl Mech Rev* 1995;48:41–119.
- [163] Li H, Luo Z, Gao L, Qin Q. Topology optimization for concurrent design of structures with multi-patch microstructures by level sets. *Comput Methods Appl Mech Eng* 2018;331:536–61.
- [164] Thomsen J. Topology optimization of structures composed of one or two materials. *Struct Optim* 1992;5:108–15.
- [165] Sigmund O, Torquato S. Design of materials with extreme thermal expansion using a three-phase topology optimization method. *J Mech Phys Solids* 1997;45:1037–67.
- [166] Gibiansky L V., Sigmund O. Multiphase composites with extremal bulk modulus. *J Mech Phys Solids* 2000;48:461–98.
-

- [167] Sigmund O. Design of multiphysics actuators using topology optimization - Part II: Two-material structures. *Comput Methods Appl Mech Eng* 2001;190:6605–27.
- [168] Luo Y, Kang Z. Layout design of reinforced concrete structures using two-material topology optimization with Drucker--Prager yield constraints. *Struct Multidiscip Optim* 2013;47:95–110.
- [169] Stegmann J, Lund E. Discrete material optimization of general composite shell structures. *Int J Numer Methods Eng* 2005;62:2009–27.
- [170] Gao T, Zhang W. A mass constraint formulation for structural topology optimization with multiphase materials. *Int J Numer Methods Eng* 2011;88:774–96.
- [171] Yin L, Ananthasuresh GK. Topology optimization of compliant mechanisms with multiple materials using a peak function material interpolation scheme. *Struct Multidiscip Optim* 2001;23:49–62.
- [172] Zuo W, Saitou K. Multi-material topology optimization using ordered SIMP interpolation. *Struct Multidiscip Optim* 2017;55:477–91.
- [173] Tavakoli R, Mohseni SM. Alternating Active-Phase Algorithm for Multimaterial Topology Optimization Problems a 115-Line Matlab Implementation. *Struct Multidiscip Optim* 2014;49:621–42.
- [174] Sanders ED, Aguiló MA, Paulino GH. Multi-material continuum topology optimization with arbitrary volume and mass constraints. *Comput Methods Appl Mech Eng* 2018;340:798–823.
- [175] Luo Z, Wang MY, Tong L, Wang S. Shape and topology optimization of compliant mechanisms using a parameterization level set method. *J Comput Phys* 2007;227:680–705.
- [176] Andreassen E, Andreasen CS. How to determine composite material properties using numerical homogenization. *Comput Mater Sci* 2014;83:488–95.
- [177] Ma Z-D, Kikuchi N, Cheng H-C. Topological design for vibrating structures. *Comput Methods Appl Mech Eng* 1995;121:259–80.